

Unravelling Complex Photo-Induced Dynamics by Femtosecond Time-Resolved Vibrational Absorption Spectroscopy

Dissertation

zur Erlangung des Doktorgrades

Dr. rer. nat.

der Mathematisch-Naturwissenschaftlichen Fakultät
der Christian-Albrechts-Universität zu Kiel

vorgelegt von

Rebecca Holtmann

Institut für Physikalische Chemie

Kiel 2023

Erster Gutachter: Prof. Dr. Friedrich Temps

Zweite Gutachterin: Prof. Dr. Melanie Schnell

Tag der mündlichen Prüfung: 19.04.2023

Zum Druck genehmigt: 19.04.2023

Eidesstattliche Erklärung

Hiermit erkläre ich, dass die vorliegende Abhandlung – abgesehen von der Beratung durch meinen Betreuer Herrn Prof. Dr. Friedrich Temps – nach Inhalt und Form meine eigene Arbeit ist. Diese Arbeit hat weder in Auszügen noch in ganzer Form einer anderen Stelle im Rahmen eines Promotionsverfahrens vorgelegen. Sie wurde in ihrer Gesamtheit nicht veröffentlicht und auch nicht zur Veröffentlichung eingereicht. Kapitel 3 dieser Arbeit wurde in einer fachwissenschaftlichen Zeitschrift veröffentlicht.

KAPITEL 3

Rebecca Holtmann, Amke Nimmrich, Hendrik Böhnke and Friedrich Temps, *“Long-lived Excited States in 7- and 9-Methylpurine Probed by fs Time-Resolved Vibrational Absorption Spectroscopy”*, in: 22nd International Conference on Ultrafast Phenomena 2020, F. Kärtner, M. Khalil, R. Li, F. Légaré and T. Tahara, eds., OSA Technical Digest (Optical Society of America, 2020), paper M4B.19.

Diese Arbeit ist unter Einhaltung der Regeln guter wissenschaftlicher Praxis der Deutschen Forschungsgemeinschaft entstanden. Ein akademischer Grad wurde mir nicht entzogen.

Kiel, Februar 2023

Rebecca Holtmann

Abstract

The present Thesis presents a study on the femtosecond time-resolved vibrational absorption spectroscopy (TVAS) of electronically excited molecules. The employed experimental setup generated probe pulses in the mid-infrared spectral region which allowed for structure-sensitive detection. Experimentally observed vibrational marker bands could be assigned to the involved molecular species by comparison with calculated vibrational spectra. Four molecular systems were selected for detailed investigation, which are highly relevant, since key steps in their photo-induced deactivation and reaction dynamics are still poorly understood. The molecules 7- and 9- methylpurine (7-MePur, 9-MePur) as well as N^6,N^6 -dimethyladenine (DMAde) have a purine scaffold as chromophore in common. However, completely different relaxation processes were detected by TVAS after photoexcitation. For 7- and 9-MePur, efficient population of long-lived excited states was observed. After $S_2(\pi\pi^*)$ photoexcitation, deactivation via the optically dark $S_1(n\pi^*)$ state occurred with $\tau(7\text{-MePur}) = 250 \pm 30$ ps and $\tau(9\text{-MePur}) = 480 \pm 60$ ps followed by intersystem crossing to the $T_1(\pi\pi^*)$ state. In contrast, the deactivation of electronically excited DMAde proceeded via a structural rearrangement in the $S_1(\pi\pi^*)$ state leading to an intramolecular charge transfer state (ICT). The latter was identified as a structure reached by pronounced twisting and wagging motions of the dimethylamino group with respect to the purine moiety. These results showed that TVAS can provide detailed insights to better understand the relationship between chemical and electronic structure that regulate the accessibility and efficiency of deactivation pathways. Furthermore, TVAS measurements of acetylacetone (AA) and methyl salicylate (MS) in acetonitrile (ACN) and cyclohexane (CHX) solutions were performed. For AA, photoproduct formation took place via two distinct pathways on the pico- and nanosecond time scales. The photoproduct was identified as the CTC isomer which arises from *cis-trans* isomerisation around the C=C double bond. For MS, photoproduct formation was found in both solvents as a novel deactivation channel. The photoproduct was assigned to a rotamer in the S_0 state and was formed by a twist of 180° of the ester moiety. TVAS did not only reveal valuable information on the mechanistic and kinetic details after photoexcitation, but was also perfectly suited to study the influence of the solvent on the photo-induced dynamics. While for AA the solvent determined the excited-state equilibrium between the CCC and CTC isomers, the excited-state lifetimes of MS with $\tau_{\text{ACN}} \approx 115$ ps and $\tau_{\text{CHX}} \approx 300$ ps strongly depended on the solvent.

Kurzzusammenfassung

Die vorliegende Arbeit stellt eine Studie zur Femtosekunden-zeitaufgelösten Schwingungsabsorptionsspektroskopie (TVAS) von elektronisch angeregten Molekülen dar. Mit dem experimentellen Aufbau wurden Abfragepulse im mittleren infraroten Spektralbereich erzeugt, die eine struktursensitive Detektion erlaubten. Dabei konnten die experimentellen charakteristischen Schwingungsbanden den beteiligten Spezies durch den Vergleich mit berechneten Schwingungsspektren zugeordnet werden. Vier relevante molekulare Systeme, deren photoinduzierte Desaktivierungs- und Reaktionsdynamik bisher wenig verstanden war, wurden für eine detaillierte Untersuchung ausgewählt. Die Moleküle 7- und 9-Methylpurin (7-MePur, 9-MePur) sowie N^6, N^6 -Dimethyladenin (DMAde) haben zwar das Puringerüst als Chromophor gemeinsam, dennoch wurden nach Photoanregung unterschiedliche Relaxationsprozesse detektiert. Für 7- und 9-MePur wurde die Bevölkerung langlebiger angeregter Zustände beobachtet. Nach $S_2(\pi\pi^*)$ -Anregung erfolgte die Desaktivierung über den $S_1(n\pi^*)$ -Zustand mit $\tau(7\text{-MePur}) = 250 \pm 30$ ps und $\tau(9\text{-MePur}) = 480 \pm 60$ ps, gefolgt von einem Übergang in den $T_1(\pi\pi^*)$ -Zustand. Im Gegensatz dazu fand im elektronisch angeregten DMAde die Desaktivierung über eine strukturelle Umordnung im $S_1(\pi\pi^*)$ -Zustand statt, die zu einem intramolekularen landungstransferierten Zustand führte. Für letzteren wurde eine Struktur festgestellt, die durch ausgeprägtes Drehen und Verkippen der Dimethylaminogruppe in Bezug zum Puringerüst erreicht wurde. Diese Ergebnisse zeigten, dass die TVAS detaillierte Einblicke lieferte, um den Zusammenhang zwischen chemischer und elektronischer Struktur, der die Zugänglichkeit und Effizienz von Desaktivierungskanälen reguliert, besser verstehen zu können. Darüberhinaus wurden TVAS-Messungen für Acetylaceton (AA) und Salicylsäuremethylester (MS) in Acetonitril (ACN) und in Cyclohexan (CHX) durchgeführt. Für AA fand die Bildung eines Photoproduktes über zwei Kanäle auf der Piko- und Nanosekundenzeitskala statt. Das Photoprodukt ist das CTC-Isomer, welches über *cis-trans* Isomerisierung um die C=C Doppelbindung erhalten wurde. Für MS erfolgte die Photoproduktbildung in beiden Lösungsmitteln als neuer Desaktivierungspfad. Das Photoprodukt wurde einem Rotamer im S_0 -Zustand zugeordnet und über eine 180° -Drehung der Estergruppe gebildet. Die TVAS lieferte damit nicht nur wertvolle Informationen über die mechanistischen und kinetischen Details nach Photoanregung, sondern war auch gut geeignet, um den Einfluss des Lösungsmittels auf die photoinduzierte Dynamik zu untersuchen. Während das Lösungsmittel bei AA das Gleichgewicht zwischen den CCC- und CTC-Isomeren im angeregten Zustand bestimmte, hingen die Lebenszeiten des angeregten Zustands von MS mit $\tau_{\text{ACN}} \approx 115$ ps und $\tau_{\text{CHX}} \approx 300$ ps stark vom Lösungsmittel ab.

Contents

I	Introduction and Experimental Techniques	1
1	Introduction	3
2	Experimental and Computational Methods	19
2.1	Time-resolved fluorescence up-conversion	19
2.2	Time-resolved electronic absorption spectroscopy	20
2.2.1	Data analysis by singular value decomposition	22
2.3	Time-resolved vibrational absorption spectroscopy	24
2.3.1	Experimental setup	24
2.3.2	Detection unit and measurement conditions	28
2.3.3	Data processing and data analysis	30
2.3.4	Assignment of the experimental vibrational bands	32
2.4	Quantum chemical ab initio calculations	33
2.4.1	The Møller-Plesset approach	37
2.4.2	The coupled-cluster method	38
II	Results and Discussion	47
3	Long-lived Excited States in 7- and 9-Methylpurine Probed by fs Time-Resolved Vibrational Absorption Spectroscopy	49
3.1	Introduction	50
3.2	Experimental Details	50
3.3	Results and Discussion	51
4	Population of long-lived excited states in 7- and 9-methylpurine unveiled by fs time-resolved vibrational absorption spectroscopy	55
4.1	Introduction	56
4.2	Methods	59

4.3	Results	61
4.4	Discussion	71
4.5	Conclusions	76
4.6	Supporting Information	81
5	Unravelling the photo-induced dynamics of N^6,N^6-dimethyladenine by femtosecond time-resolved spectroscopy from the UV to the MIR	95
5.1	Introduction	97
5.2	Methods	100
5.3	Results	104
5.4	Discussion	117
5.5	Conclusions	122
5.6	Supporting Information	129
6	<i>Cis-trans</i> isomerisation dynamics of UV-excited acetylacetone unveiled by femtosecond time-resolved vibrational absorption spectroscopy	137
6.1	Introduction	138
6.2	Methods	140
6.3	Results	142
6.4	Discussion	149
6.5	Conclusions	153
6.6	Supporting Information	160
7	Spectroscopic and theoretical study on the ultrafast deactivation dynamics and dual fluorescence of methyl salicylate	165
7.1	Introduction	166
7.2	Methods	170
7.3	Results	173
7.4	Discussion	186
7.5	Conclusions	190
7.6	Supporting Information	195

III Concluding Discussion	205
8 Discussion	207
8.1 Experimental requirements	207
8.2 Data analysis and interpretation	208
9 Summary	213
IV Appendix	219

Part I

Introduction and Experimental Techniques

Commonly, spectroscopic methods that have emerged since then are based on the so-called pump-probe principle, which is schematically presented in Fig. 1.1.

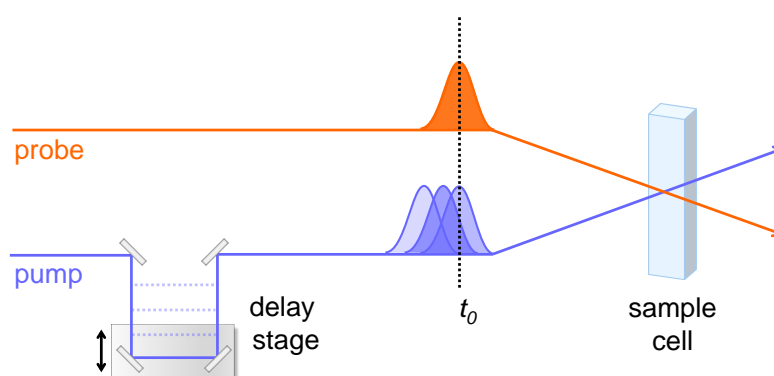


Figure 1.1: Schematic illustration of the pump–probe principle that is used in ultrafast time-resolved spectroscopy.

Here, two ultrashort laser pulses, namely the pump (purple) and probe (orange) pulse, are focused into the sample cell that contains the molecules of interest. In the sample cell, the pump and probe pulses are spatially and temporally overlapped. While the pump pulse transfers the molecules to an excited state, the molecular response is monitored via the interaction between the excited molecules and the probe pulse. More precisely, the molecules are further excited by the absorption of the probe light. Concurrently, this can be understood as a snapshot of the excited-state population in its respective state at a specific time. In order to record a series of those snapshots to follow the evolution of the molecules over time, the temporal arrival of the pump pulse in the sample cell is varied by an optical delay stage as depicted in Fig. 1.1. Hence, the pump–probe technique allows one to detect the ensuing dynamics of the molecules after photoexcitation as function of pump–probe time delay (Δt). Thereby, the accessible temporal window to follow the molecular dynamics is defined by the length of the delay stage. When the pump and probe laser pulses reach the sample cell simultaneously, this is commonly referred to as *time-zero* t_0 ($\Delta t = 0$) of a pump–probe experiment.

Typically, narrow-band pump pulses in the ultraviolet or visible spectral region are applied, which induce a transition to an electronically excited state. In contrast, the probe pulses are spectrally broad to detect complete spectra at each delay step. Transitions to higher-lying electronic states are stimulated by employing broadband white-light probe pulses spanning from 325 nm up to 700 nm. Alternatively, probe pulses in the mid-infrared (mIR) spectral region ($4000\text{--}800\text{ cm}^{-1}$)^{4–15} induce transitions between distinct vibrational levels. These ultrafast spectroscopic techniques are referred to as femtosecond time-resolved electronic absorption spectroscopy (TEAS) and femtosecond time-resolved vibrational absorption spectroscopy (TVAS), respectively.

In the present Thesis, mid-infrared probe pulses are used as main tool to allow for structure-sensitive detection. This means that the observed experimental signals are connected to a specific structural motif in the molecule.

In Fig. 1.2a), a schematic illustration of an exemplary deactivation pathway of an electronically excited molecule, isomer A, is visualised. The excitation to the S_1 state by a pump pulse at λ_{exc} is followed by a rapid funneling into a conical intersection (CI). At the CI, deactivation leads back to the (hot) ground state (GS) and/or to the photoproduct isomer B. Each of the involved species

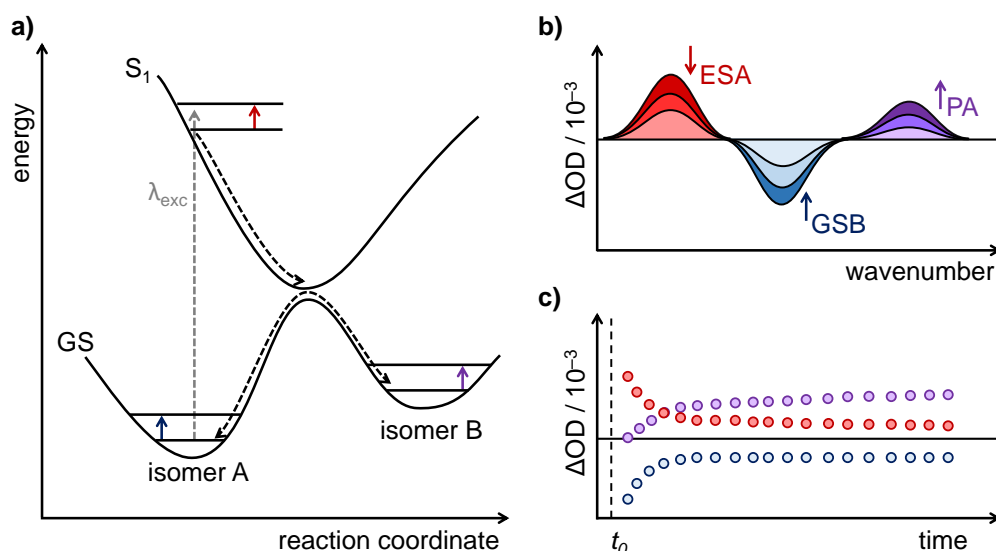


Figure 1.2: a) Schematic visualisation of the deactivation and reaction pathways (dashed black arrows) of isomer A after excitation at λ_{exc} (grey dashed arrow). The spectro-temporal evolution of isomer A can be followed by detection of the vibrational transitions (vertical coloured arrows) which arise from absorption of the mid-IR probe pulses. In the b) corresponding transient vibrational spectra and c) time profiles, the negative ground-state bleach (GSB) is displayed in blue, whereas vibrational absorption in the excited state (ESA) and photoproduct absorption (PA) of isomer B are coloured in red and purple, respectively. The coloured arrows in b) show the temporal evolutions of each vibrational band in the time-resolved spectra.

has a unique molecular and vibrational structure. As a consequence, each will show different vibrational transitions, depicted as vertical coloured arrows in Fig. 1.2a). These vibrational transitions are detected using laser pulses in the mid-infrared spectral region as probe pulses. Thereby, the different species can readily be distinguished and identified owing to their distinct absorption patterns. As the overall absorption spectrum thus highly depends on the exact composition of the molecular ensemble, altering the delay time between the pump and the probe pulses allows for detailed insights into the photo-induced dynamics.

The actual output of a UV/vis-pump and mIR-probe experiment, shown in Fig. 1.2b), is a series of vibrational absorption difference spectra $\Delta OD(\lambda, \Delta t)$. The difference in absorption ΔOD is obtained by subtracting the absorption of the unexcited sample $A(\lambda)$ from the absorption of the excited sample $A^*(\lambda, \Delta t)$:

$$\Delta OD(\lambda, \Delta t) = A^*(\lambda, \Delta t) - A(\lambda) \quad (1.1)$$

As displayed in the vibrational absorption difference spectra in Fig. 1.2b), several vibrational bands arising from different electronic and vibrational states may contribute to the overall signal. After photoexcitation, the negative band coloured in blue corresponds to ground-state bleaching (GSB). Since the GS is depopulated by the pump pulse, this results in a lower absorption compared to the unexcited sample, leading to negative values for ΔOD . Concurrently, the GSB reflects the inverted experimental FTIR spectrum of the investigated molecule in its electronic GS. Thus, the repopulation of the GS (GSR, ground-state recovery) is easily accessible via TVAS. In contrast, the assignment of positive signals (coded in red and purple) is more challenging because they may originate from excited-state absorption (ESA) of the initially excited molecule, from formation of photoproducts (PA), and/or from vibrationally hot intermediates in the excited or ground state, respectively. In addition, electronic deactivation dynamics often involves vibrational relaxation (VR) from a vibrationally excited state towards its relaxed minimum. This is again observed as positive contribution in the data. In an excited electronic state, VR is generally characterised by spectral narrowing and a pronounced blue-shift of the signal towards later times, until the relaxed state is reached. A similar spectro-temporal behaviour is observed for so-called hot ground-state absorption (HGSA). While the negative GSB signals originate from the vibrationally relaxed electronic ground state, contributions from highly excited vibrational levels in the electronic GS give rise to HGSA. The latter appears as positive band, whose spectral position is red-shifted with respect to the corresponding relaxed vibrational band in the electronic GS. HGSA signatures are blue-shifting at later times and typically observed when the excited state is short-lived ($\tau < 1$ ps).

From the analysis of the transient vibrational spectra, the time profiles presented in Fig. 1.2c) are obtained. A detailed description of the data analysis is given in Chapter 2. The time profiles visualise the temporal evolutions of the involved species and yield time constants that describe the underlying dynamics after photoexcitation.

Although the recorded time-resolved vibrational difference spectra contain all information needed to follow the dynamics, disentangling the spectra is by no means a trivial task. To identify the molecular species, their vibrational spectra are theoretically predicted by quantum chemical calculations. Thus, TVAS becomes state-specific as experimentally detected vibrational marker bands in

different electronic states are assigned and identified by comparison with the calculations. Based on this information, a deactivation mechanism after photoexcitation can be derived. Therefore, the combination of TVAS and quantum chemical calculations is a powerful tool to shed light on the electronic relaxation and reaction processes. In addition, a detailed understanding of the relationship between chemical and electronic structure is obtained.

Although this Thesis focuses on femtosecond time-resolved vibrational absorption spectroscopy, where pump pulses in the UV and mid-infrared probe pulses have been used, in parts other spectroscopic techniques like time-correlated single photon counting (TCSPC), time-resolved fluorescence spectroscopy by the up-conversion technique (TFLS) as well as time-resolved electronic absorption spectroscopy (TEAS) have been employed. Since TCSPC and TFLS unveil radiative deactivation channels, the information obtained from those measurements is limited to the dynamics proceeding on potential energy surfaces (PES) of optically bright states. In contrast, non-radiative relaxation pathways, formation of photoproducts and intermediates, as well as ground-state dynamics can be investigated by means of TEAS. Here, the spectral probe window is limited to the UV/vis region. Consequently, processes below $\lambda \leq 325$ nm like detection of the ground-state recovery, or the formation of photoproducts and intermediates absorbing in the UV spectral region are not feasible. More importantly, an unambiguous assignment of the molecular species that give rise to the observed contributions in the data remains elusive. In addition, the experimental bands are spectrally broad and tend to overlap, which makes it difficult to distinguish electronically similar molecular species. The above-mentioned limitations can be overcome by TVAS, because this powerful method allows for structure-sensitive detection.

The TVAS experiment has only recently been set up in our work group.¹⁶ The aim of the present Thesis is to establish and further develop the experiment. To this end, detailed studies have been performed by investigating four selected molecular systems with the TVAS experiment. An overview of the studied compounds is shown in Fig. 1.3. On the one hand, these systems are highly relevant, since key steps of their photo-induced dynamics are still not understood. On the other hand, they cover a wide range of possible electronic deactivation and reaction processes that can occur after photoexcitation.

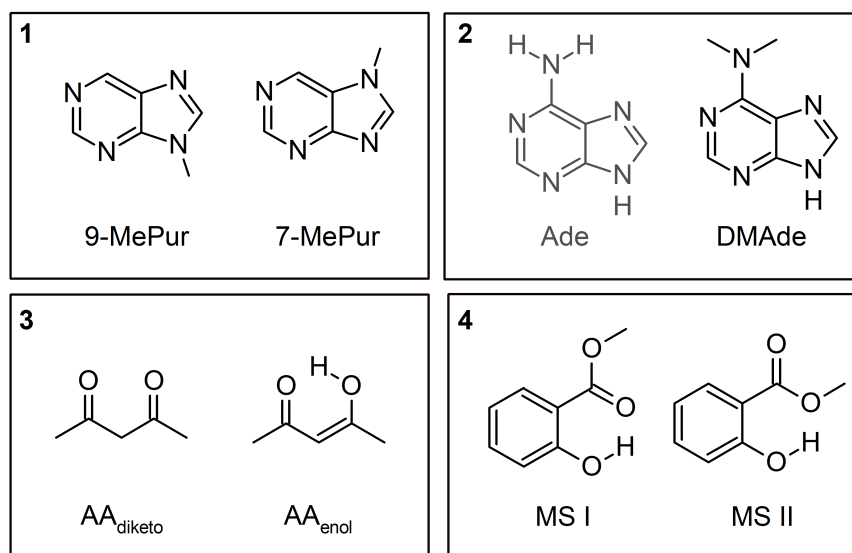


Figure 1.3: Overview of the four selected molecular systems which have been investigated in the present Thesis by femtosecond time-resolved vibrational absorption spectroscopy. Adenine (Ade) is shown here only for comparison with *N*⁶,*N*⁶-dimethyladenine (DMAde) and therefore coloured in grey.

The photo-induced dynamics of the following molecules, whose chemical structures are depicted in Fig. 1.3, have been investigated by femtosecond time-resolved vibrational absorption spectroscopy:

- 1) 9- and 7-methylpurine (9-MePur, 7-MePur),
- 2) *N*⁶,*N*⁶-dimethyladenine (DMAde), a derivative of the nucleobase adenine (Ade),
- 3) acetylacetone (AA) in its enolic form, and
- 4) methyl salicylate (MS) in its rotameric forms I and II.¹

A short introduction to the above-mentioned molecular systems will be provided in the following. They will be covered in detail in the respective chapters.

1) The compounds 7- and 9-methylpurine are methylated analogues of the nucleobase purine. These molecules are highly relevant and important model

¹We note here that different conventions have been used for naming the two rotamers in the literature. We use the logical convention to label the thermo stable species as “rotamer MS I” and the next one as “rotamer MS II” (see Fig. 1.3).

systems regarding the photochemistry of DNA and RNA building blocks. Purine is the parent molecule of the canonical DNA nucleobases adenine (Ade) and guanine (Gua), whose electronic relaxation pathways have been extensively studied in the last decades.^{17–23} For the canonical DNA nucleobases, the initially excited state is rapidly depopulated due to the accessibility of conical intersections (CIs).¹⁹ The latter connects the excited state with the electronic ground state, making efficient non-radiative deactivation channels available. This is reflected by ultrashort excited-state lifetimes of $\tau < 1$ ps for adenine and guanine.^{18,19,24–27} In contrast, their parent molecule purine and its methylated isomer 9-MePur show population of much longer-lived excited states, which have been detected by means of transient electronic absorption spectroscopy.²⁸ The authors²⁸ postulated that the initially excited $S_2(\pi\pi^*)$ state deactivates rapidly via internal conversion (IC) to the optically dark $S_1(n\pi^*)$ state, followed by intersystem crossing (ISC) to a long-lived triplet state. Distinct evidence for their proposed mechanism remains elusive, though. Furthermore, they suggested that purine and 9-MePur exhibit similar photo-induced deactivation pathways. However, a solvent-dependent tautomeric equilibrium between the 7H- and 9H-tautomers of purine is observed.^{28–33} Consequently, both tautomers may coexist in solution in the electronic ground state. Another prominent example for 7H/9H-tautomers is Ade where the excited-state lifetimes of both tautomers differ drastically. While an excited-state time constant of $\tau \approx 200$ fs was determined for the 9H-tautomer of Ade, a significantly longer value of $\tau \approx 8$ ps was found for its 7H tautomeric form,^{18,27,34} indicating the initial assumption that both purine tautomers might exhibit identical dynamics subsequent to photoexcitation might not hold true. As TEAS lacks structure sensitivity, it was not possible to distinguish between different tautomers by direct means. Although the tautomers contribute individually to the detected signals after photoexcitation, the recorded time-resolved data reflect the sum of both contributions, which are no longer clearly assignable to the respective tautomers. In particular, when the concentration or the absorption coefficient of a tautomer is small, it may be impossible to separate its contribution to the experimental data. Accordingly, two main questions regarding the photo-induced dynamics of purine and its methylated isomers remain elusive: Do 7H-/9H-Pur and 7-/9-MePur exhibit similar electronic deactivation pathways taking place on comparable time scales? And do the detected long-lived excited-state signals originate from the optically dark $S_1(n\pi^*)$ and the triplet state as

suggested in the literature?²⁸ Thus, transient vibrational absorption spectroscopy, allowing for structure-sensitive detection, is an attractive spectroscopic method for the investigation of purine, 7- and 9-methylpurine. Since the TVAS results of purine in different solvents (ACN- d_3 , D_2O and CD_3OD) were part of a Master's thesis³³ in our work group, the present Thesis focuses on the dynamics of 7- and 9-methylpurine, where tautomerism is hindered by methylation at the N7 or N9 position, respectively.

2) N^6,N^6 -dimethyladenine (DMAde) is structurally related to both purine and adenine (cf. Fig. 1.3). In DMAde, the amino hydrogens are substituted by methyl groups, making new deactivation channels accessible. Contrary to other nucleobase derivatives, DMAde shows dual fluorescence in various solvents.^{35–40} It is proposed that the dual fluorescence arises from two distinct excited states: the locally excited state (LE) and a twisted intramolecular charge transfer (TICT) state.^{35–40} The prototypical and intensively studied molecule regarding fluorescence from an intramolecular charge transfer state is 4-(N,N -dimethylamino)benzonitrile (DMABN).^{41–67} There, photoexcitation leads to an intramolecular electron transfer from the dimethylamino nitrogen to the aromatic ring. Concurrently, a twisting motion by 90° of the dimethylamino group with respect to the aromatic ring is assumed to proceed in the excited state. Since similar observations as those for DMABN have been reported for DMAde,^{35–40} its anomalous emission band in the visible spectral range is tendentially ascribed to a TICT state. However, the origin and the underlying mechanism of the unusual emission properties of DMAde are still controversially discussed in the literature and remain an open issue. Since the formation of a TICT species is accompanied by a pronounced structural rearrangement of the molecule, TVAS is perfectly suited to ultimately identify the involved species after photoexcitation.

3) Acetylacetone (AA) is the prototypical aliphatic β -diketone and known for its keto–enol tautomerism. Two tautomeric forms of AA, the diketonic and enolic species, are observed (cf. Fig. 1.3). The enolic species is stabilised by an intramolecular hydrogen bond.^{68–71} Analogously to purine, the ratio between the diketonic and enolic tautomers strongly depends on the molecular environment. While the enol is favoured in the gas phase and in apolar, aprotic solvents (> 90 %),^{70,72,73} the diketone coexists in sizeable amounts in polar solvents (40–

80 %).^{69,73,74} In the gas phase, UV photoexcitation leads to population of a triplet state, followed by fragmentation of the molecule, as confirmed by the detection of OH and CH₃ fragments.^{75–80} In contrast, the photo-induced dynamics of AA in the liquid phase are governed by fast deactivation processes.⁸¹ An experimental study⁸¹ of AA in various solvents by TEAS revealed that upon excitation to the optically bright S₂($\pi\pi^*$) state an ultrafast excited-state intramolecular proton transfer (ESIPT) takes place. Subsequently, the optically dark S₁($n\pi^*$) state is populated via internal conversion, which can be followed by rotamerisation in the excited state. This leads to the formation of so-called non-chelated enolic isomers, which lack the stabilising intramolecular hydrogen bond.^{68–71} However, the photochemical pathways towards these non-chelated isomers as well as which isomer or isomers is/are formed remain unknown. Therefore, AA is selected to be studied by TVAS in deuterated acetonitrile (ACN-d₃) and cyclohexane (CHX) solution to unambiguously identify the photoproduct(s) and to gain a detailed understanding on the molecular processes after UV photoexcitation in the liquid phase.

4) Methyl salicylate (MS) shows dual fluorescence, but its origin as well as the photo-induced dynamics of MS in general are still poorly understood. Moreover, MS is a prototypical species for many derivatives. While the fluorescence of MS in the visible spectral range is assigned to arise from a proton-transferred species, which is formed via an intramolecular proton transfer in the excited state (ESIPT),^{82–87} the species emitting in the near-UV remains elusive. In this context, two main possibilities are controversially discussed in the literature. The near-UV band is either explained by the co-existence of a second ground-state rotamer,^{84,85,88–94} named MS II, next to the thermodynamically stable one (MS I), or it is ascribed to a fraction of the excited-state population whose relaxation does not proceed via the ESIPT reaction.^{86,87,95–97} The latter implies that two competing deactivation channels are accessible for MS I after photoexcitation. One fraction of the initially excited molecules undergoes an ultrafast ESIPT process within $\tau < 100$ fs leading to the proton-transferred species of MS I, while the other fraction directly returns back to the GS, which then gives rise to the observed fluorescence in the near-UV. Since most of the studies on methyl salicylate focus on the mechanism and the involved species in the dual fluorescence, investigation of non-radiative deactivation pathways has been largely neglected.

Therefore, TVAS is applied to shed light on the underlying deactivation pathways as well as to gain detailed insight into the molecular species that are formed after excitation of methyl salicylate in acetonitrile (ACN-d₃) and cyclohexane (CHX) solution.

This brief look at the investigated molecular systems underlines that important details regarding their photochemical and photophysical behaviour are still unknown. TVAS is perfectly suited to address these open questions discussed above and to overcome the afore-mentioned limitations of other spectroscopic techniques. Furthermore, the selected molecules cover a wide range of possible electronic deactivation and reaction processes that can occur after photoexcitation. This includes not only radiative and non-radiative processes like fluorescence, internal conversion, or intersystem crossing, but also photoproduct formation and structural rearrangements, e.g., transfer of a proton, or *cis-trans* isomerisation in the ground and excited states, respectively. Concurrently, this makes the four selected molecular systems ideal candidates to evaluate the TVAS experiment itself. These measurements, which I will report in this Thesis below, form the basis to shed light on the advantages and possibilities as well as on the experimental limitations of TVAS as an ultrafast spectroscopic method.

Comprehensive overviews on the experimental findings for the above-described molecular systems, obtained in the present Thesis, as well as the latest state of research can be found in Chapters 3–7. While the published contribution in Chapter 3 only provides a short overview on the results obtained for 7- and 9-methylpurine, a more detailed description of the data is presented in Chapter 4. Experimental details on the employed femtosecond time-resolved spectroscopic techniques alongside with a short introduction to quantum chemical *ab initio* calculations are given in Chapter 2. Eventually, Chapter 8 contains a critical evaluation of the TVAS experiment, before a summary provided in Chapter 9 completes the Thesis.

References

- (1) Dantus, M.; Rosker, M. J.; Zewail, A. H. *J. Chem. Phys.* **1987**, *87*, 2395–2397.
- (2) Zewail, A. H. *Science* **1988**, *242*, 1645–1653.
- (3) Zewail, A. H. *Angew. Chem. Int. Ed.* **2000**, *39*, 2586–2631.
- (4) Adamczyk, K.; Prémont-Schwarz, M.; Pines, D.; Pines, E.; Nibbering, E. T. J. *Science* **2009**, *326*, 1690–1694.
- (5) Roberts, G. M.; Marroux, H. J. B.; Grubb, M. P.; Ashfold, M. N. R.; Orr-Ewing, A. J. *J. Phys. Chem. A* **2014**, *118*, 11211–11225.
- (6) Röttger, K.; Marroux, H. J. B.; Grubb, M. P.; Coulter, P. M.; Böhnke, H.; Henderson, A. S.; Galan, M. C.; Temps, F.; Orr-Ewing, A. J.; Roberts, G. M. *Angew. Chem. Int. Ed.* **2015**, *54*, 14719–14722.
- (7) Hoffmann, F.; Ekimova, M.; Bekçioğlu-Neff, G.; Nibbering, E. T.; Sebastiani, D. *J. Phys. Chem. A* **2016**, *120*, 9378–9389.
- (8) Röttger, K.; Marroux, H. J. B.; Böhnke, H.; Morris, D. T. J.; Voice, A. T.; Temps, F.; Roberts, G. M.; Orr-Ewing, A. J. *Faraday Discuss.* **2016**, *194*, 683–708.
- (9) Röttger, K.; Marroux, H. J. B.; Chemin, A. F. M.; Elsdon, E.; Oliver, T. A. A.; Street, S. T. G.; Henderson, A. S.; Galan, M. C.; Orr-Ewing, A. J.; Roberts, G. M. *J. Phys. Chem. B* **2017**, *121*, 4448–4455.
- (10) Orr-Ewing, A. J. *Chem. Soc. Rev.* **2017**, *46*, 7597–7614.
- (11) Ingle, R. A.; Roberts, G. M.; Röttger, K.; Marroux, H. J. B.; Sönnichsen, F. D.; Yang, M.; Szyc, Ł.; Harabuchi, Y.; Maeda, S.; Temps, F.; Orr-Ewing, A. J. *Chem. Phys.* **2018**, *515*, 480–492.
- (12) Straub, S.; Brünker, P.; Lindner, J.; Vöhringer, P. *Phys. Chem. Chem. Phys.* **2018**, *20*, 21390–21403.
- (13) Straub, S.; Brünker, P.; Lindner, J.; Vöhringer, P. *Angew. Chem. Int. Ed.* **2018**, *57*, 5000–5005.
- (14) Vöhringer, P. *Dalton Trans.* **2020**, *49*, 256–266.
- (15) Codescu, M.-A.; Weiß, M.; Brehm, M.; Kornilov, O.; Sebastiani, D.; Nibbering, E. T. J. *J. Phys. Chem. A* **2021**, *125*, 1845–1859.

- (16) Böhnke, H. Electronic Deactivation and Reaction Dynamics of H-bonded Molecular Systems Studied by Femtosecond Time-Resolved Vibrational Absorption Spectroscopy, Dissertation, Christian-Albrechts-Universität zu Kiel, 2019.
- (17) Callis, P. R. *Annu. Rev. Phys. Chem.* **1983**, *34*, 329–357.
- (18) Cohen, B.; Hare, P. M.; Kohler, B. *J. Am. Chem. Soc.* **2003**, *125*, 13594–13601.
- (19) Crespo-Hernández, C. E.; Cohen, B.; Hare, P. M.; Kohler, B. *Chem. Rev.* **2004**, *104*, 1977–2019.
- (20) Shukla, M.; Leszczynski, J. *J. Biomol. Struct. Dyn.* **2007**, *25*, 93–118.
- (21) Middleton, C. T.; de La Harpe, K.; Su, C.; Law, Y. K.; Crespo-Hernández, C. E.; Kohler, B. *Annu. Rev. Phys. Chem.* **2009**, *60*, 217–239.
- (22) Kleinermanns, K.; Nachtigallova, D.; de Vries, M. S. *Int. Rev. Phys. Chem.* **2013**, *32*, 308–342.
- (23) Schreier, W. J.; Gilch, P.; Zinth, W. *Annu. Rev. Phys. Chem.* **2015**, *66*, 497–519.
- (24) Pecourt, J. M.; Peon, J.; Kohler, B. *J. Am. Chem. Soc.* **2001**, *123*, 10370–10378.
- (25) Peon, J.; Zewail, A. H. *Chem. Phys. Lett.* **2001**, *348*, 255–262.
- (26) Kang, H.; Jung, B.; Kim, S. K. *J. Chem. Phys.* **2003**, *118*, 6717–6719.
- (27) Gustavsson, T.; Sharonov, A.; Onidas, D.; Markovitsi, D. *Chem. Phys. Lett.* **2002**, *356*, 49–54.
- (28) Crespo-Hernández, C. E.; Martínez-Fernández, L.; Rauer, C.; Reichardt, C.; Mai, S.; Pollum, M.; Marquetand, P.; González, L.; Corral, I. *J. Am. Chem. Soc.* **2015**, *137*, 4368–4381.
- (29) Gonnella, N. C.; Roberts, J. D. *J. Am. Chem. Soc.* **1982**, *104*, 3162–3164.
- (30) Schumacher, M.; Günther, H. *J. Am. Chem. Soc.* **1982**, *104*, 4167–4173.
- (31) Majoube, M.; Henry, M.; Vergoten, G. *J. Raman Spectrosc.* **1994**, *25*, 233–243.
- (32) Broo, A.; Holmén, A. *Chem. Phys.* **1996**, *211*, 147–161.

- (33) Nimmrich, A. Time-resolved vibrational spectroscopy of the nucleic acid chromophore purine in excited singlet and triplet states, Master Thesis, Christian-Albrechts-Universität zu Kiel, 2018.
- (34) Pancur, T.; Schwalb, N. K.; Renth, F.; Temps, F. *Chem. Phys.* **2005**, *313*, 199–212.
- (35) Albinsson, B. *J. Am. Chem. Soc.* **1997**, *119*, 6369–6375.
- (36) Andréasson, J.; Holmén, A.; Albinsson, B. *J. Phys. Chem. B* **1999**, *103*, 9782–9789.
- (37) Parusel, A. B.; Rettig, W.; Rotkiewicz, K. *J. Phys. Chem. A* **2002**, *106*, 2293–2299.
- (38) Schwalb, N. K.; Temps, F. *Phys. Chem. Chem. Phys.* **2006**, *8*, 5229–5235.
- (39) Schwalb, N. K.; Temps, F. *J. Phys. Chem. A* **2009**, *113*, 13113–13123.
- (40) Demeter, A.; Druzhinin, S. I.; Kovalenko, S. A.; Senyushkina, T. A.; Zachariasse, K. A. *J. Phys. Chem. A* **2011**, *115*, 1521–1537.
- (41) Lippert, E.; Lüder, W.; Moll, F.; Nägele, W.; Boos, H.; Prigge, H.; Seibold-Blankenstein, I. *Angew. Chem.* **1961**, *73*, 695–706.
- (42) Rotkiewicz, K.; Grellmann, K.; Z. R. Grabowski *Chem. Phys. Lett.* **1973**, *19*, 315–318.
- (43) Baumann, W.; Bischof, H.; Fröhling, J. C.; Brittinger, C.; Rettig, W.; Rotkiewicz, K. *J. Photochem. Photobiol. A Chem.* **1992**, *64*, 49–72.
- (44) Schuddeboom, W.; Jonker, S. A.; Warman, J. M.; Leinhos, U.; Kühnle, W.; Zachariasse, K. A. *J. Phys. Chem.* **1992**, *96*, 10809–10819.
- (45) Gorse, A. D.; Pesquer, M. *J. Phys. Chem.* **1995**, *99*, 4039–4049.
- (46) Hashimoto, M.; Hamaguchi, H. O. *J. Phys. Chem.* **1995**, *99*, 7875–7877.
- (47) Zachariasse, K. A.; Grobys, M.; Von Der Haar, T.; Hebecker, A.; Il'ichev, Y. V.; Morawski, O.; Rückert, I.; Kühnle, W. *J. Photochem. Photobiol. A Chem.* **1997**, *105*, 373–383.
- (48) Chudoba, C.; Kummrow, A.; Dreyer, J.; Stenger, J.; Nibbering, E. T.; Elsaesser, T.; Zachariasse, K. A. *Chem. Phys. Lett.* **1999**, *309*, 357–363.
- (49) Dreyer, J.; Kummrow, A. *J. Am. Chem. Soc.* **2000**, *122*, 2577–2585.

- (50) Grabowski, Z. R.; Rotkiewicz, K.; Rettig, W. *Chem. Rev.* **2003**, *103*, 3899–4031.
- (51) Kwok, W. M.; George, M. W.; Grills, D. C.; Ma, C.; Matousek, P.; Parker, A. W.; Phillips, D.; Toner, W. T.; Towrie, M. *Angew. Chem. Int. Ed.* **2003**, *42*, 1826–1830.
- (52) Kwok, W. M.; Ma, C.; George, M. W.; Grills, D. C.; Matousek, P.; Parker, A. W.; Phillips, D.; Toner, W. T.; Towrie, M. *Phys. Chem. Chem. Phys.* **2003**, *5*, 1043–1050.
- (53) Ma, C.; Kwok, W. M.; Matousek, P.; Parker, A. W.; Phillips, D.; Toner, W. T.; Towrie, M. *J. Phys. Chem. A* **2002**, *106*, 3294–3305.
- (54) Köhn, A.; Hättig, C. *J. Am. Chem. Soc.* **2004**, *126*, 7399–7410.
- (55) Druzhinin, S. I.; Ernsting, N. P.; Kovalenko, S. A.; Lustres, L. P.; Senyushkina, T. A.; Zachariasse, K. A. *J. Phys. Chem. A* **2006**, *110*, 2955–2969.
- (56) Gustavsson, T.; Coto, P. B.; Serrano-Andrés, L.; Fujiwara, T.; Lim, E. C. *J. Chem. Phys.* **2009**, *131*, 031101.
- (57) Rhinehart, J. M.; Mehlenbacher, R. D.; McCamant, D. *J. Phys. Chem. B* **2010**, *114*, 14646–14656.
- (58) Coto, P. B.; Serrano-Andrés, L.; Gustavsson, T.; Fujiwara, T.; Lim, E. C. *Phys. Chem. Chem. Phys.* **2011**, *13*, 15182–15188.
- (59) Rhinehart, J. M.; Challa, J. R.; McCamant, D. W. *J. Phys. Chem. B* **2012**, *116*, 10522–10534.
- (60) Park, M.; Kim, C. H.; Joo, T. *J. Phys. Chem. A* **2013**, *117*, 370–377.
- (61) Gómez, I.; Castro, P. J.; Reguero, M. *J. Phys. Chem. A* **2015**, *119*, 1983–1995.
- (62) Kochman, M. A.; Tajti, A.; Morrison, C. A.; Miller, R. J. *J. Chem. Theory Comput.* **2015**, *11*, 1118–1128.
- (63) Georgieva, I.; Aquino, A. J.; Plasser, F.; Trendafilova, N.; Köhn, A.; Lischka, H. *J. Phys. Chem. A* **2015**, *119*, 6232–6243.
- (64) Segado, M.; Mercier, Y.; Gómez, I.; Reguero, M. *Phys. Chem. Chem. Phys.* **2016**, *18*, 6875–6884.
- (65) Curchod, B. F.; Sisto, A.; Martínez, T. J. *J. Phys. Chem. A* **2017**, *121*, 265–276.

- (66) Mani, T.; Grills, D. C. *J. Phys. Chem. A* **2018**, *122*, 7293–7300.
- (67) Kochman, M. A.; Durbeej, B. *J. Phys. Chem. A* **2020**, *124*, 2193–2206.
- (68) Tayyari, S. F.; Zeegers-Huyskens, T.; Wood, J. L. *Spectrochim. Acta* **1979**, *35A*, 1289–1295.
- (69) Dannenberg, J. J.; Rios, R. *J. Phys. Chem.* **1994**, *98*, 6714–6718.
- (70) Howard, D. L.; Kjaergaard, H. G.; Huang, J.; Meuwly, M. *J. Phys. Chem. A* **2015**, *119*, 7980–7990.
- (71) Srinivasan, R.; Feenstra, J. S.; Park, S. T.; Xu, S.; Zewail, A. H. *J. Am. Chem. Soc.* **2004**, *126*, 2266–2267.
- (72) Folkendt, M. M.; Weiss-Lopez, B. E.; Chauvel, J. P.; True, N. S. *J. Phys. Chem.* **1985**, *89*, 3347–3352.
- (73) Emsley, J.; Freeman, N. J. *J. Mol. Struct.* **1987**, *161*, 193–204.
- (74) Hibbert, F.; Emsley, J. *Adv. Phys. Org. Chem.* **1990**, *26*, 255–379.
- (75) Yoon, M.-C.; Choi, Y. S.; Kim, S. K. *J. Chem. Phys.* **1999**, *110*, 11850–11855.
- (76) Upadhyaya, H. P.; Kumar, A.; Naik, P. D. *J. Chem. Phys.* **2003**, *118*, 2590–2598.
- (77) Xu, S.; Park, S. T.; Feenstra, J. S.; Srinivasan, R.; Zewail, A. H. *J. Phys. Chem. A* **2004**, *108*, 6650–6655.
- (78) Poisson, L.; Roubin, P.; Coussan, S.; Soep, B.; Mestdagh, J. M. *J. Am. Chem. Soc.* **2008**, *130*, 2974–2983.
- (79) Bhattacharjee, A.; Pemmaraju, C. D.; Schnorr, K.; Attar, A. R.; Leone, S. R. *J. Am. Chem. Soc.* **2017**, *139*, 16576–16583.
- (80) Squibb, R. J.; Sapunar, M.; Ponzi, A.; Richter, R.; Kivimäki, A.; Plekan, O.; Finetti, P.; Sisourat, N.; Zhaunerchyk, V.; Marchenko, T.; Journal, L.; Guillemin, R.; Cucini, R.; Coreno, M.; Grazioli, C.; Fraia, M. D.; Callegari, C.; Prince, K. C.; Decleva, P.; Simon, M.; Eland, J. H. D.; Doslic, N.; Feifel, R.; Piancastelli, M. N. *Nat. Commun.* **2018**, *9*, 1–7.
- (81) Verma, P. K.; Koch, F.; Steinbacher, A.; Nuernberger, P.; Brixner, T. *J. Am. Chem. Soc.* **2014**, *136*, 14981–14989.
- (82) Weller, A. *Naturwissenschaften* **1955**, *42*, 175–176.

- (83) Weller, A. Z. *Elektrochem.* **1956**, 60, 1144–1147.
- (84) Herek, J.; Pedersen, S.; Bañares, L.; Zewail, A. H. *J. Chem. Phys.* **1992**, 97, 9046–9061.
- (85) Law, K. Y.; Shoham, J. *J. Phys. Chem.* **1994**, 98, 3114–3120.
- (86) Zhou, P.; Hoffmann, M. R.; Han, K.; He, G. *J. Phys. Chem. B* **2015**, 119, 2125–2131.
- (87) Ling, F.; Liu, D.; Li, S.; Li, W.; Zhang, B.; Wang, P. *J. Chem. Phys.* **2019**, 151, 094302.
- (88) Ford, D.; Thistlethwaite, P. J.; Woolfe, G. *J. Chem. Phys. Lett.* **1980**, 69, 246–250.
- (89) Acuña, A. U.; Catalán, J.; Toribio, F. *J. Phys. Chem.* **1981**, 85, 241–245.
- (90) Toribio, F.; Catalán, J.; Amat, F.; Acuña, A. U. *J. Phys. Chem.* **1983**, 87, 817–822.
- (91) Helmbrook, L. A.; Kenny, J. E.; Kohler, B. E.; Scott, G. W. *J. Phys. Chem.* **1983**, 87, 280–289.
- (92) Orton, E.; Morgan, M. A.; Pimentel, G. C. *J. Phys. Chem.* **1990**, 94, 7936–7943.
- (93) Catalán, J. *Phys. Chem. Chem. Phys.* **2012**, 14, 8903–8909.
- (94) Acuña, A. U.; Amat-Guerri, F.; Catalán, J.; González-Tablas, F. *J. Phys. Chem.* **1980**, 84, 629–631.
- (95) Massaro, R. D.; Blaisten-Barojas, E. *J. Chem. Phys.* **2011**, 135, 164306.
- (96) Ghosh, S.; Thomas, J.; Huang, W.; Xu, Y.; Jäger, W. *J. Phys. Chem. Lett.* **2015**, 6, 3126–3131.
- (97) Holt, E. L.; Krokidi, K. M.; Turner, M. A.; Mishra, P.; Zwier, T. S.; Rodrigues, N. D.; Stavros, V. G. *Phys. Chem. Chem. Phys.* **2020**, 22, 15509–15519.

Experimental and Computational Methods

In this Thesis, a broad variety of femtosecond time-resolved spectroscopic techniques based on the pump–probe principle was employed to untangle the underlying electronic deactivation and reaction dynamics of the four molecular systems. Additionally, the obtained results were aided by quantum chemical calculations. The used time-resolved fluorescence spectroscopy by the up-conversion method (TFLS) as well as transient electronic absorption spectroscopy (TEAS) are only briefly explained, as they are already well established in our work group.^{1–8} Instead, this Chapter focuses on the time-resolved vibrational absorption spectroscopy (TVAS). Furthermore, a short introduction to the ab initio calculations is given. This includes the Hartree–Fock (HF) approach as well as single-reference methods like MP2, configuration interaction (CI) and coupled cluster (CC). MP2 and CC2 calculations were performed in the present Thesis.

2.1 Time-resolved fluorescence up-conversion

Femtosecond time-resolved fluorescence spectroscopy by the up-conversion technique (TFLS) provides first information about the optically bright excited states and their lifetimes. The experimental setup has been described in detail elsewhere.^{1–3} In short, a Ti:Sa femtosecond laser (Clark, MXR CPA 2001) with laser pulses of 150 fs duration full width at half maximum (FWHM) at $\lambda = 775$ nm with 1.01 kHz repetition rate was used for the experiment. Firstly, pump pulses in the UV spectral region had to be generated to electronically excite the molecules. For this purpose, laser pulses at 520 nm, or 620 nm were obtained from a home-built non-collinear optical parametric amplifier (NOPA) and temporally compressed to 35–50 fs (FWHM) with a prism compressor. The details of the NOPA setup and its working principle are well established^{3,6,9–11} and will not be explained here. Subsequent second harmonic generation (SHG) yielded UV pump pulses at either $\lambda_{\text{exc}} = 266$ nm, or $\lambda_{\text{exc}} = 305$ nm with pulse

energies of 350 nJ. The pump pulses were focused into the sample flow cell, which had an optical path length of 1 mm. The fluorescence emitted by the photo-excited molecules was then collimated by a pair of parabolic mirrors (Melles-Griot, $f = 119$ mm). The fluorescence as well as another fraction of the Ti:Sa fundamental ($E = 70 \mu\text{J}$ per pulse) were focused into a 0.1 mm BBO crystal ($\theta = 51^\circ$, $\phi = 30^\circ$). Here, the Ti:Sa fundamental was used for the gate pulses, since a sum frequency signal was only generated (SFG) when the gate pulse was temporally and spatially overlapped with the emitted fluorescence. While a type I non-collinear SFG process was applied in the UV wavelength range of $\lambda_{\text{fl}} = 320\text{--}360$ nm, type II phase-matching conditions were used in the visible region from $\lambda_{\text{fl}} = 410\text{--}560$ nm. Since a measurement was carried out at a single emission wavelength λ_{fl} , the BBO crystal had to be tilted by a few degrees to record the respective SFG signals at other emission wavelengths. The up-converted light was then focused into the detection unit. The latter consisted of a monochromator (Jobin-Yvon HR 10), a photomultiplier (Hamamatsu R1527P), a preamplifier (Stanford Research SR 445) and a gated single-photon counter (Stanford Research SR 400). To record fluorescence time profiles, the gate pulses were delayed up to $\Delta t = 2$ ns with respect to the pump pulses by a linear translation stage (Physik Instrumente). The measurements were carried out under magic angle (54.7°) conditions. The time profiles in the UV as well as in the visible range were analysed simultaneously using a nonlinear least-squares fitting routine based on the Levenberg-Marquardt algorithm implemented in MATHEMATICA.¹² Each time profile was fitted by a sum of exponentials convoluted with a Gaussian accounting for the instrument response function (IRF). In this Thesis, excitation at $\lambda_{\text{exc}} = 266$ nm was used for N^6,N^6 -dimethyladenine and the purine nucleobases, whereas methyl salicylate was excited at $\lambda_{\text{exc}} = 305$ nm.

2.2 Time-resolved electronic absorption spectroscopy

Since the information about the excited-state dynamics obtained from the TFLS measurements is limited to the processes proceeding on the PES of optically bright excited electronic states, the experimental studies were supplemented by time-resolved electronic absorption spectroscopy (TEAS). By applying broadband probe pulses in the visible spectral region, non-radiative deactivation pathways, formation of photoproducts, and the recovery of the electronic ground state

can be followed in time. The used femtosecond time-resolved electronic absorption spectrometer has also been built around the above-mentioned Clark MXR CPA 2001 Ti:Sa laser system. A detailed description of the setup is given elsewhere.^{4–6,8} In short, a home-built non-collinear optical parametric amplifier provided laser pulses at 533 nm, or 630 nm, which were temporally compressed to 30 fs (FWHM) with a prism compressor. Afterwards, pump pulses at $\lambda_{\text{exc}} = 266$ nm, or $\lambda_{\text{exc}} = 313$ nm with energies of 300–400 nJ per pulse were obtained via second harmonic generation. N^6,N^6 -dimethyladenine was excited at $\lambda_{\text{exc}} = 266$ nm, whereas the excitation wavelength was altered to $\lambda_{\text{exc}} = 313$ nm for methyl salicylate. The pump pulses were focused into the sample flow cell, which had an optical path length of 1 mm. Another fraction of the laser fundamental was focused into a moving CaF_2 plate preparing broadband probe pulses in the visible region from $325 \text{ nm} \leq \lambda_{\text{probe}} \leq 700 \text{ nm}$. After splitting them into probe and reference beams, the probe pulse was spatially and temporally overlapped with the pump pulse in the sample flow cell. Finally, the probe and reference pulses were spectrally dispersed in a prism spectrograph and detected separately with two full frame transfer CCD cameras (Series 2000, Entwicklungsbüro Stresing, Berlin). Prior to white-light generation, the probe pulses passed a motorised, computer-controlled delay stage to record transient difference spectra as function of time. Here, a maximal pump–probe time delay of $\Delta t = 1.7$ ns was achieved. To improve data quality, optical choppers were inserted into the beam path of the pump and probe pulses, respectively.^{5,6,8} Every second probe pulse was blocked as the chopper was working at 505 Hz, whereas the chopper for the pump pulse was operating at 252.5 Hz. All measurements were carried out under magic angle conditions. Additionally, the pure solvent was measured directly after the sample to correct for chirp and coherent artifacts like cross-phase modulation (XPM). By subtracting the solvent from the sample measurement, a time-zero, background- and solvent-corrected data matrix was obtained. This experimental data matrix was then analysed globally by singular value decomposition^{13–16} (SVD) which is shortly described in Subsection 2.2.1. The SVD-based data analysis routine implemented in MATHEMATICA¹² was written in our work group by F. Renth.¹⁷

2.2.1 Data analysis by singular value decomposition

During the transient electronic absorption experiment, a large number of absorption difference spectra as function of pump–probe time delay are recorded, which are combined in a spectro-temporal data matrix A . A is an $m \times n$ matrix, where m gives the different delay times and n the wavelengths, respectively. Thus, A_{ij} corresponds to a measurement at time t_i and wavelength λ_j .^{15,16} The number of the involved molecular species n_i , also referred to as the rank of the data matrix A (in absence of measurement errors), can be determined by singular value decomposition.^{13–16} Since SVD is a mathematical procedure, it is independent of any kinetic model. This means that no prior knowledge of the investigated chemical sample and its mechanistic details are required.

A detailed description of the SVD-based data analysis as established in our group can be found elsewhere.^{6–8} In short, the data matrix A is decomposed into the product of three matrices according to Equation 2.1.^{13–16}

$$A = USV^T \quad (2.1)$$

The singular values are given in descending order on the diagonal of matrix S . The matrices U and V^T are the so-called left and right singular vectors and contain the traces in the time domain (U) and in the spectral domain (V).^{13,14} While singular values s_i with $s_i \gg 0$ carry the spectro-temporal information of an experimental data set, small singular values represent noise. From the number of significant singular values, the rank n_i of the data matrix can be estimated, which ideally corresponds to the number of spectrally distinguishable molecular species. To further verify n_i , the signal-to-noise ratio of the SVD time traces and SVD spectra can be inspected. Once the rank of the data matrix A is determined, a reduced representation \tilde{A} of the data matrix is obtained (cf. Equation 2.2) by considering only the n_i relevant time traces and spectra to describe the original data matrix with sufficient precision. This leads to a significantly reduced size of S , U and V .^{13–16}

$$\tilde{A} = \tilde{U}\tilde{S}\tilde{V}^T \quad (2.2)$$

The singular value decomposition of an experimental data matrix A as well as the rank approximation yielding the reduced data matrix \tilde{A} are schematically visualised in Fig. 2.1. In a next step, the singular value-weighted time traces are described in a global manner by nonlinear least-squares fitting using a sum of n_i

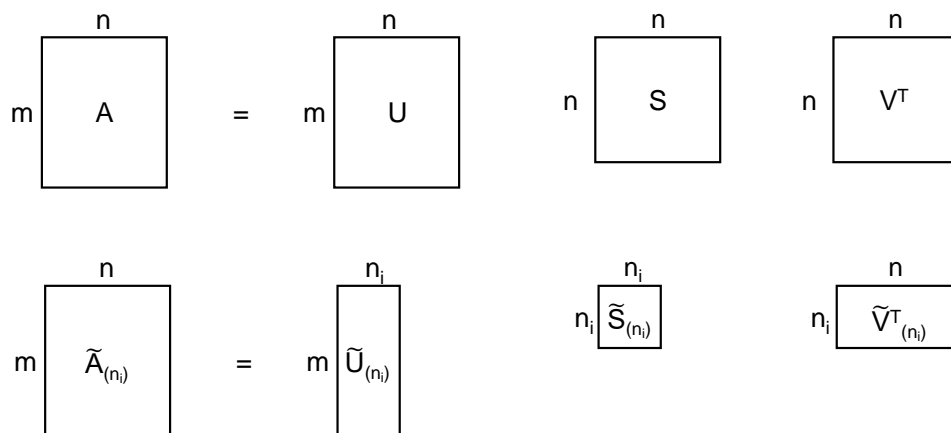
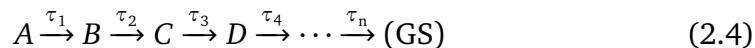


Figure 2.1: Schematic representation of the singular value decomposition of a data matrix A and rank approximation yielding the reduced data matrix \tilde{A} . Adapted from *Practical Data Analysis in Chemistry*, 1st ed. by Marcel Maeder and Yorck-Michael Neuhold, Model-Free Analyses, p. 214, 218 ©2007 by Elsevier with permission from Elsevier.

exponentials convoluted with a Gaussian accounting for the IRF. This yields a set of global time components τ_i as well as a matrix B that contains the respective amplitudes A_i . Since only n_i , with $n_i \ll n$, time traces are considered, a minimal number of fitting parameters is necessary. At the same time, noise is significantly reduced if a singular value decomposition is performed beforehand. After the global fit to the SVD time traces, the so-called decay-associated difference spectra (DADS) are calculated:

$$\text{DADS} = B^T \cdot \tilde{V}^T \quad (2.3)$$

Each DADS corresponds to a single global decay time component τ_i and reflects its wavelength-dependent amplitude. Proceeding from the DADS and by applying a kinetic model, the evolution-associated difference spectra (EADS) are obtained. For sequential deactivation processes, as observed for the investigated molecules in this Thesis, the EADS were calculated according to the following kinetic scheme:



The letters A, B, C and D represent the spectrally distinguishable molecular species (e.g., electronic states, or product species) that are involved during the deactivation process after photoexcitation. If a permanent offset was detected experimentally, e.g., arising from a long-lived photoproduct, or excited state, a

step function with $\tau_n \rightarrow \infty$ was fitted to the data to describe the remaining signal towards late delay times. As the EADS reflect the spectral evolutions of the involved electronic states, EADS1 represents the transient difference spectrum at time zero ($\Delta t \approx 0$). Therefore, it is assigned to molecules in the Franck–Condon (FC) region of the electronic state initially excited by absorption of a pump photon. From there, the rise of EADS2 proceeds with τ_1 , and its decay with τ_2 etc., until the molecules finally return to the electronic GS with τ_n .⁶

All in all, the described data analysis based on SVD provides deep insight into the photo-induced deactivation and reaction dynamics of a particular molecule, e.g., by identification of the number of the involved molecular species, and by inspecting the DADS and EADS. Furthermore, the fitting procedure is considerably facilitated and noise is efficiently separated from the experimental data.^{13–16}

2.3 Time-resolved vibrational absorption spectroscopy

Time-resolved vibrational absorption spectroscopy (TVAS) is a pump–probe technique. Similar to TEAS, the sample molecules are excited electronically, but their spectro-temporal evolution is probed by broadband laser pulses in the mid-infrared spectral region. As mentioned in Chapter 1, the TVAS experiment has only recently been set up in our work group by H. Böhnke.^{18,19} His dissertation does not only provide a detailed description of the experimental setup, but also contains a comprehensive characterisation of the experiment (e.g., temporal resolution, conversion efficiencies, spectral shape of the mid-infrared probe pulses etc.).¹⁸ Information on similar TVAS experiments can be found, e.g., in Ref. [20–34].

In the following, the experimental TVAS setup in our group will be introduced. The generation of the pump and probe pulses will be explained first. Afterwards, the detection unit as well as the acquisition and analysis of the experimental data will be presented.

2.3.1 Experimental setup

In Fig. 2.2 a schematic overview on the experimental setup of the transient vibrational absorption spectrometer is given. A detailed presentation of the experiment is depicted in Fig. 2.4.

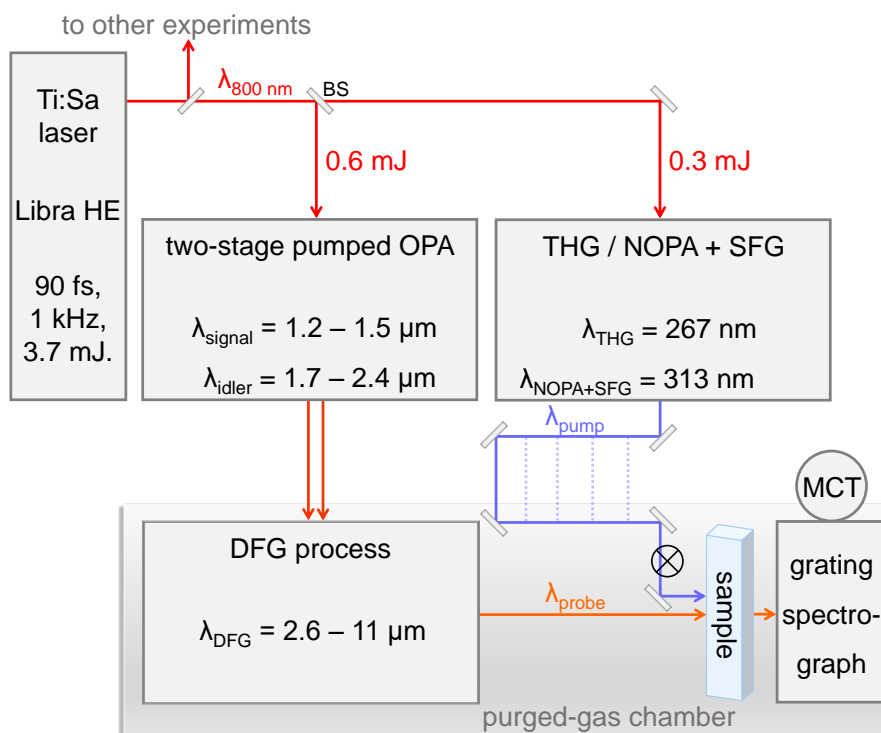


Figure 2.2: Schematic representation of the time-resolved vibrational absorption spectroscopy setup based on the pump-probe principle.

For the experiment an energy of 0.9 mJ / pulse is used provided by a femtosecond Ti:Sa laser (Coherent Libra HE, 1 kHz, 3.7 mJ / pulse) with laser pulses centered at 800 nm and a pulse duration of 90 fs (FWHM). As illustrated in Fig. 2.2, the laser fundamental is first split into two parts by a beam splitter (BS) with energies of 0.6 mJ per pulse for the generation of the broadband mid-infrared probe pulses and 0.3 mJ per pulse for the UV pump pulses, respectively. In this Thesis, two different excitation wavelengths, $\lambda_{\text{exc}} = 267 \text{ nm}$ and $\lambda_{\text{exc}} = 313 \text{ nm}$, were used to excite the sample molecules. The generation of $\lambda_{\text{exc}} = 267 \text{ nm}$ was achieved via third harmonic generation (THG) of the laser fundamental. For this purpose, a commercial THG “Femtokit” was inserted into the pump beam path (FKE-800-100, Femtokit FK series, Eksma Optics). The THG setup is schematically presented in Fig. 2.3. First, the polarisation of the laser fundamental at 800 nm was adjusted vertically to the propagation direction of the beam by a half-wave plate ($\lambda/2$). Afterwards, a type I SHG process (BBO_{SHG}) provided horizontally polarised laser pulses at 400 nm. Prior to the THG process, a group delay compensation plate (CP) as well as a second half-wave plate for

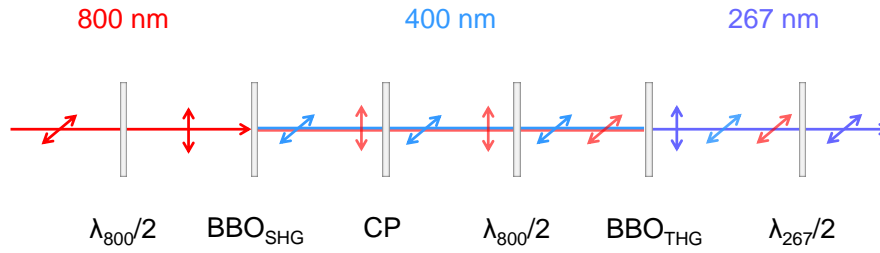


Figure 2.3: Schematic representation of the pump pulse generation for $\lambda_{\text{exc}} = 267 \text{ nm}$ using the THG Femtokit. Laser pulses at 800 nm are coloured in red, at 400 nm in light blue and at 267 nm in purple. The double arrows indicate the polarisation direction of the different laser pulses.

the remaining fraction at 800 nm were employed. Finally, horizontally polarised pump pulses at 267 nm with an energy of $2 \mu\text{J}$ per pulse were obtained.

To generate tunable pump pulses in the UV and visible spectral region, the THG Femtokit had to be replaced by a home-built NOPA, enabling access to wavelengths from 480 to 660 nm (cf. Fig. 2.4). For the generation of $\lambda_{\text{exc}} = 313 \text{ nm}$, the NOPA was adjusted to yield laser pulses at 508 nm which were temporally compressed to 50 fs (FWHM) with a prism compressor. In a second step, a SFG process (BBO, $\theta = 37.4^\circ$, $\phi = 90^\circ$) of the NOPA output and the laser fundamental ($60 \mu\text{J}$ per pulse) provided pump pulses at 313 nm with pulse energies of 300 nJ.

After passing a motorised optical translation stage (M-521.DG, Physik Instrumente), the pump pulses were loosely focused into the home-built sample flow cell, which had an optical path length of 0.1 mm. The translation stage is indicated by the dashed purple lines in Fig. 2.2. Furthermore, an optical chopper (MC2000, Thorlabs) was inserted into the beam path. Since the chopper was operating at 500 Hz, every second pump pulse was blocked.

The generation of tunable mid-infrared probe pulses ranging from $2.6 \mu\text{m}$ to $11 \mu\text{m}$ was realised by a two-stage pumped optical parametric amplifier (OPA), followed by a difference frequency generation (DFG) process.^{18,19,22,23} Firstly, the laser fundamental at 800 nm was split into three parts. A small fraction at 800 nm was focused into a sapphire window ($d = 2 \text{ mm}$) preparing a broadband white-light continuum, which was used as seed pulse for the first amplification stage. Here, the vertically polarised seed pulses were focused into

the type II OPA crystal (BBO, $\theta = 27^\circ$, $\phi = 30^\circ$), where they were temporally and spatially overlapped with the second fraction of the horizontally polarised laser fundamental (125 μJ per pulse). This led to the generation of signal and idler pulses. The idler pulses were eliminated by a dichroic mirror. The signal pulses were now used as “new” seed pulses which were amplified by a third fraction of the laser fundamental. After this second amplification process, signal and idler pulses with energies of 90–150 μJ per pulse were obtained, which corresponds to an efficiency of approximately 25 %. By varying the phase matching angle of the OPA crystal, tunable signal $\lambda_{\text{signal}} = 1.2\text{--}1.5\ \mu\text{m}$ and idler $\lambda_{\text{idler}} = 1.7\text{--}2.4\ \mu\text{m}$ pulses were generated. While undesired remaining spectral components were removed by a long-pass filter, the signal and idler were guided in a collinear way to a dichroic mirror to spatially separate both beams. The idler passed the dichroic mirror, in contrast to the signal which was reflected to a movable translation stage to adjust the distance travelled with respect to the fixed distance of the idler beam. After that, both beams were recombined and focused into the DFG crystal (AgGaS₂, $\theta = 39^\circ$, $\phi = 45^\circ$, type I). This resulted in generation of broadband mid-infrared probe laser pulses which were tunable from $\lambda_{\text{DFG}} = 2.6\text{--}11\ \mu\text{m}$ by rotating the DFG crystal. A long-pass filter (germanium plate, $d = 0.2\ \text{mm}$) was used to remove remaining components in the near-IR, before the broadband mid-IR probe pulses passed the sample flow cell. The pump and probe pulses were spatially and temporally overlapped in the sample cell. Finally, the probe pulses reached a grating spectrograph (iHR320, HORIBA). Here they were spectrally dispersed and then detected on a liquid-nitrogen cooled 32-pixel MCT detector array. To avoid absorption of the mid-IR light by atmospheric CO₂ and water vapor, which would result in a reduced mid-IR probe intensity, a sealed box (cf. Fig. 2.2, purged-gas chamber) was built around the mid-IR beam path. During the measurements this box was continuously purged with dried air (purge generator: PG 85 L, cmc-Instruments).

2.3.2 Detection unit and measurement conditions

The detection and data acquisition unit (femtosecond laser pulse acquisition system, FPAS-6416, Infrared Systems Development Corporation) consists of the computer-controlled grating spectrometer, a boxcar-type integrator system and a multi-element (32-pixel) MCT detector array. After the mid-infrared probe pulses

passed the sample cell, the transmitted probe light was collimated and focused onto the entrance slit (0–2 mm) of the grating spectrometer. Subsequently, the probe pulses were guided to the grating and spectrally dispersed before they hit the liquid-nitrogen cooled MCT detector array which consists of 32 pixels. In each detector element, a change of the bias current proportional to the absorbed mid-infrared probe intensity was induced. Finally, the detector signals were captured and integrated by the boxcar-type integrator and its output was digitised and stored by an AD-converter. In principle, one could choose between three different gratings with 75, 150 or 300 grooves/mm. In this Thesis exclusively the grating with 75 grooves/mm, corresponding to a spectral resolution of 26 nm, was used. The components of the spectrometer and the acquisition system (e.g., size of the entrance slit, selection and position of the grating) were controllable via the integrated LabVIEW software.

The output of the TVAS experiment is a number of spectrally resolved absorption difference spectra $\Delta OD(\lambda, \Delta t)$ recorded as function of pump–probe time delay. The time delay Δt between both pulses was achieved via the translation stage, equipped with a retroreflector, which was inserted into the beam path of the pump beam. By moving the stage, the temporal arrival of the pump pulses in the sample flow cell with respect to the probe pulses could be precisely varied, so that spectra at different points in time were measured. Here, a maximal time delay of $\Delta t \approx 1$ ns was achieved. If the pump and probe pulses travelled exactly the same optical distance, i.e., reached the sample cell at the same point in time, this corresponds to $\Delta t = 0$ which had to be roughly determined before each measurement. For this, the sample cell was exchanged by a germanium plate. By scanning the entire stage and overlapping the pump and probe pulses spatially on the solid sample, $\Delta t = 0$ was obtained. Afterwards, the spatial overlap of both laser pulses inside the germanium sample was optimised in order to maximise the signal intensity originating from the solid sample. A solid ZnSe sample was used to determine the temporal resolution (≈ 150 fs) of the experiment.¹⁸ After these preparatory steps, the solid sample was replaced by the liquid one. The probe beam path into the spectrometer was optimised and the diameter of the entrance slit of the spectrometer was kept as small as possible. The box covering the mid-IR probe beam was purged with dry air for about an hour, then the measurement was started. Since every second pump pulse was blocked by the chopper, transient spectra with and without photo-exciting the

sample were measured. The time-resolved vibrational difference spectra were calculated according to:

$$\Delta OD(\lambda, \Delta t) = -\log \frac{I_{\text{probe}}^*(\lambda, \Delta t)}{I_{\text{probe}}^0(\lambda)} \quad (2.5)$$

In Equation 2.5, I_{probe}^* denotes the intensity of the broadband mid-infrared probe pulses after passing the excited sample (chopper open), whereas I_{probe}^0 corresponds to the probe intensity travelled through the unexcited sample (chopper closed). Depending on the measurement conditions (e.g., signal intensity, spectral range and stability of the probe pulses), 3000–5000 laser pulses per delay step were used. The measurement routine implemented in LabVIEW was written in the work group by K. Röttger.

In this Thesis, deuterated acetonitrile (ACN- d_3) and cyclohexane (Uvasol grade) were used as solvents because they provide a high transmission of the mid-IR probe intensity in the investigated spectral range between 1150–1750 cm^{-1} . For the home-built sample flow cell, CaF_2 windows ($d = 2$ mm, Korth Kristalle), solvent-resistant O-rings (Chemraz, Greene Tweed & Co. GmbH) and a 0.1 mm teflon spacer were used. Furthermore, solvent-resistant tubes connected the sample cell with the sample reservoir to recycle the sample continuously using a peristaltic pump (Reglo analog, MS-2/6, Ismatec). The concentration of the samples was adjusted to $OD \approx 0.3$ – 0.4 at the excitation wavelength. Before and after measuring a particular spectral range, static UV/vis absorption spectra were recorded to rule out any photodegradation of the investigated sample.

2.3.3 Data processing and data analysis

Each measurement covered a spectral range of 150 cm^{-1} and was repeated between 20 and 30 times. Afterwards, a baseline correction of the averaged raw data was performed using the KOALA programme (Kinetics Observed After Light Absorption).³⁵ For this, up to 5 user-defined spectral regions, where no vibrational signatures appear, were chosen and fitted with a linear or quadratic function. Subsequently, the obtained background function was subtracted from the experimental data. To ensure a reasonable baseline correction, a measurement started a few picoseconds before $\Delta t = 0$ and small temporal steps of 100 to 200 fs were employed to record a sufficient number (20–40) of transient spectra

without any molecular contributions. After $\Delta t \approx 5\text{--}8$ ps, logarithmic delay steps were applied until the maximum time delay of $\Delta t \approx 1$ ns was reached.

For the liquid sample $\Delta t = 0$ was estimated from coherent artifacts that occurred at very early times. These artifacts are induced by the pump pulses and are summarised as transient lensing,^{18,35–38} lasting between 1.0 ps and 2.5 ps. Its duration and intensity mainly depend on the investigated spectral range, but also on the pump energy, the sample concentration and on the solvent.¹⁸ As a result, the molecular signals at early delay times were strongly superimposed by high-intensity spectral contributions arising from transient lensing. Since these contributions cannot be subtracted from the experimental data, in the following only spectra after the transient lensing process are visualised and were considered in the data analysis.

After baseline correction of the raw data, the time-resolved vibrational spectra were globally modelled by a sum of Gaussian functions according to the following equation:

$$y = y_0 + \sum_i \frac{A_i}{w_i \sqrt{\pi/2}} \cdot \exp \left(-2 \cdot \frac{(\lambda - \lambda_i^c)^2}{w_i^2} \right) \quad (2.6)$$

In Equation 2.6, y_0 was set to zero because it corresponds to the baseline of each transient vibrational spectrum. The parameter A_i is the amplitude, w_i the spectral width and λ_i^c the central position of a single Gaussian, respectively. The global Gaussian band fit was performed in the Origin³⁹ programme describing 100 transient spectra simultaneously, whereby each vibrational band was fitted by a single Gaussian. For vibrational bands that originated from the same molecular species, e.g., the ground-state bleach signals, the amplitudes were coupled:

$$A_i = A_j \cdot f_i \quad (2.7)$$

The Gaussian band fit was done in the wavelength regime. Commonly, vibrational spectra are presented in wavenumbers. Thus, for visualisation, the data were converted from nanometers into wavenumbers. To extract time profiles, the respective amplitudes A_i of the involved molecular species determined by the spectral band fit were plotted as function of pump–probe time delay. Global time constants describing the deactivation processes after photoexcitation were obtained by simultaneous fitting of the time profiles using a sum of exponentials. Since the spectral range of a measurement was determined by the spectral

bandwidth ($\sim 150\text{ cm}^{-1}$) of the mid-IR probe pulses, individual measurements from different spectral regions were spliced together. The obtained overview was then again analysed in a global manner. Here, sums of up to 20 Gaussian functions were used to describe 100 transient spectra simultaneously.

2.3.4 Assignment of the experimental vibrational bands

To understand and interpret the results of the TVAS measurements, the experimentally detected vibrational signals must be assigned to a specific molecular structure in its respective electronic state. For this, the experimental findings were aided by quantum chemical calculations. This included optimisation of the molecular structure in different electronic states and calculation of the associated frequency spectra in the ground and excited singlet and triplet states, respectively. The recorded experimental vibrational spectra were compared with the calculated ones to identify the involved molecular species. Furthermore, molecular properties like dipole moments μ , oscillator strengths f and vertical excitation energies (VEEs) were computed. Minimum energy structures and vibrational wavenumbers in the electronic ground state were calculated using second-order Møller-Plesset (MP2) perturbation theory under the resolution of the identity (RI-MP2) approximation.^{40–42} Exclusively for acetylacetone and its isomers, density functional theory (DFT) at the B3LYP-D3 level^{43–47} implemented in the Gaussian09 suite⁴⁸ was employed. Corresponding calculations for excited states were performed using the second-order coupled-cluster method under the resolution of the identity approximation (RI-CC2).^{49–53} The RI-MP2/CC2 calculations were done on isolated molecules in vacuo in the TURBOMOLE programme package.⁵⁴ The harmonic vibrational wavenumbers were scaled by factors of 0.95–0.99 recommended from extensive benchmarking^{55–59} to match the experimental FTIR spectrum.

In the following, a brief overview on the above-mentioned ab initio methods will be provided. More detailed descriptions on this topic can be found in textbooks.^{60–64}

2.4 Quantum chemical ab initio calculations

In computational chemistry, chemical problems are addressed by theoretical calculations of molecular properties. Dipole moments, ionisation potentials as well as IR, NMR and UV spectra can be predicted theoretically.⁶¹ In addition, quantum chemical calculations do not only provide valuable information on the molecular structure e.g., bond lengths, or torsion angles, but also the energies of molecules, intermediates and transition states can be computed.⁶¹ If only physical constants are used, these methods are summarised as ab initio calculations.^{61,64} One of the most prominent and simplest examples of the latter is called Hartree-Fock (HF) theory which was already reported in 1928.⁶⁵ The central goal of ab initio calculations is solving the electronic Schrödinger equation.^{61,64} For this purpose, the atomic nuclei and the electrons are considered separately due to their mass difference; this is known as the Born–Oppenheimer approximation.⁶⁶ Thus, the motion of the electrons is described in a field of all nuclei, whose locations are fixed. This leads to a reduced Hamiltonian:^{60,63}

$$\hat{H}_{\text{el}} = -\frac{\hbar^2}{2m_e} \sum_i^n \nabla_i^2 - \sum_i^n \sum_I^N \frac{Z_I e^2}{4\pi\epsilon_0 r_{li}} + \frac{1}{2} \sum_{ij}^n \frac{e^2}{4\pi\epsilon_0 r_{ij}}. \quad (2.8)$$

The first sum in Equation 2.8 is the operator for the kinetic energy of n electrons, the second represents the Coulomb attraction between n electrons and N nuclei and the third describes the interelectronic repulsion. Solving the Schrödinger equation using \hat{H}_{el} yields the electronic wave function which depends on the coordinates of the electrons and on the nuclear configuration. The total wave function ψ^o can be written as the product of single-electron wave functions (= spatial orbitals) and is called Hartree product:^{60,64}

$$\psi^o = \psi_a^o(1)\psi_b^o(2)\dots\psi_n^o(n). \quad (2.9)$$

Here, ψ^o depends on the coordinates of all electrons, whereas $\psi_a^o(1)$ considers the coordinates of electron 1, $\psi_a^o(2)$ of electron 2 and so on. However, the overall wave function must be antisymmetric to account for the characteristics of electrons as fermions (spin of 1/2 and indistinguishability). To meet these requirements, the overall wave function is expressed as a Slater determinant Φ_{SD} instead of the product of single-electron wave functions (ψ^o). The expression

for Φ_{SD} is given in Equation 2.10. Here, a spatial orbital wave function has to be multiplied with a spin function, denoted as α and β . This leads to a spin orbital $\phi_a(i)$ which is also referred to as molecular orbital (MO). The columns of the Slater determinant contain the single-electron wave functions (MOs) and the rows the coordinates of the electrons, respectively.⁶⁴

$$\Phi_{\text{SD}}(a, b, \dots n) = \frac{1}{\sqrt{n!}} = \begin{vmatrix} \phi_a(1) & \phi_b(1) & \dots & \phi_z(1) \\ \phi_a(2) & \phi_b(2) & \dots & \phi_z(2) \\ \vdots & \vdots & \ddots & \vdots \\ \phi_a(n) & \phi_b(n) & \dots & \phi_z(n) \end{vmatrix} \quad (2.10)$$

The energy of a single determinant is a function of these spin orbitals:

$$E = \langle \Phi | \hat{H} | \Phi \rangle \quad (2.11)$$

In the Hartree-Fock approach, which will not be explained in detail here, the spin orbitals $\phi_a(i)$ are varied systematically until the energy reaches a minimum. The energy of a spin orbital can be calculated using the pseudo-eigenvalue Hartree-Fock equation:^{60,63,64}

$$\epsilon_a \phi_a(1) = \hat{F}(1) \phi_a(1) \quad (2.12)$$

In Equation 2.12, the eigenvalue is the orbital energy ϵ_a and the eigenfunction is the spin orbital ϕ_a of electron 1. The expression of the one-electron Fock operator $\hat{F}(1)$ is given by:⁶³

$$\hat{F}(1) = \hat{H}^{\text{core}}(1) + \sum_{j=1}^{n/2} [2\hat{J}_j(1) - \hat{K}_j(1)] \quad (2.13)$$

In Equation 2.13, $\hat{H}^{\text{core}}(1)$ is the core Hamiltonian for electron 1 and includes the kinetic energy of an electron and the attraction to all the nuclei. The sum, appearing in the second part, describes repulsive contributions from all other $n - 1$ electrons. Here, \hat{J}_j is the Coulomb operator and \hat{K}_j the exchange operator. For n electrons, the sum is over $n/2$ occupied spatial orbitals, whereby the factor 2 is required because each spatial orbital is occupied with two electrons. \hat{J}_j

accounts for the electron–electron repulsion in an averaged way. More precisely, electron 1 feels the presence of all other $n - 1$ electrons as a fixed distribution of charge (mean-field approximation). However, this means that the instantaneous interaction between the electrons, i.e., the correlation of electrons is neglected at this point.^{61,63} The energy of a single orbital ϵ_a is then calculated by Equation 2.14.⁶³

$$\epsilon_a = \hat{H}_{aa}^{\text{core}} + \sum_{j=1}^{n/2} (2J_{aj} - K_{aj}) \quad (2.14)$$

The sum of the orbital energies of all occupied orbitals is determined by:⁶³

$$\sum_{a=1}^{n/2} \epsilon_a = \sum_{a=1}^{n/2} \hat{H}_{aa}^{\text{core}} + \sum_{a=1}^{n/2} \sum_{j=1}^{n/2} (2J_{aj} - K_{aj}) \quad (2.15)$$

In Equation 2.15, each electronic interaction is considered twice. Therefore, the absolute HF energy has to be corrected and a factor V_{NN} is added, which corresponds to the sum of the interactions between the nuclei. This leads to the following equation:⁶³

$$E_{\text{HF}} = 2 \sum_{a=1}^{n/2} \epsilon_a - \sum_{a=1}^{n/2} \sum_{j=1}^{n/2} (2J_{aj} - K_{aj}) + V_{NN} \quad (2.16)$$

The HF energy E_{HF} can be calculated by solving the Hartree–Fock equation according to Equation 2.12 for each spin orbital. As mentioned previously, the Fock operator itself depends on the orbitals of all other $n - 1$ electrons except for the one being calculated.^{60,63} Consequently, to set up the Fock operator, all other orbitals must be known initially, which is (usually) not the case. For that reason, the iterative self-consistent field (SCF) approach is applied. Here, initial guesses for the spin orbitals are provided, then the Fock operator is set up and the HF equations are solved yielding a new, improved set of spin orbitals which are utilised in the second cycle. This procedure is repeated until the energy is minimised and the convergence criteria are reached. The Hartree–Fock self-consistent field cycle is schematically depicted in Fig. 2.5.

To initialise the iterative SCF cycle, Roothaan and Hall suggested that each molecular orbital $\phi_a(i)$ in Equation 2.12 is represented by a linear combination of atomic orbitals (LCAO). This means, a set of known basis functions χ is used

to express the unknown molecular orbitals. In principle, any function may be chosen as long as it contains the essential properties of the function for the MOs.

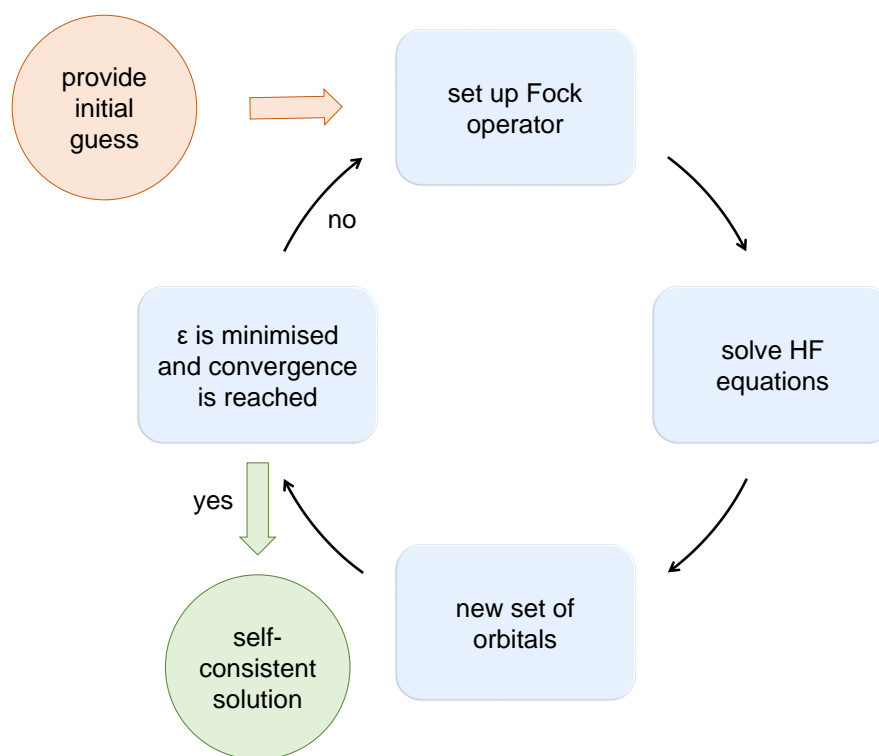


Figure 2.5: Schematic representation of the iterative Hartree–Fock self-consistent field procedure (HF-SCF).

For the basis set approximation the following equation is obtained:⁶⁴

$$\phi_a(i) = \sum_{\alpha}^{M_{\text{basis}}} c_{\alpha i} \chi_{\alpha} \quad (2.17)$$

In Equation 2.17, $c_{\alpha i}$ are the expansion coefficients used as initial guesses to start the HF-SCF cycle and setting up the Fock operator. The combination of Equation 2.12 and 2.17 leads to the so-called Roothaan–Hall equations:^{60,61}

$$FC = SC\epsilon \quad (2.18)$$

In Equation 2.18, F represents the Fock matrix, matrix C contains the coefficients $c_{\alpha i}$ and matrix ϵ the orbital energies on its diagonal, respectively.⁶⁰ Thus, Equa-

tion 2.18 corresponds to a matrix-eigenvalue problem, where F is diagonalised, and then the coefficients c_{ai} and the energy ϵ are determined iteratively via the SCF procedure.

2.4.1 The Møller-Plesset approach

As mentioned previously, Hartree–Fock considers the interactions between electrons in an averaged way. More precisely, an electron feels all other electrons as a fixed distribution of charge, however instantaneous interactions between electrons are neglected at this point.^{61,63} Consequently, different approaches taking the correlation of electrons into account were developed.⁶¹ One of them is based on perturbation theory and known as Møller-Plesset (MP) method. The idea of perturbation theory is to describe a complex system as a perturbed version of a simpler one.⁶¹ This means that in addition to the above-mentioned Hartree-Fock energy, a correction term is introduced to account for the electron correlation. By adding this perturbation term $E^{(2)}$, a corrected HF energy, referred to as MP2 energy, is obtained (2 for second order of perturbation):^{60,61}

$$E_{\text{MP2}} = E_{\text{HF}}^{\text{total}} + E^{(2)} \quad (2.19)$$

While $E_{\text{HF}}^{\text{total}}$ is the Hartree–Fock energy (Equation 2.16), $E^{(2)}$ is a sum of terms that contains the excitation of an electron pair from occupied to virtual (unoccupied) molecular orbitals. This results in a lower electronic energy because these virtual orbitals allow electrons to better avoid each other, as they have more possibilities to move around.⁶¹ Since the complexity of MP2 increases significantly with the number of electrons and orbitals, MP2 calculations require much more computational time compared to HF.⁶¹ In order to save computational costs, the frozen-core (FC) approximation, where excitation of core orbitals is excluded, and the resolution of identity (RI) can be employed.⁶³ In RI-MP2 calculations, charge distributions are approximated by using auxiliary basis sets.^{40,64,67} An improvement of MP2 calculations, known as spin-component scaling (SCS-MP2), was introduced by Grimme.⁶⁸ Here, the MP2 correlation energy $E^{(2)}$ is the sum of a same spin ($\alpha\alpha$, $\beta\beta$) and an opposite spin ($\alpha\beta$, $\beta\alpha$) component:^{63,68}

$$E^{(2)} = p_{\text{ss}}E_{\text{ss}}^{(2)} + p_{\text{os}}E_{\text{os}}^{(2)} \quad (2.20)$$

These two empirical parameters (scaling factors), $p_{ss} = 1/3$ and $p_{os} = 1.2$, were obtained via extensive benchmarking.⁶⁸

Along with density function theory (DFT), MP2 is one of the most commonly used methods for ground-state calculations. It accounts for 80–90 % of the correlation energy.⁶⁴ In this Thesis, RI-MP2^{40–42} and RI-SCS-MP2^{40,41,67} calculations were employed for the electronic ground state, whereas excited-state calculations were performed at the RI-CC2^{49–53} and RI-SCS-CC2^{49–53,69} level of theory, whereby CC stands for coupled cluster which will be shortly introduced in the following.

2.4.2 The coupled-cluster method

Another approach to include electron correlation is the full configuration interaction (full CI) treatment. The basic idea is using the Hartree-Fock Slater determinant as reference configuration and adding further “excited” Slater determinants, where electrons are removed from occupied orbitals and placed into virtual orbitals. Thus, the occupied spin orbitals (indices a, b and c) are taken from the HF wave function:^{60,61,64}

$$\Phi_0 = |\phi_1 \phi_2 \dots \phi_a \phi_b \dots \phi_n| \quad (2.21)$$

For the excited configurations occupied orbitals are substituted by virtual ones (indices p, q and r). While in Equation 2.22 one electron is excited from the spin orbital ϕ_a to the virtual orbital ϕ_p , in Equation 2.23 two electrons are transferred, one from ϕ_a to ϕ_p and one from ϕ_b to ϕ_q which leads to singly and doubly excited configurations, respectively:^{60,61}

$$\Phi_a^p = |\phi_1 \phi_2 \dots \phi_p \phi_b \dots \phi_n| \quad (2.22)$$

$$\Phi_{ab}^{pq} = |\phi_1 \phi_2 \dots \phi_p \phi_q \dots \phi_n| \quad (2.23)$$

In CI, the exact wave function Ψ is the sum of all possible configurations which can be understood as a linear combination of determinants:⁶⁰

$$\Psi = c_0 \Phi_0 + \sum_{a,p} c_a^p \Phi_a^p + \sum_{\substack{a<b \\ p<q}} c_{ab}^{pq} \Phi_{ab}^{pq} + \sum_{\substack{a<b<c \\ p<q<r}} c_{abc}^{pqr} \Phi_{abc}^{pqr} + \dots \quad (2.24)$$

In Equation 2.24, Φ_0 is the HF Slater determinant, the first sum represents singly excited configurations, the second and third doubly and triply excited determinants and so on. If all possible configurations are included, this corresponds to the full configuration interaction wave function (= full CI). In Equation 2.24, the CI expansion coefficients c are weighting factors that show to what extent a certain electronic configuration contributes to the total wave function Ψ .⁶¹ The HF determinant is most important followed by doubly excited determinants. Additionally, single, triple and quadruple excitations contribute to the total wave function, whereas higher excitations play a minor role.⁶⁴ Due to high computational costs, full CI is only feasible for small molecules. Therefore, truncated CI methods are commonly used where some terms in Equation 2.24 are neglected. For example, in CIS calculations only single excitations are considered and in CISD singly and doubly excited states are included.

Analogously to CI, the coupled-cluster (CC) method uses a HF Slater determinant as reference. Here, an electron excitation operator \hat{T} acts on the HF wave function which allows for promotion of electrons into virtual orbitals:^{61,63}

$$\Psi = e^{\hat{T}} \Phi_{\text{HF}} \quad \text{with} \quad \hat{T} = \hat{T}_1 + \hat{T}_2 + \dots + \hat{T}_n \quad (2.25)$$

In Equation 2.25, n corresponds to the number of electrons. Thus, \hat{T}_1 excites one and \hat{T}_2 two electrons into virtual orbitals, respectively.⁶⁴

$$\begin{aligned} T_1 \Phi_{\text{HF}} &= \sum_i^{\text{occ}} \sum_a^{\text{vir}} t_i^a \Phi_i^a \\ T_2 \Phi_{\text{HF}} &= \sum_{i < j}^{\text{occ}} \sum_{a < b}^{\text{vir}} t_{ij}^{ab} \Phi_{ij}^{ab} \end{aligned} \quad (2.26)$$

The expansion coefficients t are referred to as cluster amplitudes. The operator $e^{\hat{T}}$ is defined by a Taylor-series expansion:⁶³

$$e^{\hat{T}} = 1 + \frac{\hat{T}^2}{2!} + \frac{\hat{T}^3}{3!} + \dots = \sum_{k=0}^{\infty} \frac{\hat{T}^k}{k!} \quad (2.27)$$

In this context, $e^{\hat{T}}$ can also be written as:

$$e^{\hat{T}} = 1 + T_1 + \left(T_2 + \frac{1}{2}T_1^2\right) + \left(T_3 + T_2T_1 + \frac{1}{6}T_1^3\right) + \left(T_4 + T_3T_1 + \frac{1}{2}T_2^2 + \frac{1}{2}T_2T_1^2 + \frac{1}{24}T_1^4\right) + \dots \quad (2.28)$$

The Equation 2.28 shows that a certain level of excitation is expressed as product of excitations. For example, T_3 , T_2T_1 as well as T_1^3 correspond to triply excited states. Commonly, to minimise computational costs, the excitation operator \hat{T} is truncated, so that not all terms of $e^{\hat{T}}$ are considered. Accordingly, CCD includes only coupled-cluster doubles ($e^{\hat{T}_2} = 1 + \hat{T}_2 + 0.5\hat{T}_2^2 + \dots$), CCSD singles and doubles ($e^{\hat{T}_1+\hat{T}_2}$) and CCSDT also contains triples ($e^{\hat{T}_1+\hat{T}_2+\hat{T}_3}$). However, higher excitations, e.g., quadruple excitations are approximated by the product of double excitations ($0.5\hat{T}_2^2$).^{62,63} In the nineteen-nineties, second-order coupled cluster (CC2), which combines CCSD and perturbation theory, was introduced.^{64,70,71} CC2 includes singly excited states as in CCSD, whereas the contribution of the doubles is obtained based on perturbation theory.^{64,70,71} Although the accuracy of the CC2 total energy is comparable to MP2, CC2 is well established for the calculation of excitation energies and molecular properties.^{49,64} Analog to MP2, the resolution of the identity (RI) and spin-component scaling (SCS) which were explained previously can be employed to second-order coupled cluster leading to RI-SCS-CC2.^{49–53,69}

References

- (1) Schwalb, N. K.; Temps, F. *J. Phys. Chem. A* **2009**, *113*, 13113–13123.
- (2) Pancur, T.; Schwalb, N. K.; Renth, F.; Temps, F. *Chem. Phys.* **2005**, *313*, 199–212.
- (3) Röttger, K. Ultrafast Deactivation Dynamics of Structurally Modified and Hydrogen-Bonded DNA and RNA Building Blocks, Dissertation, Christian-Albrechts-Universität zu Kiel, 2013.
- (4) Renth, F.; Siewertsen, R.; Strübe, F.; Mattay, J.; Temps, F. *Phys. Chem. Chem. Phys.* **2014**, *16*, 19556–19563.
- (5) Megow, S.; Fitschen, H. L.; Tuzek, F.; Temps, F. *J. Phys. Chem. Lett.* **2019**, *10*, 6048–6054.
- (6) Wang, S. Ultrafast Photoisomerization Dynamics of Photochromic Molecular Switches Affected by Their Environment and Ultrafast Energy Transfer, Dissertation, Christian-Albrechts-Universität zu Kiel, 2018.
- (7) Stange, U. C. Electronic Dynamics of Monomers, Dimers and Oligomers of Purine Nucleobases Studied by Femtosecond Time-Resolved Spectroscopy, Dissertation, Christian-Albrechts-Universität zu Kiel, 2018.
- (8) Megow, S. Ultrafast Dynamics of Spin-Crossover Complexes with Photochromic Ligands Investigated by Time-Resolved Electronic Absorption Spectroscopy, Dissertation, Christian-Albrechts-Universität zu Kiel, 2022.
- (9) Wilhelm, T.; Piel, J.; Riedle, E. *Opt. Lett.* **1997**, *22*, 1494–1496.
- (10) Cerullo, G.; De Silvestri, S. *Rev. Sci. Instrum.* **2003**, *74*, 1–18.
- (11) Siewertsen, R.; Renth, F.; Temps, F.; Sönnichsen, F. *Phys. Chem. Chem. Phys.* **2009**, *11*, 5952–5961.
- (12) *Mathematica Version 10.3*; Wolfram Research, Inc.: Champaign, IL, USA, 2015.
- (13) Maeder, M.; Neuhold, Y.-M., *Practical Data Analysis in Chemistry*, 1st ed.; Elsevier: Amsterdam, 2007.
- (14) *Essential Numerical Computer Methods*; Johnson, M., Ed.; Academic Press, Elsevier: Burlington, USA, 2010.

- (15) Van Stokkum, I. H. M.; Larsen, D. S.; Van Grondelle, R. *Biochim. Biophys. Acta* **2004**, 1657, 82–104.
- (16) Ruckebusch, C.; Sliwa, M.; Pernot, P.; de Juan, A.; Tauler, R. *J. Photochem. Photobiol. C* **2012**, 13, 1–27.
- (17) Renth, F, Unpublished results.
- (18) Böhnke, H. Electronic Deactivation and Reaction Dynamics of H-bonded Molecular Systems Studied by Femtosecond Time-Resolved Vibrational Absorption Spectroscopy, Dissertation, Christian-Albrechts-Universität zu Kiel, 2019.
- (19) Böhnke, H.; Bahrenburg, J.; Ma, X.; Röttger, K.; Näther, C.; Rode, M. F.; Sobolewski, A. L.; Temps, F. *Phys. Chem. Chem. Phys.* **2018**, 20, 2646–2655.
- (20) Adamczyk, K.; Prémont-Schwarz, M.; Pines, D.; Pines, E.; Nibbering, E. T. J. *Science* **2009**, 326, 1690–1694.
- (21) Hamm, P.; Wiemann, S.; Zurek, M.; Zinth, W. *Opt. Lett.* **1994**, 19, 1642–1644.
- (22) Hamm, P.; Kaundl, R. A.; Stenger, J. *Opt. Lett.* **2000**, 25, 1798–1800.
- (23) Kaundl, R. A.; Wurm, M.; Reimann, K.; Hamm, P.; Weiner, A. M.; Woerner, M. *J. Opt. Soc. Am. B* **2000**, 17, 2086–2094.
- (24) Roberts, G. M.; Marroux, H. J. B.; Grubb, M. P.; Ashfold, M. N. R.; Orr-Ewing, A. J. *J. Phys. Chem. A* **2014**, 118, 11211–11225.
- (25) Röttger, K.; Marroux, H. J. B.; Grubb, M. P.; Coulter, P. M.; Böhnke, H.; Henderson, A. S.; Galan, M. C.; Temps, F.; Orr-Ewing, A. J.; Roberts, G. M. *Angew. Chem. Int. Ed.* **2015**, 54, 14719–14722.
- (26) Hoffmann, F.; Ekimova, M.; Bekçioğlu-Neff, G.; Nibbering, E. T.; Sebastiani, D. *J. Phys. Chem. A* **2016**, 120, 9378–9389.
- (27) Röttger, K.; Marroux, H. J. B.; Böhnke, H.; Morris, D. T. J.; Voice, A. T.; Temps, F.; Roberts, G. M.; Orr-Ewing, A. J. *Faraday Discuss.* **2016**, 194, 683–708.
- (28) Röttger, K.; Marroux, H. J. B.; Chemin, A. F. M.; Elsdon, E.; Oliver, T. A. A.; Street, S. T. G.; Henderson, A. S.; Galan, M. C.; Orr-Ewing, A. J.; Roberts, G. M. *J. Phys. Chem. B* **2017**, 121, 4448–4455.

- (29) Orr-Ewing, A. J. *Chem. Soc. Rev.* **2017**, 46, 7597–7614.
- (30) Ingle, R. A.; Roberts, G. M.; Röttger, K.; Marroux, H. J. B.; Sönnichsen, F. D.; Yang, M.; Szyc, Ł.; Harabuchi, Y.; Maeda, S.; Temps, F.; Orr-Ewing, A. J. *Chem. Phys.* **2018**, 515, 480–492.
- (31) Straub, S.; Brünker, P.; Lindner, J.; Vöhringer, P. *Phys. Chem. Chem. Phys.* **2018**, 20, 21390–21403.
- (32) Straub, S.; Brünker, P.; Lindner, J.; Vöhringer, P. *Angew. Chem. Int. Ed.* **2018**, 57, 5000–5005.
- (33) Vöhringer, P. *Dalton Trans.* **2020**, 49, 256–266.
- (34) Codescu, M.-A.; Weiß, M.; Brehm, M.; Kornilov, O.; Sebastiani, D.; Nibbering, E. T. J. *J. Phys. Chem. A* **2021**, 125, 1845–1859.
- (35) Grubbs, M.; Orr-Ewing, A. J.; Ashfold, M. N. R. *Rev. Sci. Instrum.* **2014**, 85, 064104.
- (36) Terazima, M. *Chem. Phys. Lett.* **1994**, 230, 87–92.
- (37) Yang, J.; Song, Y. *Opt. Lett.* **2009**, 34, 157–159.
- (38) Kopczynski, M.; Lenzer, T.; Oum, K.; Seehusen, J.; Seidel, M. T.; Ushakov, V. G. *Phys. Chem. Chem. Phys.* **2005**, 7, 2793–2803.
- (39) Origin, Version 2018G; OriginLab Corporation Northampton, MA, USA.
- (40) Weigend, F.; Häser, M. *Theor. Chem. Acc.* **1997**, 97, 331–340.
- (41) Hättig, C.; Hellweg, A.; Köhn, A. *Phys. Chem. Chem. Phys.* **2006**, 8, 1159–1169.
- (42) Weigend, F. *Phys. Chem. Chem. Phys.* **2006**, 8, 1057–1065.
- (43) Lee, C.; Yang, W.; Parr, R. G. *Phys. Rev. B* **1988**, 37, 785–789.
- (44) Miehlisch, B.; Savin, A.; Stoll, H.; Preuss, H. *Chem. Phys. Lett.* **1989**, 157, 200–206.
- (45) Becke, A. D. *Phys. Rev. A* **1988**, 38, 3098–3100.
- (46) Becke, A. D. *J. Chem. Phys.* **1993**, 98, 5648–5652.
- (47) Grimme, S.; Antony, J.; Ehrlich, S.; Krieg, H. *J. Chem. Phys.* **2010**, 132, 154104.

- (48) Frisch, M. J.; Trucks, G. W.; Schlegel, H. B.; Scuseria, G. E.; Robb, M. A.; Cheeseman, J. R.; Scalmani, G.; Barone, V.; Mennucci, B.; Petersson, G. A.; Nakatsuji, H.; Caricato, M.; Li, X.; Hratchian, H. P.; Izmaylov, A. F.; Bloino, J.; Zheng, G.; Sonnenberg, J. L.; Hada, M.; Ehara, M.; Toyota, K.; Fukuda, R.; Hasegawa, J.; Ishida, M.; Nakajima, T.; Honda, Y.; Kitao, O.; Nakai, H.; Vreven, T.; Montgomery, J. A.; Peralta, J. E.; Ogliaro, F.; Bearpark, M.; Heyd, J. J.; Brothers, E.; Kudin, K. N.; Staroverov, V. N.; Kobayashi, R.; Normand, J.; Raghavachari, K.; Rendell, A.; Burant, J. C.; Iyengar, S. S.; Tomasi, J.; Cossi, M.; Rega, N.; Millam, J. M.; Klene, M.; Knox, J. E.; Cross, J. B.; Bakken, V.; Adamo, C.; Jaramillo, J.; Gomperts, R.; Stratmann, R. E.; Yazyev, O.; Austin, A. J.; Cammi, R.; Pomelli, C.; Ochterski, J. W.; Martin, R. L.; Morokuma, K.; Zakrzewski, V. G.; Voth, G. A.; Salvador, P.; Dannenberg, J. J.; Dapprich, S.; Daniels, A. D.; Farkas, Foresman, J. B.; Ortiz, J. V.; Cioslowski, J.; Fox, D. J., *Gaussian 09, Revision D.01*, Gaussian Inc., Wallingford CT, 2013.
- (49) Hättig, C.; Weigend, F. *J. Chem. Phys.* **2000**, *113*, 5154–5161.
- (50) Hättig, C.; Hald, K. *Phys. Chem. Chem. Phys.* **2002**, *4*, 2111–2118.
- (51) Hättig, C. *J. Chem. Phys.* **2003**, *118*, 7751–7761.
- (52) Hättig, C.; Köhn, A. *J. Chem. Phys.* **2002**, *117*, 6939–6951.
- (53) Hättig, C.; Köhn, A.; Hald, K. *J. Chem. Phys.* **2002**, *116*, 5401–5410.
- (54) TURBOMOLE V7.0 2015, a development of University of Karlsruhe and Forschungszentrum Karlsruhe GmbH, 1989-2007 TURBOMOLE GmbH, since 2007; available from <http://www.turbomole.com>.
- (55) Frieese, D. H.; Törk, L.; Hättig, C. *J. Chem. Phys.* **2014**, *141*, 194106.
- (56) Irikura, K. K.; Johnson III, R. D.; Kacker, R. N. *J. Phys. Chem. A* **2005**, *109*, 8430–8437.
- (57) Andersson, M. P.; Uvdal, P. *J. Phys. Chem. A* **2005**, *109*, 2937–2941.
- (58) Kesharwani, M. K.; Brauer, B.; Martin, J. M. *J. Phys. Chem. A* **2015**, *119*, 1701–1714.
- (59) Sinha, P.; Boesch, S. E.; Gu, C.; Wheeler, R. A.; Wilson, A. K. *J. Phys. Chem. A* **2004**, *108*, 9213–9217.
- (60) Atkins, P. W.; Friedman, R. S., *Molecular Quantum Mechanics*, 3rd ed.; Oxford University Press: Oxford, 1997.

- (61) Lewars, E. G., *Computational Chemistry*, 2nd ed.; Springer: Dordrecht Heidelberg London New York, 2011.
- (62) Szabo, A.; Ostlund, N. S., *Modern Quantum Chemistry: Introduction to Advanced Electronic Structure Theory*, 1st ed.; Dover Publications Inc.: Mineola, New York, 1996.
- (63) Levine, I. N., *Quantum Chemistry*, 7th ed.; Pearson Education: Upper Saddle River, 2013.
- (64) Jensen, F., *Introduction to Computational Chemistry*, 2nd ed.; John Wiley & Sons, Ltd: Chichester, 2007.
- (65) Hartree, D. R. *Math. Proc. Cambridge Philos. Soc.* **1928**, *24*, 89–110.
- (66) Born, M.; Oppenheimer, R. *Ann. Phys.* **1927**, *389*, 457–484.
- (67) Weigend, F.; Häser, M.; Patzelt, H.; Ahlrichs, R. *Chem. Phys. Lett.* **1998**, *294*, 143–152.
- (68) Grimme, S. *J. Chem. Phys.* **2003**, *118*, 9095–9102.
- (69) Hellweg, A.; Grün, S. A.; Hättig, C. *Phys. Chem. Chem. Phys.* **2008**, *10*, 4119–4127.
- (70) Christiansen, O.; Koch, H.; Jørgensen, P. *Chem. Phys. Lett.* **1995**, *243*, 409–418.
- (71) Christiansen, O.; Koch, H.; Jørgensen, P.; Helgaker, T. *Chem. Phys. Lett.* **1996**, *263*, 530–539.

Part II

Results and Discussion

Long-lived Excited States in 7- and 9-Methylpurine Probed by fs Time-Resolved Vibrational Absorption Spectroscopy

REBECCA HOLTMANN, AMKE NIMMRICH, HENDRIK BÖHNKE AND FRIEDRICH TEMPS

Institute of Physical Chemistry, Christian-Albrechts-University Kiel, Olshausenstr. 40, D-24098 Kiel, Germany

Published in: 22nd International Conference on Ultrafast Phenomena 2020, F. Kärtner, M. Khalil, R. Li, F. Légaré and T. Tahara, eds., OSA Technical Digest (Optical Society of America, 2020), paper M4B.19.

OWN CONTRIBUTIONS TO THIS PUBLICATION:

- femtosecond time-resolved fluorescence up-conversion,
- femtosecond time-resolved vibrational absorption spectroscopy,
- analyses of all experimental data,
- quantum chemical calculations for ground- and excited-state species,
- writing the manuscript.

Abstract

Transient vibrational absorption spectroscopy elucidates common deactivation pathways after UV photoexcitation for 7- and 9-methylpurine. However, 9-methylpurine exhibits an additional relaxation channel revealed by indirect observation of the excited $^1\pi\pi^*$ state.

3.1 Introduction

The canonical purine nucleobases adenine and guanine feature ultrashort excited-state lifetimes of $\tau < 1$ ps due to fast non-radiative deactivation pathways mediated by conical intersections (CIs) which connect the excited electronic state(s) to the ground state (GS).¹ In contrast, the parent molecule purine and its 9-methylpurine derivative have long-lived excited states, which have been detected by transient electronic absorption spectroscopy (TEAS).² Here, we report on the ensuing dynamics after photoexcitation of 7-methyl- and 9-methylpurine (7-MePur, 9-MePur) using transient vibrational absorption spectroscopy (TVAS) as ideal chemical structure-sensitive technique. The measured time-resolved spectra show a highly efficient population of long-lived excited states of $^1n\pi^*$ and $^3\pi\pi^*$ character. A concurrent partial electronic ground state recovery (GSR) in $\tau \approx 12$ ps occurs for both isomers, an additional nanosecond relaxation channel has been identified only in 9-MePur.

3.2 Experimental Details

The employed excitation pulses at $\lambda_{\text{exc}} = 267$ nm were generated by frequency tripling of an 800 nm fs Ti:Sa laser and focused into the sample flow-cell with 0.1 mm optical pathlength and CaF₂ windows. Broadband mid-infrared probe pulses were provided by difference frequency generation in AgGaS₂ of the signal and idler pulses from a two-stage optical parametric amplifier pumped by the Ti:Sa fundamental.³ Minimum energy structures and vibrational wavenumbers for the GS and the excited states of interest were calculated at the RI-SCS-MP2/def2-TZVPP and RI-SCS-CC2/def2-TZVPP levels of theory, respectively.

3.3 Results and Discussion

The experimental results for 7-MePur and 9-MePur are summarized in Fig. 3.1 in the panels labeled **A** and **B**, respectively. The top row on the left (**A1**, **B1**) shows the calculated vibrational spectra for the GS and the observed excited states ($^1\pi\pi^*$, $^1n\pi^*$, $^3\pi\pi^*$), the middle row (**A2**, **B2**) displays the recorded two-dimensional spectro-temporal transient absorption maps after excitation of the optically bright $^1\pi\pi^*$ states of the molecules, and the bottom row (**A3**, **B3**) presents the extracted temporal profiles for several selected vibrational bands. The solid lines in the time profiles show global fits to the experimental data by sums of exponentials.

Considering first our results for 7-MePur, the measurements in the 1635–1335 cm^{-1} spectral range show several strong ground state bleach (GSB) bands, whose positions agree nicely with the calculated GS wavenumbers. Although an energy barrier in the excited state preventing GSR was predicted,² the GS recovers partially (by $\approx 25\%$) within $\tau = 13$ ps. Furthermore, pronounced positive contributions at 1515 cm^{-1} and 1372 cm^{-1} are detected and assigned aided by the calculations to the optically dark $^1n\pi^*$ state. A blue-shift and a spectral narrowing of these bands are clearly visible at early times and attributed to vibrational cooling to the $^1n\pi^*$ minimum within, again, $\tau = 13$ ps. As the $^1n\pi^*$ signals decay with $\tau_2 = 250$ ps, positive bands at, e.g., 1550 cm^{-1} and 1390 cm^{-1} arise at later times. Supported by our calculations, these signals are ascribed to the $^3\pi\pi^*$ state. The $^1n\pi^*$ -to- $^3\pi\pi^*$ switching is nicely showcased in the 1500–1565 and 1375–1400 cm^{-1} windows (cf. Fig. 3.1-A2).

The interpretation of the results for 9-MePur is more challenging, because multiple overlapping bands can be located in our observation window (1635–1315 cm^{-1}). From the GSB signals at 1353 and 1345 cm^{-1} , which are not affected by excited-state contributions, we deduce a significantly higher GSR fraction ($\approx 50\%$) within $\tau = 10$ ps for the 9-MePur than for the 7-MePur isomer. In contrast, the intensities of the GSB signals at 1603 and 1585 cm^{-1} decrease further at late times. This is explained by a superimposed broad positive band that decays with $\tau_3 = 3.5$ ns (see blue circles and line for 1603 cm^{-1} in Fig. 3.1-B3). Our quantum chemical calculations predict an intense vibrational band of the $^1\pi\pi^*$ state in this region. Hence, we propose an additional nanosecond deactivation

channel for 9-MePur via the relaxed $^1\pi\pi^*$ state. Suitable vibrational marker bands for the relaxed $^1n\pi^*$ state are located at 1490 and 1375 cm^{-1} . Compared to 7-MePur, a significant longer $^1n\pi^*$ excited-state lifetime of $\tau_2 = 480$ ps was found. Again, these bands feature a blue-shift at early times, indicating vibrational relaxation towards the $^1n\pi^*$ minimum. Vibrational marker bands of the $^3\pi\pi^*$ state are detected at 1535, 1405 and 1330 cm^{-1} . In addition to

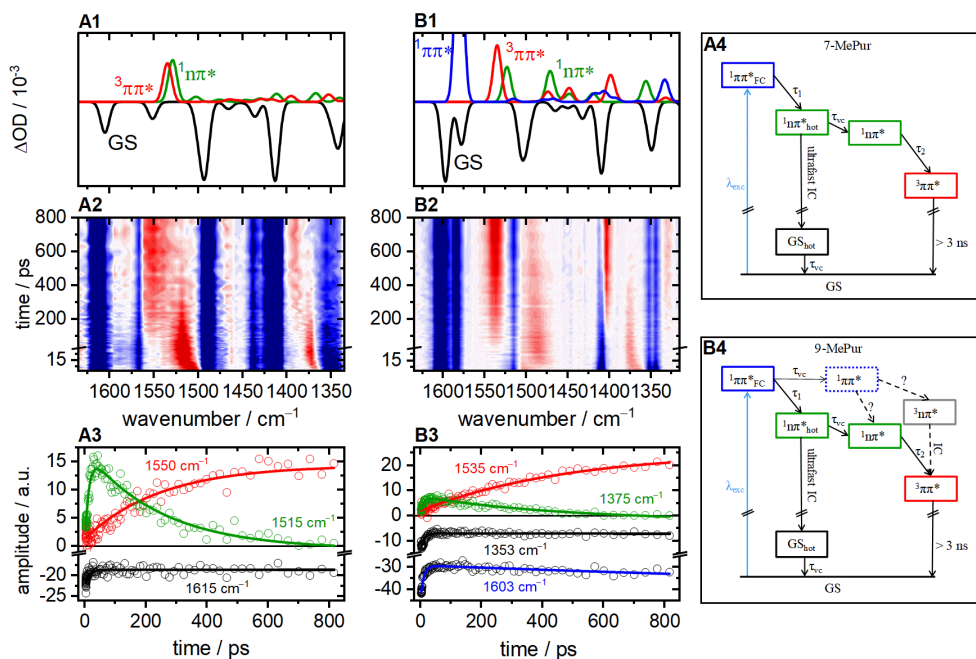


Figure 3.1: Summary of the experimental results for 7-MePur (A) and 9-MePur (B). **A1** and **B1**: Computed vibrational spectra for the GS (black) and the $^1\pi\pi^*$ (blue), $^1n\pi^*$ (green) and $^3\pi\pi^*$ (red) states. **A2** and **B2**: Spectro-temporal absorption maps after 267 nm excitation, with negative signals coded in blue and positive signals in red. **A3** and **B3**: Selected time profiles for the assigned electronic states. **A4** and **B4**: Proposed non-radiative electronic deactivation pathways.

the above-described TVAS measurements, we used time-resolved fluorescence up-conversion to assess the ultrafast internal conversion processes originating from the initially excited $^1\pi\pi^*$ to the $^1n\pi^*$ state and determined lifetimes of $\tau_1 = 0.28$ ps for 7-MePur and $\tau_1 = 0.35$ ps for 9-MePur. Collecting all available data, we propose the electronic deactivation schemes sketched in Fig. 3.1-A4 and B4. In summary, our results reveal two similar deactivation pathways for

both isomers: Recovery of the GS from the $^1\pi\pi^*$ via the $^1n\pi^*$ state followed by vibrational cooling in $\tau = 10 - 13$ ps, and intersystem crossing from the $^1n\pi^*$ to a $^3\pi\pi^*$ state in $\tau_2 = 250$ ps for 7-MePur and $\tau_2 = 480$ ps for 9-MePur. Although a fraction of the excited-state population is trapped in the $^1\pi\pi^*$ minimum, relaxation back to the electronic GS is enhanced for 9-MePur. The latter might be the reason for the functionalization of the nucleobases at the N9 rather than the N7 position when incorporated into the DNA. We note further that our results are comparable to data for plain 7H- and 9H-purine. Consequentially, our measurements provide valuable information on the relationship between chemical and electronic structure of the DNA building blocks regulating the electronic deactivation pathways after photoexcitation.

References

- (1) Crespo-Hernández, C. E.; Cohen, B.; Hare, P. M.; Kohler, B. *Chem. Rev.* **2004**, *104*, 1977–2019.
- (2) Crespo-Hernández, C. E.; Martínez-Fernández, L.; Rauer, C.; Reichardt, C.; Mai, S.; Pollum, M.; Marquetand, P.; González, L.; Corral, I. *J. Am. Chem. Soc.* **2015**, *137*, 4368–4381.
- (3) Böhnke, H.; Bahrenburg, J.; Ma, X.; Röttger, K.; Näther, C.; Rode, M. F.; Sobolewski, A. L.; Temps, F. *Phys. Chem. Chem. Phys.* **2018**, *20*, 2646–2655.

Population of long-lived excited states in 7- and 9-methylpurine unveiled by fs time-resolved vibrational absorption spectroscopy

REBECCA HOLTMANN, AMKE NIMMRICH, HENDRIK BÖHNKE AND FRIEDRICH TEMPS

Institute of Physical Chemistry, Christian-Albrechts-University Kiel, Olshausenstr. 40, D-24098 Kiel, Germany

OWN CONTRIBUTIONS TO THIS MANUSCRIPT:

- steady-state UV/vis, fluorescence and FTIR spectroscopy,
- time-correlated single photon counting measurements,
- femtosecond time-resolved fluorescence up-conversion,
- femtosecond time-resolved vibrational absorption spectroscopy,
- analyses of all experimental data,
- quantum chemical calculations for ground- and excited-state species,
- writing the manuscript.

The femtosecond time-resolved vibrational absorption spectroscopy measurements and quantum chemical calculations for ground- and excited-state species for purine were part of A. Nimmrich's Master's thesis.

Abstract

The photo-induced dynamics of 7- and 9-methylpurine (7-MePur, 9-MePur) are investigated as the parent systems for purine-based DNA building blocks by structure-sensitive time-resolved vibrational absorption spectroscopy (TVAS) after photoexcitation at $\lambda_{\text{exc}} = 267$ nm. The results are supported by time-resolved fluorescence spectroscopy (TFLS) and quantum chemical ab initio calculations. The obtained TVAS data reveal clear signatures of the excited $S_2(\pi\pi^*)$, $S_1(n\pi^*)$ and $T_1(\pi\pi^*)$ electronic states in the ensuing dynamics. Accordingly, after promotion to the $S_2(\pi\pi^*)$ state, the excited-state population is transferred to the vibrationally excited $S_1(n\pi^*)$ state by ultrafast internal conversion within $\tau_1 \leq 350$ fs. The subsequent common deactivation pathways proceed from the $S_1(n\pi^*)$ state for both isomers, namely rapid recovery of the electronic ground state associated with vibrational cooling within $\tau_2 \leq 13$ ps and intersystem crossing to the $T_1(\pi\pi^*)$ state with $\tau_3(7\text{-MePur}) = 250 \pm 30$ ps and $\tau_3(9\text{-MePur}) = 480 \pm 60$ ps, respectively. Exclusively for 9-MePur, an additional relaxation channel via the relaxed $S_2(\pi\pi^*)$ state is identified that deactivates on the nanosecond time scale with $\tau_4(9\text{-MePur}) = 3.50 \pm 0.20$ ns. No signatures by the $S_2(\pi\pi^*)$ state can be seen in the TVAS data for 7-MePur. Since the canonical nucleobases adenine (Ade) and guanine (Gua) typically feature excited-state lifetimes of $\tau < 1$ ps, the long-lived excited states reported for 7-MePur and 9-MePur highlight the crucial effects of the structural modifications in Ade and Gua on the relaxation dynamics.

4.1 Introduction

The mechanisms that are responsible for rapid energy dissipation ensuring the high UV photostability of the DNA and its building blocks have been intensively studied in the last decades.^{1–18} The canonical purine nucleobases adenine (Ade) and guanine (Gua) exhibit ultrashort excited-state lifetimes of $\tau < 1$ ps.^{2–7} The initially excited state is rapidly depopulated due to the accessibility of conical intersections (CIs) connecting the excited state with the electronic ground state (GS).^{7,14} These deactivation funnels provide ultrafast and efficient non-radiative relaxation channels back to the GS preventing potentially harmful reactions that may lead to photodamage. In contrast, the photo-induced dynamics of purine

(Pur), the parent molecule of Ade and Gua, received much less attention.^{15,19–22} Like other purine nucleobases, the purine chromophore exhibits an equilibrium between the 9H- and 7H-tautomers (7H-Pur and 9H-Pur), the tautomer ratios strongly depend on the molecular environment. For example, while 9H-Pur dominates in the gas phase and in acetonitrile (> 90 %),^{21,23,24} the 7H-tautomer coexists in high concentrations in protic solvents ranging from ~ 50 % in water to ~ 80 % in methanol.^{21,23–25} The chemical structures of the 7H- and 9H-forms of Pur alongside with their methylated analogues 7- and 9-methylpurine (7-MePur and 9-MePur) are shown in Fig. 4.1.

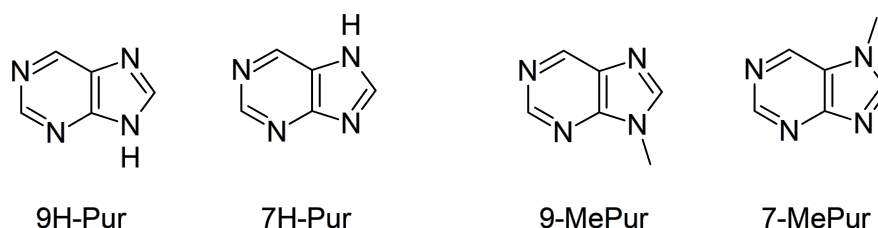


Figure 4.1: Chemical structures of the 9H- and 7H-tautomers of Pur (9H-Pur and 7H-Pur) alongside with their methylated analogues 9- and 7-methylpurine (9-MePur and 7-MePur).

The first femtosecond time-resolved study on the deactivation pathways of electronically excited purine and its methylated derivative 9-MePur in various solvents has been published in 2015.¹⁵ The authors combined transient electronic absorption spectroscopy (TEAS) with static *ab initio* calculations and surface-hopping simulations to elucidate the underlying relaxation mechanism. Contrary to the canonical nucleobases Ade and Gua, TEAS revealed population of long-lived excited states for 7H-/9H-Pur and 9-MePur.¹⁵ The authors proposed that after excitation to the $S_2(\pi\pi^*)$ state a rapid internal conversion (IC) to the optically dark $S_1(n\pi^*)$ state takes place within $\tau = 150\text{--}300$ fs. Subsequently, vibrational cooling towards the $S_1(n\pi^*)$ minimum was concluded to occur within $\tau \sim 10$ ps, followed by intersystem crossing (ISC) within $\tau = 195\text{--}645$ ps towards a long-lived triplet state. Ground-state recovery (GSR) takes place from the triplet state, since other relaxation pathways back to the electronic GS were essentially excluded due to an energy barrier of 0.6 eV in the excited state predicted by the employed CASPT2 calculations. Based on their data, the authors further concluded that the excited-state lifetimes and deactivation mechanisms are similar for 9H- and 7H-Pur.¹⁵

However, ultrafast spectroscopic measurements on electronically excited DNA and its monomeric building blocks demonstrated that structural modifications alter excited-state lifetimes and open up new deactivation channels.^{5,6,8,12,17,26–28} These studies unveil the complexity of the photochemistry and photodynamics of purine nucleobases and highlight that the interplay between chemical and electronic structure for these molecules is still not well understood.

Turning back to Pur, it is practically impossible to distinguish between its 7H- and 9H-tautomers using TEAS because the method lacks structure sensitivity. Although both tautomers contribute individually to the detected signals after photoexcitation, the recorded time-resolved data reflect the sum of their contributions which are no longer clearly assignable to a respective tautomer. Thus, two main questions regarding the photo-induced dynamics of purine and its methylated isomers remain elusive: (i) Do 7H-/9H-Pur and 7-/9-MePur exhibit similar electronic deactivation pathways taking place on comparable time scales? To the best of our knowledge, the processes upon photoexcitation of 7-MePur in the liquid phase have not yet been reported. And (ii), do the detected long-lived excited-state signals originate from the optically dark $S_1(n\pi^*)$ and the T_1 state as suggested in the literature,¹⁵ or are there even contributions from the originally excited $S_2(\pi\pi^*)$ state? Electronic state-specific spectroscopic as opposed to kinetic signatures of these states are highly desirable to answer this question.

In this work, we use femtosecond time-resolved vibrational absorption spectroscopy (TVAS) as an ideal structure-sensitive method for the investigation of 7- and 9-methylpurine. The results are aided by time-resolved fluorescence spectroscopy (TFLS) and by ab initio calculations. The parent molecule Pur has also been investigated in different solvents to elucidate the effect of 7H-/9H-tautomerism. The obtained results are summarised in the SI, since we will focus on the dynamics of 7- and 9-methylpurine, where tautomerism is hindered by methylation at the N7 and N9 position, respectively. In the following, a detailed description of the obtained results for 7- and 9-MePur in acetonitrile (ACN) is presented. Preliminary results have already been published.²⁹

4.2 Methods

Materials and static spectra

7- and 9-methylpurine were purchased from HDH Pharma (purity $\geq 95\%$) and used as received. All static and time-resolved measurements in this work were performed in acetonitrile (ACN, Uvasol grade) or deuterated acetonitrile (ACN- d_3). The recorded static fluorescence spectra were solvent corrected and multiplied with the fluorescence correction curve (FCC). Time-correlated single photon counting (TCSPC) measurements were recorded using the PicoQuant FluorTime 200 fluorescence lifetime spectrometer which has a time resolution of ~ 25 ps. Steady-state vibrational spectra were measured on an IFS66 Fourier Transform infrared spectrometer (Bruker) using a liquid-nitrogen cooled MCT detector. During the measurements the sample chamber was purged with dry air (PG 85 L, cmc-Instruments). The sample cell with an optical path length of 0.1 mm was equipped with CaF_2 windows for the subsequent TVAS measurements.

Time-resolved fluorescence spectroscopy

A detailed description of the experimental setup for the transient fluorescence measurements by the up-conversion technique can be found elsewhere.^{8,27,30,31} In short, a home-built non-collinear optical parametric amplifier (NOPA) generated laser pulses at 520 nm which were temporally compressed to 32 fs (FWHM) with a prism compressor. In a second step, pump pulses at $\lambda_{\text{exc}} = 260$ nm with a pulse energy of 350 nJ were obtained via second harmonic generation (SHG). The pump pulses were focused into the sample flow cell which had an optical path length of 1 mm. The emitted fluorescence was collimated by a pair of parabolic mirrors (Melles-Griot, $f = 119$ mm) and focused into a 0.1 mm BBO crystal ($\theta = 54.4^\circ$, $\phi = 0^\circ$). Another fraction of the Ti:Sa fundamental at $\lambda = 775$ nm was used for the gate pulses, which were also focused into the BBO crystal. By overlapping the gate pulses and the emitted fluorescence spatially and temporally in the BBO crystal, the sum frequency signal (SFG) was generated. Then the up-converted light was focused into the detection unit. The latter consisted of a monochromator (Jobin-Yvon HR 10), a photomultiplier (Hamamatsu R1527P), a preamplifier (Stanford Research SR 445) and a gated single-photon counter

(Stanford Research SR 400). To record transient fluorescence time profiles, the gate pulses were delayed up to $\Delta t = 1.4$ ns with respect to the pump pulses by a linear translation stage (Physik Instrumente). The measurements were carried out under magic angle (54.7°) conditions. The time profiles were fitted individually by a sum of exponentials convoluted with a Gaussian accounting for the instrument response function (IRF).

Time-resolved vibrational absorption spectroscopy

The femtosecond time-resolved vibrational absorption spectrometer^{32–34} has been built around a Ti:Sa laser system (Coherent, Libra HE, 1 kHz, 3.7 mJ / pulse) delivering light pulses of 90 fs duration (FWHM) at $\lambda = 800$ nm. Frequency tripling of the Ti:Sa fundamental yielded excitation pulses at $\lambda_{\text{exc}} = 267$ nm (0.6 μJ / pulse). They were loosely focused into a home-built sample flow cell with CaF_2 windows and an optical path length of 0.1 mm. Every second pump pulse was blocked by a synchronised optical chopper operating at 500 Hz. Another fraction of the laser fundamental was used to pump a two-stage optical parametric amplifier (OPA), which provided tunable signal and idler pulses. Subsequently, broadband mid-infrared probe pulses were generated by difference frequency generation (DFG) in AgGaS_2 of the signal and idler pulses.^{33,34} The pump and probe beams were spatially and temporally overlapped in the sample flow cell. The transmitted probe light was then guided to the grating spectrograph and spectrally dispersed before impinging on the liquid-nitrogen cooled 32-pixel MCT detector array. Transient vibrational difference spectra were recorded as function of pump–probe time delay. After baseline correction of the raw data in the KOALA programme,³⁵ the recorded transient spectra at each time delay were globally modelled by a sum of Gaussians. To extract time profiles, the respective amplitudes determined by the spectral band fitting were plotted against pump–probe time delay and fitted simultaneously using a sum of exponentials.

Quantum chemical calculations

The minimum energy structures and vibrational wavenumbers of 7- and 9-methylpurine in the electronic ground state were calculated at the RI-SCS-MP2 level of

theory^{36–38} employing the def2-TZVPP basis set.³⁸ For excited-state calculations of the minimum energy structures, vibrational spectra as well as vertical excitation energies, the RI-SCS-CC2 method^{39–44} with the def2-TZVPP basis set³⁸ was used. All calculations were performed on isolated molecules in vacuo using the TURBOMOLE 7.0 programme package.⁴⁵ The calculated harmonic vibrational wavenumbers in the ground state and in the excited states were scaled by factors of 0.97–0.98 as recommended in the literature from extensive benchmarking.^{46,47}

4.3 Results

Quantum chemical calculations

The investigations of 7-MePur and 9-MePur were initiated by quantum chemical calculations. The minimum energy structures for 7- and 9-methylpurine in the electronic ground state (GS) as well as in the first two excited singlet (S_1 and S_2) and in the first triplet (T_1) states were computed. A converged minimum energy structure in the S_2 state was found only for 9-MePur. Drawings of the optimised structures are given in the Supporting Information (SI) in Fig. 4.8.

Starting from the planar minimum energy structure in the electronic GS, the vertical excitation energies (VEEs), the oscillator strengths f and the involved molecular orbitals (MOs) for each electronic transition for 7- and 9-MePur are presented in Table 4.1. The characters of the excited states were determined by inspection of the involved molecular orbitals and the oscillator strengths.

For 7-MePur, the S_1 excited state is located at a VEE of 4.56 eV above the GS and identified as an optically dark $n\pi^*$ state due to its small oscillator strength of $f = 0.0033$. In contrast, the S_2 state at 4.92 eV and the S_3 state at 5.52 eV show $\pi\pi^*$ character, exhibiting significantly higher oscillator strengths with $f = 0.0794$ and $f = 0.0746$. In addition, the triplet states T_1 and T_2 are predicted at a VEE of 4.30 eV and 4.56 eV above the GS, respectively. Both are characterised as $\pi\pi^*$ states.

The energetic order of the singlet excited states is preserved for 9-MePur. However, the $S_1(n\pi^*)$ and $S_2(\pi\pi^*)$ states are shifted to slightly higher energies (4.68 eV and 5.06 eV). A lower oscillator strength of $f = 0.0561$ is calculated for the $S_3(\pi\pi^*)$ state. As for 7-MePur, the T_1 state at a VEE of 4.13 eV has $\pi\pi^*$ character, whereas the T_2 at a VEE of 4.51 eV is identified as $n\pi^*$ state.

Table 4.1: Calculated vertical excitation energies (VEEs) from the electronic GS along with the characters, oscillator strengths f and involved molecular orbitals (MOs) for each transition for 7- and 9-MePur.

isomer	state	character	VEE / eV	f	MOs
7-MePur	S ₁	$n\pi^*$	4.56	0.0033	HOMO-2 \rightarrow LUMO (90 %)
	S ₂	$\pi\pi^*$	4.92	0.0794	HOMO \rightarrow LUMO (75 %) HOMO-1 \rightarrow LUMO+2 (14 %)
	S ₃	$\pi\pi^*$	5.52	0.0746	HOMO-1 \rightarrow LUMO (74 %) HOMO \rightarrow LUMO+2 (8 %)
	T ₁	$\pi\pi^*$	4.30	–	HOMO \rightarrow LUMO (78 %) HOMO-1 \rightarrow LUMO (12 %)
	T ₂	$\pi\pi^*$	4.56	–	HOMO-1 \rightarrow LUMO (67 %) HOMO \rightarrow LUMO (16 %)
9-MePur	S ₁	$n\pi^*$	4.68	0.0020	HOMO-2 \rightarrow LUMO (91 %)
	S ₂	$\pi\pi^*$	5.06	0.0741	HOMO \rightarrow LUMO (43 %) HOMO-1 \rightarrow LUMO+2 (26 %) HOMO \rightarrow LUMO+2 (14 %)
	S ₃	$\pi\pi^*$	5.53	0.0561	HOMO-1 \rightarrow LUMO (50 %) HOMO \rightarrow LUMO (31 %)
	T ₁	$\pi\pi^*$	4.13	–	HOMO \rightarrow LUMO (85 %)
	T ₂	$n\pi^*$	4.51	–	HOMO-2 \rightarrow LUMO (87 %)

Static absorption and fluorescence spectra

The static UV/vis absorption and fluorescence spectra of 7- and 9-MePur in ACN are depicted in Fig. 4.2. Both isomers show intense UV absorption bands. While the first maximum is centered at 268 nm for 7-MePur, a small blue-shift is observed for 9-MePur as predicted theoretically (cf. Table 4.1). Based on the quantum chemical calculations, this absorption band is assigned to the optically bright $S_2(\pi\pi^*)$ state. The $S_3(\pi\pi^*)$ state is shifted to higher energies for both compounds. Thus, excitation pulses at $\lambda_{\text{exc}} = 267$ nm will primarily populate the $S_2(\pi\pi^*)$ state. For both isomers a shoulder is present at longer wavelengths ($\lambda > 285$ nm) which most likely originates from the optically dark $S_1(n\pi^*)$ state. Although the absorption band for 7-MePur is spectrally broadened, this shoulder appears to be more pronounced for 9-MePur.

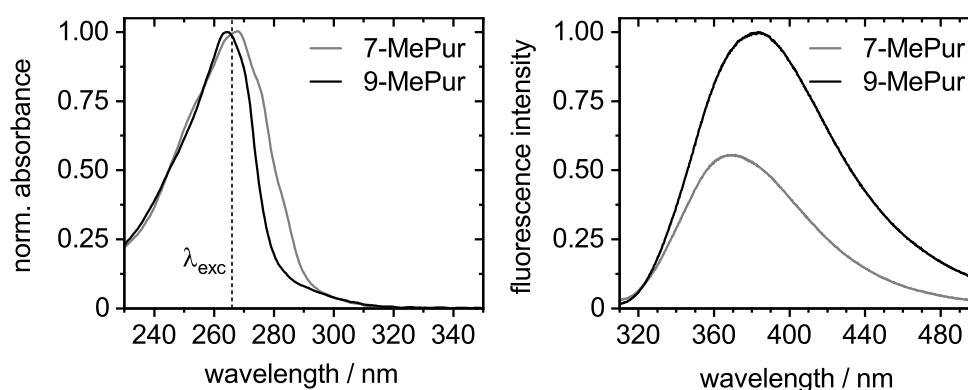


Figure 4.2: Static absorption (left) and fluorescence (right) spectra of 7-MePur (grey) and 9-MePur (black) in ACN. The relative fluorescence intensity of 9-MePur is normalised to unity at $\lambda = 383$ nm.

The static fluorescence spectra in ACN, displayed on the right in Fig. 4.2, were recorded after excitation at $\lambda_{\text{exc}} = 265$ nm. 9-MePur shows an emission band with a maximum located at 383 nm, whose intensity extends into the visible spectral range. In contrast, the fluorescence observed for 7-MePur is less intense and its maximum is blue-shifted to 370 nm. More detailed insights into the underlying dynamics are obtained from time-resolved fluorescence spectroscopy (TFLS).

Time-resolved fluorescence spectroscopy

Time-resolved fluorescence measurements provide information about the lifetimes of the optically bright excited states. An overview of the experimental results from TFLS by the up-conversion technique and from TCSPC measurements on 7-MePur and 9-MePur in ACN is given in Fig. 4.3.

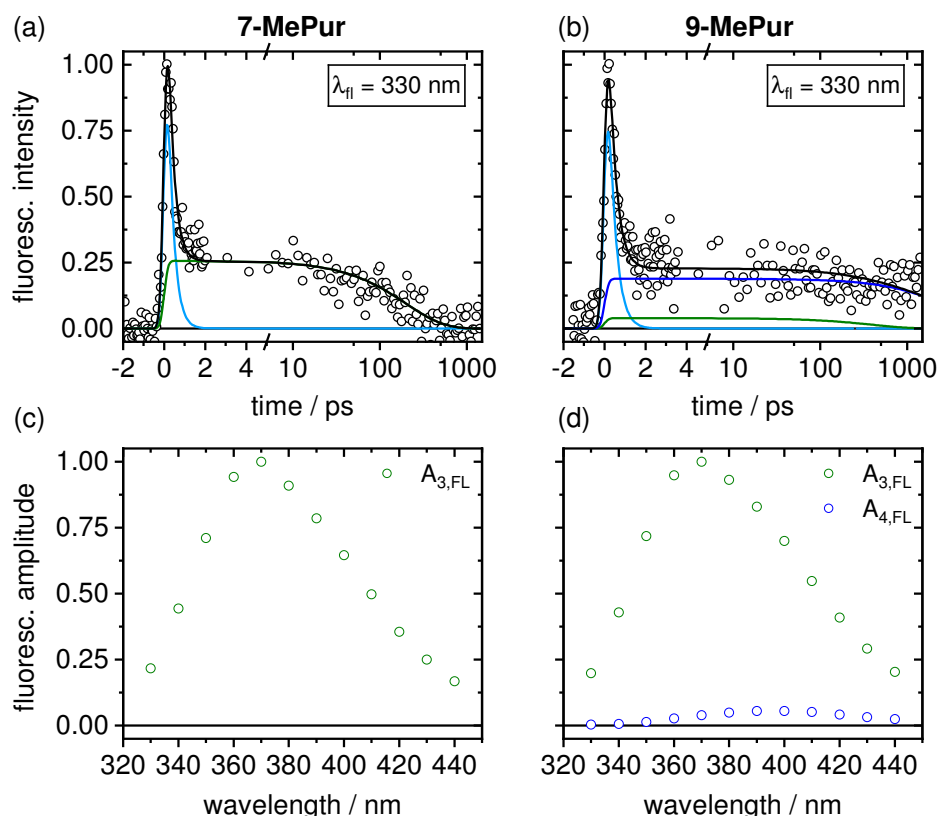


Figure 4.3: TFLS and TCSPC measurements on 7- and 9-MePur in ACN after photoexcitation. (a) TFLS time profile at $\lambda_{fl} = 330$ nm for 7- and (b) 9-MePur after excitation at $\lambda_{exc} = 260$ nm. Shown are the experimental data (circles) and the fit (black line) obtained by a sum of exponentials (light blue, green and blue) convoluted with the IRF. At early times up to 5 ps a linear scale is used, thereafter a logarithmic scale is chosen. (c) Wavelength-dependent amplitudes obtained from the global fit of the TCSPC time profiles from $\lambda_{fl} = 330$ –440 nm for 7- and (d) 9-MePur, respectively.

The TFLS data were recorded at $\lambda_{fl} = 330$ nm in ACN after $S_2(\pi\pi^*)$ excitation at $\lambda_{exc} = 260$ nm. Inspection of the TFLS time profiles for both isomers shows that the early-time dynamics are dominated ($A_{1,FL} = 87$ %, light blue curve) by

ultrafast processes. The following time components given with statistical 2σ uncertainty limits were found for 7- and 9-MePur:

$$\tau_{1,FL}(7\text{-MePur}) = 0.28 \pm 0.06 \text{ ps}$$

$$\tau_{1,FL}(9\text{-MePur}) = 0.35 \pm 0.09 \text{ ps}$$

While the fluorescence of 7-MePur decays and reaches the baseline after $\Delta t \sim 700$ ps, the fluorescence of 9-MePur is longer lived, reflected by a remaining offset at $\Delta t = 1.4$ ns. Thus, additional time components are needed to describe the TFLS time profiles towards late times. Therefore, supplementary TCSPC measurements after excitation at $\lambda_{exc} = 265$ nm recorded from $\lambda_{fl} = 330\text{--}440$ nm are used to shed light on the dynamics taking place on the pico- to nanosecond time scale. The obtained TCSPC time profiles were analysed in a global manner by a sum of exponentials taking into account the IRF and yielded the following time components with included systematic error limits:

$$\tau_{3,FL}(7\text{-MePur}) = 200. \pm 10.0 \text{ ps}$$

$$\tau_{3,FL}(9\text{-MePur}) = 400. \pm 15.0 \text{ ps}$$

$$\tau_{4,FL}(9\text{-MePur}) = 3.50 \pm 0.20 \text{ ns}$$

In line with the TFLS results, TCSPC shows that apart from $\tau_{1,FL}$, longer time constants are observed for both isomers. It should be noted here that τ_2 , which was obtained from TVAS, was not detected either with TFLS or TCSPC.

The wavelength-dependent TCSPC amplitudes are plotted in Fig. 4.3(c, d). For both isomers, $A_{3,FL}$ reaches its maximum at $\lambda_{fl} = 370$ nm. While the plotted amplitudes nicely reflect the static fluorescence spectrum for 7-MePur (cf. Fig. 4.2), the maximum of $A_{FL,4}$ for 9-MePur is red-shifted to $\lambda_{fl} = 400$ nm. Thus, the excited-state species associated with the nanosecond time component $\tau_{4,FL}$ appears to be responsible for the red-shift observed in the static fluorescence spectrum of 9-MePur.

All in all the time-resolved fluorescence data suggests that the initially excited optically bright $S_2(\pi\pi^*)$ state is rapidly depopulated via internal conversion (IC) to the optically dark $S_1(n\pi^*)$ state. This IC process is described with the ultrafast time component $\tau_{1,FL}$ obtained from TFLS. Subsequently, the optically dark $S_1(n\pi^*)$ state decays on the picosecond time scale with $\tau_{3,FL}$. Exclusively for

9-MePur, a nanosecond time component $\tau_4(9\text{-MePur}) = 3.50 \pm 0.20$ ns is needed to describe the decay of the fluorescence towards late delay times, indicating that the electronic deactivation of 9-MePur proceeds via another long-lived excited-state species. The most relevant data to identify the involved species after photoexcitation are provided by TVAS and presented in the following.

Time-resolved vibrational absorption spectroscopy

First, the results for 7-MePur will be presented. An overview of the experimental TVAS results for 7-MePur in the spectral range from 1635 cm^{-1} to 1335 cm^{-1} is given in Fig. 4.4. This overview consists of three individual measurements spliced together. The experimental time-resolved vibrational spectra after photoexcitation are shown in Fig. 4.4(b). A colour gradient from blue at early times to yellow to orange at later times is used. The coloured arrows indicate the temporal evolution of the detected vibrational bands. Several negative signals are observed which correspond to ground-state bleaching (GSB), since the GS is depopulated due to absorption of the excitation pulse. The positions of the GSB bands nicely agree with the inverted calculated GS vibrational spectrum depicted in black in Fig. 4.4(a). Based on the calculation, the signals mainly originate from deformation vibrations of the purine ring. For instance, vibrations arising from the methyl group at the N7 position are located at 1500 , 1466 and 1436 cm^{-1} . The experimental FTIR spectrum of 7-MePur in ACN-d_3 and visualisations of the vibrational marker modes in the different electronic states can be found in the SI in Fig. 4.9–4.12, respectively. In the investigated time window of $\Delta t \sim 815$ ps, the GS partially recovers by 25 %. Accordingly, a major fraction of the initially excited molecules stays in the excited state, indicating efficient population of a long-lived (excited) successor state. Indeed, positive signatures at 1515 and 1372 cm^{-1} are directly present at early delay times. Vibrational marker bands of the optically dark $S_1(n\pi^*)$ state are calculated at 1529 and 1368 cm^{-1} (cf. Fig. 4.4(a)). Thus, the early-time contributions originate from the $S_1(n\pi^*)$ state. Both S_1 bands feature a pronounced blue-shift and spectral narrowing at early delay times which indicate vibrational cooling from the vibrationally hot $S_1(n\pi^*)$ state towards its relaxed minimum. As the relaxed $S_1(n\pi^*)$ state decays, positive bands at 1550 and 1390 cm^{-1} are rising in intensity towards later times. By the calculations, they are attributed to the

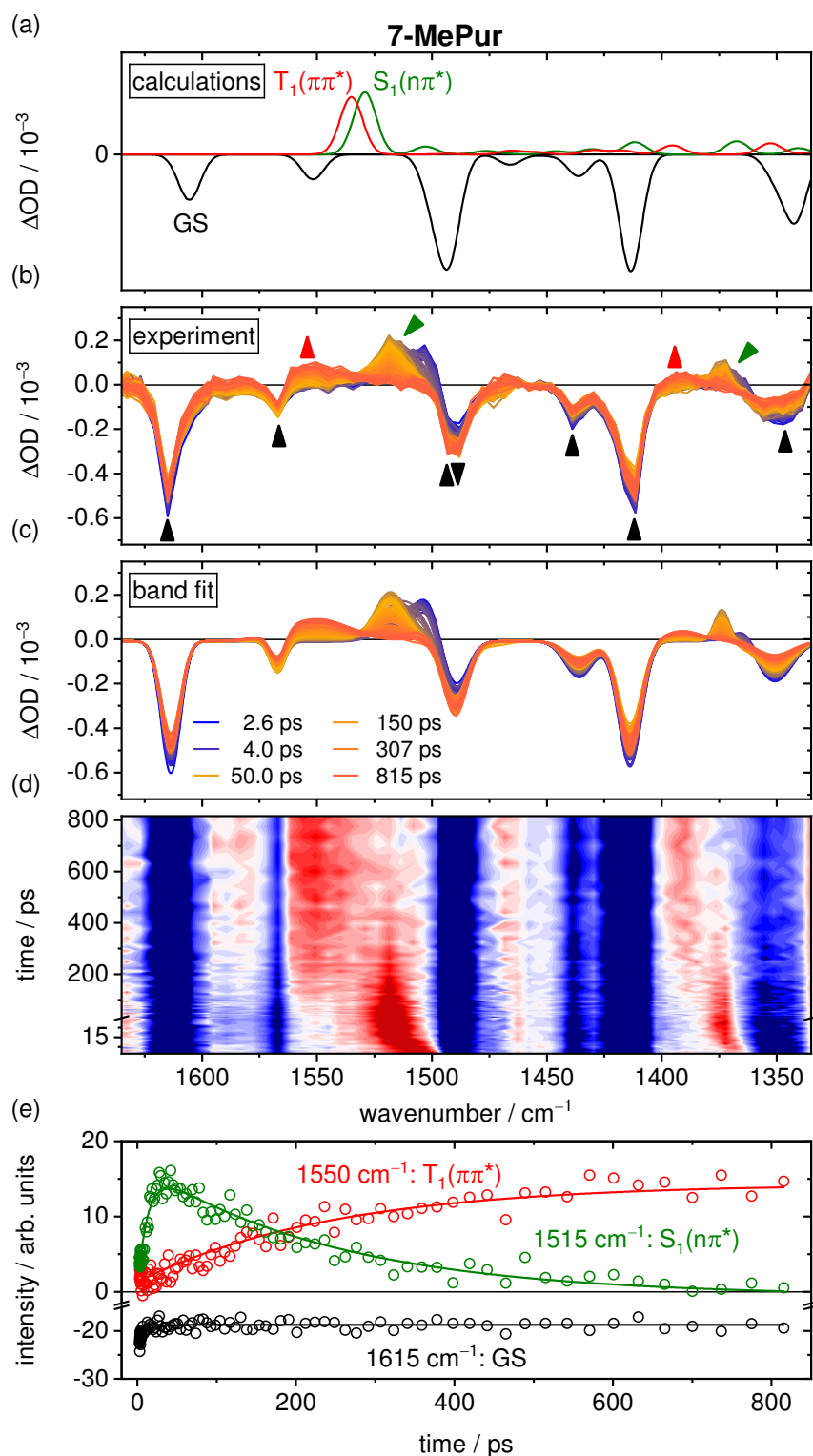


Figure 4.4: TVAS results for 7-MePur in ACN-d₃ after excitation at $\lambda_{\text{exc}} = 267 \text{ nm}$. (a) Computed vibrational spectra for the GS (black), the $S_1(n\pi^*)$ (green) and $T_1(\pi\pi^*)$ (red) states. (b) Recorded TVA spectra at different time delays. (c) Global Gaussian band fit to the experimental TVA spectra. (d) Spectro-temporal absorption map with negative (blue) and positive (red) signals. (e) Selected time profiles of the involved species. Shown are the respective amplitudes determined by the global band fit (open circles) and the global fit (straight lines) using a sum of two exponentials.

$T_1(\pi\pi^*)$ state. The positions of the experimental bands show good agreement with the calculated $T_1(\pi\pi^*)$ bands at 1535 and 1396 cm^{-1} (cf. Fig. 4.4(a)). The TVAS results clearly reveal that the deactivation of electronically excited 7-MePur proceeds via an El-Sayed⁴⁸ allowed intersystem crossing (ISC) from the relaxed $S_1(n\pi^*)$ to the long-lived $T_1(\pi\pi^*)$ state. The ISC process is nicely visualised in the coloured spectro-temporal absorption map in Fig. 4.4(d).

The transient spectra can be described by a global band fit using a sum of Gaussians as displayed in Fig. 4.4(c). To gain detailed insights into the ground and excited-state kinetics, the amplitudes obtained from the global band fit are plotted as function of pump–probe time delay and described in a global manner as shown for three selected time profiles in Fig. 4.4(e). Two global time components given with statistical 2σ uncertainty limits were found:

$$\tau_{2,\text{TVAS}}(7\text{-MePur}) = 13.0 \pm 1.00 \text{ ps}$$

$$\tau_{3,\text{TVAS}}(7\text{-MePur}) = 250. \pm 30.0 \text{ ps}$$

Although several GSB bands are superimposed by vibrational signatures arising from excited-state absorption, the time profile at 1615 cm^{-1} (black) shows that the GS recovers monoexponentially with $\tau_{2,\text{TVAS}}$. The $S_1(n\pi^*)$ state at 1515 cm^{-1} (green) grows in with $\tau_{2,\text{TVAS}}$ before it decays on longer time scales with $\tau_{3,\text{TVAS}}$. Concurrently, the population of the $T_1(\pi\pi^*)$ state at 1550 cm^{-1} (red) is described with $\tau_{3,\text{TVAS}}$. The value of $\tau_{3,\text{TVAS}}$ nicely agrees with the results from the time-resolved fluorescence measurements. As the decay of the triplet state back to the electronic GS very likely occurs on the nano-to-microsecond time scale, this process is not accessible with our time-resolved experiments.

The overview of the experimental TVAS results for 9-MePur in the spectral range from 1635 cm^{-1} to 1315 cm^{-1} is presented in Fig. 4.5. As before, this overview consists of three individual measurements which were merged. The negative signals are attributed to GSB bands and show good agreement with the calculated GS vibrational spectrum in Fig. 4.5(a). The experimental FTIR spectrum of 9-MePur in ACN-d_3 and visualisations of the marker modes in the different electronic states are given in the SI in Fig. 4.9 and in Fig. 4.13–4.16, respectively. In contrast to 7-MePur, a significantly higher ground-state recovery (GSR) of 50 % is determined. Thus, only about half of the initially excited molecules reach the long-lived successor state. The positive signals at 1505,

1490 and 1375 cm^{-1} are detected at early delay times and ascribed to the $S_1(n\pi^*)$ state. The corresponding S_1 marker modes are predicted theoretically at 1528, 1476 and 1360 cm^{-1} (cf. Fig. 4.5(a)). The observed band at 1505 cm^{-1} is less well described by the calculated one (1528 cm^{-1}), since it shifts into the GSB at 1515 cm^{-1} . For that reason, the spectral position of the this band at later times is difficult to determine. As for 7-MePur, vibrational relaxation towards the relaxed $S_1(n\pi^*)$ minimum is reflected by a pronounced blue-shift and spectral narrowing of the respective signals. Further, as the relaxed $S_1(n\pi^*)$ state decays, long-lived excited-state signals at 1535, 1405 and 1330 cm^{-1} grow in at later times. Their spectral positions nicely agree with the calculated marker bands at 1540, 1402 and 1336 cm^{-1} for the $T_1(\pi\pi^*)$ state (cf. Fig. 4.5(a)). Again, the electronic deactivation involves an ISC process from the $S_1(n\pi^*)$ minimum to the long-lived $T_1(\pi\pi^*)$ state.

From the global band fit of the experimental transient spectra in Fig. 4.5(c), the time profiles are obtained to extract the temporal evolution of the involved species after photoexcitation. For 9-MePur, selected time profiles are presented in Fig. 4.5(e). Three time components were needed to describe the dynamics:

$$\tau_{2,\text{TVAS}}(9\text{-MePur}) = 10.0 \pm 1.00 \text{ ps}$$

$$\tau_{3,\text{TVAS}}(9\text{-MePur}) = 480. \pm 60.0 \text{ ps}$$

$$\tau_{4,\text{TVAS}}(9\text{-MePur}) = 3.50 \text{ ns (fixed)}$$

It should be noted here that the statistical 2σ uncertainty limits for $\tau_{4,\text{TVAS}}$ are missing because its value was fixed at 3.5 ns, which was obtained from TCSPC measurements shown previously. Considering the time profiles, the experimental data of 9-MePur are more complex, because multiple bands from different molecular species tend to overlap in the investigated spectral region from 1635–1315 cm^{-1} . Exclusively the GSBs at 1355 cm^{-1} and 1346 cm^{-1} are not affected by other excited-state signatures and show incomplete repopulation within $\tau_{2,\text{TVAS}}$. In contrast, the intensity of the GSB at 1603 cm^{-1} initially increases before finally decaying on the nanosecond time scale with $\tau_{4,\text{TVAS}}$ at later times as visualised by the time profile at 1603 cm^{-1} in Fig. 4.5(e). This spectro-temporal behaviour can only be explained by a superimposed positive signal which decays with $\tau_{4,\text{TVAS}}$. Judging from the excited-state calculations, a highly intense vibrational band originating from the $S_2(\pi\pi^*)$ state is predicted

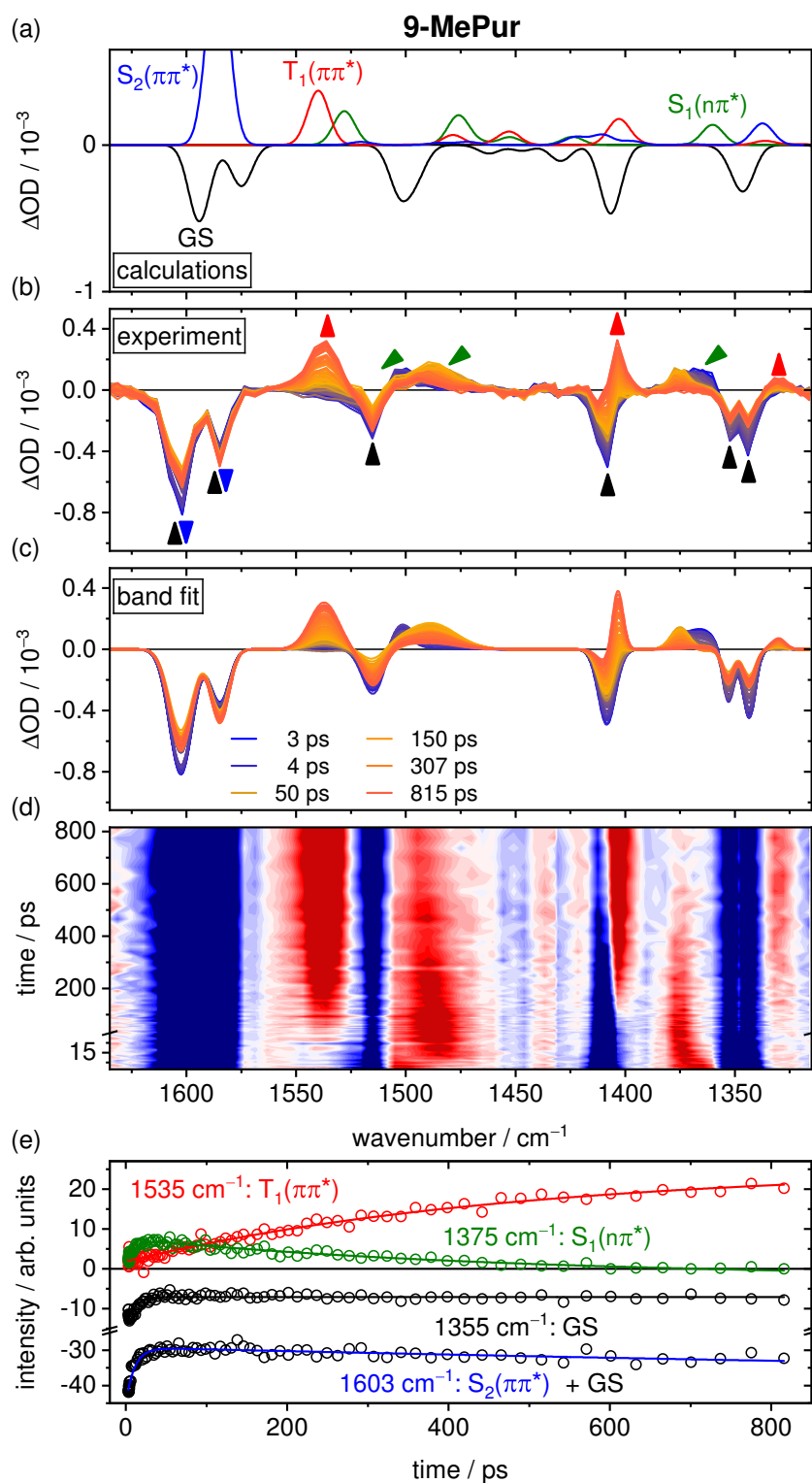


Figure 4.5: TVAS results for 9-MePur in ACN-d₃ after excitation at $\lambda_{\text{exc}} = 267$ nm. (a) Computed vibrational spectra for the GS (black), $S_2(\pi\pi^*)$ (blue), the $S_1(n\pi^*)$ (green) and $T_1(\pi\pi^*)$ (red) states. (b) Recorded TVA spectra at different time delays. (c) Global Gaussian band fit to the experimental TVA spectra. (d) Spectro-temporal absorption map with negative (blue) and positive (red) signals. (e) Selected time profiles of the involved species. Shown are the respective amplitudes determined by the global band fit (open circles) and the global fit (straight lines) using a sum of three exponentials.

theoretically in this spectral region (cf. blue spectrum in Fig. 4.5(a)). Thus, an additional deactivation channel via the relaxed $S_2(\pi\pi^*)$ state is suggested for 9-MePur. The time component $\tau_{4,\text{TVAS}}$ is therefore ascribed to the lifetime of the $S_2(\pi\pi^*)$ state. Importantly, this relaxation pathway was not detected for 7-MePur.

The time profile for the $S_1(n\pi^*)$ state (green) at 1375 cm^{-1} reveals that vibrational relaxation from the hot $S_1(n\pi^*)$ state to the $S_1(n\pi^*)$ minimum takes place with $\tau_{2,\text{TVAS}}$. The S_1 state then decays and populates the long-lived $T_1(\pi\pi^*)$ state. Both processes are described by $\tau_{3,\text{TVAS}}$. Again, this value shows good agreement with the time-resolved fluorescence data. The obtained results from the TFLS and TVAS measurements for 9H-Pur in ACN- d_3 and 7D-Pur in CD_3OD are summarised in the SI.

4.4 Discussion

In the following, the results presented in Section 4.3 are discussed, starting with the electronic structure and the results obtained from static spectroscopy before turning to the ultrafast spectroscopic measurements. On this basis, a deactivation scheme for 7- and 9-methylpurine will be proposed.

Electronic structure and static spectra

Fig. 4.6 shows single point calculations of the GS, $S_2(\pi\pi^*)$, $S_1(n\pi^*)$ as well as of the T_1 and T_2 states for both isomers to visualise the energetic order of the involved states at the converged minimum structures in the GS, $S_2(\pi\pi^*)$, $S_1(n\pi^*)$ and the $T_1(\pi\pi^*)$ states. For 7-MePur, a minimum structure in the $S_2(\pi\pi^*)$ state could not be obtained which may point at a steep gradient of the potential energy surface (PES) in the Franck–Condon region of the $S_2(\pi\pi^*)$ state. In addition, some states show strongly mixed $\pi\pi^*$ and $n\pi^*$ characters as noted in Fig. 4.6. Exclusively at the converged $S_1(n\pi^*)$ minimum structure, a change of the energetic ordering of the triplet states occurs for 7- and 9-MePur. Here, the T_1 state has $n\pi^*$ character, while at the other minimum structures, the T_1 state corresponds to a $\pi\pi^*$ state. The $T_2(\pi\pi^*)$ and $S_1(n\pi^*)$ states are very close in energy with $\Delta E_{7\text{-MePur}} = 0.33\text{ eV}$ and $\Delta E_{9\text{-MePur}} = 0.16\text{ eV}$ at the

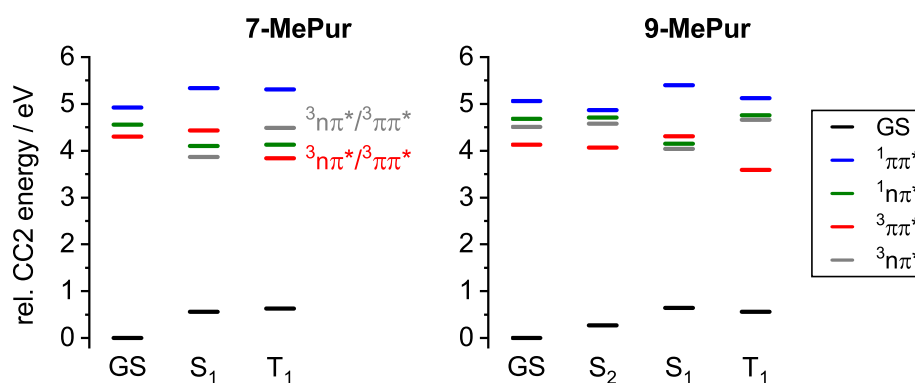


Figure 4.6: Single point calculations of the GS, $S_2(\pi\pi^*)$, $S_1(n\pi^*)$ and the T_1 and T_2 states at the converged minimum structures in the GS, $S_2(\pi\pi^*)$, $S_1(n\pi^*)$ and the $T_1(\pi\pi^*)$ for 7- and 9-MePur, respectively. The triplet states at the converged minimum structure of the T_1 state for 7-MePur exhibit mixed $\pi\pi^*$ and $n\pi^*$ character.

converged $S_1(n\pi^*)$ minimum. Calculations on 9-MePur considering the solvent demonstrated that the $S_1(n\pi^*)$ state shows a solvent-dependent shift to higher energies, whereas the $S_2(\pi\pi^*)$ state remains almost unchanged.¹⁵ In ACN, a blue-shift of 0.19 eV was theoretically predicted for the $S_1(n\pi^*)$ state.¹⁵ Hence, it may become energetically degenerate with the $T_2(\pi\pi^*)$ state in ACN solution. This energetic proximity of the excited singlet and triplet states may be the reason for the efficient ISC process observed for both isomers. Furthermore, the $T_1(n\pi^*)$ state (coloured in grey) is also located nearby with $\Delta E_{7\text{-MePur}} = 0.23$ eV and $\Delta E_{9\text{-MePur}} = 0.11$ eV.

At the converged $S_2(\pi\pi^*)$ minimum structure, the $S_2(\pi\pi^*)$, $S_1(n\pi^*)$ and $T_2(n\pi^*)$ are almost degenerate in energy making conversions between these states highly probable. The energetic proximity of these three states is in good agreement with results obtained for 9-MePur and Pur from MS-CASPT2/SA3-CASSCF(16,12) calculations.¹⁵

The computed vertical excitation energies for 7- and 9-MePur (cf. Table 4.1) suggest that the absorption band centered at ~ 268 nm primarily arises from a transition to the excited $S_2(\pi\pi^*)$ state. Although the $S_3(\pi\pi^*)$ state located at 5.52 eV (7-MePur) and 5.53 eV (9-MePur) may contribute to the UV absorption band, the employed excitation wavelengths of $\lambda_{\text{exc}} = 260\text{--}267$ nm will mainly populate the $S_2(\pi\pi^*)$ state.¹⁵ Aided by the calculations and in line with the

literature, the shoulder observed at $\lambda > 285$ nm in the static absorption spectra is assigned to the optically dark $S_1(n\pi^*)$ state.¹⁵

In the static fluorescence spectra, the band maximum for 9-MePur does not only appear red-shifted by 13 nm compared to 7-MePur, but also extends into the visible range. These differences originate from another emitting state which was detected by time-resolved spectroscopy. Exclusively for 9-MePur, an excited-state species, decaying with $\tau_{4,FL} = 3.5 \pm 0.20$ ns, gives rise to fluorescence at longer wavelengths ($\lambda_{fl} > 400$ nm). This long-lived fluorescence is most likely ascribed to arise from the relaxed $S_2(\pi\pi^*)$ state.

Femtosecond time-resolved dynamics

The obtained results from the time-resolved experiments provide valuable new details on the electronic relaxation pathways of both isomers. The time constants after UV photoexcitation of 7- and 9-methylpurine and Pur are summarised in Table 4.2. The values from the TEAS measurements in ACN¹⁵ are given for comparison.

Table 4.2: Time components τ_i with statistical 2σ uncertainty limits for 7-MePur, 9-MePur and Pur after photoexcitation in acetonitrile.

molecule	τ_1 / ps	τ_2 / ps	τ_3 / ps	τ_4 / ns
7-MePur ^a	0.28 ± 0.06	13.0 ± 1.00	250 ± 30.0	–
9-MePur ^a	0.35 ± 0.09	10.0 ± 1.00	480 ± 60.0	3.50 ± 0.20
9-MePur ^b	0.15 ± 0.05	10.0 ± 1.00	350 ± 10.0	–
Purine ^a	0.34 ± 0.07	9.00 ± 1.50	340 ± 55.0	0.88 ± 0.03
Purine ^b	0.19 ± 0.05	10.0 ± 3.00	360 ± 20.0	–

^athis work, ^bRef. [15].

For all compounds, the ultrafast time constant τ_1 is assigned to internal conversion from the initially populated Franck–Condon region of the $S_2(\pi\pi^*)$ state to the $S_1(n\pi^*)$ state. Subsequently, vibrational relaxation from the vibrationally hot $S_1(n\pi^*)$ state towards its relaxed minimum occurs with τ_2 . This process is reflected by a pronounced blue-shift and spectral narrowing of the experimentally observed vibrational bands of the $S_1(n\pi^*)$ state in the TVAS data.

Concurrently, the ground state is rapidly recovered from the vibrationally hot $S_1(n\pi^*)$ state. The time component τ_2 is further associated with vibrational cooling in the electronic GS. While τ_2 possesses almost similar values for all purine nucleobases, the values determined for the GSR differ strongly. Although an energy barrier in the excited state preventing ultrafast IC to the GS was predicted theoretically by CASPT2,¹⁵ the parent molecule Pur shows a GSR of $\text{GSR}_{\text{Pur}} = 60\%$ which is slightly decreased to $\text{GSR}_{9\text{-MePur}} = 50\%$ for 9-MePur. In contrast, the GS of 7-MePur is only repopulated by $\text{GSR}_{7\text{-MePur}} = 25\%$. This suggests that the accessibility of deactivation channels leading back to the GS is strongly influenced by the functionalisation at the N9/N7 position.

After reaching the S_1 minimum, intersystem crossing to the triplet manifold takes place with τ_3 . For 9-MePur, a significantly longer excited-state lifetime of $\tau_3(9\text{-MePur}) = 480 \pm 60$ ps is observed compared to 7-MePur with $\tau_3(7\text{-MePur}) = 250 \pm 30$ ps. The same trend is found for their parent molecule Pur in different solvents (cf. SI). In deuterated methanol, in which the 7D-tautomer of Pur dominates, an excited-state lifetime of $\tau_3(\text{Pur}) = 180 \pm 50$ ps was obtained, while for the 9H-tautomer predominating in ACN- d_3 , the S_1 state is longer-lived with $\tau_3(\text{Pur}) = 340 \pm 55$ ps. Previous ultrafast spectroscopic measurements on electronically excited DNA and its monomeric building blocks underlined that minor structural modifications strongly influence the excited-state lifetimes and underlying deactivation pathways.^{5,6,8,12,17,26–28} For example, the position of the H atom has a crucial impact on the photo-induced dynamics observed for Ade.^{5,6,8} The 9H-tautomer exhibits an excited-state lifetime of $\tau \sim 200$ fs.^{5,6,8} In contrast, a significantly longer time constant of $\tau \sim 8$ ps was attributed to its 7H tautomeric form.^{5,6,8} At the same time, investigation of the nucleosides and nucleotides of Ade¹⁷ showed that functionalisation at the N9 position has virtually no effect on the excited-state dynamics,⁶ whereas substitution at N7 actually alters the excited-state lifetime as observed here for 7- and 9-MePur. These studies impressively highlight that structural modifications regulate and open up new deactivation channels for purine nucleobases.

The time constants summarised in Table 4.2 nicely agree with the literature,¹⁵ but $\tau_1(7\text{-MePur})$ and $\tau_1(9\text{-MePur})$ as well as $\tau_3(9\text{-MePur})$ determined by TFLS and TVAS are slightly longer compared to the TEAS data. This may have various reasons. On the one hand, slightly different excitation wavelengths of $\lambda_{\text{exc}} = 260$ nm and $\lambda_{\text{exc}} = 266$ nm were used for the TFLS and TEAS measurements,

which might cause the differences observed for the ultrafast time constant τ_1 . On the other hand, FTIR spectroscopy of Pur in different solvents clearly revealed a solvent-dependent mixture of both tautomeric forms for Pur, e.g., the 7H-tautomer coexists in small amounts ($\sim 10\%$) in ACN- d_3 .²⁴ However, both tautomers of Pur are excited at $\lambda_{\text{exc}} = 260\text{--}267\text{ nm}$, thus a contribution of the 7H tautomeric form to the experimental TEAS data has to be expected which may have an impact on the obtained time constants. A mixture of tautomers is excluded for the methylated purine analogues 7- and 9-MePur which facilitated the data analysis and interpretation.

It should be noted here that the decay of the triplet state back to the electronic GS very likely occurs on the nano-to-microsecond time scale¹⁹ which is not accessible with our time-resolved experiments.

Aided by quantum chemical calculations, our TVAS data suggest a novel deactivation channel via population of the relaxed $S_2(\pi\pi^*)$ state after photoexcitation of 9-MePur and Pur. This was further confirmed by time-resolved fluorescence measurements yielding excited-state lifetimes of $\tau_4(9\text{-MePur}) = 3.5 \pm 0.20\text{ ns}$ and $\tau_4(\text{Pur}) = 0.88 \pm 0.03\text{ ns}$. From the $S_2(\pi\pi^*)$ state, either an IC to the $S_1(n\pi^*)$ state, or an El-Sayed⁴⁸ allowed ISC to the $T_2(n\pi^*)$ state can be expected. Unfortunately, these processes take place on longer time scales which are not accessible with our time-resolved measurements. Supported by the calculations, these three states are very close in energy ($\Delta E(S_2-S_1) = 0.16\text{ eV}$ and $\Delta E(S_2-T_2) = 0.29\text{ eV}$) at the converged $S_2(\pi\pi^*)$ minimum structure, making conversions between these states highly probable. However, deactivation via the $S_2(\pi\pi^*)$ state seems to play a minor role reflected by the observed small amplitudes which range between 1 to 10 % for 9-MePur.

The results for 7- and 9-MePur in ACN are summarised in the deactivation schemes visualised in Fig. 4.7. To the best of our knowledge, this work is the first experimental and theoretical study on the photodynamics of 7-MePur. Furthermore, the findings for Pur and 9-MePur are in good agreement with the literature.¹⁵ The previously proposed deactivation mechanism by Crespo-Hernández et al. was confirmed and updated based on the new findings of this work. For 9-MePur relaxation via the long-lived $S_2(\pi\pi^*)$ state and for both isomers repopulation of the GS from the hot $S_1(n\pi^*)$ state were identified as novel deactivation pathways. Importantly, significant differences regarding the accessibility and efficiency of the relaxation pathways in electronically excited 7-

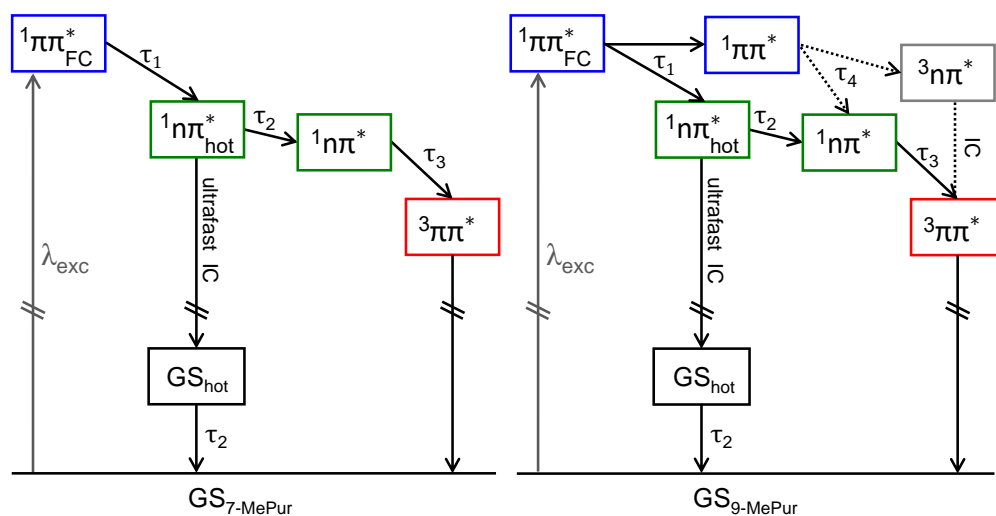


Figure 4.7: Proposed electronic deactivation pathways for 7-MePur (left) and 9-MePur (right) in ACN after photoexcitation.

and 9-MePur were elucidated. The results of 7- and 9-MePur are comparable to those for 7D- and 9H-Pur.

4.5 Conclusions

The photo-induced dynamics of 7- and 9-MePur were investigated in ACN solution by time-resolved vibrational absorption spectroscopy. The obtained results were aided by quantum chemical calculations and time-resolved fluorescence measurements. After excitation to the Franck–Condon region of the optically bright $S_2(\pi\pi^*)$ state, rapid IC to the vibrationally excited $S_1(n\pi^*)$ state takes place. Once in the S_1 state, ultrafast IC back to the electronic GS, and vibrational cooling towards the relaxed $S_1(n\pi^*)$ state are observed, followed by ISC to the triplet manifold. Exclusively for 9-MePur (and Pur) a novel deactivation channel via the relaxed $S_2(\pi\pi^*)$ state is proposed. The latter features an excited-state lifetime of $\tau_4(9\text{-MePur}) = 3.5 \pm 0.20$ ns and $\tau_4(\text{Pur}) = 0.88 \pm 0.03$ ns. Thus, contrary to other purine-based compounds, efficient population of a long-lived excited state occurs for Pur and its methylated isomers. Our data clearly revealed that methylation at the N7 and N9 position does not only influence the efficiency of particular deactivation pathways, (e.g., ground-state recovery), but also reg-

ulates their accessibility. These new insights provide a deeper understanding on the relationship between chemical and electronic structure for purine-based compounds and DNA building blocks. While functionalisation on the N9 position allows for rapid and efficient funneling back into the electronic GS, substitution at the C2 and/or C6 position appears to alter the topology of the excited-state potential energy surface in such a way that the population of long-lived excited states becomes inaccessible. The latter then results in ultrashort excited-state lifetimes of $\tau < 1$ ps as observed for the purine nucleobases adenine, guanine and hypoxanthine.

References

- (1) Callis, P. R. *Annu. Rev. Phys. Chem.* **1983**, *34*, 329–357.
- (2) Pecourt, J. M.; Peon, J.; Kohler, B. *J. Am. Chem. Soc.* **2001**, *123*, 10370–10378.
- (3) Peon, J.; Zewail, A. H. *Chem. Phys. Lett.* **2001**, *348*, 255–262.
- (4) Kang, H.; Jung, B.; Kim, S. K. *J. Chem. Phys.* **2003**, *118*, 6717–6719.
- (5) Gustavsson, T.; Sharonov, A.; Onidas, D.; Markovitsi, D. *Chem. Phys. Lett.* **2002**, *356*, 49–54.
- (6) Cohen, B.; Hare, P. M.; Kohler, B. *J. Am. Chem. Soc.* **2003**, *125*, 13594–13601.
- (7) Crespo-Hernández, C. E.; Cohen, B.; Hare, P. M.; Kohler, B. *Chem. Rev.* **2004**, *104*, 1977–2019.
- (8) Pancur, T.; Schwalb, N. K.; Renth, F.; Temps, F. *Chem. Phys.* **2005**, *313*, 199–212.
- (9) Shukla, M.; Leszczynski, J. *J. Biomol. Struct. Dyn.* **2007**, *25*, 93–118.
- (10) Schwalb, N. K.; Temps, F. *Science* **2008**, *322*, 243–245.
- (11) Middleton, C. T.; de La Harpe, K.; Su, C.; Law, Y. K.; Crespo-Hernández, C. E.; Kohler, B. *Annu. Rev. Phys. Chem.* **2009**, *60*, 217–239.
- (12) Röttger, K.; Siewertsen, R.; Temps, F. *Chem. Phys. Lett.* **2012**, *536*, 140–146.
- (13) Kleinermanns, K.; Nachtigallova, D.; de Vries, M. S. *Int. Rev. Phys. Chem.* **2013**, *32*, 308–342.
- (14) Schreier, W. J.; Gilch, P.; Zinth, W. *Annu. Rev. Phys. Chem.* **2015**, *66*, 497–519.
- (15) Crespo-Hernández, C. E.; Martínez-Fernández, L.; Rauer, C.; Reichardt, C.; Mai, S.; Pollum, M.; Marquetand, P.; González, L.; Corral, I. *J. Am. Chem. Soc.* **2015**, *137*, 4368–4381.
- (16) Böhnke, H.; Röttger, K.; Ingle, R. A.; Marroux, H. J.; Bohnsack, M.; Orr-Ewing, A. J.; Temps, F. *Phys. Chem. Chem. Phys.* **2018**, *20*, 20033–20042.
- (17) Stange, U. C.; Temps, F. *Chem. Phys.* **2018**, *515*, 441–451.

- (18) Chan, R. C.-T.; Ma, C.; Wong, A. K.-W.; Chan, C. T.-L.; Chow, J. C.-L.; Kwok, W.-M. *J. Phys. Chem. Lett.* **2022**, 302–311.
- (19) Quiñones, E.; Arce, R. *J. Am. Chem. Soc.* **1989**, 111, 8218–8223.
- (20) Schneider, M.; Hain, T.; Fischer, I. *ChemPhysChem* **2009**, 10, 634–636.
- (21) Borin, A. C.; Serrano-Andrés, L.; Fülcher, M. P.; Roos, B. O. *J. Phys. Chem. A* **1999**, 103, 1838–1845.
- (22) Mburu, E.; Matsika, S. *J. Phys. Chem. A* **2008**, 112, 12485–12491.
- (23) Broo, A.; Holmén, A. *Chem. Phys.* **1996**, 211, 147–161.
- (24) Nimmrich, A. Time-resolved vibrational spectroscopy of the nucleic acid chromophore purine in excited singlet and triplet states, Master Thesis, Christian-Albrechts-Universität zu Kiel, 2018.
- (25) Gonnella, N. C.; Roberts, J. D. *J. Am. Chem. Soc.* **1982**, 104, 3162–3164.
- (26) Parusel, A. B.; Rettig, W.; Rotkiewicz, K. *J. Phys. Chem. A* **2002**, 106, 2293–2299.
- (27) Schwalb, N. K.; Temps, F. *J. Phys. Chem. A* **2009**, 113, 13113–13123.
- (28) Demeter, A.; Druzhinin, S. I.; Kovalenko, S. A.; Senyushkina, T. A.; Zachariasse, K. A. *J. Phys. Chem. A* **2011**, 115, 1521–1537.
- (29) Holtmann, R.; Nimmrich, A.; Böhnke, H.; Temps, F. In *22nd Int. Conf. Ultrafast Phenom. 2020*, Optical Society of America: 2020, M4B.19.
- (30) Schwalb, N. K.; Michalak, T.; Temps, F. *J. Phys. Chem. B* **2009**, 113, 16365–16376.
- (31) Mewes, L.; Ingle, R. A.; Megow, S.; Böhnke, H.; Baranoff, E.; Temps, F.; Chergui, M. *Inorg. Chem.* **2020**, 59, 14643–14653.
- (32) Böhnke, H.; Bahrenburg, J.; Ma, X.; Röttger, K.; Näther, C.; Rode, M. F.; Sobolewski, A. L.; Temps, F. *Phys. Chem. Chem. Phys.* **2018**, 20, 2646–2655.
- (33) Hamm, P.; Kaindl, R. A.; Stenger, J. *Opt. Lett.* **2000**, 25, 1798–1800.
- (34) Kaindl, R. A.; Wurm, M.; Reimann, K.; Hamm, P.; Weiner, A. M.; Woerner, M. *J. Opt. Soc. Am. B* **2000**, 17, 2086–2094.
- (35) Grubbs, M.; Orr-Ewing, A. J.; Ashfold, M. N. R. *Rev. Sci. Instrum.* **2014**, 85, 064104.

- (36) Weigend, F.; Häser, M. *Theor. Chem. Acc.* **1997**, *97*, 331–340.
- (37) Hättig, C.; Hellweg, A.; Köhn, A. *Phys. Chem. Chem. Phys.* **2006**, *8*, 1159–1169.
- (38) Weigend, F.; Häser, M.; Patzelt, H.; Ahlrichs, R. *Chem. Phys. Lett.* **1998**, *294*, 143–152.
- (39) Hättig, C.; Weigend, F. *J. Chem. Phys.* **2000**, *113*, 5154–5161.
- (40) Hättig, C.; Hald, K. *Phys. Chem. Chem. Phys.* **2002**, *4*, 2111–2118.
- (41) Hättig, C. *J. Chem. Phys.* **2003**, *118*, 7751–7761.
- (42) Hellweg, A.; Grün, S. A.; Hättig, C. *Phys. Chem. Chem. Phys.* **2008**, *10*, 4119–4127.
- (43) Hättig, C.; Köhn, A. *J. Chem. Phys.* **2002**, *117*, 6939–6951.
- (44) Hättig, C.; Köhn, A.; Hald, K. *J. Chem. Phys.* **2002**, *116*, 5401–5410.
- (45) TURBOMOLE V7.0 2015, a development of University of Karlsruhe and Forschungszentrum Karlsruhe GmbH, 1989-2007 TURBOMOLE GmbH, since 2007; available from <http://www.turbomole.com>.
- (46) Frieese, D. H.; Törk, L.; Hättig, C. *J. Chem. Phys.* **2014**, *141*, 194106.
- (47) Kesharwani, M. K.; Brauer, B.; Martin, J. M. *J. Phys. Chem. A* **2015**, *119*, 1701–1714.
- (48) El-Sayed, M. A. *J. Chem. Phys.* **1963**, *38*, 2834–2838.

4.6 Supporting Information

The calculated minimum energy structures in the electronic ground state (GS) as well as in the first excited singlet $S_1(n\pi^*)$ and triplet $T_1(\pi\pi^*)$ states for 7- and 9-methylpurine are presented in Fig. 4.8. Exclusively for 9-MePur, a converged minimum energy structure in the $S_2(\pi\pi^*)$ state was found. At the $T_1(\pi\pi^*)$ minimum, a slight out-of-plane distortion of the C6 and N3 atoms is observed for both isomers. Apart from that, all other computed minimum structures are planar.

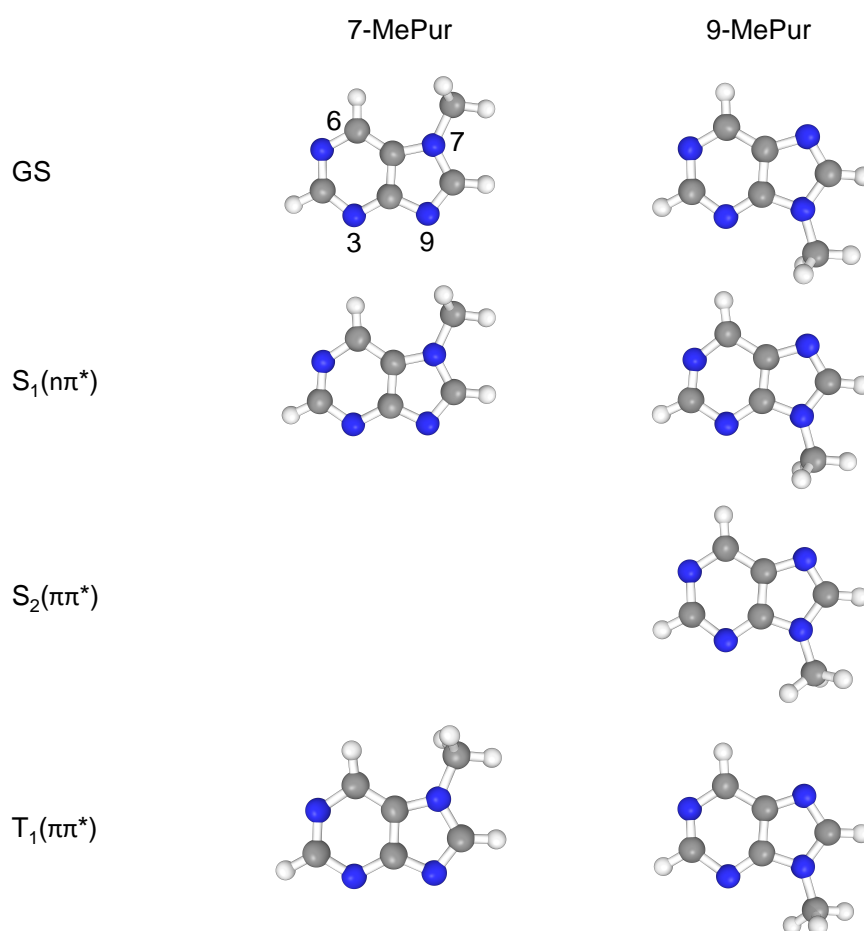


Figure 4.8: Minimum energy structures of 7-MePur (left) and 9-MePur (right) in the electronic GS and in the excited $S_1(n\pi^*)$, $S_2(\pi\pi^*)$ and $T_1(\pi\pi^*)$ states, respectively. For 7-MePur no minimum structure in the $S_2(\pi\pi^*)$ state could be obtained.

The experimental FTIR spectra of 7- and 9-MePur alongside with the calculated vibrational spectra in different electronic states are depicted in Fig. 4.9. The calculated vibrational spectra of the GS (black) nicely agree with the experimental FTIR spectra recorded in ACN-d₃ (grey). While for 9-MePur two vibrational bands at 1355 cm⁻¹ and 1346 cm⁻¹ are observed experimentally, they appear as single vibrational band at 1346 cm⁻¹ in the computed spectrum. However, the envelop of this band contains two overlapping vibrational modes located at 1351 cm⁻¹ and 1345 cm⁻¹ which are displayed in Fig. 4.13.

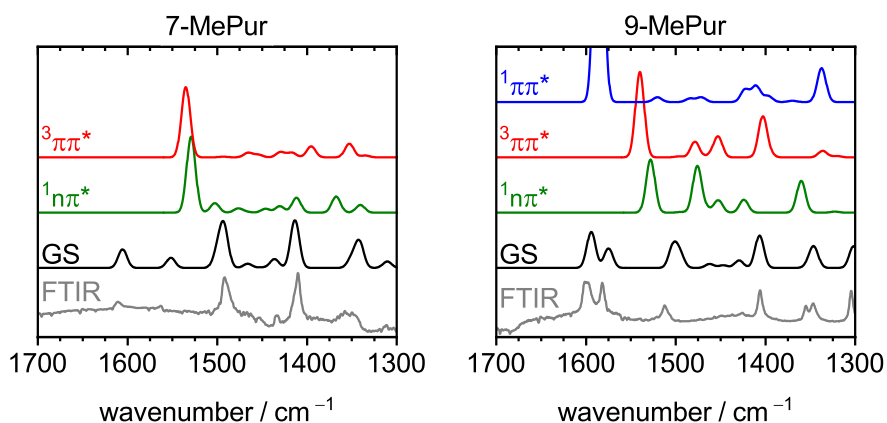


Figure 4.9: Calculated and experimental vibrational spectra for 7-MePur (left) and 9-MePur (right) in the spectral region from 1300–1700 cm⁻¹. Shown are the calculated vibrational spectra in the electronic GS, the S₂($\pi\pi^*$), the S₁($n\pi^*$) and the T₁($\pi\pi^*$) states coloured in black, blue, green and red, respectively. The experimental FTIR spectra (grey) of both isomers were recorded in ACN-d₃.

Visualisations of the calculated vibrational marker modes in the electronic GS and in the different excited states in the spectral region from 1700 cm^{-1} to 1300 cm^{-1} can be found in Fig. 4.10–4.16. The calculated wavenumbers are given first and are scaled by factors of 0.97–0.98. The experimentally detected vibrational wavenumbers in ACN- d_3 observed in the FTIR and TVAS measurements are given in parenthesis.

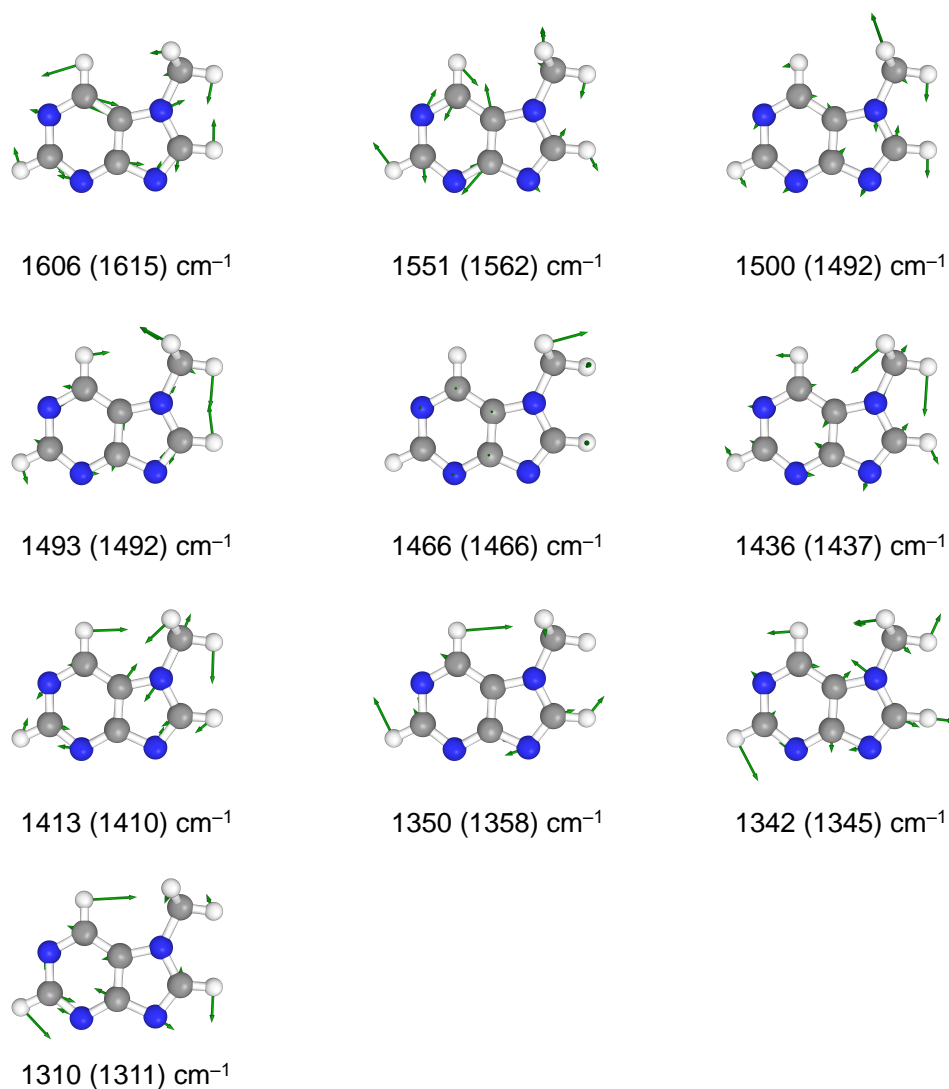


Figure 4.10: The experimental (in ACN- d_3) and calculated vibrational marker modes of 7-MePur in the electronic GS. The calculated values are given first and are scaled by a factor of 0.97. Experimental values are given in parenthesis.

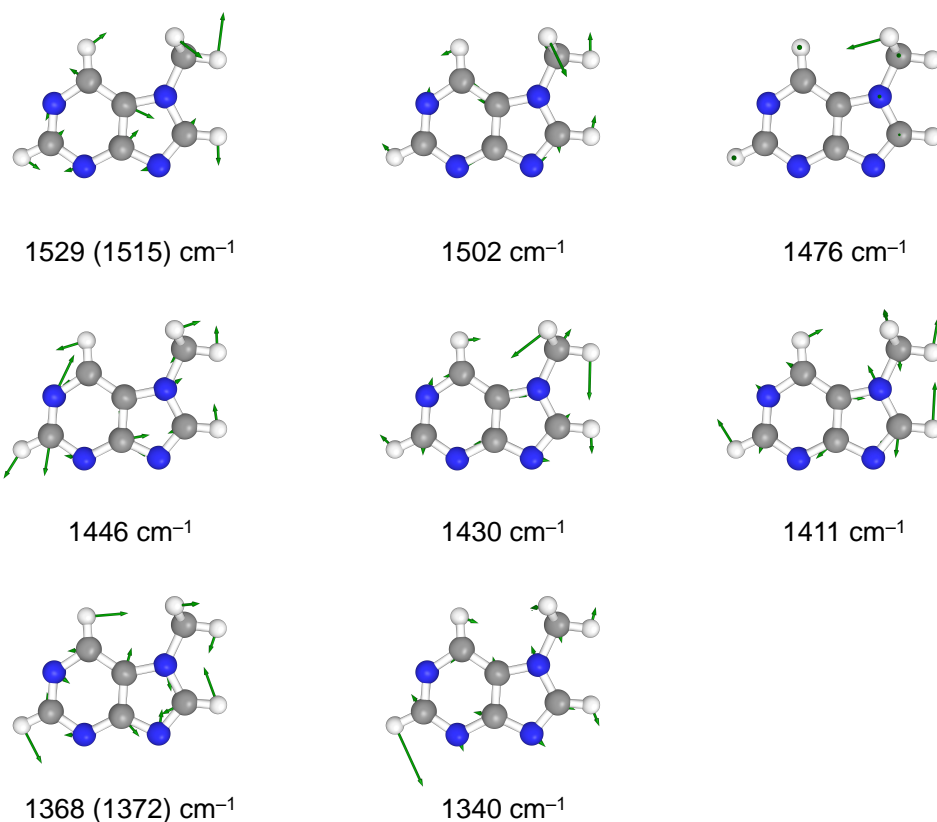


Figure 4.11: The experimental (in ACN- d_3) and calculated vibrational marker modes of 7-MePur in the $S_1(n\pi^*)$ state. The calculated values are given first and are scaled by a factor of 0.98. Experimental values are given in parenthesis.

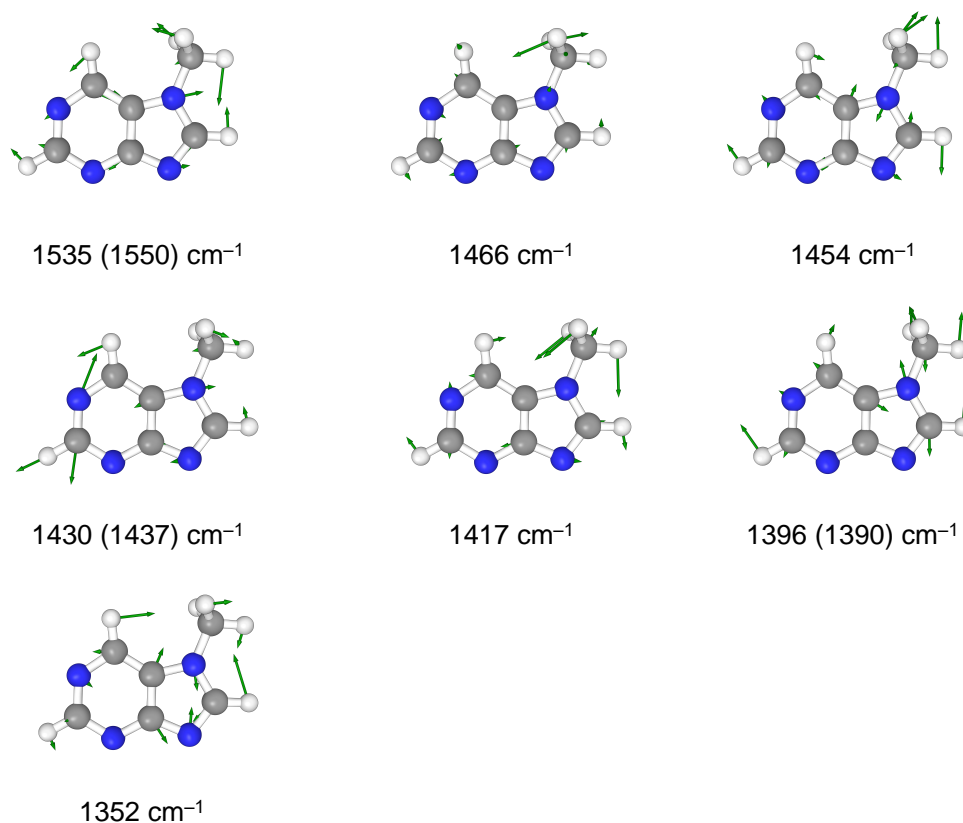


Figure 4.12: The experimental (in ACN- d_3) and calculated vibrational marker modes of 7-MePur in the $T_1(\pi\pi^*)$ state state. The calculated values are given first and are scaled by a factor of 0.98. Experimental values are given in parenthesis.

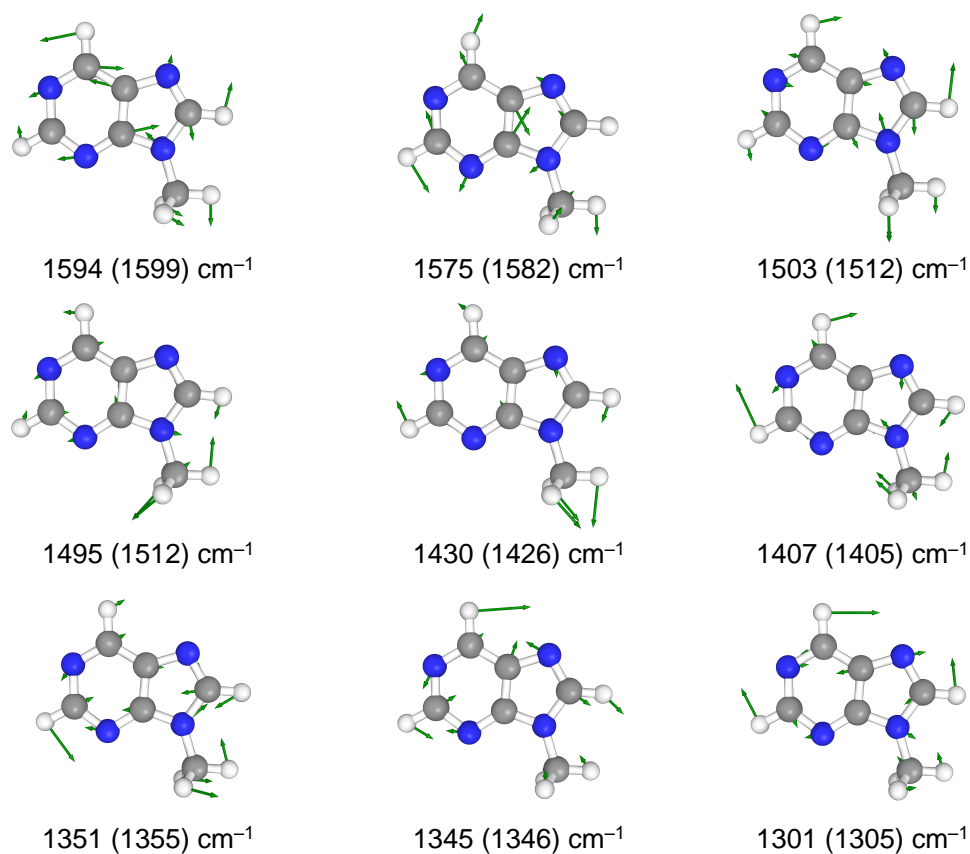


Figure 4.13: The experimental (in ACN- d_3) and calculated vibrational marker modes of 9-MePur in the electronic GS. The calculated values are given first and are scaled by a factor of 0.97. Experimental values are given in parenthesis.

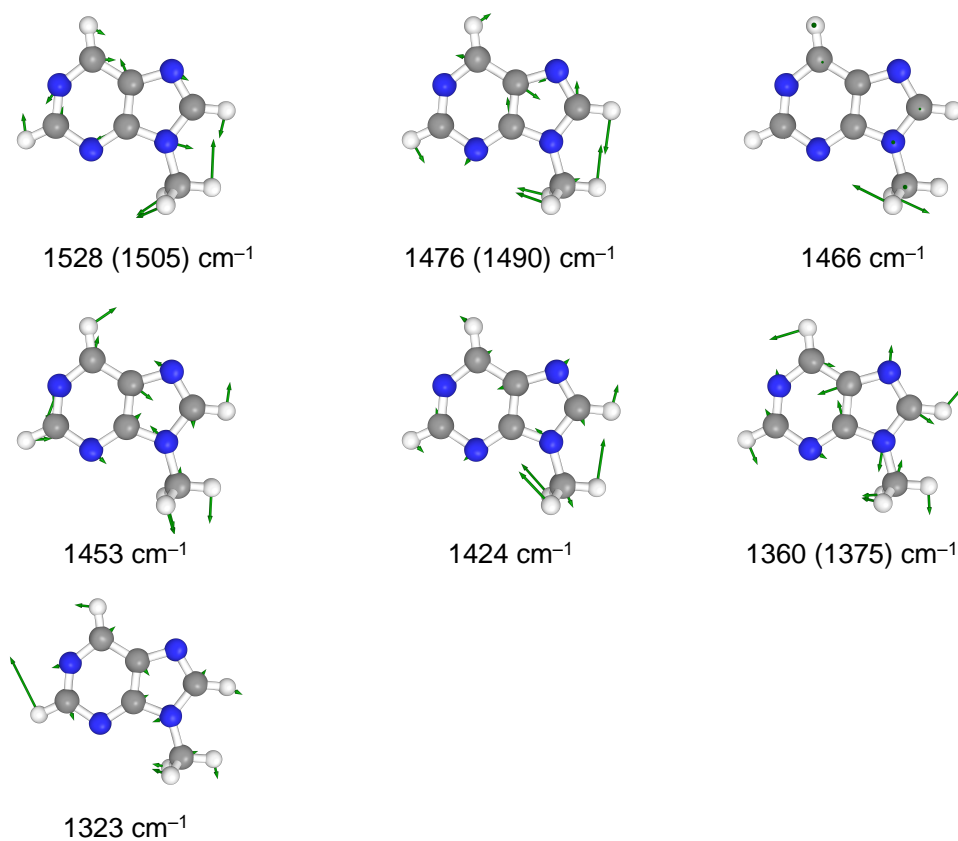


Figure 4.14: The experimental (in ACN- d_3) and calculated vibrational marker modes of 9-MePur in the $S_1(n\pi^*)$ state. The calculated values are given first and are scaled by a factor of 0.975. Experimental values are given in parenthesis.

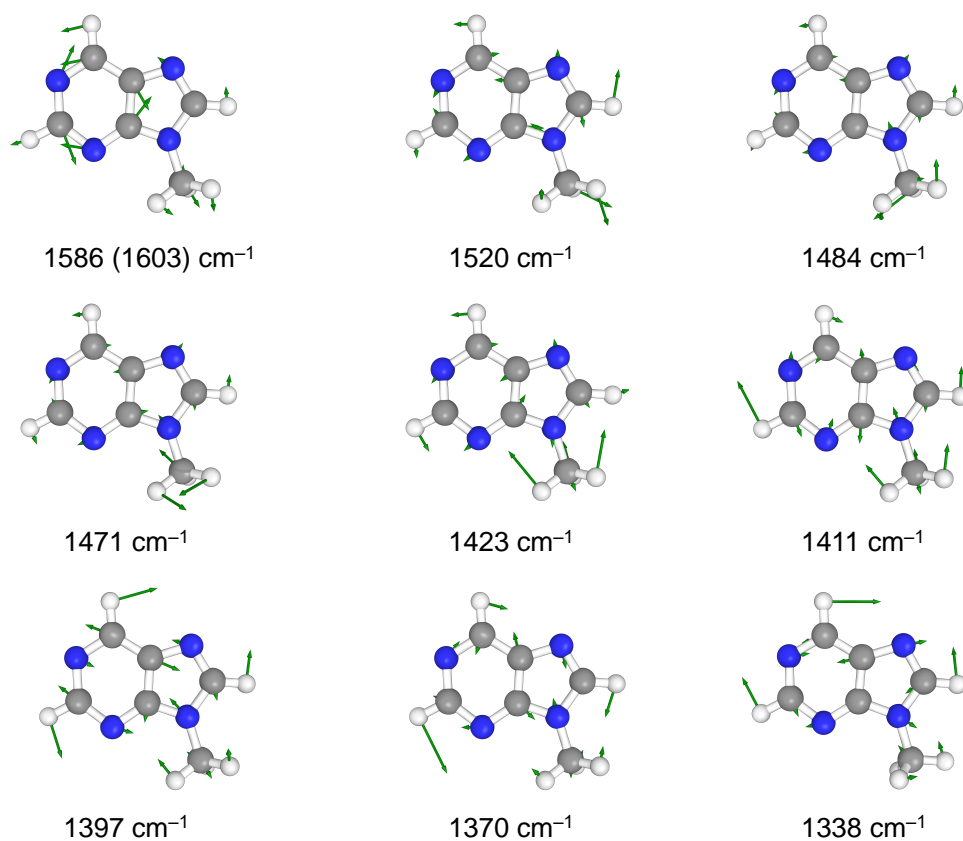


Figure 4.15: The experimental (in ACN- d_3) and calculated vibrational marker modes of 9-MePur in the $S_2(\pi\pi^*)$ state state. The calculated values are given first and are scaled by a factor of 0.975. Experimental values are given in parenthesis.

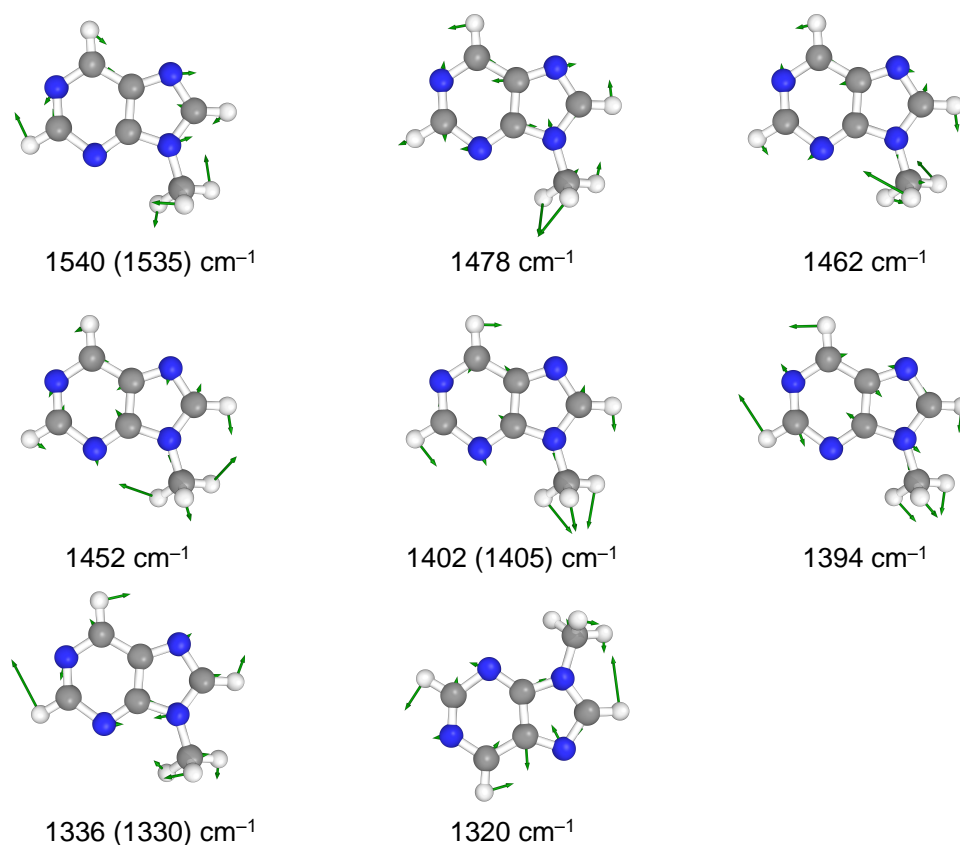


Figure 4.16: The experimental (in ACN- d_3) and calculated vibrational marker modes of 9-MePur in the $T_1(\pi\pi^*)$ state state. The calculated values are given first and are scaled by a factor of 0.975. Experimental values are given in parenthesis.

Time-resolved dynamics of purine

An overview of the results of purine (Pur) in ACN obtained from static spectroscopy and time-resolved fluorescence measurements is presented in Fig. 4.17. As mentioned previously, the 9H-tautomer of Pur dominates in ACN, but its 7H tautomeric form coexists in small amounts of $\sim 10\%$ in ACN solution. In the absorption spectrum an intense band is located at 264 nm which extends up to ~ 310 nm. Based on quantum chemical calculations²³ and in line with the literature,¹⁴ the band at 264 nm is assigned to the $S_2(\pi\pi^*)$ state, while the optically dark $S_1(n\pi^*)$ state appears red-shifted at ~ 290 nm. Furthermore, a shoulder at 240 nm is observed which arises by transitions to the $S_3(n\pi^*)$ and

$S_4(\pi\pi^*)$ states, respectively. In the static fluorescence spectrum of Pur in ACN an emission band in the UV at 367 nm is observed. Compared to its methylated isomer 9-MePur, its fluorescence is less intense ($\sim 70\%$) and appears blue-shifted by 16 nm.

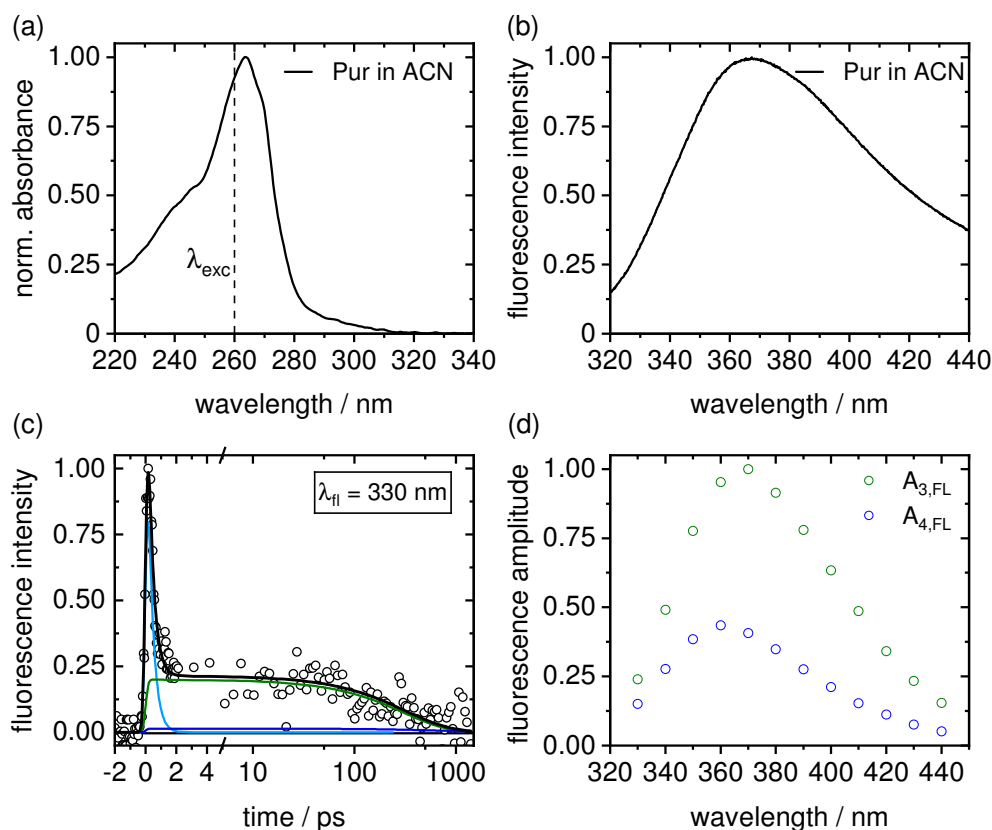


Figure 4.17: (a) Static absorption and (b) fluorescence spectra of Pur in ACN. (c) Presentation of the TFLS time profile at $\lambda_{fl} = 330$ nm for Pur in ACN after excitation at $\lambda_{exc} = 260$ nm. Shown are the experimental data (circles) and the fit (black line) obtained by a sum of exponentials (light blue, green and blue) convoluted with the IRE. At early times up to 5 ps a linear scale is used, thereafter a logarithmic scale is chosen. (d) Wavelength-dependent amplitudes obtained from the global fit of the TCSPC time profiles recorded from $\lambda_{fl} = 330$ –440 nm.

TCSPC time profiles were recorded after excitation at $\lambda_{exc} = 265$ nm in 10 nm steps from $\lambda_{fl} = 330$ to 440 nm. The global data analysis of the TCSPC

time profiles yielded the following time components given with statistical 2σ uncertainty limits for Pur in ACN:

$$\tau_{3,FL}(\text{Pur}) = 330. \pm 15.0 \text{ ps}$$

$$\tau_{4,FL}(\text{Pur}) = 0.88 \pm 0.03 \text{ ns}$$

As for its methylated analogues, $\tau_{3,FL}$ and $\tau_{4,FL}$ are attributed to the lifetimes of the excited $S_1(n\pi^*)$ and $S_2(\pi\pi^*)$ states, respectively. Since the TCSPC measurements reveal higher amplitudes of $A_4 = 0.2\text{--}0.4$, it is assumed that the deactivation via the relaxed $S_2(\pi\pi^*)$ state with $\tau_{4,FL}$ is more pronounced for Pur compared to 9-MePur.

Three time components were obtained for Pur in ACN from the TFLS measurements using the up-conversion technique:

$$\tau_{1,FL}(\text{Pur}) = 0.34 \pm 0.07 \text{ ps (88 \%)}$$

$$\tau_{3,FL}(\text{Pur}) = 310 \text{ ps (fixed)}$$

$$\tau_{4,FL}(\text{Pur}) = 0.90 \text{ ns (fixed)}$$

As $\tau_{3,FL}$ and $\tau_{4,FL}$ show very small amplitudes, their values were fixed during the data analysis. Therefore, the statistical 2σ uncertainty limits are missing for $\tau_{3,FL}$ and $\tau_{4,FL}$. The fluorescence time profile at $\lambda_{fl} = 330 \text{ nm}$ is dominated by the ultrashort time component $\tau_{1,FL}$. The time component $\tau_{3,FL}$ nicely agrees with the TEAS results reported in the literature.²³

However, the most relevant data to unambiguously identify the involved species are again obtained from TVAS. The results for Pur in CD_3OD and ACN-d_3 after excitation at $\lambda_{exc} = 267 \text{ nm}$ are presented in Fig. 4.18 and Fig. 4.19, respectively. While measurements in CD_3OD serve to elucidate the deactivation processes of the 7D-tautomer, ACN-d_3 is used for the 9H tautomeric form. The TVAS measurements of Pur reveal vibrational signatures of the excited $S_2(\pi\pi^*)$, $S_1(n\pi^*)$ and $T_1(\pi\pi^*)$ electronic states. As for the methylated analogues, vibrational marker modes of the different excited states are detected in both solvents. Selected time profiles of the involved species are displayed in Fig. 4.20.

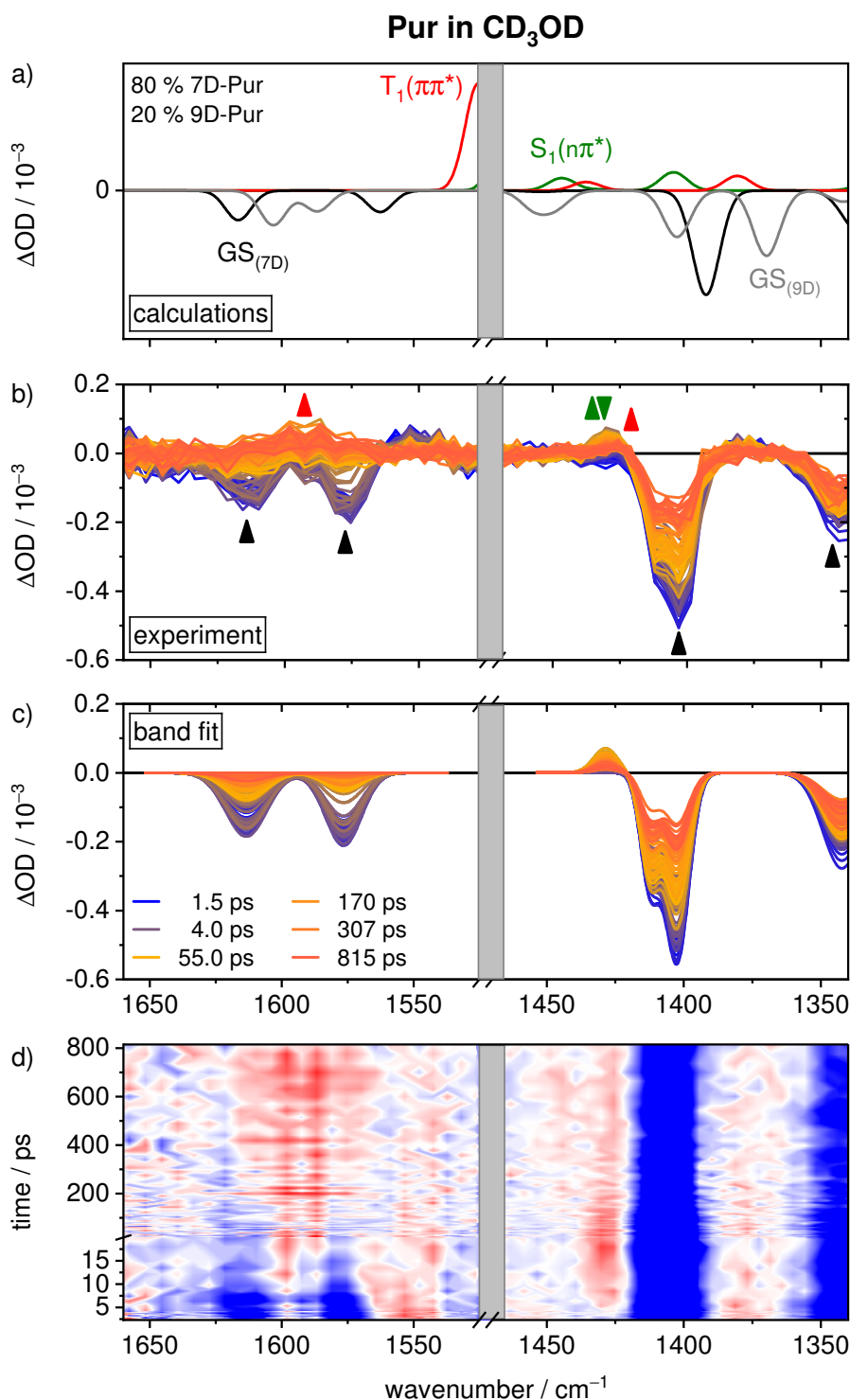


Figure 4.18: TVAS results for Pur in CD₃OD after excitation at $\lambda_{\text{exc}} = 267$ nm. a) Computed vibrational spectra of Pur for the GS (black), the $S_1(n\pi^*)$ (green) and $T_1(\pi\pi^*)$ (red) states. b) Recorded TVA spectra at different time delays. The coloured arrows indicate the temporal evolution of the vibrational bands. c) Gaussian band fit to the experimental TVA spectra. d) Two-dimensional spectro-temporal absorption map with negative signals coded in blue and positive signals in red.

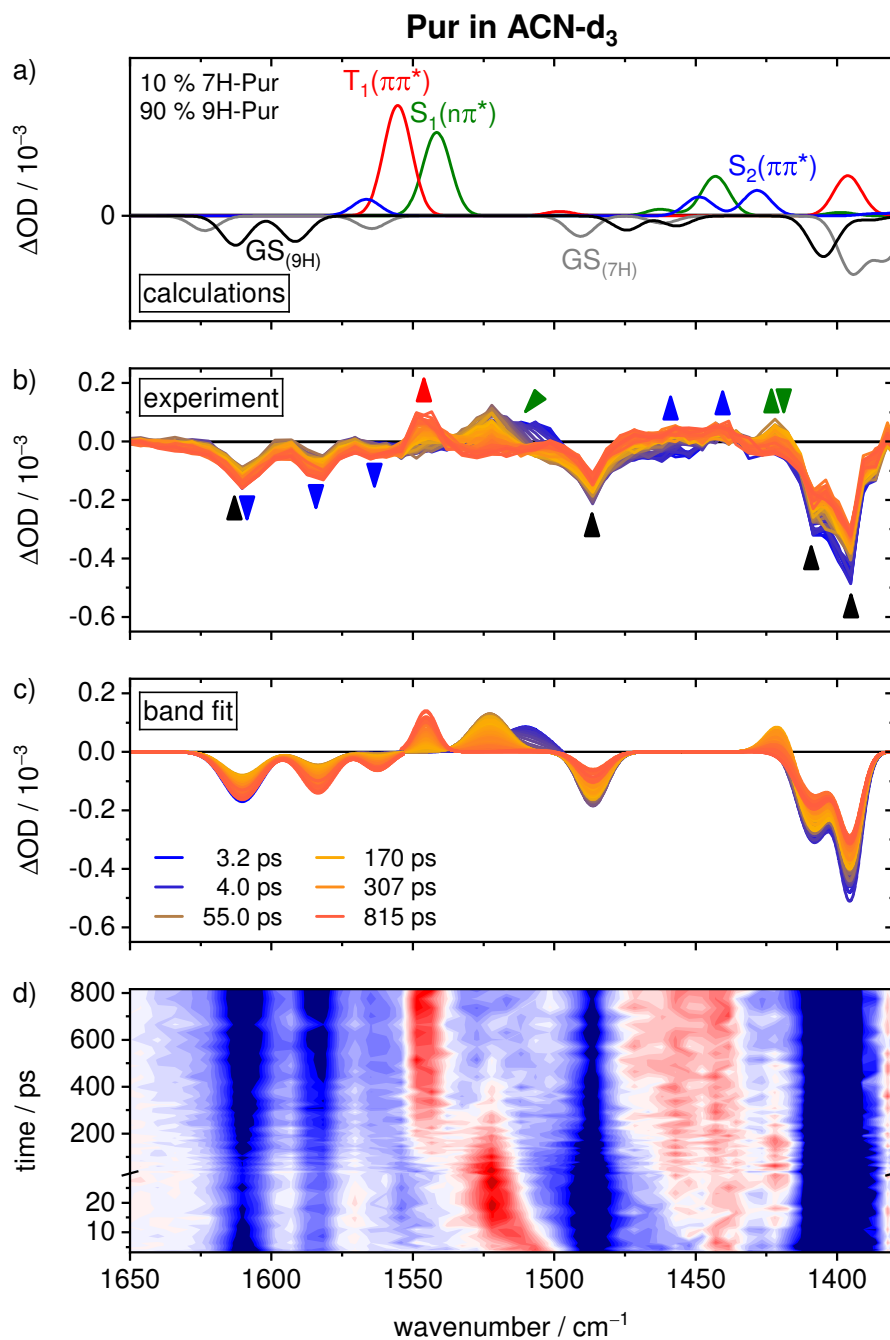


Figure 4.19: TVAS results for Pur in ACN-d₃ after excitation at $\lambda_{\text{exc}} = 267$ nm. a) Computed vibrational spectra of Pur for the GS (black), the $S_2(\pi\pi^*)$ (blue), the $S_1(n\pi^*)$ (green) and $T_1(\pi\pi^*)$ (red) states. b) Recorded TVA spectra at different time delays. The coloured arrows indicate the temporal evolution of the vibrational bands. c) Gaussian band fit to the experimental TVA spectra. d) Two-dimensional spectro-temporal absorption map with negative signals coded in blue and positive signals in red.

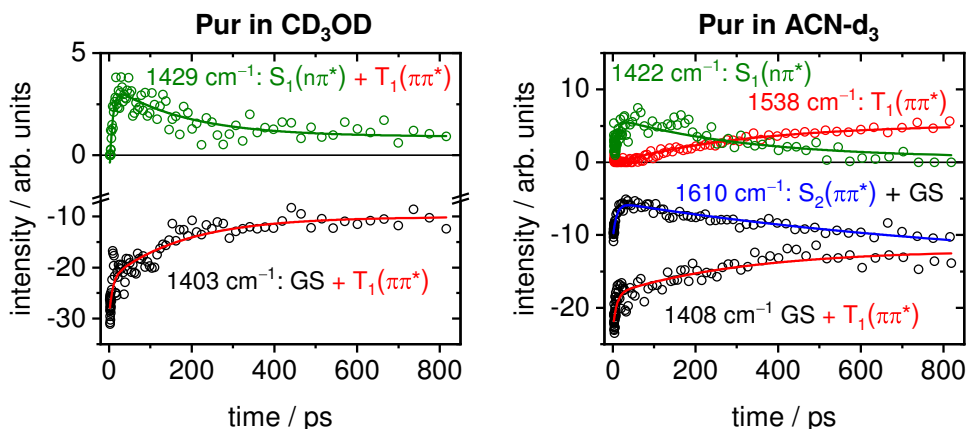


Figure 4.20: Selected time profiles of the involved species for Pur in CD₃OD (left) and ACN-d₃ (right) after excitation at $\lambda_{\text{exc}} = 267$ nm. Shown are the respective amplitudes determined by the global band fit (open circles) and the global fit (straight lines) using a sum of three exponentials. The time profiles for the GS, the $S_1(n\pi^*)$ and the $T_1(\pi\pi^*)$ states are coloured in black, green and red, respectively. The GSB bands at 1610, 1408, 1403 cm⁻¹ are superimposed by excited-state contributions from the $S_2(\pi\pi^*)$ and $T_1(\pi\pi^*)$ states indicated by the straight blue and red lines.

In good agreement with the time-resolved fluorescence measurements, the following time constants given with statistical 2σ uncertainty limits are obtained from the global data analysis:

$$\begin{aligned} \tau_{2,\text{TVAS}}(7\text{D-Pur}) &= 8.00 \pm 2.00 \text{ ps} & \tau_{2,\text{TVAS}}(9\text{H-Pur}) &= 9.00 \pm 1.50 \text{ ps} \\ \tau_{3,\text{TVAS}}(7\text{D-Pur}) &= 180. \pm 50.0 \text{ ps} & \tau_{3,\text{TVAS}}(9\text{H-Pur}) &= 340. \pm 55.0 \text{ ps} \\ & & \tau_{4,\text{TVAS}}(9\text{H-Pur}) &= 1.00 \text{ ns (fixed)} \end{aligned}$$

Unravelling the photo-induced dynamics of N^6,N^6 -dimethyladenine by femtosecond time-resolved spectroscopy from the UV to the MIR

REBECCA HOLTMANN, VIVIAN LUKASZCZUK, BIRTHE BEHR AND FRIEDRICH TEMPS

Institute of Physical Chemistry, Christian-Albrechts-University Kiel, Olshausenstr. 40, D-24098 Kiel, Germany.

Manuscript in preparation.

OWN CONTRIBUTIONS TO THIS MANUSCRIPT:

- Steady-state UV/vis, fluorescence and FTIR spectroscopy,
- quantum chemical calculations,
- time-correlated single photon counting measurements,
- femtosecond time-resolved fluorescence up-conversion,
- femtosecond time-resolved vibrational absorption spectroscopy,
- analyses of all experimental data,
- writing of the manuscript.

Abstract

N^6,N^6 -dimethyladenine (DMAde) is a derivative of the nucleobase adenine (Ade). Contrary to other nucleobase derivatives, it exhibits dual fluorescence that is assumed to originate from two distinct excited-state species: the locally excited (LE) state and a twisted intramolecular charge transfer (TICT) state. To ultimately identify the involved species as well as to untangle the underlying processes after photoexcitation, we employed a variety of femtosecond time-resolved spectroscopic techniques: fluorescence spectroscopy (TFLS) using the up-conversion technique, electronic absorption spectroscopy (TEAS) and vibrational absorption spectroscopy (TVAS). By quantum chemical calculations, we obtained two minimum structures in the $S_1(\pi\pi^*)$ state which are separated by a shallow potential energy barrier of 0.05 eV. One structure, identified as the $S_1(\pi\pi_{LE}^*)$ structure, is characterised by C^2 -puckering, which is already known from adenine. In contrast, the global minimum structure $S_1(\pi\pi_{TWICT}^*)$ shows a twist by $\sim 60^\circ$ of the NMe_2 group with respect to the purine frame. Additionally, this group is strongly tilted. Thus, sp^3 hybridisation of the amino nitrogen is maintained in the excited state. Owing to the structure sensitivity of TVAS, we detected the previously predicted ICT structure for the first time. Furthermore, a novel excited-state species was identified and ascribed to a diffuse distribution of vibrationally hot structures with partial twisting and wagging angles of the NMe_2 group (= pTWICT). From our results, the following deactivation mechanism for DMAde is proposed: After excitation to the optically bright $S_1(\pi\pi^*)$ state, relaxation from the Franck–Condon (FC) region towards the minimum of the $S_1(\pi\pi_{LE}^*)$ state takes place within $\tau_1 \sim 0.3$ ps. Subsequently, the $S_1(\pi\pi_{LE}^*)$ state rapidly deactivates back to the electronic ground state (GS) or populates the $S_1(\pi\pi_{TWICT}^*)$ minimum within $\tau_2 \sim 1.6$ ps. The $S_1(\pi\pi_{TWICT}^*)$ state is long-lived with an excited-state lifetime of $\tau_4 \sim 1$ ns. In addition to the observed fluorescence from the TWICT minimum, intersystem crossing (ISC) towards a triplet state is suggested as a new deactivation channel. The relaxation of the pTWICT structures is associated with $\tau_3 \sim 20$ ps. Our results highlight that the photo-induced dynamics of DMAde is complex and can only be understood by using different time-resolved spectroscopic techniques in combination with quantum chemical calculations.

5.1 Introduction

Numerous studies within the last two decades have focused on the photophysics of the DNA and DNA building blocks to gain detailed insight into the underlying electronic deactivation dynamics that is responsible for their high UV photostability.^{1–10} While the canonical nucleobase adenine (Ade) features ultra-short excited-state lifetimes of $\tau < 1$ ps,^{2,3,11–14} *N*⁶,*N*⁶-dimethyladenine (DMAde), where the amino hydrogens are substituted by methyl groups, shows population of long-lived excited states.^{15–18} Contrary to other nucleobase derivatives, DMAde and its *N*9 alkylated analogues, the nucleoside *N*⁶,*N*⁶-dimethyladenosine (DMAdo), or *N*⁶,*N*⁶-dimethyl-9-methyladenine exhibit dual fluorescence in various solvents.^{15–20} The static absorption and fluorescence spectra in acetonitrile (ACN) and methanol (MeOH) alongside with the chemical structure of DMAde are given in Fig. 5.1. The observed absorption band at 275 nm is attributed to

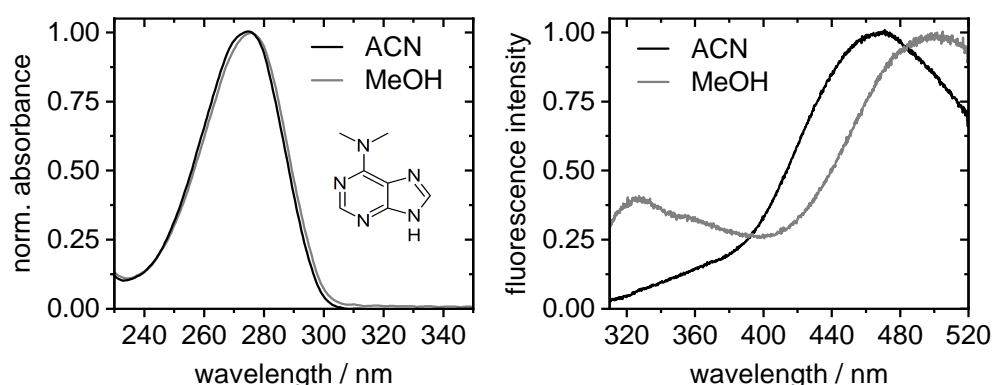


Figure 5.1: Chemical structure and static absorption (left) and fluorescence (right) spectra of DMAde in ACN (black) and MeOH (grey) after photoexcitation at $\lambda_{\text{exc}} = 266$ nm.

a transition to the optically bright $^1\pi\pi^*$ (L_a) state. In the static fluorescence spectra, two separated emission bands are visible in both solvents. The weak band in the UV resembles the static fluorescence of the parent molecule Ade.^{21,22} Therefore, it is assigned to the locally excited (LE) state associated with an ultrashort excited-state lifetime.^{15–20} The intense band in the visible region was proposed to arise from a twisted intramolecular charge transfer (TICT) state.^{15–20} However, this assignment is still discussed in the literature and the origin of the red-shifted fluorescence remains elusive.^{15–20}

The prototypical and intensively studied molecule regarding dual fluorescence is 4-(*N,N*-dimethylamino)benzonitrile (DMABN).^{23–49} As for DMAde, its fluorescence in the UV arises from the LE state, whereas the red-shifted band is attributed to an ICT state. Both the LE and the ICT state correspond to potential energy minima in the S_1 state.^{26,29,32,43,47,50} In the excited state, an electron is transferred from the dimethylamino group to the aromatic ring. Thus, the dimethylamino group acts as electron donor and has a pyramidal structure in the electronic ground state (GS). After photo-induced electron transfer, the positively charged amino nitrogen possesses a planar structure. This results in an altered hybridisation of the dimethylamino nitrogen from sp^3 to sp^2 upon photoexcitation.^{29,32} The ICT transition is accompanied by a structural rearrangement of the molecule. In this context, different structures have been proposed.^{24,26,27,29,30,32,38,40,42,43,46,51} The twisted ICT (TICT) structure shows an internal rotation of the dimethylamino group by $\vartheta = 90^\circ$ with respect to the aromatic ring plane.^{24,51} This results in a decoupling of these two moieties. For the wagged ICT (WICT) structure this decoupling is achieved by a tilting motion of the dimethylamino group.^{26,27,43} Indeed, other ICT structures like a planar (PICT), a rehybridized (RICT), or a partially twisted (pTICT) geometry are controversially discussed in the literature.^{29,30,32,38,40,42,43,50} For DMABN, the ICT transition becomes accessible due to the proximity of the L_a and L_b excited states.^{23,29} When the energetic distance between these states increases, as it is the case for 4-Aminobenzonitrile (DABN), the amino analogue of DMABN, the ICT emission band disappears.^{26,30,32,43} Further characteristic properties of (T)ICT states are their high dipole moments, which is in the range of 13–20 D^{26,32,43,44,50} for DMABN, as well as their sensitivity to the molecular environment, e.g., the solvent. With increasing solvent polarity, the (T)ICT state is stabilised and its emission undergoes a red-shift. In the gas phase or in nonpolar solvents, the (T)ICT state may become inaccessible because it is shifted to higher energies.^{32,43}

Some of these trends pointing at an ICT transition are also observed for DMAde and its N9 alkylated analogues. Unfortunately, only few experimental and theoretical studies are available in the literature.^{15–20} Static fluorescence spectra revealed a strong solvent dependence of the fluorescence in the visible. While it dominates in ACN, MeOH or dioxane, it is quenched in water.^{15–19} Concurrently, its maximum features a red-shift in polar solvents, which implies a stabilisation of the corresponding electronic state (cf. Fig. 5.1).^{15,17–19} However, this band

is even present in nonpolar solvents like *n*-hexane or cyclohexane (CHX).^{15,18} Nevertheless, unambiguous experimental evidence for a (T)ICT transition being responsible for the red-shifted fluorescence of DMAde has not yet been provided.

Time-resolved spectroscopic measurements revealed first insights into the photo-induced deactivation dynamics of DMAde.^{16–18} Based on femtosecond time-resolved fluorescence spectroscopy (TFLS) in water and dioxane,¹⁷ a four-state model was suggested. After excitation to the optically bright $^1\pi\pi^*$ (L_a) state, the Franck–Condon region is left rapidly, reaching the L_a minimum. This process is followed by partial recovery of the GS within $\tau < 1$ ps. Another fraction of the initially excited molecules gets trapped in the $^1\pi\pi^*$ (L_b) and/or $^1n\pi^*$ state, where a solvent-dependent time constant of $\tau = 1.5$ – 10 ps was found. Longer time components of $\tau = 60$ ps in water and $\tau = 1.4$ ns in dioxane were determined for the red-fluorescing state in the visible region.¹⁷ Other experimental studies provided lifetimes in the visible which were also in the range of nanoseconds, e.g., 1.15 ns in ACN,¹⁸ 1.3 ns in cyclohexane, or 1.9 ns in tetrahydrofurane,¹⁵ reflecting the forbidden character of this transition, which was ascribed to a TICT state. As first signals from this TICT state were present after 4–5 ps, a direct population from the L_a state was assumed.¹⁷ Based on transient electronic absorption data from 2011, Demeter et al.¹⁸ reduced this deactivation scheme to a two-state model, because the $^1\pi\pi^*$ (L_b) and $^1n\pi^*$ state represent only minor deactivation channels. Consistent with the previously reported results, they proposed that the TICT state is reversibly populated from the LE state, implying a precursor–successor relationship.

The TICT mechanism was also supported by theoretical studies on DMAde.^{15,20} In this context, a higher dipole moment of $\mu \sim 6$ D was calculated for the predicted TICT structure, whereas a value of $\mu = 2.11$ – 3.37 D was obtained for the GS.²⁰ At a twisted geometry, the vertical excitation energies showed that, for the lowest transition, electron density is transferred from the dimethylamino group to the purine frame, which is again characteristic for a TICT transition.²⁰ From semiempirical calculations,¹⁵ minimum energy structures of DMAde in the GS and in the excited state were computed by scanning both the twist and the pyramidalisation angle, namely ϑ and ω , respectively. For the GS, a minor twist angle of $\vartheta = 10^\circ$ and a dipole moment of 2.1 D were obtained, while the LE structure is more planar and a dipole moment of 4.0 D was calculated. Reaching a twist angle of $\vartheta = 90^\circ$, a significantly higher dipole moment of 6.9 D

was predicted. As ICT states are sensitive to solvent polarity, the authors also applied calculations in ACN as an example for a polar, aprotic solvent. In ACN, a stabilisation of the TICT structure was observed, so that both the LE ($\vartheta, \omega = 0^\circ$) and the TICT state ($\vartheta = 90^\circ, \omega = 0^\circ$) correspond to minima on the S_1 potential energy surface (PES). In ACN, the TICT state represents the global minimum and both structures are separated by an energy barrier of ~ 1.3 kcal/mol.¹⁵

Those studies impressively highlighted that methylation of the amino group in DMAde opens up new deactivation pathways that take place on significantly longer time scales. However, the involved structures are still subject of ongoing discussions. Although experimental and theoretical studies^{15–20} point at a twisted ICT transition for DMAde in the S_1 state, this assignment remains vague due to the lack of structural sensitivity of the used spectroscopic techniques. Thus, there are still questions that have not been answered yet: (i) Does the fluorescence in the visible really arise from a TICT state? (ii) Is the TICT state populated from the Franck–Condon region or from the locally excited state? Thus, does a precursor–successor relationship exist, or do both species evolve independently after photoexcitation? (iii) Are other excited states like the $^1\pi\pi^*$ (L_b) or the $^1n\pi^*$ state populated during the deactivation processes? To answer these questions, we used different femtosecond time-resolved spectroscopic techniques and complemented our experimental findings by ab initio quantum chemical calculations.

5.2 Methods

N^6, N^6 -dimethyladenine was purchased from Sigma Aldrich (purity ≥ 98 %) and used as received. The time-resolved measurements were performed in acetonitrile (ACN, Uvasol grade) or in deuterated acetonitrile (ACN- d_3).

Time-resolved fluorescence spectroscopy

A detailed description of the experimental setup for the time-resolved fluorescence measurements using the up-conversion technique has been given elsewhere.^{17,52} In short, a home-built non-collinear optical parametric amplifier (NOPA) provided laser pulses at 520 nm which were temporally compressed to 35 fs (FWHM) with a prism compressor. In a second step, pump pulses at $\lambda_{\text{exc}} =$

266 nm with an energy of 350 nJ per pulse were obtained via second harmonic generation (BBO, $\theta = 43.9^\circ$, $\phi = 90^\circ$). The pump pulses were then focused into the sample flow cell which had an optical path length of 1 mm. The emitted fluorescence was collimated by a pair of parabolic mirrors (Melles–Griot, $f = 119$ mm) and focused into a 0.1 mm BBO crystal ($\theta = 51^\circ$, $\phi = 30^\circ$). Another fraction of the Ti:Sa fundamental at $\lambda = 775$ nm with an energy of 70 μ J per pulse was used for the gate pulses, which were also focused into the BBO crystal. By overlapping the gate pulses and the emitted fluorescence spatially and temporally in the BBO crystal, the sum frequency signal was generated (SFG) which was then detected. While a type I non-collinear SFG process was applied in the UV wavelength range of $\lambda_{\text{fl}} = 320\text{--}350$ nm, type II phase-matching conditions were used in the visible region from $\lambda_{\text{fl}} = 440\text{--}540$ nm. Since a measurement was carried out at a single emission wavelength λ_{fl} , the BBO crystal had to be tilted by a few degrees to record the respective SFG signals at other emission wavelengths. The up-converted light was then focused into the detection unit. The latter consisted of a monochromator (Jobin-Yvon HR 10), a photomultiplier (Hamamatsu R1527P), a preamplifier (Stanford Research SR 445) and a gated single-photon counter (Stanford Research SR 400). To record transient fluorescence time profiles, the gate pulses were delayed up to $\Delta t \sim 1.9$ ns with respect to the pump pulses by a linear translation stage (Physik Instrumente). All measurements were carried out under magic angle (54.7°) conditions. The measured time profiles in the UV as well as in the visible range were fitted globally by a sum of exponentials convoluted with a Gaussian accounting for the instrument response function (IRF).

To reconstruct transient fluorescence spectra $T_{\text{fluo}}(\lambda, t)$, Equation 5.1 was used:^{17,53,54}

$$T_{\text{fluo}}(\lambda, t) = I_{\text{stat}}(\lambda) \cdot \frac{I(\lambda, t)}{I_{\infty}} \quad (5.1)$$

Here, I_{stat} is the intensity of the static fluorescence spectrum, $I(\lambda, t)$ is the intensity of the normalised time profile at a given wavelength λ and I_{∞} corresponds to the normalised time-integrated intensity (cf. Equation 5.2):

$$I_{\infty} = \sum_i A_i \cdot \tau_i \quad (5.2)$$

Previously, the intensity of the static fluorescence spectrum was corrected by multiplication with the fluorescence correction curve (FCC).

Time-resolved electronic absorption spectroscopy

The femtosecond time-resolved electronic absorption spectrometer has been built around a Clark MXR CPA 2001 Ti:Sa laser system delivering light pulses of 150 fs duration full width at half maximum (FWHM) at $\lambda = 775$ nm and a 1.01 kHz repetition rate.^{55,56} In short, a home-built non-collinear optical parametric amplifier (NOPA) provided laser pulses at 533 nm, which were temporally compressed to 30 fs (FWHM) with a prism compressor. Afterwards, pump pulses at $\lambda_{\text{exc}} = 266$ nm with an energy of 400 nJ per pulse were obtained via second harmonic generation (BBO, $\theta = 47.9^\circ$, $\phi = 90^\circ$). The pump pulses were then focused into the sample flow cell, which had an optical path length of 1 mm. Another fraction of the laser fundamental was focused into a moving CaF₂ plate to prepare broadband probe pulses in the visible region from $325 \text{ nm} \leq \lambda_{\text{probe}} \leq 700 \text{ nm}$. After splitting them into probe and reference beams, the probe pulses were spatially and temporally overlapped with the pump pulses in the sample flow cell. Finally, the probe and reference pulses were spectrally dispersed in a prism spectrograph and then detected separately with two full frame transfer CCD cameras. Prior to white-light generation, the probe pulses passed a motorised computer-controlled delay stage to record transient difference spectra as function of delay time. Here, a maximal pump–probe time delay of $\Delta t = 1.7$ ns was accessible. To improve the data quality, optical choppers were inserted into the beam path of the pump and probe pulses, respectively. Every second probe pulse was blocked as the chopper was working at 505 Hz, whereas the chopper for the pump pulse was operating at 252.5 Hz. All measurements were carried out under magic angle conditions. After time-zero and solvent correction, the experimental data were analysed globally by singular value decomposition (SVD).⁵⁷

Time-resolved vibrational absorption spectroscopy

The femtosecond time-resolved vibrational absorption spectrometer^{58–60} has been built around a Coherent Libra HE Ti:Sa laser system delivering light pulses of 90 fs duration full width at half maximum (FWHM) at $\lambda = 800$ nm with 1 kHz repetition rate. Frequency tripling of the Ti:Sa fundamental yielded excitation pulses at $\lambda_{\text{exc}} = 267$ nm (0.6 μJ / pulse). They were loosely focused into a home-built sample flow cell with CaF₂ windows and an optical path length of

0.1 mm. Every second pump pulse was blocked by a synchronised optical chopper operating at 500 Hz. Another fraction of the laser fundamental was used to pump a two-stage optical parametric amplifier (OPA), which provided tunable signal and idler pulses. Subsequently, broadband mid-infrared probe pulses were generated by difference frequency generation (DFG) in AgGaS₂ of the signal and idler pulses.^{59,60} The pump and probe beams were spatially and temporally overlapped in the sample flow cell. The transmitted probe light was then guided to the grating spectrograph and spectrally dispersed before impinging on the liquid-nitrogen cooled 32-pixel MCT detector array. Transient vibrational difference spectra were then recorded as function of pump–probe delay. After baseline correction of the raw data employing the programme KOALA,⁶¹ the recorded transient spectra at each time delay were globally modelled by a sum of Gaussian functions. To extract time profiles, the respective amplitudes determined by the spectral band fitting were plotted vs. pump–probe delay time and fitted in a global manner using a sum of exponentials. In the spectral range from 1650–1500 cm^{−1} the description of the experimental data by a sum of Gaussian functions was not sufficient due to spectral shifts, spectral narrowing and superposition of the observed signals. Therefore, the amplitudes at single probe wavelengths were plotted as function of time to extract the temporal evolution of the involved species.

Quantum chemical calculations

The minimum energy structure and vibrational wavenumbers of DMAde in the electronic ground state were calculated at the RI-SCS-MP2 level of theory^{62–64} employing the aug-cc-pVDZ basis set.⁶⁵ For excited-state calculations of the minimum energy structures, vibrational spectra as well as vertical excitation energies, the RI-SCS-CC2 method^{66–71} with the aug-cc-pVDZ basis set⁶⁵ was used. All calculations were performed in vacuo using the TURBOMOLE 7.0 programme package.⁷² The calculated harmonic vibrational wavenumbers in the ground state and in the excited states were scaled by factors of 0.97 and 0.985 as recommended in the literature from extensive benchmarking.^{73–75} The potential energy barrier in the excited state was computed using the Woelfling tool,⁷² which is implemented in the TURBOMOLE 7.0 programme package.⁷² This method provided an initial guess for a transition state by self-consistent

optimisation of the reaction path. The transition state guess was then used as starting point for a transition state optimisation. Again, the RI-SCS-CC2 method^{66–71} was employed using the aug-cc-pVDZ⁶⁵ and the def2-SVP⁶⁴ basis sets, respectively.

5.3 Results

First insights into the photo-induced deactivation dynamics of DMAde in ACN are derived from femtosecond time-resolved fluorescence measurements (TFLS) as well as transient electronic absorption spectroscopy (TEAS). More extensive and decisive results were subsequently provided by transient vibrational absorption spectroscopy (TVAS) as structure-sensitive tool. The obtained results are presented in the following. However, we first turn to our findings from quantum chemical calculations, as they prove essential as a basis for the understanding and interpretation of the experimental data.

Quantum chemical calculations

To begin, starting from the minimum energy structure of DMAde in the electronic GS, vertical excitation energies (VEEs) were calculated at the RI-SCS-CC2/aug-cc-pVDZ level of theory. The characters, VEEs and oscillator strengths f of the excited states as well as the natural transition orbitals (NTOs),⁷⁶ participating in the transitions are summarised in Table 5.1. The characters of the states were determined based on the involved orbitals. The respective NTOs are depicted in Fig. 5.13 in the SI. The first excited singlet state S_1 is located at a VEE of 4.87 eV

Table 5.1: Calculated vertical excitation energies (VEEs) from the GS minimum energy structure alongside with the characters, the oscillator strengths f and the involved natural transition orbitals (NTOs) of each transition.

state	character	VEE/ eV	f	NTOs
S_1	$\pi\pi^*$	4.87	0.3682	HOMO \rightarrow LUMO (86 %)
S_2	$\pi\pi^*$	4.97	0.0040	HOMO \rightarrow LUMO+1 (65 %)
				HOMO–1 \rightarrow LUMO+2 (23 %)

above the GS and is characterised as HOMO–LUMO transition. From inspection

of the NTOs and the oscillator strength of $f = 0.3682$, this state is identified as $^1\pi\pi^*$ (L_a) state. The S_2 state is very close in energy ($\Delta E = 0.1$ eV) and exhibits $\pi\pi^*$ character as well. Due to the weak oscillator strength of $f = 0.0040$, it is assigned as $^1\pi\pi^*$ (L_b) state. Here, four orbitals are involved, whereby the HOMO–LUMO+1 transition dominates with a share of 65 %. During this transition, electron density is transferred from the dimethylamino nitrogen to the purine ring, indicating the charge transfer character of this transition (cf. SI, Fig. 5.13).

Additionally, minimum energy structures in the GS (RI-SCS-MP2/aug-cc-pVDZ) and in the first excited state (RI-SCS-CC2/aug-cc-pVDZ) were calculated. Two different minimum structures were found independently on the potential energy hypersurface of the S_1 state. They are given in Fig. 5.2. Furthermore, molecular and geometric parameters, e.g., dipole moments μ , bond lengths and twisting angles ϑ , for each structure are presented in Table 5.2. Here, the twist angle ϑ is defined as the average of the torsion angles ϑ' (N1–C6–N10–C11) and ϑ'' (N1–C6–N10–C12):

$$\vartheta = 0.5 \times (|\vartheta'| + |\vartheta''|) \quad (5.3)$$

Aliphatic amines often act as electron donors in molecules that exhibit intramolecular charge transfer transitions.³² In general, the amino nitrogen has a pyramidal structure in the GS. After photo-induced electron transfer, the positively charged amino nitrogen often possesses a planar structure. Thus, the hybridisation of the amino nitrogen changes from sp^3 to sp^2 .^{29,32} To estimate the pyramidalisation of the amino nitrogen (N10) in DMAde, the distance between N10 and the plane containing C11, C12 and C6 was calculated (cf. Table 5.2, $d(N10)$). The distance between C6 and the plane defined by N1, C5 and N10 (cf. Table 5.2, $d(C6)$) was determined analogously and accounts for the pyramidalisation of C6, respectively. As illustrated in Fig. 5.2, the GS structure exhibits an almost planar purine scaffold, which is confirmed by a small value of $d(C6) = 0.015$ Å. In contrast, the amino nitrogen N10 is pyramidalised, as indicated by $d(N10) = 0.197$ Å. Further, the dimethylamino group shows a slight rotation by $\vartheta \sim 15^\circ$ with respect to the purine ring plane. The most important feature of the minimum structure in the S_1 state, labelled $S_1(\pi\pi_{LE}^*)$, is the C²-puckering, which is already known from Ade.^{77–84} Here, the C2 atom moves out of the purine plane. This leads to a longer bond length especially for N1–C2 and C4–C5 (cf. Table 5.2). In the $S_1(\pi\pi_{LE}^*)$ structure, the dimethylamino group is more

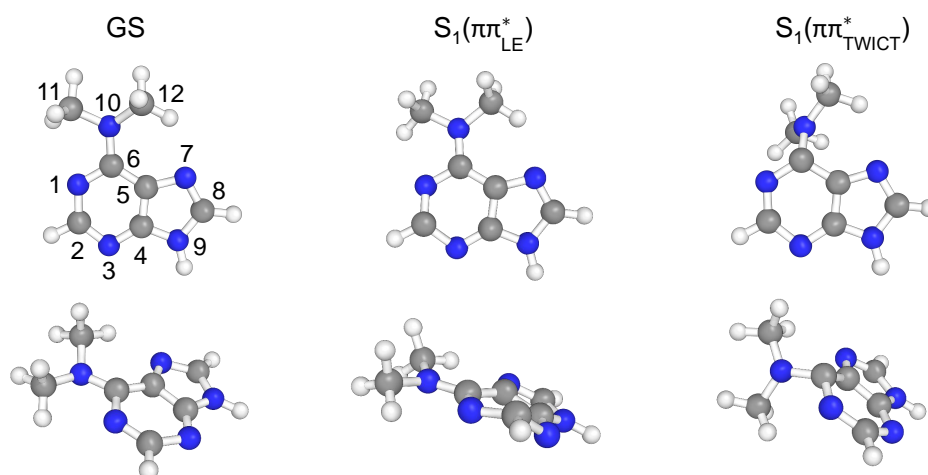


Figure 5.2: Top views (first row) and side views (second row) of the calculated minimum energy structures of DMAde in the electronic GS and in the $S_1(\pi\pi_{LE}^*)$ and $S_1(\pi\pi_{TWICT}^*)$ excited states, respectively.

planar compared to the GS structure. This is indicated by a significantly smaller value of $d(N10) = 0.087 \text{ \AA}$. Moreover, a smaller twist angle of $\vartheta \sim 7^\circ$ is observed.

In contrast, the global minimum structure in the S_1 state features a pronounced twist of $\vartheta \sim 61^\circ$ of the dimethylamino group relative to the purine frame. Additionally, this group is strongly tilted, so that sp^3 hybridisation of N10 is maintained in the excited state. The pyramidal structure of N10 is confirmed by a value of $d(N10) = 0.158 \text{ \AA}$. Not only pronounced structural modifications are observed, but also the charge transfer character of the HOMO–LUMO transition from this structure is clearly visible from the involved orbitals (cf. SI, Fig. 5.13). For these reasons, this structure is named twisted wagged ICT (TWICT). Moreover, in the $S_1(\pi\pi_{TWICT}^*)$ structure, C6 is strongly pyramidalised, with $d(C6) = 0.390 \text{ \AA}$, and the bond length C6–N10 is elongated with 1.46 \AA compared to the GS and $S_1(\pi\pi_{LE}^*)$ structure with values of 1.37 \AA . In addition, the increased dipole moment from $\mu_{GS} = 2.29 \text{ D}$ to $\mu_{LE} = 3.50 \text{ D}$ to $\mu_{TWICT} = 5.11 \text{ D}$ points towards the charge transfer character of the TWICT structure in the $S_1(\pi\pi^*)$ state. The energy difference between the LE and the TWICT structure in the S_1 state is $\Delta E \sim 0.23 \text{ eV}$, whereby the TWICT structure represents the global minimum.

To elucidate the deactivation dynamics after photoexcitation, knowledge of the potential energy barrier height that connects these two structures in the excited state is of great importance. Therefore, a transition state optimisation

Table 5.2: Molecular and structural properties of the minimum energy structures in the ground and excited state, respectively. Given are the dipole moments μ , the twist angles ϑ , distinct bond lengths and pyramidalisations (d) of C6 and the dimethylamino nitrogen N10.

	GS	$S_1(\pi\pi_{LE}^*)$	$S_1(\pi\pi_{TWICT}^*)$
μ / D	2.29	3.50	5.11
ϑ / °	14.87	6.96	61.33
C6–N10 / Å	1.368	1.368	1.462
N1–C2 / Å	1.356	1.414	1.340
C4–C5 / Å	1.411	1.433	1.416
$d(\text{C6})$ / Å	0.015	0.011	0.390
$d(\text{N10})$ / Å	0.197	0.087	0.158

was done using the Woelfling tool which is implemented in the TURBOMOLE 7.0 programme package.⁷² Here, the reaction path between the LE and the TWICT minimum in the S_1 state was calculated and then optimised. From that, a shallow energy barrier of $\Delta E = 0.05$ eV (1.15 kcal/mol) was computed. These results were confirmed by single point calculations of the structures with the higher aug-cc-pVTZ⁶⁵ basis set. These findings form the basis for understanding and assigning the experimental data given in the following.

Time-resolved fluorescence spectroscopy

The measured fluorescence time profiles at four selected emission wavelengths in the spectral range from $\lambda_{\text{fl}} = 330\text{--}540$ nm are depicted in Fig. 5.3. All recorded time profiles can be found in the Supporting Information (SI, Fig. 5.10 and Fig. 5.11). In the following, all obtained time constants are given along with the statistical 2σ uncertainty limits. In the UV, the fluorescence is short-lived and decays bi-exponentially:

$$\tau_1 = 0.40 \pm 0.06 \text{ ps}$$

$$\tau_2 = 1.60 \pm 0.10 \text{ ps}$$

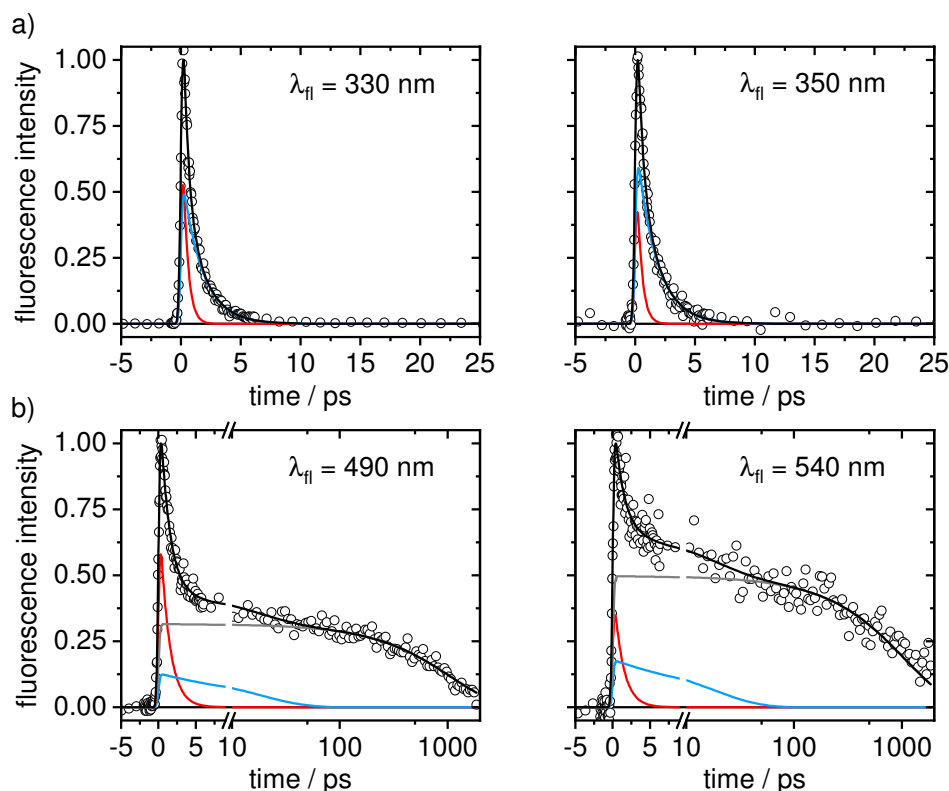


Figure 5.3: Time profiles at four selected emission wavelengths: a) in the UV and b) in the visible region for DMAde in ACN after excitation at $\lambda_{\text{exc}} = 266$ nm. Shown are the experimental data (open circles) and the global fit (black) obtained by a sum of exponentials (red, blue and grey) convoluted with the IRE, respectively. For the time profiles at $\lambda_{\text{fl}} = 490$ nm and 540 nm a linear scale is used up to 10 ps, thereafter a logarithmic scale is chosen.

In contrast, the fluorescence at wavelengths of $\lambda_{\text{fl}} > 350$ nm is longer-lived and still detectable after $\Delta t \sim 2$ ns. Here, three time constants are obtained from the global data analysis:

$$\tau_2 = 1.24 \pm 0.06 \text{ ps}$$

$$\tau_3 = 18.0 \pm 4.00 \text{ ps}$$

$$\tau_4 = 1.07 \pm 0.06 \text{ ns}$$

Comparison of the recorded TFLS data for both spectral ranges reveals significant differences: The ultrashort time component $\tau_1 = 0.40 \pm 0.06$ ps is absent at emission wavelengths of $\lambda_{\text{fl}} > 350$ nm. While time constant τ_2 is almost identical

in both spectral ranges, the longer time components $\tau_3 = 18.0 \pm 4.00$ ps and $\tau_4 = 1.07 \pm 0.60$ ns are observed only in the visible spectral region. In line with these results, TCSPC measurements of DMAde in ACN after excitation at $\lambda_{\text{exc}} = 265$ nm provided a time constant of $\tau_4 = 0.90 \pm 0.03$ ns (cf. SI, Fig. 5.12). Due to the 25 ps time resolution of the TCSPC experiment, the faster processes that were detected by TFLS using the up-conversion technique were not accessible.

In a next step, transient fluorescence spectra at selected time delays were reconstructed^{17,53,54} and are presented in Fig. 5.4a). At early times, the fluorescence in the UV dominates. It can be seen that this emission extends into the visible range. After $\Delta t = 10$ ps, however, this band has decayed back to the baseline, so that only fluorescence at longer wavelengths remains to later times. However, its intensity is very weak and thus the individual transient fluorescence spectra were normalised with respect to their maxima as shown in Fig. 5.4b). The fluorescence in the visible dominates towards later times. In addition, a red-shift of the fluorescence from 440 nm to 480 nm is observed.

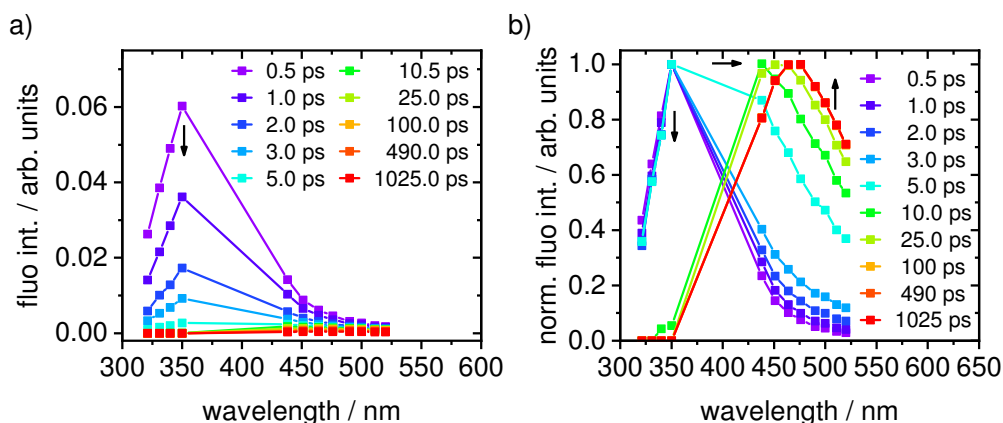


Figure 5.4: a) Reconstructed transient fluorescence spectra at selected time delays and b) normalised transient fluorescence spectra of DMAde in ACN after excitation at $\lambda_{\text{exc}} = 266$ nm.

All in all, the fluorescence in the UV and in the visible region exhibit very different excited-state lifetimes. Moreover, the TFLS data suggest a sequential process in which the long-lived fluorescence in the visible range increases as the UV fluorescence decays. Nevertheless, the molecular species that are involved after photoexcitation of DMAde remain elusive solely from the time-resolved fluorescence data. For example, whether the previously calculated $S_1(\pi\pi_{\text{LE}}^*)$ and

$S_1(\pi\pi_{\text{TWICT}}^*)$ excited states structures are responsible for the dual fluorescence needs to be further elucidated using TEAS and TVAS.

Time-resolved electronic absorption spectroscopy

To gain further insight into the electronic deactivation dynamics, DMAde was investigated by TEAS. The obtained colour-coded two-dimensional spectro-temporal absorption map for DMAde in ACN is presented in Fig. 5.5 together with the transient spectra at selected time delays after photoexcitation at $\lambda_{\text{exc}} = 266$ nm.

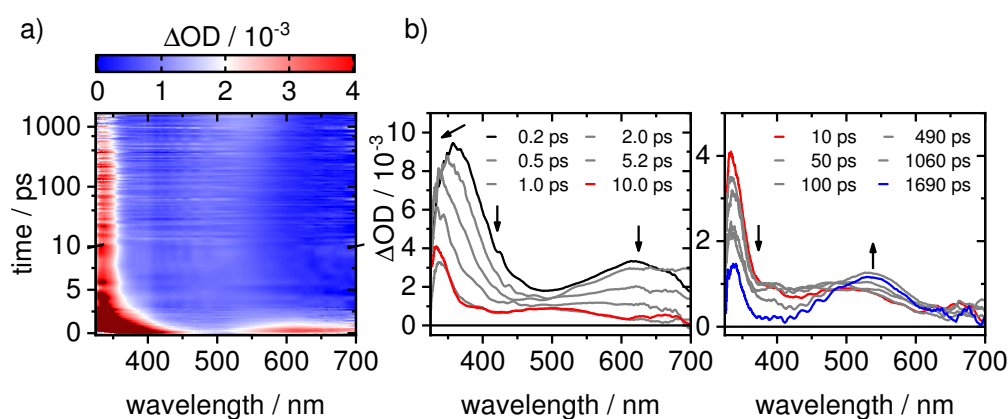


Figure 5.5: a) Colour-coded two-dimensional spectro-temporal absorption map of DMAde in ACN after excitation at $\lambda_{\text{exc}} = 266$ nm. A linear scale is used up to 10 ps, a logarithmic scale is chosen thereafter. b) Recorded transient absorption spectra at selected time delays. The arrows indicate the temporal evolutions of the observed ESA bands.

Three positive signals arising from excited-state absorption (ESA) are observed. The transient spectrum at $\Delta t = 0.2$ ps is dominated by a broad ESA band in the UV ranging from 325–450 nm. Further, a second ESA signal at longer wavelengths with a maximum at ~ 630 nm is detected which decays almost completely within $\Delta t = 10$ ps. Concurrently, the intense ESA band in the UV undergoes a pronounced blue-shift and spectral narrowing until it reaches its new maximum at 335 nm after a few picoseconds. Subsequently, this long-lived ESA slowly decreases, while a new ESA band at ~ 540 nm grows in towards later times.

After time-zero and solvent correction, the experimental data was analysed by singular value decomposition (SVD). Here, four SVD components were needed to describe the data. Hence, the singular value weighted time traces were fitted in a global manner by a sum of three exponentials convoluted with a Gaussian accounting for the IRF. Furthermore, a step function, describing the residual signal after $\Delta t \geq 1.7$ ns was used. From that three global time components were obtained:

$$\tau_1 = 0.28 \pm 0.04 \text{ ps}$$

$$\tau_2 = 1.66 \pm 0.12 \text{ ps}$$

$$\tau_4 = 1.00 \pm 0.25 \text{ ns}$$

These time components agree well with the TFLS results, although $\tau_3 = 18.0 \pm 4.00$ ps was not required to describe the TEAS data. Therefore, τ_3 is missing here. The value of τ_3 probably plays a minor role, as its amplitude in the TFLS data is smaller than 15 %.

From the SVD data analysis, the decay-associated difference spectra (DADS) and the evolution-associated difference spectra (EADS) were calculated and are displayed in Fig. 5.6. Each DADS corresponds to a single global decay time

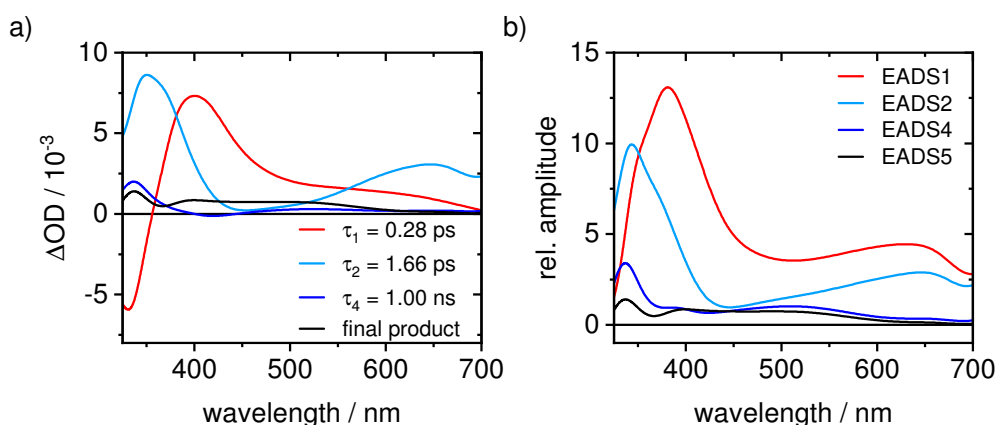


Figure 5.6: a) Decay-associated difference spectra (DADS) and b) evolution-associated difference spectra (EADS) obtained by the global SVD-based analysis of the experimental TEAS data for DMAd in ACN after excitation at $\lambda_{\text{exc}} = 266$ nm.

component τ_i and reflects its wavelength-dependent amplitudes. The DADS

of τ_2 and τ_4 and the final product spectrum exhibit positive amplitudes in the investigated spectral region. Solely the ultrashort time constant $\tau_1 = 0.28 \pm 0.04$ ps shows negative values in the UV from 325–355 nm.

As the TFLS results suggested a sequential deactivation process, the EADS were calculated according to the following kinetic scheme:



where A, B, C, D and P (final product) stand for the sequentially involved species. The first EADS, EADS1 (cf. Fig. 5.6b)), corresponds to the photo-induced absorption changes at early times and is therefore assigned to molecules in the Franck–Condon region of the initially excited $^1\pi\pi^*$ state. EADS1 shows one intense band in the UV with a maximum at 380 nm and a second one in the visible at 640 nm which arise by excited-state absorption to higher lying electronic states. Furthermore, a shoulder at ~ 350 nm is observable. EADS1 evolves with $\tau_1 = 0.28 \pm 0.04$ ps towards EADS2 which features at first sight a similar spectral shape as EADS1. From that it can be assumed that the electronically excited molecules still move on the PES in the $^1\pi\pi^*$ state. However, the evolution to EADS2 involves a pronounced blue-shift of the UV band by 35 nm before its maximum at 345 nm is reached. This band also undergoes spectral narrowing, which results in a significantly reduced intensity around 450 nm. At 640 nm the intensity slightly drops compared to EADS1. Based on the similarity to EADS1 and on its spectro-temporal behaviour, EADS2 is ascribed to the $S_1(\pi\pi_{LE}^*)$ minimum of DMAd. In accordance with the TFLS results, $\tau_2 = 1.66 \pm 0.12$ ps is therefore attributed to the lifetime of the LE state. For EADS4, a significantly reduced intensity of the band in the UV is observed and its maximum is slightly blue-shifted to 335 nm compared to EADS2. While a broad and less intense band is centered around 510 nm, the band at 640 nm decreased to zero. As EADS4 is connected to $\tau_4 = 1.00 \pm 0.25$ ns, it is associated with the long-lived excited-state species that was detected in the visible region by TFLS and described previously. It is noted again that no EADS was associated with $\tau_3 = 18.0 \pm 4.00$ ps. The spectral evolution ends with the EADS5, which is formed with $\tau_4 = 1.00 \pm 0.25$ ns and corresponds to the remaining signal at $\Delta t \geq 1.7$ ns.

With this, two involved excited-state species have been tentatively identified, the $S_1(\pi\pi_{\text{FC}}^*)$ and $S_1(\pi\pi_{\text{LE}}^*)$ state, respectively. Still, the origin of the long-lived excited-state species as well as the observed final offset remain unknown.

Time-resolved vibrational absorption spectroscopy

An overview of the transient vibrational absorption spectra (TVAS) after excitation at $\lambda_{\text{exc}} = 267$ nm focusing on the spectral range from 1650 cm^{-1} to 1225 cm^{-1} in ACN- d_3 is given in Fig. 5.7. This overview consists of four individual measurements spliced together. For plotting of the transient spectra, a colour gradient from blue at early delay times to yellow to orange at late times is chosen.

In general, negative signals in Fig. 5.7 arise from ground-state bleaching (GSB), whereas positive contributions can either be assigned to excited-state absorption (ESA), hot ground-state species or to formation of a photoproduct. To visualise the temporal evolutions of the observed signals, a colour-coded two-dimensional absorption map is presented in Fig. 5.7(c). Here, negative signals are coded in blue and positive signals are shown in red. The inverted experimental FTIR spectrum of DMAd in ACN- d_3 (black) is presented in Fig. 5.7(a). The negative signal at 1600 cm^{-1} is very intense compared to other vibrational bands in the GS. Therefore, the spectral region from 1650 cm^{-1} to 1515 cm^{-1} has been scaled in the transient spectra by a factor of 0.1. Furthermore, the calculated vibrational spectra of the $S_1(\pi\pi_{\text{TWICT}}^*)$ (dark blue) and the $T_1(\pi\pi^*)$ (red) states are displayed to directly assign the observed experimental bands.

After photoexcitation of DMAd, several negative signals are observed which obviously correspond to ground-state bleaching. Based on the calculated vibrational spectrum in the electronic GS, these signals mainly originate from deformation vibrations of the purine ring and of the methyl groups. However, the predominating band at 1600 cm^{-1} corresponds to the stretching vibration of the C6–N10 bond. This vibrational motion can also be found at 1425 and 1404 cm^{-1} , albeit less pronounced. The calculated vibrational spectrum of DMAd in the GS as well as visualisations of the vibrational modes in the spectral region from 1650 – 1225 cm^{-1} are given in the SI (cf. Fig. 5.14 and Fig. 5.15). In the investigated time window up to $\Delta t \sim 800$ ps, the GS recovers by 85–90 % and features an asymptotic permanent offset, surviving on the nanosecond time scale.

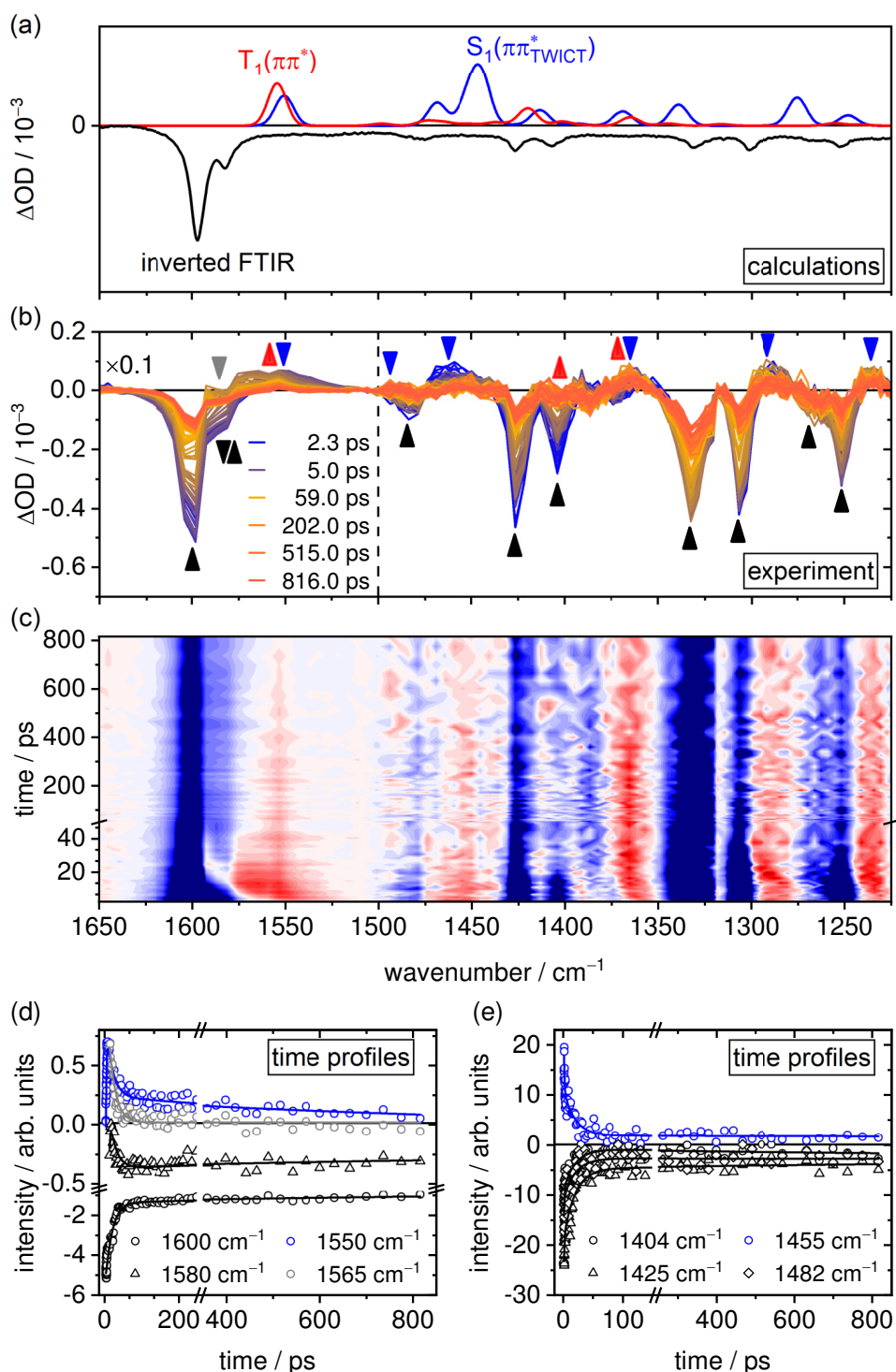


Figure 5.7: TVAS of DMAde after excitation at $\lambda_{\text{exc}} = 267$ nm in ACN-d₃. (a) Inverted experimental FTIR spectrum in ACN-d₃ and computed vibrational spectra of the $S_1(\pi\pi^*_{\text{TWICT}})$ and $T_1(\pi\pi^*)$ states, (b) transient spectra at different delay times, (c) spectro-temporal absorption map with negative signals coded in blue and positive signals in red and exemplary time profiles at (d) single wavelengths in the spectral region from 1650–1500 cm⁻¹ of the GS (black), the TWICT structure (blue) and the excited-state intermediate (grey) and (e) time profiles from the global Gaussian band fitting in the spectral region from 1520–1385 cm⁻¹.

However, some GS signals apparently show complete recoveries only because these bands are superimposed by positive signals. The observed positive bands are directly present at $\Delta t \sim 2$ ps and are located at 1550, 1455, 1360, 1290 and 1230 cm^{-1} . As can be seen from the colour-coded 2D map, these contributions are spectrally broad and feature a blue-shift at early times. This spectro-temporal behaviour points at certain vibrational cooling in the excited state. Subsequently, the positive bands decay in intensity. Spectral narrowing is clearly visible, especially at 1550 cm^{-1} , at later times. After $\Delta t = 816$ ps, minor contributions of the positive signals remain, e.g., at 1550 and 1360 cm^{-1} . From the previously shown TFLS and TEAS data, signals from the $S_1(\pi\pi_{\text{LE}}^*)$ state can be excluded due to its short excited-state lifetime of $\tau \sim 1.6$ ps. However, the positions of the experimental and calculated (values in parentheses) bands for the TWICT structure in the S_1 state nicely agree. Thus, the excited-state signals at 1550 (1551), 1455 (1446), 1360 (1370), 1290 (1275) and 1230 cm^{-1} (1248 cm^{-1}) are assigned to the $S_1(\pi\pi_{\text{TWICT}}^*)$ state. We note in advance here that this appears to be the first clear experimental evidence for the TWICT mechanism for DMAde. The calculated TWICT bands at 1470, 1413 and 1340 cm^{-1} are not observed experimentally, because they overlap with negative signals from the GS resulting in an apparently complete GSR (e.g., at 1480 or 1404 cm^{-1}).

Further, we postulate the formation of a novel excited-state intermediate feature at 1580 cm^{-1} . The intense and broad positive signal around 1550 cm^{-1} consists of two ESA bands. While the red part at 1550 cm^{-1} is clearly assigned to the TWICT state, the blue part at 1580 cm^{-1} shows a very pronounced blue-shift, so that the GSB at 1585 cm^{-1} is apparently refilled at early times, before it becomes negative again. This spectro-temporal behaviour is an indication for the presence of vibrationally hot structures in the excited state. Besides, this band is spectrally very broad, which may suggest that slightly “washed-out” structures contribute to this ESA band. According to our calculations, a signal of the $S_1(\pi\pi_{\text{TWICT}}^*)$ structure is not expected in this spectral region. Therefore, we ascribe this intermediate excited-state species to a diffuse distribution of vibrationally hot structures in the S_1 state with partial twisting and wagging angles (= pTWICT).

Extracting the temporal evolution of the involved species was difficult because the transient spectra reveal a complex picture: On the one hand, the ESA signals are weak in intensity on the other hand, bands of different electronic states tend

to overlap. In the spectral range from 1650–1500 cm⁻¹ the description of the experimental data by a sum of Gaussians was not sufficient due to spectral shifts, spectral narrowing and superposition of the observed signals. Therefore, the amplitudes at single probe wavelengths were plotted as function of time. The obtained time profiles shown in Fig. 5.7(d) were modelled globally using a sum of exponentials. The corresponding time profiles from the global Gaussian band fit in the spectral region from 1520–1385 cm⁻¹ are presented in Fig. 5.7(e). From the data analysis of the four individual measurements, three time components were determined:

$$\tau_2 \approx 2.00 \pm 0.90 \text{ ps}$$

$$\tau_3 \approx 20.0 \pm 4.00 \text{ ps}$$

$$\tau_4 = 1.07 \text{ ns (fixed)}$$

In the spectral range from 1650–1500 cm⁻¹, the GS signal at 1600 cm⁻¹ recovers with τ_2 , τ_3 and τ_4 , whereas the TWICT structure in the S₁ state at 1550 cm⁻¹ grows in with τ_2 and then decays with τ_3 and τ_4 . Since the rise of the excited-state intermediate at 1565 cm⁻¹ is superimposed by a signal from the TWICT state, only its monoexponential decay with τ_3 was described in the global fit. In the spectral region from 1520–1385 cm⁻¹, the GS at 1425 cm⁻¹ is again repopulated with τ_2 , τ_3 and τ_4 . In contrast, the signal amplitude A_4 becomes slightly negative for the GSB bands at 1404 and 1482 cm⁻¹ because, as described previously, these GSB signals show almost complete recovery due to superposition with positive signals towards later times. From a quantitative investigation of the time profile of the GSB at 1600 cm⁻¹, the ratio of the initial GSB and the obtained asymptotic negative offset at late times yielded a GSR of $\Phi_{\text{GS(ACN)}} = 0.85$, which implies that a small fraction of the initially excited molecules stays in the excited state or forms (yet unknown) products. Furthermore, the rise of the TWICT structure with τ_2 is not visible at 1455 cm⁻¹. It may be overlapped with the GS, or cannot be resolved due to its weak intensity. The ultrashort time constant τ_1 detected in the TFLS and TEAS measurements is missing in the TVAS data as the early-time dynamics at $\Delta t < 1.5 \text{ ps}$ are not accessible due to coherent artifacts around $\Delta t \approx 0$. However, the combination of quantum chemical calculations and structure-sensitive transient vibrational absorption spectroscopy clearly revealed vibrational signatures of the long-lived excited-state species that

was identified as $S_1(\pi\pi_{\text{TWICT}}^*)$ structure. Thus, the deactivation of DMAde via an intramolecular charge transfer state, namely the $S_1(\pi\pi_{\text{TWICT}}^*)$ structure, which was theoretically predicted in Section 5.3, is experimentally confirmed.

5.4 Discussion

Based on the above results, a model for the electronic deactivation mechanism for DMAde after photoexcitation can be developed. We start by focussing on the electronic and chemical structures of DMAde, before turning to the ultrafast spectroscopic results.

Electronic and chemical structure

Although our quantum chemical calculations showed that the $S_1(\pi\pi^*)$ and the $S_2(\pi\pi^*)$ states are very close in energy, the molecules will mainly be excited to the $S_1(\pi\pi^*)$, namely the L_a state, because it carries most of the oscillator strength (cf. Table 5.1). Furthermore, the $S_2(\pi\pi^*)$, identified as L_b state, as well as the $S_4(n\pi^*)$ state are shifted to higher energies at the converged minimum structures in the GS, the $S_1(\pi\pi_{\text{LE}}^*)$, the $S_1(\pi\pi_{\text{TWICT}}^*)$ and the $T_1(\pi\pi^*)$ states as illustrated in Fig. 5.8. In accordance with Demeter et al.,¹⁸ we therefore conclude that the $S_2(\pi\pi^*)$ and the $S_4(n\pi^*)$ states are not involved during the electronic deactivation processes after excitation at $\lambda_{\text{exc}} = 267$ nm. However, analogously to DMABN, the proximity of the $S_1(\pi\pi^*)$ and $S_2(\pi\pi^*)$ states seems to be crucial for the accessibility of the intramolecular charge transfer transition.^{23,29} After all, the quantum chemical calculations support the ICT mechanism for DMAde. In the first place, the pronounced structural modifications proceeding in the S_1 state lead to the $S_1(\pi\pi_{\text{TWICT}}^*)$ minimum structure as described in Section 5.3. Similar to DMABN, a rotational motion around the C6–N10 bond is observed. While DMABN features a full twist by 90° , a smaller twist angle of $\vartheta \sim 60^\circ$ was calculated for DMAde. In addition, an elongation of the molecular bond between the carbon atom of the phenyl ring and the dimethylamino nitrogen by ~ 0.05 – 0.06 Å was found for DMABN in theoretical studies^{43–45} and was assumed to facilitate internal twisting around this particular bond. In DMAde, the bond length between C6 and N10 increases by 0.094 Å when going from the minimum structure in the GS to the TWICT structure in the S_1 state (cf. Table 5.2). This

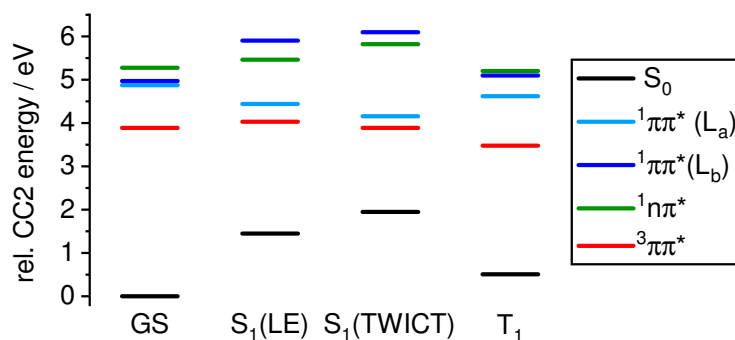


Figure 5.8: Single point calculations for the GS, S₁($\pi\pi^*$), S₂($\pi\pi^*$), S₄($n\pi^*$) and $^3\pi\pi^*$ states for DMAde at the converged minimum energy structures in the GS, the S₁($\pi\pi^*_{LE}$), the S₁($\pi\pi^*_{TWICT}$) and the T₁($\pi\pi^*$) states, respectively.

significantly larger value can be explained by the additionally observed tilting motion of the dimethylamino group, which results in a pyramidalisation of N10 (cf. Table 5.2). Thus, contrary to DMABN, sp^3 hybridisation is maintained in DMAde in the first excited state, leading to the *twisted wagged* ICT (i.e. TWICT) structure. The calculated GS and S₁($\pi\pi^*_{LE}$) structures exhibit smaller twist angles of $\vartheta_{GS} \sim 15^\circ$ and $\vartheta_{LE} \sim 7^\circ$ which nicely agree with the literature.¹⁵ Second, the large dipole moment $\mu_{TWICT} = 5.11$ D points at the charge transfer character of this structure. Similar values for μ_{TWICT} ranging from 5–8 D were determined theoretically and experimentally.^{15,18} The computed dipole moments of $\mu_{GS} = 2.29$ D and $\mu_{LE} = 3.50$ D agree well with respective results in the literature.^{15,18,20}

In this work, the S₁($\pi\pi^*_{TWICT}$) structure represents the global minimum of the S₁ state. This nicely explains why the fluorescence from the TWICT state is very pronounced even in nonpolar solvents such as CHX and *n*-hexane.^{15,18} In contrast, previous calculations on DMABN^{43,45,49} and DMAde¹⁵ predicted the S₁($\pi\pi^*_{LE}$) state being the global minimum in the excited state. In these earlier studies,^{15,43,45,49} the S₁($\pi\pi^*_{TWICT}$) structure solely became the global minimum in the excited state, when a polar solvent like ACN or H₂O was considered. Our calculations were performed in vacuo, so any effect of the solvent has not yet been taken into account. Although the S₁($\pi\pi^*_{LE}$) and particularly the S₁($\pi\pi^*_{TWICT}$) states are expected to be stabilised in polar solvents, according to our calculations the energetic order of the electronic states will be preserved. We note here that a recently published theoretical study on DMABN showcased that spin-component scaling (SCS) techniques, which were also used in this work,

ensure a correct energetic ordering of the $S_1(\pi\pi_{LE}^*)$ and $S_1(\pi\pi_{TWICT}^*)$ structures, respectively.⁴⁹ Nonetheless, high-level calculations considering the solvent have to be carried out in the near future to shed light on the influence of the molecular environment on the molecular dynamics and the ICT mechanism.

As described in Section 5.3, the $S_1(\pi\pi_{LE}^*)$ and $S_1(\pi\pi_{TWICT}^*)$ structures are separated by a potential energy barrier of $\Delta E = 0.05$ eV (4.82 kJ/mol). We interpret this barrier rather as a plateau-like region that has to be passed to finally reach the TWICT minimum. Consequently, the molecules do not experience a steep potential energy gradient when traveling from the $S_1(\pi\pi_{LE}^*)$ to the $S_1(\pi\pi_{TWICT}^*)$ state. While the molecules stay on the plateau for some time and explore the PES, a structural rearrangement towards partially twisted and wagged structures takes place. A similar picture and subsequent radiative deactivation of these partially twisted structures located on the plateau in the S_1 state was recently suggested for DMABN in ACN.⁴³

Surprisingly, the $S_1(\pi\pi_{LE}^*)$ structure features C^2 -puckering which is already known from the parent molecule Ade and assumed to be responsible for the ultrafast electronic deactivation of the latter.^{77–84} In this context, a conical intersection (CI) between the initially excited state and the GS is rapidly reached via an out-of-plane motion of the C^2 –H bond.

Based on these theoretically predicted findings, the results of the femtosecond time-resolved spectroscopic techniques now provide more insight into the dynamics of DMAde after photoexcitation.

Femtosecond time-resolved dynamics

The obtained time components of all performed time-resolved experiments nicely agree with each other and are summarised in Table 5.3. Overall four time components are necessary to describe the photo-induced dynamics of DMAde. Furthermore, a permanent offset at late delay times was observed by TEAS, which formally corresponds to a fifth time constant $\tau_5 \rightarrow \infty$. This is consistent with the quantum yield for GSR of $\Phi_{GS(ACN)} = 0.85$, which was determined by TVAS. In the following, these results will be discussed in some detail.

The time-resolved fluorescence measurements by the up-conversion technique served as starting point to shed light on the lifetime of the optically bright excited $S_1(\pi\pi^*)$ state of DMAde after photoexcitation. In line with a previous study in

Table 5.3: Time components τ_i with statistical 2σ uncertainty limits from the global data analyses of the experimental TFLS, TEAS and TVAS data.

	TFLS	TEAS	TVAS
τ_1 / ps	0.40 ± 0.06^a	0.28 ± 0.04	–
τ_2 / ps	1.60 ± 0.10^a	1.66 ± 0.12	2.00 ± 0.90
	1.24 ± 0.06^b		
τ_3 / ps	18.0 ± 4.00^b	–	20.0 ± 4.00
τ_4 / ns	1.07 ± 0.06^b	1.00 ± 0.25	1.07 (fixed)
τ_5 / ns	–	∞	–

^aobtained in the UV and ^b visible spectral range.

dioxane,¹⁷ the UV range is dominated by τ_1 and τ_2 , whereas longer excited-state lifetimes are detected in the visible range. Reconstruction of the transient fluorescence spectra suggests a sequential relaxation from the Franck–Condon region ($S_1(\pi\pi_{FC}^*)$) via the $S_1(\pi\pi_{LE}^*)$ to the $S_1(\pi\pi_{TWICT}^*)$ minimum. In Section 5.3, we assigned τ_1 to relaxation from the initially excited FC region towards the $S_1(\pi\pi_{LE}^*)$ minimum. Compared to the TFLS measurements, TEAS provides a slightly shorter value of the ultrafast time component with $\tau_1 = 0.28 \pm 0.04$ ps, which could be due to the higher time resolution of the experiment. From the SVD analysis, DADS1 (cf. Fig. 5.6a), red line) shows a negative contribution in the UV below 355 nm that can be ascribed to short-lived stimulated emission from the FC region. DADS1 then turns positive, reaches its maximum at 400 nm and extends up to 700 nm which corresponds to ESA from the initially excited $S_1(\pi\pi^*)$ state. The pronounced blue-shift of 35 nm as well as the spectral narrowing of the band in the UV when going from EADS1 to EADS2 (cf. Fig. 5.6b)) indicate vibrational relaxation associated with $\tau_1 = 0.28 \pm 0.04$ ps from the FC region to the $S_1(\pi\pi_{LE}^*)$ minimum. Accordingly, τ_2 is attributed to the lifetime of the relaxed $S_1(\pi\pi_{LE}^*)$ state. All time-resolved experiments yielded comparable values for τ_2 (cf. Table 5.3). Further, the observed maxima of EADS2 at 345 nm and above 600 nm nicely agree with the literature, where two ESA bands, one with a maximum at 350 nm, and a second broad ESA signal located around 750 nm were assigned to the $S_1(\pi\pi_{LE}^*)$ state.¹⁸ On the one hand, the reported time components in Ref. [18] of 0.46 ps and 1.6 ps for DMAde in ACN after excitation

at $\lambda_{\text{exc}} = 265$ nm match our results, on the other hand, the authors assigned the 0.46 ps value to the ICT reaction time and the 1.6 ps value to vibrational cooling. This contradicts our TVAS data, where $\tau_2 = 2.00 \pm 0.90$ ps corresponds to the rise of the $S_1(\pi\pi^*_{\text{TWICT}})$ structure. Moreover, the GS is partially repopulated within τ_2 .

The long-lived time constant $\tau_4 \sim 1$ ns corresponds to the lifetime of the $S_1(\pi\pi^*_{\text{TWICT}})$ structure. Owing to the structure sensitivity of TVAS, the TWICT structure was unambiguously identified as responsible for the long-lived fluorescence of DMAde. Additionally, we postulated the formation of excited-state intermediates with partial twisting and wagging angles which we called pTWICT structures. It can be assumed that these structures are formed enroute between the LE and TWICT minimum. Due to the flat PES, the molecules with pTWICT character may find another reaction coordinate that can connect the S_1 state with the GS. Therefore, the pTWICT structures can return back to the GS non-radiatively with $\tau_3 \sim 20$ ps via a $\text{CI}_{S_1/\text{GS}}$. Additionally, τ_3 reflects the dominant pathway towards GSR. The latter process cannot be followed by TEAS because it is shifted out of the spectral detection window. That could be the reason why τ_3 is absent in the TEAS data. Instead, the TEAS data revealed a permanent offset after $\Delta t \sim 1.7$ ns. In the corresponding transient spectra, the rise of an ESA centered at 540 nm is clearly visible (cf. Fig. 5.5b)). According to the literature, absorption of the triplet state of DMAde in ACN is observed at 550 nm.¹⁸ Therefore, the permanent offset is ascribed to the $T_1(\pi\pi^*)$ state that may be populated from the $S_1(\pi\pi^*_{\text{TWICT}})$ minimum within $\tau_4 \sim 1$ ns. Intersystem crossing to the triplet state also explains the permanent offset observed at 1550 and 1360 cm^{-1} as well as the apparently complete GSR at 1404 cm^{-1} in the transient vibrational spectra (cf. Fig. 5.7(b)). For that reason, the calculated vibrational spectrum for the $T_1(\pi\pi^*)$ state is given in Fig. 5.7(a). In agreement with the experiment, vibrational marker bands from the triplet manifold (cf. SI, Fig. 5.17) are expected at 1555, 1419 and 1364 cm^{-1} . Furthermore, Demeter et al. determined an intersystem crossing yield of $\Phi_{\text{ISC}(\text{ACN})} = 0.15$ ¹⁸ for DMAde which agrees with our observed quantum yield for GSR of $\Phi_{\text{GS}(\text{ACN})} = 0.85$. Although ISC from the $S_1(\pi\pi^*_{\text{TWICT}})$ to the $T_1(\pi\pi^*)$ state reflects an El-Sayed forbidden transition,⁸⁵ this rule may be softened due to the twisted geometry of the TWICT structure. Subsequent relaxation of the triplet state back to the GS

typically takes place on much longer times scales which are not accessible with our time-resolved measurements.

On this basis, the deactivation mechanism for DMAde after photoexcitation is proposed as sketched in Fig. 5.9. After excitation to the optically bright $S_1(\pi\pi^*)$ state, relaxation from the Franck–Condon region towards the minimum of the $S_1(\pi\pi_{LE}^*)$ state takes place with $\tau_1 \approx 0.3$ ps. Subsequently, the $S_1(\pi\pi_{LE}^*)$ state rapidly deactivates back to the electronic GS and populates the $S_1(\pi\pi_{TWICT}^*)$ minimum with $\tau_2 \sim 1.6$ ps. In contrast, the $S_1(\pi\pi_{TWICT}^*)$ state is long-lived with an excited-state lifetime of $\tau_4 \sim 1$ ns. In addition to the observed fluorescence from the TWICT minimum, intersystem crossing (ISC) towards a triplet state with $\tau_4 \sim 1$ ns is suggested as a new deactivation channel. The relaxation of the pTWICT structures back to the GS is associated with $\tau_3 \sim 20$ ps.

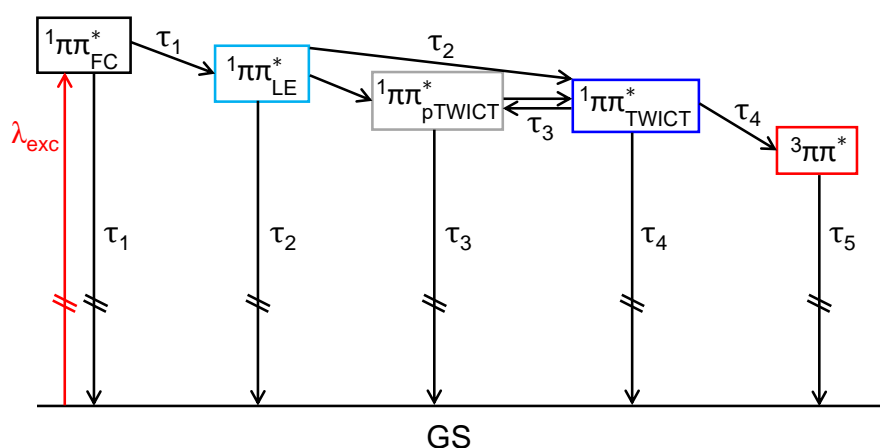


Figure 5.9: Deactivation mechanism for DMAde in ACN after photoexcitation at $\lambda_{\text{exc}} = 267$ nm.

5.5 Conclusions

To summarise, our results provide new insights into the underlying deactivation pathways of DMAde after photoexcitation. Already in 1997 the dual fluorescence of DMAde was proposed to arise from an intramolecular charge transfer state.¹⁹ Clear experimental evidence for this photo-induced ICT transition has now been provided. Aided by quantum chemical calculations, we ultimately identified the long-lived excited-state species being responsible for the anomalous emission band in the visible as $S_1(\pi\pi_{TWICT}^*)$ structure. Its formation proceeds

from the $S_1(\pi\pi_{LE}^*)$ state and involves pronounced twisting and wagging motions of the dimethylamino group. Further, several relaxation pathways back to the electronic GS were detected. After reaching the $S_1(\pi\pi_{LE}^*)$ minimum, ultrafast deactivation back to the GS and population of the $S_1(\pi\pi_{TWICT}^*)$ structure take place with $\tau_2 \sim 1.6$ ps. Subsequent decay of the latter occurs on the nanosecond time scale, followed by (partial) intersystem crossing to the triplet manifold. The photo-induced dynamics of DMAde thus follows a complex picture, which could be solely unravelled step by step using our broad variety of femtosecond time-resolved spectroscopic techniques and assistance by quantum chemical calculations.

References

- (1) Callis, P. R. *Annu. Rev. Phys. Chem.* **1983**, *34*, 329–357.
- (2) Cohen, B.; Hare, P. M.; Kohler, B. *J. Am. Chem. Soc.* **2003**, *125*, 13594–13601.
- (3) Crespo-Hernández, C. E.; Cohen, B.; Hare, P. M.; Kohler, B. *Chem. Rev.* **2004**, *104*, 1977–2019.
- (4) Shukla, M.; Leszczynski, J. *J. Biomol. Struct. Dyn.* **2007**, *25*, 93–118.
- (5) Middleton, C. T.; de La Harpe, K.; Su, C.; Law, Y. K.; Crespo-Hernández, C. E.; Kohler, B. *Annu. Rev. Phys. Chem.* **2009**, *60*, 217–239.
- (6) Schwalb, N. K.; Temps, F. *Science* **2008**, *322*, 243–245.
- (7) Doorley, G. W.; McGovern, D. A.; George, M. W.; Towrie, M.; Parker, A. W.; Kelly, J. M.; Quinn, S. J. *Angew. Chemie* **2009**, *121*, 129–133.
- (8) Kleinermanns, K.; Nachtigallová, D.; de Vries, M. S. *Int. Rev. Phys. Chem.* **2013**, *32*, 308–342.
- (9) Doorley, G. W.; Wojdyla, M.; Watson, G. W.; Towrie, M.; Parker, A. W.; Kelly, J. M.; Quinn, S. J. *J. Phys. Chem. Lett.* **2013**, *4*, 2739–2744.
- (10) Schreier, W. J.; Gilch, P.; Zinth, W. *Annu. Rev. Phys. Chem.* **2015**, *66*, 497–519.
- (11) Pecourt, J. M.; Peon, J.; Kohler, B. *J. Am. Chem. Soc.* **2001**, *123*, 10370–10378.
- (12) Peon, J.; Zewail, A. H. *Chem. Phys. Lett.* **2001**, *348*, 255–262.
- (13) Kang, H.; Jung, B.; Kim, S. K. *J. Chem. Phys.* **2003**, *118*, 6717–6719.
- (14) Gustavsson, T.; Sharonov, A.; Onidas, D.; Markovitsi, D. *Chem. Phys. Lett.* **2002**, *356*, 49–54.
- (15) Parusel, A. B.; Rettig, W.; Rotkiewicz, K. *J. Phys. Chem. A* **2002**, *106*, 2293–2299.
- (16) Schwalb, N. K.; Temps, F. *Phys. Chem. Chem. Phys.* **2006**, *8*, 5229–5235.
- (17) Schwalb, N. K.; Temps, F. *J. Phys. Chem. A* **2009**, *113*, 13113–13123.
- (18) Demeter, A.; Druzhinin, S. I.; Kovalenko, S. A.; Senyushkina, T. A.; Zachariasse, K. A. *J. Phys. Chem. A* **2011**, *115*, 1521–1537.

- (19) Albinsson, B. *J. Am. Chem. Soc.* **1997**, *119*, 6369–6375.
- (20) Andréasson, J.; Holmén, A.; Albinsson, B. *J. Phys. Chem. B* **1999**, *103*, 9782–9789.
- (21) Callis, P. R. *Chem. Phys. Lett.* **1979**, *61*, 563–567.
- (22) Onidas, D.; Markovitsi, D.; Marguet, S.; Sharonov, A.; Gustavsson, T. *J. Phys. Chem. B* **2002**, *106*, 11367–11374.
- (23) Lippert, E.; Lüder, W.; Moll, F.; Nägele, W.; Boos, H.; Prigge, H.; Seibold-Blankenstein, I. *Angew. Chem.* **1961**, *73*, 695–706.
- (24) Rotkiewicz, K.; Grellmann, K.; Z. R. Grabowski *Chem. Phys. Lett.* **1973**, *19*, 315–318.
- (25) Baumann, W.; Bischof, H.; Fröhling, J. C.; Brittinger, C.; Rettig, W.; Rotkiewicz, K. *J. Photochem. Photobiol. A Chem.* **1992**, *64*, 49–72.
- (26) Schuddeboom, W.; Jonker, S. A.; Warman, J. M.; Leinhos, U.; Kühnle, W.; Zachariasse, K. A. *J. Phys. Chem.* **1992**, *96*, 10809–10819.
- (27) Gorse, A. D.; Pesquer, M. *J. Phys. Chem.* **1995**, *99*, 4039–4049.
- (28) Hashimoto, M.; Hamaguchi, H. O. *J. Phys. Chem.* **1995**, *99*, 7875–7877.
- (29) Zachariasse, K. A.; Grobys, M.; Von Der Haar, T.; Hebecker, A.; Il'ichev, Y. V.; Morawski, O.; Rückert, I.; Kühnle, W. *J. Photochem. Photobiol. A Chem.* **1997**, *105*, 373–383.
- (30) Chudoba, C; Kummrow, A; Dreyer, J; Stenger, J; Nibbering, E. T.; Elsaesser, T.; Zachariasse, K. A. *Chem. Phys. Lett.* **1999**, *309*, 357–363.
- (31) Dreyer, J.; Kummrow, A. *J. Am. Chem. Soc.* **2000**, *122*, 2577–2585.
- (32) Grabowski, Z. R.; Rotkiewicz, K.; Rettig, W. *Chem. Rev.* **2003**, *103*, 3899–4031.
- (33) Kwok, W. M.; George, M. W.; Grills, D. C.; Ma, C.; Matousek, P; Parker, A. W.; Phillips, D.; Toner, W. T.; Towrie, M. *Angew. Chem. Int. Ed.* **2003**, *42*, 1826–1830.
- (34) Kwok, W. M.; Ma, C.; George, M. W.; Grills, D. C.; Matousek, P; Parker, A. W.; Phillips, D; Toner, W. T.; Towrie, M. *Phys. Chem. Chem. Phys.* **2003**, *5*, 1043–1050.

- (35) Ma, C.; Kwok, W. M.; Matousek, P.; Parker, A. W.; Phillips, D.; Toner, W. T.; Towrie, M. *J. Phys. Chem. A* **2002**, *106*, 3294–3305.
- (36) Köhn, A.; Hättig, C. *J. Am. Chem. Soc.* **2004**, *126*, 7399–7410.
- (37) Druzhinin, S. I.; Ernsting, N. P.; Kovalenko, S. A.; Lustres, L. P.; Senyushkina, T. A.; Zachariasse, K. A. *J. Phys. Chem. A* **2006**, *110*, 2955–2969.
- (38) Gustavsson, T.; Coto, P. B.; Serrano-Andrés, L.; Fujiwara, T.; Lim, E. C. *J. Chem. Phys.* **2009**, *131*, 031101.
- (39) Rhinehart, J. M.; Mehlenbacher, R. D.; McCamant, D. *J. Phys. Chem. B* **2010**, *114*, 14646–14656.
- (40) Coto, P. B.; Serrano-Andrés, L.; Gustavsson, T.; Fujiwara, T.; Lim, E. C. *Phys. Chem. Chem. Phys.* **2011**, *13*, 15182–15188.
- (41) Rhinehart, J. M.; Challa, J. R.; McCamant, D. W. *J. Phys. Chem. B* **2012**, *116*, 10522–10534.
- (42) Park, M.; Kim, C. H.; Joo, T. *J. Phys. Chem. A* **2013**, *117*, 370–377.
- (43) Gómez, I.; Castro, P. J.; Reguero, M. *J. Phys. Chem. A* **2015**, *119*, 1983–1995.
- (44) Kochman, M. A.; Tajti, A.; Morrison, C. A.; Miller, R. J. *J. Chem. Theory Comput.* **2015**, *11*, 1118–1128.
- (45) Georgieva, I.; Aquino, A. J.; Plasser, F.; Trendafilova, N.; Köhn, A.; Lischka, H. *J. Phys. Chem. A* **2015**, *119*, 6232–6243.
- (46) Segado, M.; Mercier, Y.; Gómez, I.; Reguero, M. *Phys. Chem. Chem. Phys.* **2016**, *18*, 6875–6884.
- (47) Curchod, B. F.; Sisto, A.; Martínez, T. J. *J. Phys. Chem. A* **2017**, *121*, 265–276.
- (48) Mani, T.; Grills, D. C. *J. Phys. Chem. A* **2018**, *122*, 7293–7300.
- (49) Kochman, M. A.; Durbeej, B. *J. Phys. Chem. A* **2020**, *124*, 2193–2206.
- (50) Sobolewski, A. L.; Domcke, W. *Chem. Phys. Lett.* **1996**, *259*, 119–127.
- (51) Rotkiewicz, K.; Grabowski, Z. R.; J. Jasny *Chem. Phys. Lett.* **1975**, *34*, 55–59.
- (52) Pancur, T.; Schwalb, N. K.; Renth, F.; Temps, F. *Chem. Phys.* **2005**, *313*, 199–212.

- (53) Maroncelli, M.; Fleming, G. R. *J. Chem. Phys.* **1987**, *86*, 6221–6239.
- (54) Eilers-König, N.; Kühne, T.; Schwarzer, D.; Vöhringer, P.; Schroeder, J. *Chem. Phys. Lett.* **1996**, *253*, 69–76.
- (55) Renth, F.; Siewertsen, R.; Strübe, F.; Mattay, J.; Temps, F. *Phys. Chem. Chem. Phys.* **2014**, *16*, 19556–19563.
- (56) Megow, S.; Fitschen, H. L.; Tuczek, F.; Temps, F. *J. Phys. Chem. Lett.* **2019**, *10*, 6048–6054.
- (57) Van Stokkum, I. H. M.; Larsen, D. S.; Van Grondelle, R. *Biochim. Biophys. Acta* **2004**, *1657*, 82–104.
- (58) Böhnke, H.; Bahrenburg, J.; Ma, X.; Röttger, K.; Näther, C.; Rode, M. F.; Sobolewski, A. L.; Temps, F. *Phys. Chem. Chem. Phys.* **2018**, *20*, 2646–2655.
- (59) Hamm, P.; Kaindl, R. A.; Stenger, J. *Opt. Lett.* **2000**, *25*, 1798–1800.
- (60) Kaindl, R. A.; Wurm, M.; Reimann, K.; Hamm, P.; Weiner, A. M.; Woerner, M. *J. Opt. Soc. Am. B* **2000**, *17*, 2086–2094.
- (61) Grubbs, M.; Orr-Ewing, A. J.; Ashfold, M. N. R. *Rev. Sci. Instrum.* **2014**, *85*, 064104.
- (62) Weigend, F.; Häser, M. *Theor. Chem. Acc.* **1997**, *97*, 331–340.
- (63) Hättig, C.; Hellweg, A.; Köhn, A. *Phys. Chem. Chem. Phys.* **2006**, *8*, 1159–1169.
- (64) Weigend, F.; Häser, M.; Patzelt, H.; Ahlrichs, R. *Chem. Phys. Lett.* **1998**, *294*, 143–152.
- (65) Weigend, F.; Köhn, A.; Hättig, C. *J. Chem. Phys.* **2002**, *116*, 3175–3183.
- (66) Hättig, C.; Weigend, F. *J. Chem. Phys.* **2000**, *113*, 5154–5161.
- (67) Hättig, C.; Hald, K. *Phys. Chem. Chem. Phys.* **2002**, *4*, 2111–2118.
- (68) Hättig, C. *J. Chem. Phys.* **2003**, *118*, 7751–7761.
- (69) Hellweg, A.; Grün, S. A.; Hättig, C. *Phys. Chem. Chem. Phys.* **2008**, *10*, 4119–4127.
- (70) Hättig, C.; Köhn, A. *J. Chem. Phys.* **2002**, *117*, 6939–6951.
- (71) Hättig, C.; Köhn, A.; Hald, K. *J. Chem. Phys.* **2002**, *116*, 5401–5410.

- (72) TURBOMOLE V7.0 2015, a development of University of Karlsruhe and Forschungszentrum Karlsruhe GmbH, 1989-2007 TURBOMOLE GmbH, since 2007; available from <http://www.turbomole.com>.
- (73) Sinha, P.; Boesch, S. E.; Gu, C.; Wheeler, R. A.; Wilson, A. K. *J. Phys. Chem. A* **2004**, *108*, 9213–9217.
- (74) Kesharwani, M. K.; Brauer, B.; Martin, J. M. *J. Phys. Chem. A* **2015**, *119*, 1701–1714.
- (75) Frieze, D. H.; Törk, L.; Hättig, C. *J. Chem. Phys.* **2014**, *141*, 194106.
- (76) Martin, R. L. *J. Chem. Phys.* **2003**, *118*, 4775–4777.
- (77) Blancafort, L. *J. Am. Chem. Soc.* **2006**, *128*, 210–219.
- (78) Conti, I.; Garavelli, M.; Orlandi, G. *J. Am. Chem. Soc.* **2009**, *131*, 16108–16118.
- (79) Hassan, W. M. I.; Chung, W. C.; Shimakura, N.; Koseki, S.; Kono, H.; Fujimura, Y. *Phys. Chem. Chem. Phys.* **2010**, *12*, 5317–5328.
- (80) Marian, C. M. *J. Chem. Phys.* **2005**, *122*, 1–13.
- (81) Perun, S.; Sobolewski, A. L.; Domcke, W. *J. Am. Chem. Soc.* **2005**, *127*, 6257–6265.
- (82) Perun, S.; Sobolewski, A. L.; Domcke, W. *Chem. Phys.* **2005**, *313*, 107–112.
- (83) Yamazaki, S.; Kato, S. *J. Am. Chem. Soc.* **2007**, *129*, 2901–2909.
- (84) Stange, U. C.; Temps, F. *Chem. Phys.* **2018**, *515*, 441–451.
- (85) El-Sayed, M. A. *J. Chem. Phys.* **1963**, *38*, 2834–2838.

5.6 Supporting Information

All fluorescence time profiles measured by the up-conversion technique in the UV and visible region are presented in Fig. 5.10 and Fig. 5.11, respectively.

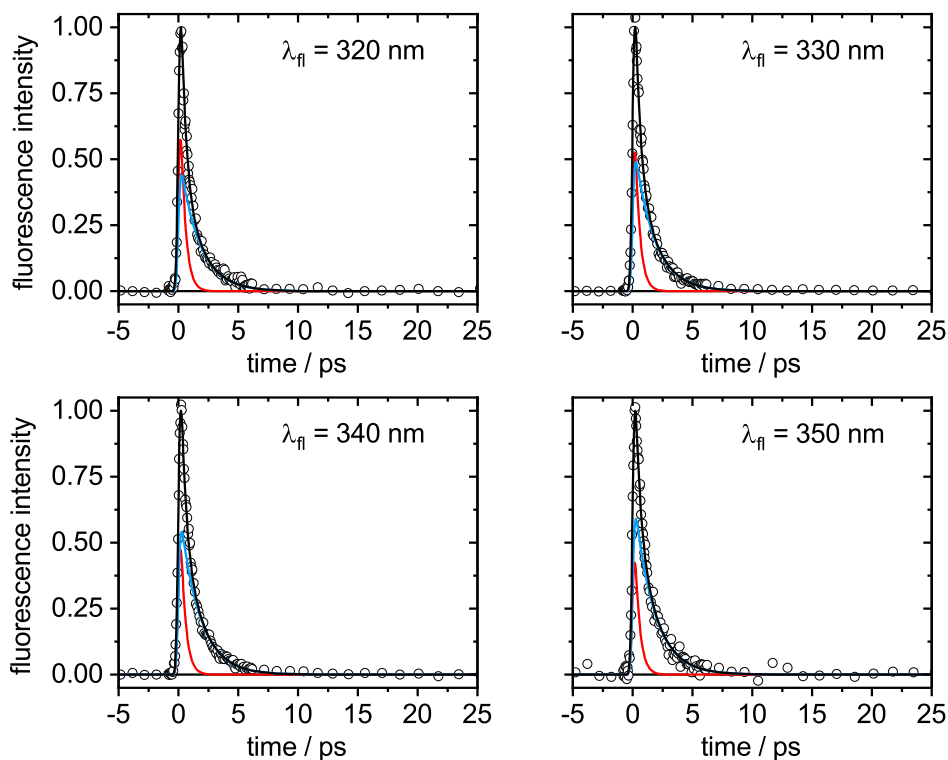


Figure 5.10: Time profiles at four emission wavelengths in the UV for DMAde in ACN after excitation at $\lambda_{exc} = 266$ nm obtained from the TFLS measurements by the up-conversion technique. Shown are the experimental data (open circles) and the global fits (black lines) obtained by a sum of exponentials (red and blue lines) convoluted with the IRF, respectively.

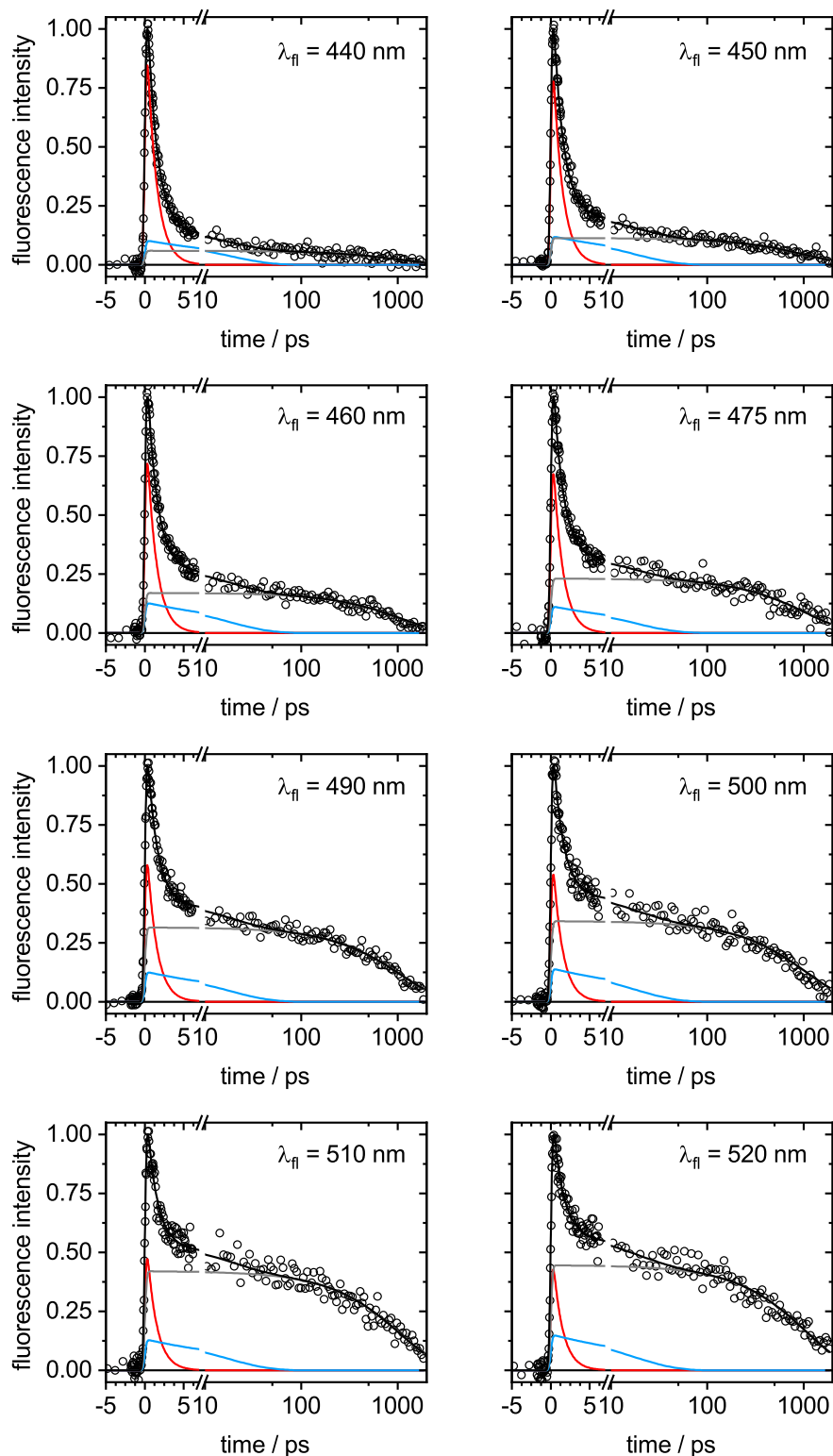


Figure 5.11: Time profiles in the visible for DMAde in ACN after excitation at $\lambda_{\text{exc}} = 266$ nm obtained from the TFLS measurements. Shown are the experimental data (open circles) and the global fits (black lines) obtained by a sum of exponentials (red, blue and grey lines) convoluted with the IRF, respectively. The time profiles are scaled linearly up to 10 ps, a logarithmic scale is used thereafter.

TCSPC time profiles were recorded after excitation at $\lambda_{\text{exc}} = 265$ nm in 20 nm steps from $\lambda_{\text{fl}} = 340$ nm to 500 nm. Two selected TCSPC time profiles at $\lambda_{\text{fl}} = 340$ nm and $\lambda_{\text{fl}} = 480$ nm of DMAde in ACN are displayed in Fig. 5.12.

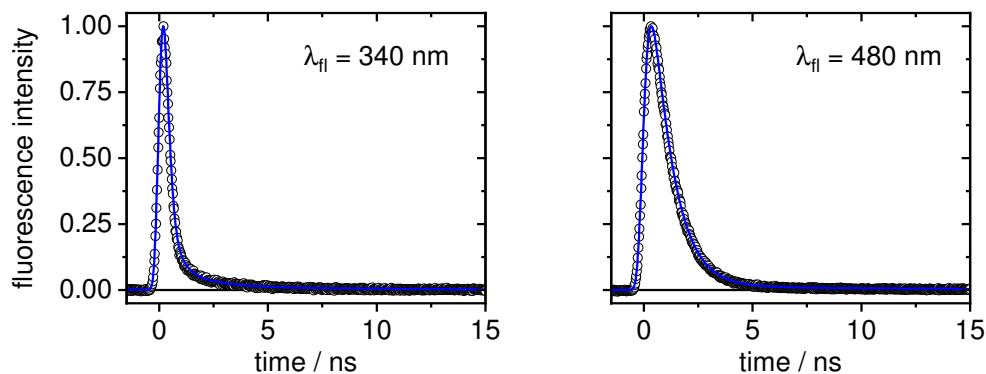


Figure 5.12: Time profiles at $\lambda_{\text{fl}} = 340$ nm and $\lambda_{\text{fl}} = 480$ nm obtained from TCSPC measurements of DMAde in ACN after excitation at $\lambda_{\text{exc}} = 265$ nm. Shown are the experimental data (open circles) and the global fits (blue lines).

The global data analysis of the TCSPC time profiles yielded the following time components with statistical 2σ uncertainty limits for DMAde in ACN:

$$\begin{aligned}\tau_{\text{UV}} &< \sigma_{\text{IRF}} \\ \tau_{\text{vis}} &= 0.90 \pm 0.03 \text{ ns}\end{aligned}$$

In the UV, the fluorescence decays within the experimental time resolution ($\tau_{\text{UV}} < \sigma_{\text{IRF}}$), while a time component of $\tau_{\text{vis}} = 0.90 \pm 0.03$ ns was determined from the global data analysis at $\lambda_{\text{fl}} = 480$ nm.

Drawings of the natural transition orbitals (NTOs) participating in the vertical electronic transitions from the GS minimum energy structure are presented in Fig. 5.13. Additionally, the NTOs of the HOMO–LUMO transition for the $S_1(\pi\pi_{\text{TWICT}}^*)$ minimum structure are shown.

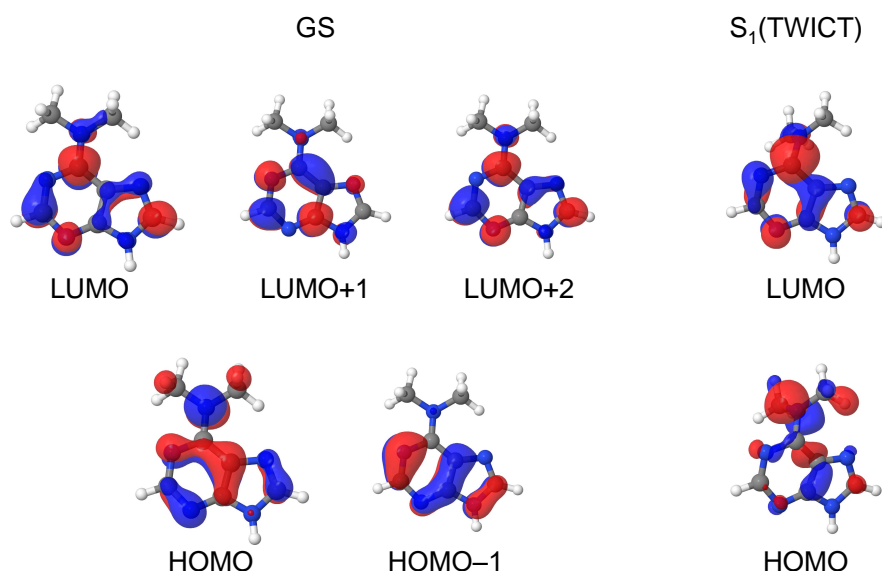


Figure 5.13: Natural transition orbitals (NTOs) that are involved in the vertical electronic transitions from the GS minimum energy structure and the NTOs of the HOMO–LUMO transition starting from the $S_1(\pi\pi^*_{\text{TWICT}})$ minimum energy structure.

The experimental FTIR spectrum in ACN- d_3 and the calculated vibrational spectra of DMAde in the GS, $S_1(\pi\pi^*_{\text{LE}})$, $S_1(\pi\pi^*_{\text{TWICT}})$ and $T_1(\pi\pi^*)$ excited states in the spectral range from 1650–1225 cm^{-1} are depicted in Fig. 5.14. Visualisations of the calculated vibrational modes in the GS and in the $S_1(\pi\pi^*_{\text{TWICT}})$ and $T_1(\pi\pi^*)$ excited states in the spectral region from 1650–1225 cm^{-1} are summarised in Fig. 5.15, Fig. 5.16 and Fig. 5.17, respectively.

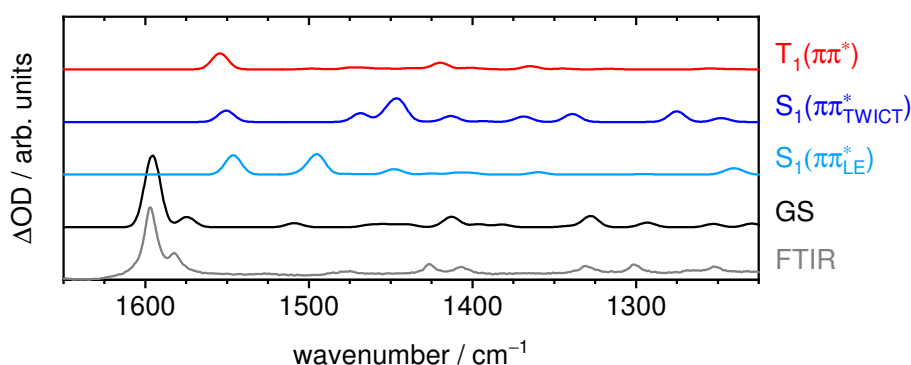


Figure 5.14: Calculated vibrational spectra in the GS, $S_1(\pi\pi^*_{\text{LE}})$, $S_1(\pi\pi^*_{\text{TWICT}})$ and $T_1(\pi\pi^*)$ excited states along with the experimental FTIR spectrum in ACN- d_3 in the spectral range from 1650–1225 cm^{-1} for DMAde.

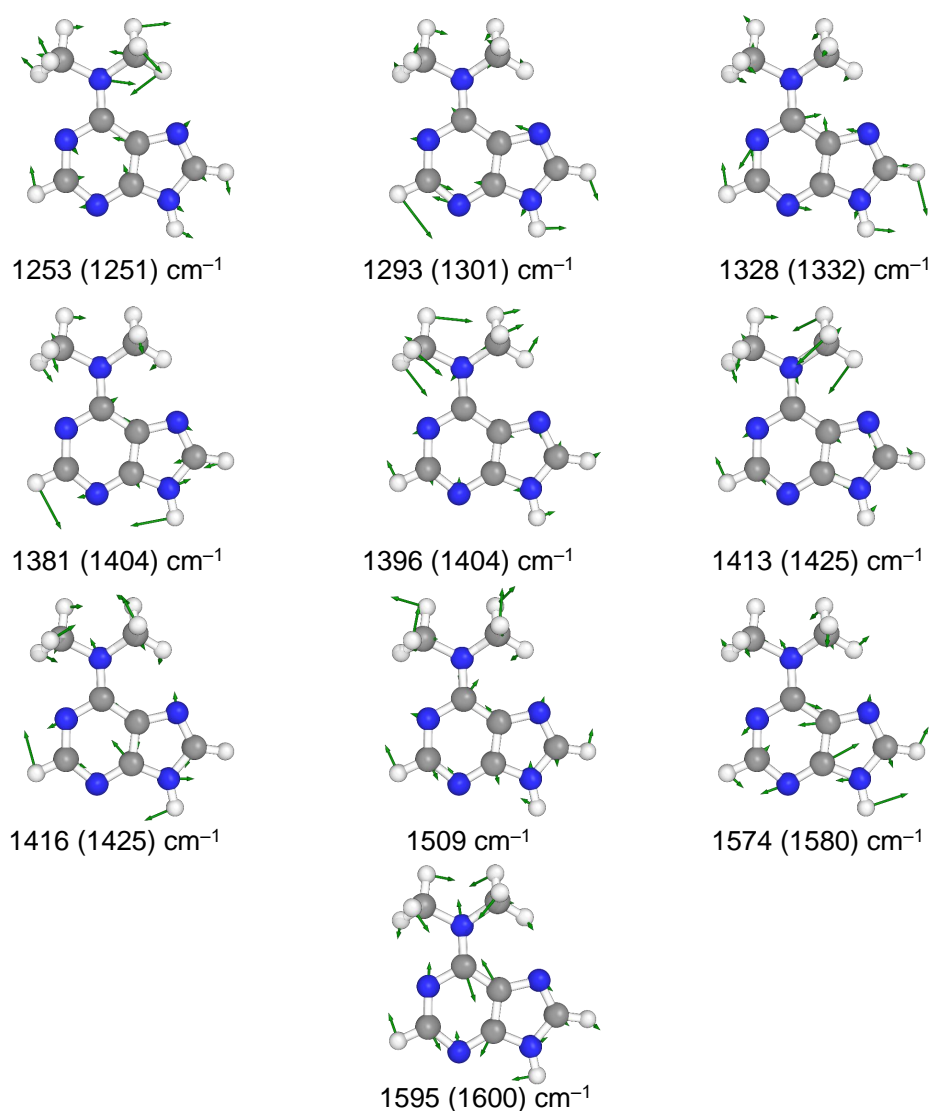


Figure 5.15: Calculated and experimental vibrational marker modes of DMAde in the electronic GS. The calculated values are given first and are scaled by a factor of 0.97. Experimental values are given in parenthesis. The calculated band at 1509 cm^{-1} was hardly to be observed experimentally. Thus, this value is missing.

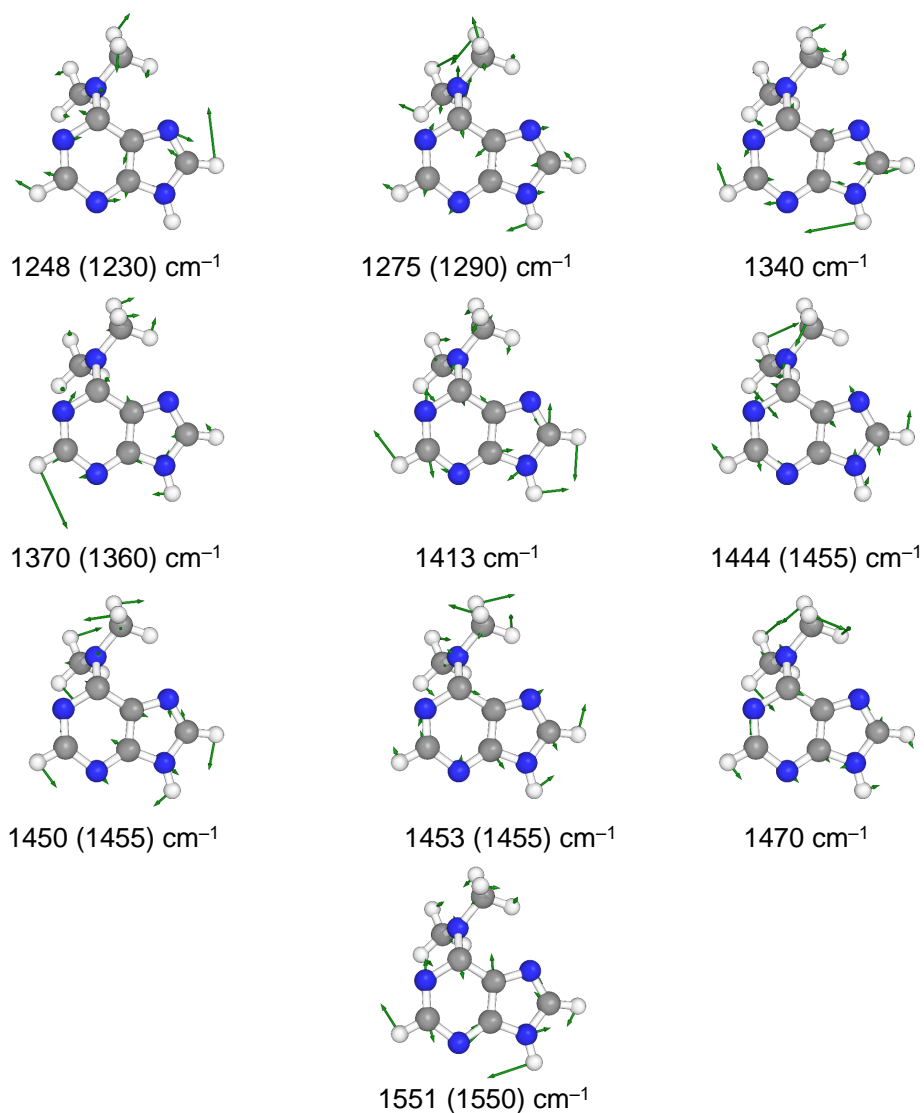


Figure 5.16: Calculated and experimental vibrational marker modes of DMAd in the $S_1(\pi\pi^*_{\text{TWICT}})$ excited state. The calculated values are given first and are scaled by a factor of 0.985. Experimental values are given in parenthesis. The calculated bands at 1470, 1413 and 1340 cm^{-1} are not observed experimentally because they overlap with negative signals from the GS.

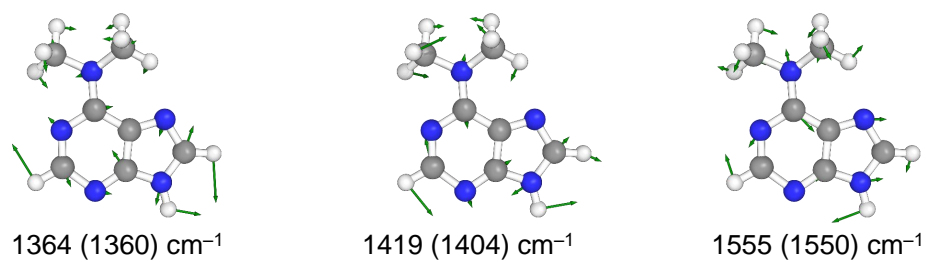


Figure 5.17: Calculated and experimental vibrational marker modes of DMAde in the $T_1(\pi\pi^*)$ excited state. The calculated values are given first and are scaled by a factor of 0.985. Experimental values are observed indirectly and are given in parenthesis.

Cis-trans isomerisation
dynamics of UV-excited
acetylacetone unveiled by
femtosecond time-resolved
vibrational absorption
spectroscopy

REBECCA HOLTSMANN, SEBASTIAN SCHATZ, BRUNA ALVES MORAIS, HENDRIK BÖHNKE
AND FRIEDRICH TEMPS

Institute of Physical Chemistry, Christian-Albrechts-University Kiel, Olshausenstr.
40, D-24098 Kiel, Germany.

Manuscript in preparation.

OWN CONTRIBUTIONS TO THIS MANUSCRIPT:

- Static spectroscopy,
- ^1H -NMR spectroscopy,
- DFT and ground-state calculations for the enol-type isomers of AA,
- femtosecond time-resolved vibrational absorption spectroscopy,
- analysis of the experimental data,
- writing of the manuscript.

Abstract

Acetylacetone (AA) is the prototypical aliphatic β -diketone – a class of molecules known for its keto–enol tautomerism. Here, we report on the successive ultrafast electronic relaxation and isomerisation dynamics of the enolic isomer after UV excitation in cyclohexane and in deuterated acetonitrile as solvents by means of structure-sensitive femtosecond transient vibrational absorption spectroscopy and quantum chemical calculations. Several relaxation channels towards ground-state recovery, intersystem crossing, and photoproduct formation are scrutinised. The photoproduct is identified as the previously proposed, but to date elusive *cis-trans-cis* (CTC) enolic form that arises after *cis-trans* isomerisation around the C=C double bond.

6.1 Introduction

The unique photophysical and photochemical dynamics of β -diketones after excitation by ultraviolet (UV) light attract major attention owing to keto–enol tautomerism.^{1–23} As illustrated in Fig. 6.1, the enolic tautomer of the prototypical β -diketone acetylacetone (AA, pentane-2,4-dione) is stabilised by intramolecular hydrogen bonding accompanied by (partial) delocalisation of the conjugated π -system compared to the diketonic form.^{1,7–9} The enolic species may, in principle, exhibit an asymmetric C_s or a symmetric C_{2v} structure. Over the years, these two possibilities have stimulated many controversial discussions.^{8–11} The majority of experimental and computational studies point at C_s symmetry and a double-well potential energy surface (PES) for the electronic ground state (GS) featuring localisation of the enolic hydrogen on one of the oxygen atoms and a low barrier for internal proton transfer.^{8,9,11} In particular, ultrafast electron diffraction measurements by Zewail and co-workers on gas-phase AA found different bond lengths of the C=O and C–OH groups.⁹ In contrast, high resolution rotational spectra by Caminati and Grabow provided strong evidence for the C_{2v} symmetric structure, where the enolic hydrogen is equally shared between both oxygen atoms.¹⁰

Furthermore, the ratio between the diketonic and enolic tautomers strongly depends on the molecular environment. In the gas phase and in apolar, aprotic solvents (e.g., cyclohexane), the enolic species is favoured (> 90 %),^{2,5,8} while

the diketone coexists in sizeable amounts in polar solvents like acetonitrile ($\sim 40\%$) and even dominates in water ($\sim 80\%$).^{5–7}

For spectroscopic investigations in the near-UV spectral region, however, the diketonic tautomer of AA remains rather inaccessible owing to the low oscillator strengths for transitions to the optically dark $^1n\pi^*$ states.²⁴ Thus, the enolic form of AA transpires as the main photoactive species and can be excited selectively even in solvents featuring coexisting amounts of both tautomeric forms due to its optically bright $S_2(\pi\pi^*)$ state.^{13,15,21,23,24}

Due to its importance in atmospheric chemistry,²⁵ the photochemistry of AA has been studied extensively in the gas phase.^{12–17} A number of experimental investigations revealed population of a triplet state after UV excitation to the $S_2(\pi\pi^*)$ state. Subsequent bond breaking processes have been found to lead to OH and CH₃ fragments.^{12–17} Furthermore, UV irradiation experiments in cryogenic matrices showed the formation of different non-chelated enolic isomers next to the canonical chelated (i.e., hydrogen-bonded) enolic form.^{23,26–30} The structures of these additional isomers, which lack the stabilising intramolecular hydrogen bond compared to the minimum energy CCC enol form, are given in Fig. 6.1 along with their commonly used notations. Here, C and T denote the *cis* and *trans* configurations with respect to the C–C, C=C and C–O bonds, respectively.

Compared to the gas phase, the liquid-phase photochemistry of AA is governed by fast electronic relaxation channels without significant fragmentation.¹⁸ In particular, Verma and co-workers recently studied the photo-induced dynamics of AA in *n*-hexane, dioxane and acetonitrile solutions by means of femtosecond time-resolved electronic absorption spectroscopy (TEAS).¹⁸ Accordingly, an excited-state intramolecular proton transfer (ESIPT) takes place within < 50 fs after promotion to the optically bright $S_2(\pi\pi^*)$ state, followed by internal conversion (IC) to the optically dark $S_1(n\pi^*)$ state on the picosecond time scale. Evolving in this intermediary $S_1(n\pi^*)$ state, a fraction of the excited-state population immediately returns to the GS of the initially excited CCC enolic species. The remaining photo-excited population evolves on the $S_1(n\pi^*)$ PES towards the formation of non-chelated enolic isomers by rotamerisation in the excited state within ~ 10 ps and subsequent slower deactivation processes in ~ 800 ps. The latter have first been observed in much earlier UV-UV flash photolysis transient

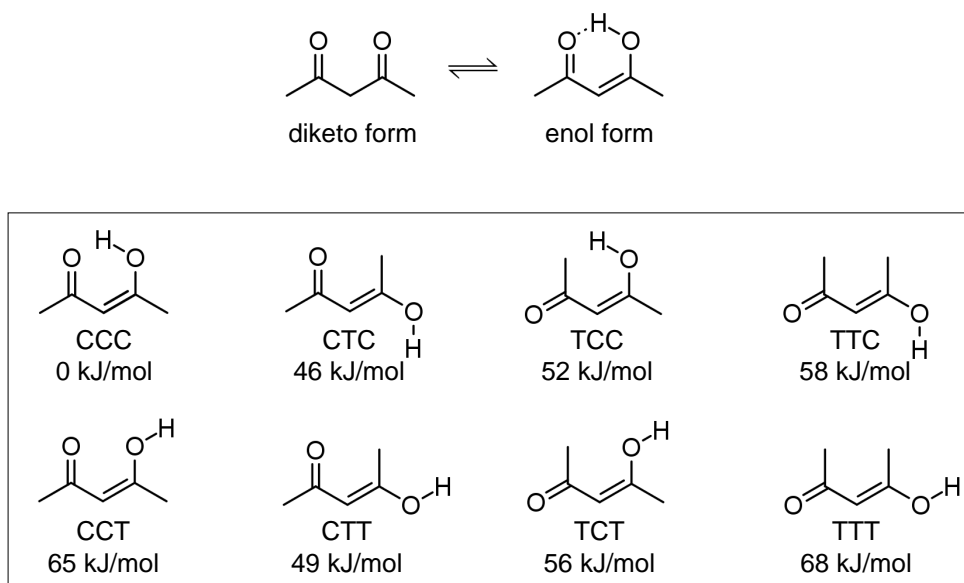


Figure 6.1: Tautomeric equilibrium of the diketo-type and enol-type isomers of AA along with an overview of the different isomers of enol-type AA arising by rotations around the C–C, C=C and C–O bonds of the CCC isomer, respectively. Relative energies refer to each isomer in the electronic ground state with respect to the thermally stable enol CCC form computed at the B2PLYP-D3(BJ)/def2-QZVP level of theory. Supplementary calculations are presented in Table 6.1 (SI).

experiments by Veierov et al.,³¹ but the primary photochemical pathways to the non-chelated enolic isomer(s) remained elusive until now.

Here, we report on a study of the ultrafast electronic relaxation dynamics of acetylacetone in its enolic CCC form upon photoexcitation at $\lambda_{\text{exc}} = 267$ nm by means of femtosecond transient vibrational absorption spectroscopy as a chemical structure-sensitive method to shed light on the associated excited-state deactivation and intramolecular *cis-trans* isomerisation pathways and for identification of the elusive photoproduct.

6.2 Methods

Static and time-resolved spectroscopic techniques

The title compound acetylacetone was purchased from Sigma Aldrich (purity ≥ 99.5 %) and used as received. All static and time-resolved measurements in

this work were performed in deuterated acetonitrile (ACN- d_3) and cyclohexane (CHX, Uvasol grade) at concentrations of 2–5 mM. The fractions of the enolic and diketonic tautomers in both solvents were determined by ^1H -NMR spectroscopy. Steady-state vibrational spectra were measured on an IFS66 Fourier Transform infrared spectrometer (Bruker) using a liquid-nitrogen cooled MCT detector. During the measurements the sample chamber was purged with dry air (PG 85 L, cmc-Instruments). The sample cell with an optical path length of 0.1 mm was equipped with CaF_2 windows.

The femtosecond time-resolved vibrational absorption spectrometer^{32–34} has been built around a Coherent Libra HE Ti:Sa laser system delivering light pulses of 90 fs duration full width at half maximum (FWHM) at $\lambda = 800$ nm and a 1 kHz repetition rate. The pump pulses at $\lambda_{\text{exc}} = 267$ nm ($1.1 \mu\text{J}$ / pulse) were obtained by third harmonic generation (THG) of the Ti:Sa fundamental and loosely focused through CaF_2 windows into a home-built sample flow cell equipped with PTFE spacers for an optical path length of 0.1 mm. Every second pump pulse was blocked by a synchronised optical chopper operating at 500 Hz. Another fraction of the laser fundamental was used to pump a two-stage optical parametric amplifier (OPA), which provided tunable signal and idler pulses. Subsequently, broadband mid-infrared probe pulses were generated by difference frequency generation (DFG) in AgGaS_2 of the signal and idler pulses.^{33,34} The pump and probe beams were spatially and temporally overlapped in the sample flow cell. The transmitted probe light was then guided to the grating spectrograph and spectrally dispersed before impinging on the liquid-nitrogen cooled 32-pixel MCT detector array. Transient vibrational difference spectra were then recorded as function of pump–probe time delay. After baseline correction of the raw data employing the programme KOALA,³⁵ the recorded transient spectra at each time delay were globally modelled using a sum of Gaussian functions. To extract time profiles, the respective amplitudes determined by the spectral band fits were plotted as function of pump–probe delay time and fitted in a global manner by a sum of exponentials.

Quantum chemical calculations

The molecular minimum energy structures and associated normal mode vibrational wavenumbers of the thermally stable CCC enolic form and its different

isomers in the electronic ground state were calculated using density functional theory (DFT) at the B3LYP-D3 level^{36–40} in combination with the 6-311++G** basis set^{41–44} as implemented in the Gaussian09 suite.⁴⁵ The relative energies for all isomers with respect to the CCC minimum energy structure were determined at the RI-SCS-MP2^{46–49}/def2-TZVPP,^{47,50} B3LYP-D3^{36–40}/6-311++G**^{41–44} and the B2PLYP-D3(BJ)^{51,52}/def2-QZVP^{50,53,54} levels of theory. The use of the B2PLYP method was guided by the recent recommendation from extensive benchmarking as one of the most accurate double-hybrid functionals for thermodynamical calculations^{51,55,56} implemented in the TURBOMOLE 7.0 programme package.⁵⁷

Geometry optimisations, calculations of vibrational modes and selected single energy points for species in the excited singlet and triplet electronic states were performed using the second-order coupled-cluster method under the resolution of the identity approximation (RI-SCS-CC2).^{49,58–62} Here, the def2-TZVPP basis set^{47,50} was used in the TURBOMOLE 7.0 programme package.⁵⁷ The calculated vibrational wavenumbers in the ground state (B3LYP-D3/6-311++G**) as well as in the excited states (RI-SCS-CC2/def2-TZVPP) were scaled by factors of 0.98 and 0.955 as recommended in the literature, respectively.^{63–65}

6.3 Results

Static UV and FTIR spectra

The measured UV absorption spectra of AA in ACN-d₃ and CHX are displayed in Fig. 6.2(a). The intense absorption band with a maximum at 270 nm clearly belongs to the S₂($\pi\pi^*$) transition of the CCC enol. The lower intensity in ACN-d₃ as polar solvent compared to the apolar CHX is explained by the coexistence of the diketo tautomer ($\sim 40\%$ by ¹H-NMR) in ACN. Owing to the much weaker oscillator strength of the forbidden S₁($n\pi^*$) transition of the diketonic tautomer,²⁴ however, selective photoexcitation of the enol is assured regardless of the solvent used. A mixture of different other enolic isomers was excluded by ¹H-NMR spectroscopy in accordance with literature.^{5,18}

The measured FTIR spectra of AA in both solvents in the spectral range from 1200–1800 cm^{–1} are presented in Fig. 6.2(b). Virtual absence of the diketonic C=O vibrations indicates that the enolic structure is favored in CHX by $\sim 90\%$ in accordance with ¹H-NMR results.

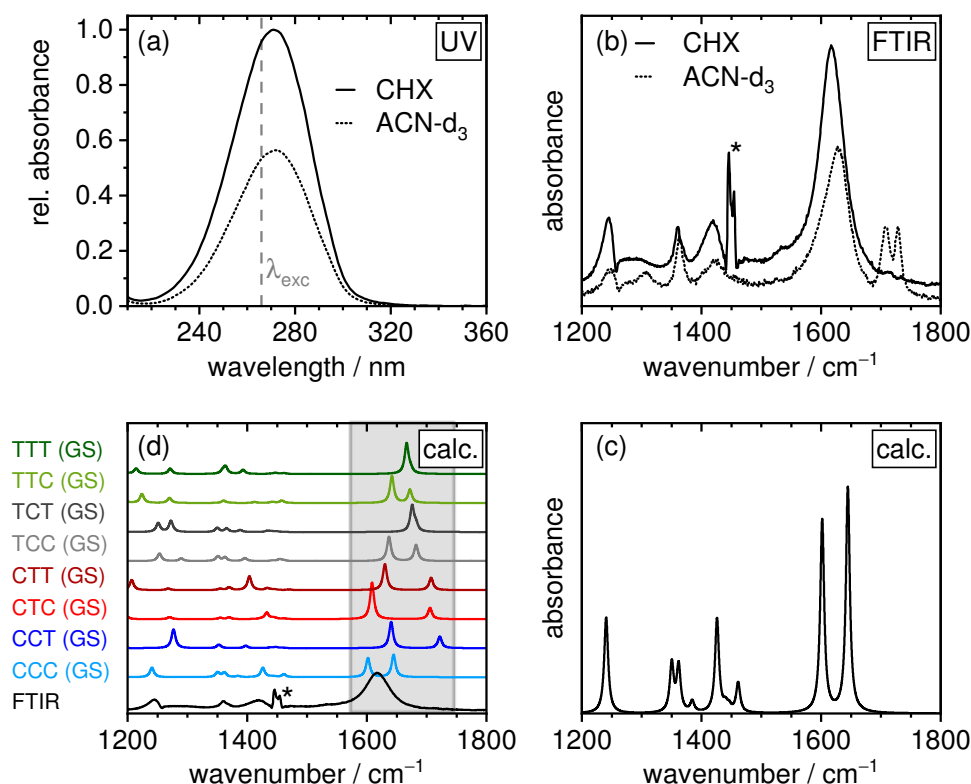


Figure 6.2: (a) UV absorption spectra of AA in CHX (straight line) and ACN-d₃ (dashed line). The relative absorbance in CHX is normalised to unity at $\lambda = 270$ nm. (b) Experimental FTIR spectra of AA in CHX and in ACN-d₃. (c) Calculated (B3LYP-D3/6-311++G**) vibrational spectrum of the CCC isomer of enolic AA. (d) Computed (B3LYP-D3/6-311++G**) ground-state vibrational spectra for all isomers of enol-type AA in the spectral range of 1200–1800 cm⁻¹. For comparison, the experimental FTIR spectrum of CCC in CHX is shown in black. The signature at 1450 cm⁻¹ in the experimental FTIR spectrum labelled with an asterisk is an artefact from the solvent.

Quantum chemical calculations

The vibrational wavenumbers of the enolic CCC species at the B3LYP-D3/6-311++G** level of theory were computed to assign the experimental bands. In the calculated spectrum in Fig. 6.2(c), two intense vibrational marker bands at 1601 and 1645 cm⁻¹ are observed for the enolic structure, which are attributed to the C=O and the C=C symmetric stretch vibration as well as to in-plane deformation vibrations of the OH group (cf. Fig. 6.6, SI). However, upon spectral broadening in solution caused by strong intramolecular hydrogen bonding,

these marker bands are represented by a single signal at 1628 cm^{-1} (ACN- d_3) and 1617 cm^{-1} (CHX) in the FTIR spectra. The two additional bands in ACN- d_3 observed at 1708 and 1728 cm^{-1} are attributed to the symmetric and antisymmetric stretch vibrations of the carbonyl bonds of the diketonic form.

As different enolic AA isomers are discussed below to be involved in the deactivation pathway after photoexcitation, additional quantum chemical calculations were carried out for all isomers depicted in Fig. 6.1. To verify the energetic order of the different isomers, the relative energy for each isomer in the electronic ground state with respect to the thermally stable CCC form was calculated at different levels of theory (B2PLYP-D3(BJ)/def2-QZVP, RI-MP2/def2-TZVPP and B3LYP-D3/6-311++G**) and is summarised in Table 6.1 (SI). Regardless of the computational method used, the energetic order of the isomers is preserved and nicely agrees with previous results reported in the literature.³⁰

Accordingly, the thermodynamically most stable, chelated CCC isomer is followed in energy by the non-chelated CTC and CTT isomers, which arise from *cis-trans* isomerisation around the C=C bond, and – for the CTT isomer – by additional rotation around the C–O bond. Except for CCT and TTT, which are the highest in energy, the remaining non-chelated enol forms are nearly iso-energetic. To distinguish between the different isomers, vibrational spectra in the GS for all isomers were computed and are displayed in Fig. 6.2(d). The associated normal modes are visually presented in Fig. 6.6 (SI). For all isomers a set of characteristic vibrational marker bands is obtained in the spectral range of $1550\text{--}1750\text{ cm}^{-1}$. In particular, the vibrational signature, i.e., the position of the vibrational marker bands and their respective spacing are significantly different for each isomer and can thus be treated as selective fingerprints for each isomer in the electronic ground state. For CTC for instance, the spacing of the two characteristic vibrational modes in this region is largest with 100 cm^{-1} , whereas for TCT and TTT these are separated by only a few wavenumbers and tend to overlap. Thus, due to their unique vibrational characteristics imprinted by their structural differences, even electronically similar isomers can be distinguished by their respective IR spectra.

Time-resolved vibrational absorption spectroscopy

The transient vibrational absorption spectra after excitation at $\lambda_{\text{exc}} = 267$ nm focusing on the spectral range from 1550 to 1720 cm^{-1} in ACN- d_3 and CHX are presented in Fig. 6.3. After photoexcitation of enolic CCC, a strong and broad negative signal at 1628 cm^{-1} (ACN- d_3) and 1617 cm^{-1} (CHX) corresponding to the respective ground-state bleach (GSB) is observed. In both solvents the GSB is partially recovered in a bi-exponential fashion and features an asymptotic permanent offset on the nanosecond time scale. Moreover, an additional time-dependent vibrational band is observed in the TVA data at 1570 cm^{-1} in ACN- d_3 . Since this band rises in intensity at early times, prior to a decay on the nanosecond time scale, this vibrational marker band is assigned to an excited-state intermediate due to its unique spectro-temporal behavior (see below). Furthermore, as this vibrational signature of the intermediary species decays, two positive bands are rising in at late delay times in ACN- d_3 (1585 and 1690 cm^{-1}) and CHX (1605 and 1700 cm^{-1}) towards a permanent positive offset, indicating the population of either a successor excited state or the formation of a long-lived photoproduct back in the electronic GS. In order to elucidate the identity of this late-time species, we turn to our vibrational mode calculations of various isomers in different electronic states (cf. Fig. 6.2(d) and Fig. 6.7, SI). Comparison with the calculated spectrum of the CTC isomer in the electronic GS, depicted in red in Fig. 6.2(d) and Fig. 6.3(a, e), the observed experimental late-time bands show good agreement with the computed CTC marker bands at 1608 and 1705 cm^{-1} (for visualisation of normal modes cf. Fig. 6.4). Furthermore, regarding our calculations of the relative energies for all enol type isomers (cf. Fig. 6.1 and Table 6.1, SI), formation of CTC is energetically favored the most. Finally, judging from our excited-state vibrational mode calculations (cf. Fig. 6.7, SI), the marker bands in our experimental data do not reflect any excited-state species. Therefore, we identify the permanent positive late-time vibrational modes in ACN- d_3 (1585 and 1690 cm^{-1}) and in CHX (1605 and 1700 cm^{-1}) as characteristic marker bands of the ground-state CTC photoproduct that arises by rotation around the C=C double bond by 180°.

To scrutinise the isomerisation pathways from the CCC isomer towards formation of the CTC ground-state species upon photoexcitation, we focus on investigation of the elusive excited-state intermediary structure. While the associated vibrational marker bands in CHX appear to be lacking or are obscured by

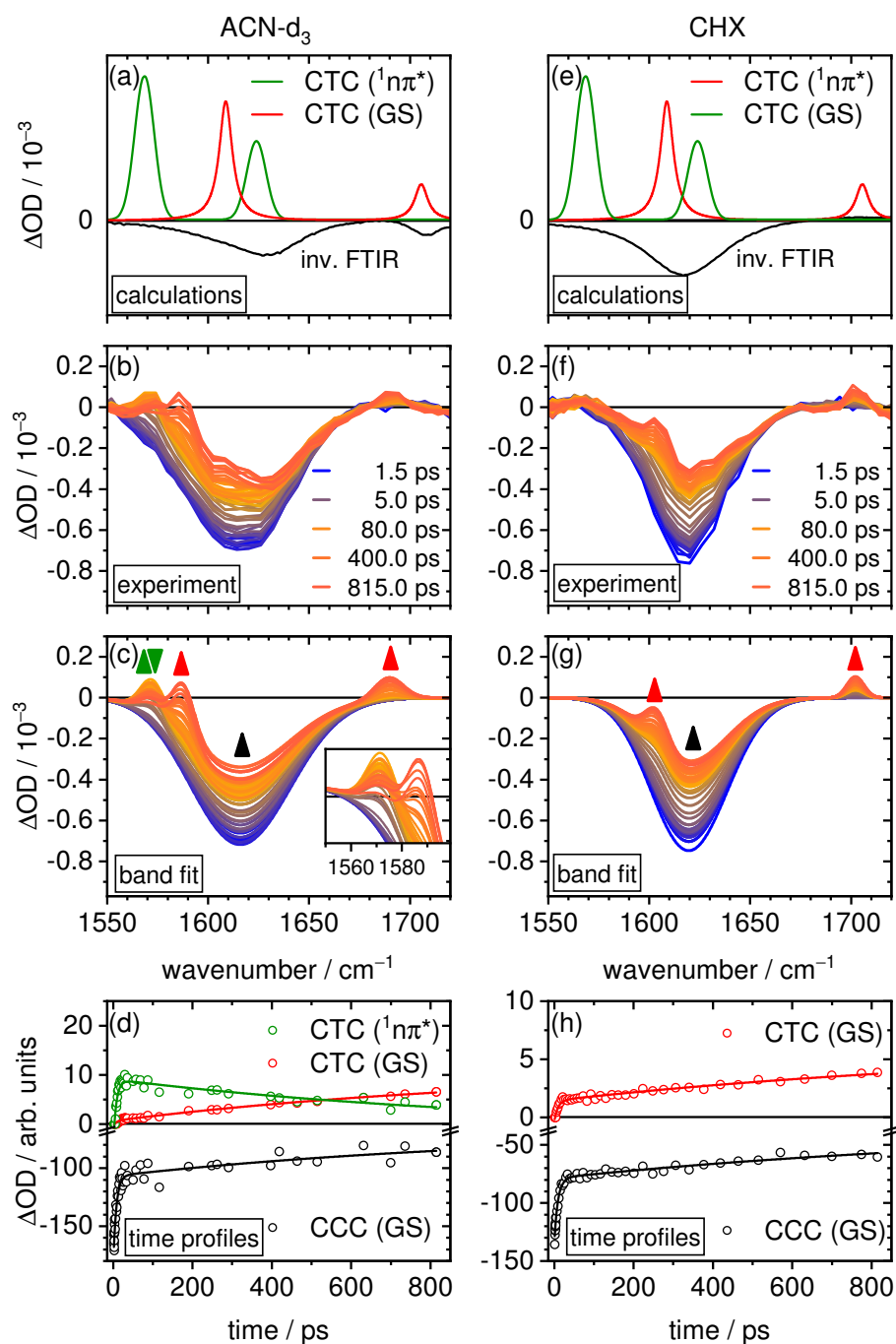


Figure 6.3: Transient vibrational absorption measurements of enol-type AA after excitation at $\lambda_{\text{exc}} = 267$ nm in ACN- d_3 (left) and CHX (right). Calculations: Computed vibrational spectra of CTC in the GS and in the $S_1(n\pi^*)$ state, respectively, alongside with the inverted experimental FTIR spectrum. Experiment: Recorded TVA spectra at different delay times. Band fit: Corresponding global Gaussian band fit to the experimental TVA spectra. Time profiles: Associated temporal evolution of CCC in the GS and of CTC in the GS as well as in the $S_1(n\pi^*)$ state, respectively.

the broad GSB, two specific vibrational marker bands are discernible in our TVA data in ACN-d₃. Here, the first band at 1570 cm⁻¹ appears well-isolated, while the second marker band at 1620 cm⁻¹ is less pronounced due to superposition with the GSB, but still distinctly manifested in the structured spectral shape of the latter. According to our excited-state calculations shown in Fig. 6.7 (SI), exclusively signals from the S₁(nπ*) state of the CTC isomer are expected in this spectral region, showcasing two vibrational marker bands at 1568 and at 1624 cm⁻¹ (cf. Fig. 6.4), in excellent agreement with the experimental findings. Thus, supported by our excited-state calculations displayed in green in Fig. 6.3(a, e), the excited-state intermediate species is identified as the CTC isomer in the S₁(nπ*) state.

To extract temporal information from the TVA data, the transient spectra were modelled simultaneously by a sum of Gaussian functions (cf. Fig. 6.3(c, g)). Corresponding time profiles for CCC (GS), CTC (GS) and CTC ¹nπ* were fitted to the experimental data using a sum of two exponentials in a global manner (cf. Fig. 6.3(d, h)). Thus, all time profiles could be described in a bi-exponential fashion by $\tau_{1(\text{ACN-d}_3)} = (8 \pm 1)$ ps and $\tau_{2(\text{ACN-d}_3)} = (900 \pm 600)$ ps and $\tau_{1(\text{CHX})} = (9 \pm 1)$ ps and $\tau_{2(\text{CHX})} = 1.25^{+1.60}_{-1.25}$ ns, respectively. As comparable time constants were retrieved by this analysis independent of the solvent used, similar deactivation and reaction pathways are expected.

Starting from $\Delta t = 1.5$ ps after photoexcitation to the prepared S₂(ππ*) state, the transient vibrational absorption spectra shown in Fig. 6.3 reflect the photodynamics after subsequent population of the intermediary S₁(nπ*) state via ultrafast IC. Here, highly non-equilibrated excited-state structures showing large amounts of excess energy are present. For both, the GSR of CCC and the product formation of CTC (GS), an effective rising component of $\tau_{1(\text{ACN-d}_3)} = (8 \pm 1)$ ps and $\tau_{1(\text{CHX})} = (9 \pm 1)$ ps was determined, indicating multi-modal dynamics including ultrafast electronic deactivation, vibrational cooling and structural rearrangement in the electronic GS (see time profiles in Fig. 6.3(d, h)). This short time constant is also found for the excited-state CTC intermediate at 1570 cm⁻¹ in ACN-d₃ and is thus attributed to vibrational cooling and structural rearrangement in the excited state. The vibrational signature of the CTC excited-state intermediate then decays within $\tau_{2(\text{ACN-d}_3)} = (900 \pm 600)$ ps and $\tau_{2(\text{CHX})} = 1.25^{+1.60}_{-1.25}$ ns concurrent with CTC (GS) product formation and GSR of CCC. Hence, τ_2 mirrors depopulation of the CTC species in the S₁(nπ*)

state and (re-)formation of the CCC and CTC ground-state reactant and product species, respectively.

Additionally, inferring from quantitative investigation of the time profile of CCC (GS), the permanent negative offset towards late delay times is indicative not only for CTC product formation, but also for intersystem crossing (ISC) to the triplet manifold. From our calculated intensities of the vibrational bands for CCC at 1645 and CTC at 1705 cm^{-1} (cf. Fig. 6.4 and Fig. 6.7, SI), a relative intensity ratio of 2:1 was determined. Comparing this ratio to the experimental initial GSB and the product intensity at late delay times, the CTC product yield in both solvents can roughly be estimated. From the GSR of CCC in ACN-d_3 ($\Phi_{\text{GS}(\text{ACN-d}_3)} \approx 0.58 \pm 0.05$, asymptotic offset), a CTC product yield of $\Phi_{\text{CTC}(\text{ACN-d}_3)} \approx 0.12 \pm 0.08$ is determined. Hence, the remaining fraction of the GSB is caused either by photo-induced fragmentation or by ISC to a triplet state. In order to exclude effects of photofragmentation on the GSB signal on the nanosecond time scale, we carried out vibrational mode calculations for all possible CCC photofragments (cf. SI, Fig. 6.8 and Fig. 6.9). Accordingly, no signs for fragmentation have been found in our TVA data. Thus, the remaining negative offset in the GSB, which remains unrelated to CTC product formation, is tentatively ascribed to triplet formation upon ISC, featuring a quantum yield of $\Phi_{\text{ISC}(\text{ACN-d}_3)} \approx 0.30 \pm 0.07$.

Analogous to our measurements in ACN-d_3 , the CTC product yield in CHX can also roughly be estimated. From the GSR of CCC ($\Phi_{\text{GS}(\text{CHX})} \approx 0.75 \pm 0.30$), a CTC product yield of $\Phi_{\text{CTC}(\text{CHX})} \approx 0.10 \pm 0.09$ was determined. The remaining permanent negative offset in the GSB of CCC is ascribed to ISC to a triplet state with $\Phi_{\text{ISC}(\text{CHX})} \approx 0.15 \pm 0.12$. Thus, despite an apparent lack of the excited-state spectro-temporal marker bands in CHX, the CTC product yield remains rather unaffected on the ultrafast time scale by the respective solvent. Note, however, as product formation is not completed within the experimentally accessible time window and the asymptotic fitting parameters are subject to the rather large error margins as given above, the exact values need to be obtained in more elaborate studies. A summary of the full spectro-temporal data analysis obtained from our TVA spectra in both solvents is given in Table 6.2 (SI).

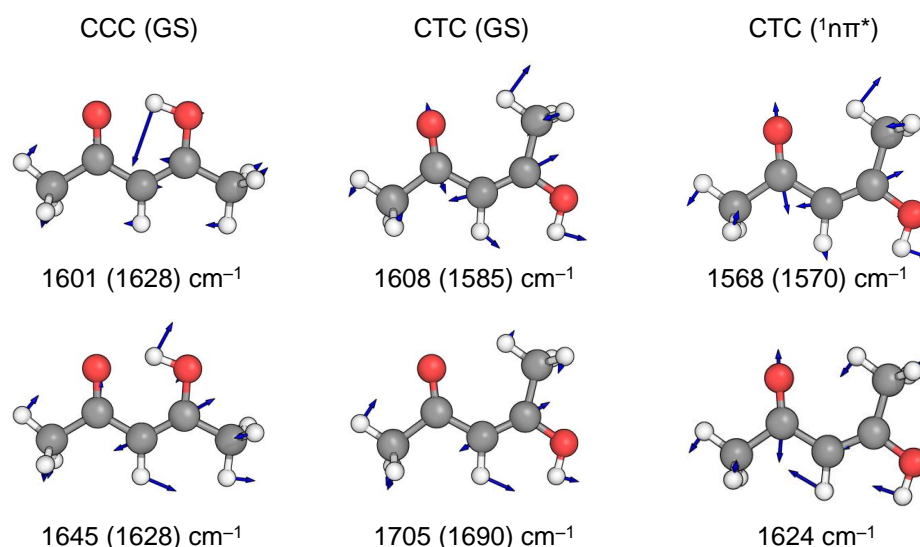


Figure 6.4: Calculated and experimental (ACN- d_3) vibrational marker modes of CCC and CTC in the GS as well as for CTC in the $S_1(n\pi^*)$ state. The calculated values are given first and are scaled by a factor of 0.98 for the GS and by 0.955 for the excited states. Experimental values are given in parenthesis. The calculated band at 1624 cm^{-1} for the CTC species in the $S_1(n\pi^*)$ state was hardly to be observed experimentally. Thus, the corresponding value is missing.

6.4 Discussion

The time-resolved vibrational experiments on the CCC isomer of enol-type AA provide new insights into its ultrafast dynamics after UV-photoexcitation and the ensuing electronic deactivation and isomerisation dynamics. Already in 1977, photo-induced isomerisation to non-chelated enol forms in the liquid phase was proposed by Veierov and co-workers.³¹ They investigated a number of β -diketones by flash photolysis, but as their methods were lacking structure sensitivity, it was impossible to distinguish between different non-chelated isomers at that time. Here, combining structure-sensitive TVAS and quantum chemical calculations, we identified the exclusive photoproduct as the CTC isomer which is formed via *cis-trans* isomerisation around the $\text{C}=\text{C}$ double bond on a bi-exponential time scale. The distinct relaxation and *cis-trans* isomerisation pathways on the specific time scales towards CTC (GS) formation are discussed in the following.

Ground-state recovery of CCC and product formation of CTC

A theoretical study by Delchev and Shterev²⁴ at the CC2/aug-cc-pVDZ level of theory predicted a barrier-free pathway via a conical intersection (CI) connecting the initially excited $S_2(\pi\pi^*)$ state with the GS. The computed molecular structure at the $CI_{1\pi\pi^*/GS}$ showed a significant elongation of the O–H distance accompanied by rotation around the C=C double bond by 90° . Proceeding from the CI, both CCC (GS) and CTC (GS) isomers can be formed via subsequent rotation by $\pm 90^\circ$. Furthermore, the authors precluded accessibility to other conical intersections for ground-state recovery via rotation around the C–C or the C–O bond. Accordingly, judging from our TVA data, a fraction of the initially excited molecules is subject to ultrafast electronic deactivation to the electronic GS accompanied by vibrational relaxation processes towards (re-)formation of the CCC (GS) and CTC (GS) isomers within $\tau_{1(ACN-d_3)} \approx 8$ ps and $\tau_{1(CHX)} \approx 9$ ps, respectively. This is in good agreement with measurements of an AA-Al complex, where GSR within ~ 10 ps was observed experimentally.¹⁸

Furthermore, an excited-state intramolecular proton transfer (ESIPT) followed by rapid internal conversion to the $S_1(n\pi^*)$ takes place within ~ 2 ps after excitation of enolic CCC to the initially prepared $S_2(\pi\pi^*)$ state as reported by Verma and co-workers.¹⁸ Following the spectro-temporal signatures in our TVA data, the excited-state population appears to be incapable of accessing a direct pathway for GSR and is thus trapped in a local minimum once on the $S_1(n\pi^*)$ potential energy surface. The same finding was recently reported in the literature, where AA was investigated in the gas phase by photoelectron spectroscopy.¹⁷ After overcoming a potential energy barrier in the $S_1(n\pi^*)$ state towards GSR within $\tau_{2(ACN-d_3)} \approx 900$ ps and $\tau_{2(CHX)} \approx 1250$ ps, excited-state depopulation followed by (re-)formation of the CCC (GS) and CTC (GS) isomers, respectively, is observed.

In summary, formation of the long-lived CTC (GS) photoproduct proceeds via two distinct dynamic pathways on the picosecond (~ 15 % via direct $1\pi\pi^*/GS$ deactivation) and nanosecond (~ 85 % via $1n\pi^*/GS$ deactivation) time scales, respectively (cf. Table 6.2, SI). Our results further suggest the exclusive formation of CTC (GS) on the ultrafast time scale as no transient signals of other enolic AA isomers were detected. This is supported by TEAS measurements on AA,¹⁸

where photoproduct absorption observed at ~ 250 nm pointed at formation of CTC (GS) and/or CTT (GS), as all other isomers of AA feature blue-shifted absorption bands towards 230 nm.^{23,29,66}

Excited-state structures in the $S_1(n\pi^*)$ state and intersystem crossing

From our TVA data, an excited-state intermediate was unambiguously observed in ACN- d_3 . Aided by the ab initio vibrational frequency calculations, this intermediate was identified as the CTC isomer in the $S_1(n\pi^*)$ state. Consequently, rotation around the C=C double bond already occurs in the excited state within $\tau_1 \approx 8$ ps as proposed previously.^{17–19,21,67–69}

In contrast, virtually no vibrational marker bands for the excited-state CTC $S_1(n\pi^*)$ isomer were observed in our TVA data in CHX solution. Still, the temporal evolution of CTC (GS) product formation proceeds essentially unchanged compared to the dynamics in ACN- d_3 , indicating similar deactivation dynamics in both solvents. However, while the involved electronically excited states seem to remain unaltered, the associated molecular structures clearly appear to be highly specific to the solvent used. Hence, we propose an intricate equilibrium between the CCC and CTC isomers in the $S_1(n\pi^*)$ state, which is affected by the strength of the intramolecular hydrogen bonding in the respective solvent used. While ACN- d_3 as a polar solvent appears to stabilise the rotated CTC $S_1(n\pi^*)$ intermediate in the excited state by weakening the intramolecular hydrogen bond, a considerable amount of the excited-state population in CHX is likely to retain the CCC structural motif after IC from the $S_2(\pi\pi^*)$ to the $S_1(n\pi^*)$ state. According to our excited-state calculations, the corresponding vibrational marker bands of CCC in the $S_1(n\pi^*)$ state are shifted out of our detection window (cf. Fig. 6.7, SI). Thus, the intermediary excited-state species in CHX is solely manifested in the temporal evolution for CTC (GS) photoproduct formation in the spectral region under investigation.

This proposed excited-state equilibrium in the $S_1(n\pi^*)$ state is corroborated by TEAS measurements of the unsymmetrical benzoylacetone,¹⁹ where an excited-state intermediate was observed, whose signal intensity also showed strong dependence on the solvent. In accordance with our findings for AA, almost no

excited-state absorption of the intermediate was detectable in *n*-hexane, whereas it was very pronounced in ACN and DMSO.

To elucidate the intersystem crossing pathways originating from the intermediary $S_1(n\pi^*)$ state, we performed geometry optimisations and vibrational mode calculations for the triplet manifold. As reported in the literature,^{16,21,30} the order of the $^3\pi\pi^*$ and $^3n\pi^*$ energies varies for the CCC and CTC structures, and they become nearly degenerate as electronic deactivation proceeds. While our computations converged for the lowest triplet-state minimum structures $T_1(\pi\pi^*)_{\text{CCC}}$ and $T_1(n\pi^*)_{\text{CTC}}$, (cf. Fig. 6.7, SI), attempts failed for optimisation of higher-lying triplet states due to strong multi-configurational characters at the RI-SCS-CC2/def2-TZVPP level of theory. Therefore, we performed single point calculations of the GS, $S_1(n\pi^*)$, $S_2(\pi\pi^*)$, $T_1(\pi\pi^*/n\pi^*)$ and $T_2(n\pi^*/\pi\pi^*)$ states for the CCC and CTC isomers at the converged minimum structures in the GS, $S_1(n\pi^*)$ and $T_1(\pi\pi^*/n\pi^*)$ states, respectively (cf. Fig. 6.10, SI). Most strikingly, the electronic energies for the triplet states become virtually iso-energetic [$E(^3\pi\pi^*)_{\text{CCC}} = 3.70$ eV, $E(^3n\pi^*)_{\text{CCC}} = 3.84$ eV] with one another and with the electronic energy of the $S_1(n\pi^*)$ state [$E(^1n\pi^*)_{\text{CCC}} = 3.82$ eV] at the $S_1(n\pi^*)$ minimum structure of the CCC isomer. Similar results were obtained for the CTC isomer at the $S_1(n\pi^*)$ minimum structure [$E(^1n\pi^*)_{\text{CTC}} = 4.66$ eV, $E(^3n\pi^*)_{\text{CTC}} = 4.42$ eV and $E(^3\pi\pi^*)_{\text{CTC}} = 4.43$ eV]. Thus, we tentatively propose an El-Sayed allowed intersystem crossing⁷⁰ originating from the intermediary $S_1(n\pi^*)$ state either directly to the $T_1(\pi\pi^*)$ state or to the $T_2(\pi\pi^*)$ state followed by barrierless ultrafast IC to the $T_1(n\pi^*)$ state, which is observed indirectly by a permanent negative offset in the GSB of CCC (GS) at late times. Triplet relaxation and ISC back to the electronic GS typically take place on the microsecond-to-millisecond time scales, which are not accessible to our ultrafast time-resolved experiment.

All in all, the described processes and time components are in nice agreement with previous transient electronic absorption measurements.^{18,19} The evidently formed photoproduct was identified as the ground-state CTC isomer, and the excited-state intermediate as the CTC isomer in the $S_1(n\pi^*)$ state. Our results highlight the influence of the solvent as well as the complexity of photo-induced processes even for small molecules like AA. Derived from our results, the proposed relaxation mechanism for enol-type AA is illustrated in Fig. 6.5.

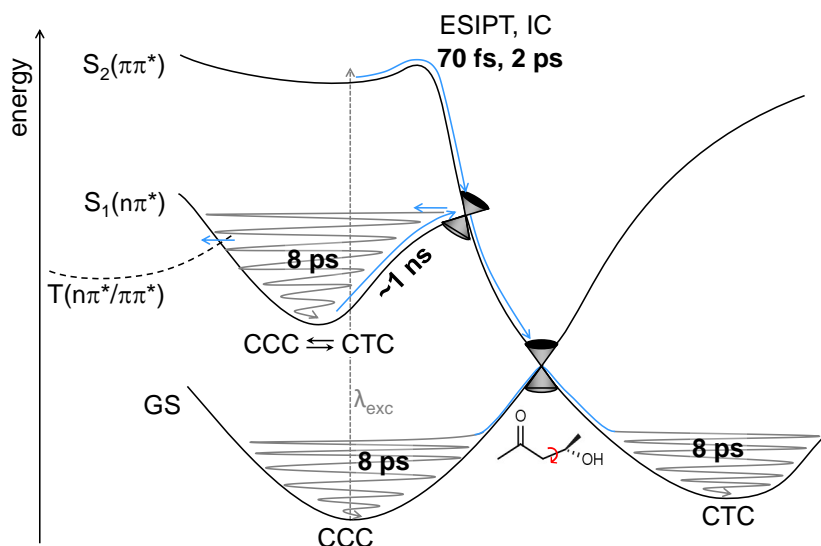


Figure 6.5: Proposed electronic deactivation and *cis-trans* isomerisation dynamic pathways for enol-type AA in the liquid phase after UV-photoexcitation. ESIPT and ultrafast internal conversion processes within the first two picoseconds following $S_2(\pi\pi^*)$ excitation have been studied elsewhere.¹⁸

6.5 Conclusions

We reported on the successive ultrafast electronic relaxation and isomerisation dynamics of the enolic tautomer of acetylacetone after excitation at $\lambda_{exc} = 267$ nm in cyclohexane and in deuterated acetonitrile as solvents. The ensuing processes were probed by femtosecond time-resolved vibrational absorption spectroscopy (TVAS), which allowed for chemical structure-sensitive detection. Aided by quantum chemical DFT and ab initio calculations of ground-state and excited-state isomers, our results provided new insights and a more detailed understanding of the dynamic processes after UV-photoexcitation of AA in the liquid phase. Following excitation to the bright $S_2(\pi\pi^*)$ state, several relaxation channels are identified: (i) We observed ground-state recovery of the initially excited enolic CCC (GS) isomer, and formation of a long-lived photoproduct via two distinct pathways on the picosecond and nanosecond time scales via direct $^1\pi\pi^*/GS$ and $^1n\pi^*/GS$ deactivation, respectively. The photoproduct was identified as the previously proposed, but to date elusive *cis-trans-cis* (CTC) enolic form of AA in the electronic ground state that arises after *cis-trans* isomerisation around the C=C double bond already prior to return of the electronic GS. (ii)

Intersystem crossing from the intermediary $S_1(n\pi^*)$ state to the triplet manifold was found to take place within ~ 1 ns. Further, the solvent effect on an excited-state equilibrium between transient CCC and CTC species in the $S_1(n\pi^*)$ state was discussed. Finally, no evidence for formation of other enol-type isomers or photo-induced fragmentation of AA was found in solution, although this is an important channel in the gas phase.

References

- (1) Tayyari, S. F.; Zeegers-Huyskens, T.; Wood, J. L. *Spectrochim. Acta* **1979**, 35A, 1289–1295.
- (2) Folkendt, M. M.; Weiss-Lopez, B. E.; Chauvel, J. P.; True, N. S. *J. Phys. Chem.* **1985**, 89, 3347–3352.
- (3) Nakanishi, H.; Morita, H.; Nagakura, S. *Bull. Chem. Soc. Jpn.* **1977**, 50, 2255–2261.
- (4) Hush, N. S.; Livett, M. K.; Peel, J. B.; Willett, G. D. *Aust. J. Chem.* **1987**, 40, 599–609.
- (5) Emsley, J.; Freeman, N. J. *J. Mol. Struct.* **1987**, 161, 193–204.
- (6) Hibbert, F.; Emsley, J. *Adv. Phys. Org. Chem.* **1990**, 26, 255–379.
- (7) Dannenberg, J. J.; Rios, R. *J. Phys. Chem.* **1994**, 98, 6714–6718.
- (8) Howard, D. L.; Kjaergaard, H. G.; Huang, J.; Meuwly, M. *J. Phys. Chem. A* **2015**, 119, 7980–7990.
- (9) Srinivasan, R.; Feenstra, J. S.; Park, S. T.; Xu, S.; Zewail, A. H. *J. Am. Chem. Soc.* **2004**, 126, 2266–2267.
- (10) Caminati, W.; Grabow, J.-U. *J. Am. Chem. Soc.* **2006**, 128, 854–857.
- (11) Broadbent, S. A.; Burns, L. A.; Chatterjee, C.; Vaccaro, P. H. *Chem. Phys. Lett.* **2007**, 434, 31–37.
- (12) Yoon, M.-C.; Choi, Y. S.; Kim, S. K. *J. Chem. Phys.* **1999**, 110, 11850–11855.
- (13) Upadhyaya, H. P.; Kumar, A.; Naik, P. D. *J. Chem. Phys.* **2003**, 118, 2590–2598.
- (14) Xu, S.; Park, S. T.; Feenstra, J. S.; Srinivasan, R.; Zewail, A. H. *J. Phys. Chem. A* **2004**, 108, 6650–6655.
- (15) Poisson, L.; Roubin, P.; Coussan, S.; Soep, B.; Mestdag, J. M. *J. Am. Chem. Soc.* **2008**, 130, 2974–2983.
- (16) Bhattacharjee, A.; Pemmaraju, C. D.; Schnorr, K.; Attar, A. R.; Leone, S. R. *J. Am. Chem. Soc.* **2017**, 139, 16576–16583.

- (17) Squibb, R. J.; Sapunar, M; Ponzi, A; Richter, R; Kivimäki, A; Plekan, O; Finetti, P; Sisourat, N; Zhaunerchyk, V; Marchenko, T; Journal, L; Guillemain, R; Cucini, R; Coreno, M; Grazioli, C; Fraia, M. D.; Callegari, C; Prince, K. C.; Decleva, P; Simon, M; Eland, J. H. D.; Doslic, N; Feifel, R; Piancastelli, M. N. *Nat. Commun.* **2018**, *9*, 1–7.
- (18) Verma, P. K.; Koch, F.; Steinbacher, A.; Nuernberger, P.; Brixner, T. *J. Am. Chem. Soc.* **2014**, *136*, 14981–14989.
- (19) Verma, P. K.; Steinbacher, A.; Koch, F.; Nuernberger, P.; Brixner, T. *Phys. Chem. Chem. Phys.* **2015**, *17*, 8459–8466.
- (20) Sarkar, S. K.; Weragoda, G. K.; Ranaweera, R. A. A. U.; Gudmundsdottir, A. D. *J. Phys. Chem. B* **2015**, *119*, 2668–2676.
- (21) Chen, X.-B.; Fang, W.-H.; Phillips, D. L. *J. Phys. Chem. A* **2006**, *110*, 4434–4441.
- (22) Xie, B.; Cui, G.; Fang, W.-H. *J. Chem. Theory Comput.* **2017**, *13*, 2717–2729.
- (23) Coussan, S; Ferro, Y; Trivella, A; Rajzmann, M; Roubin, P; Wieczorek, R; Manca, C; Piecuch, P; Kowalski, K; Włoch, M; Kucharski, S. A.; Musiał, M *J. Phys. Chem. A* **2006**, *110*, 3920–3926.
- (24) Delchev, V. B.; Shterev, I. G. *Comp. Theor. Chem.* **2011**, *967*, 152–159.
- (25) Zhou, S.; Barnes, I.; Zuh, T.; Bejan, I.; Albu, M.; Benter, T. *Environ. Sci. Technol.* **2008**, *42*, 7905–7910.
- (26) Gutierrez-Quintanilla, A.; Chevalier, M.; Crepin, C. *Phys. Chem. Chem. Phys.* **2016**, *18*, 20713–20725.
- (27) Lozada-Garcia, R. R.; Ceponkus, J.; Chevalier, M.; Chin, W.; Mestdagh, J.-M.; Crépin, C. *Phys. Chem. Chem. Phys.* **2012**, *14*, 3450–3459.
- (28) Nagashima, N.; Kudoh, S.; Takayanagi, M.; Nakata, M. *J. Phys. Chem. A* **2001**, *105*, 10832–10838.
- (29) Trivella, A; Roubin, P; Theule, P; Rajzmann, M; Coussan, S; Manca, C *J. Phys. Chem. A* **2007**, *111*, 3074–3081.
- (30) Trivella, A; Wassermann, T. N.; Mestdagh, J.-M.; Manca Tanner, C; Marinelli, F; Roubin, P; Coussan, S *Phys. Chem. Chem. Phys.* **2010**, *12*, 8300–8310.

- (31) Veierov, D; Bercovici, T; Fischer, E; Mazur, Y; Yogev, A *J. Am. Chem. Soc.* **1977**, *99*, 2723–2729.
- (32) Böhnke, H.; Bahrenburg, J.; Ma, X.; Röttger, K.; Näther, C.; Rode, M. F.; Sobolewski, A. L.; Temps, F. *Phys. Chem. Chem. Phys.* **2018**, *20*, 2646–2655.
- (33) Hamm, P.; Kaindl, R. A.; Stenger, J. *Opt. Lett.* **2000**, *25*, 1798–1800.
- (34) Kaindl, R. A.; Wurm, M.; Reimann, K.; Hamm, P.; Weiner, A. M.; Woerner, M. *J. Opt. Soc. Am. B* **2000**, *17*, 2086–2094.
- (35) Grubbs, M.; Orr-Ewing, A. J.; Ashfold, M. N. R. *Rev. Sci. Instrum.* **2014**, *85*, 064104.
- (36) Lee, C.; Yang, W.; Parr, R. G. *Phys. Rev. B* **1988**, *37*, 785–789.
- (37) Miehlisch, B.; Savin, A.; Stoll, H.; Preuss, H. *Chem. Phys. Lett.* **1989**, *157*, 200–206.
- (38) Becke, A. D. *Phys. Rev. A* **1988**, *38*, 3098–3100.
- (39) Becke, A. D. *J. Chem. Phys.* **1993**, *98*, 5648–5652.
- (40) Grimme, S.; Antony, J.; Ehrlich, S.; Krieg, H. *J. Chem. Phys.* **2010**, *132*, 154104.
- (41) Clark, T.; Chandrasekhar, J.; Spitznagel, G. W.; Von Rague Schleyer, P. J. *Comput. Chem.* **1983**, *4*, 294–301.
- (42) Frisch, M. J.; Pople, J. A.; Binkley, J. S. *J. Chem. Phys.* **1984**, *80*, 3265–3269.
- (43) McLean, A. D.; Chandler, G. *J. Chem. Phys.* **1980**, *72*, 5639–5648.
- (44) Krishnan, R; Binkley, J. S.; Seeger, R; Pople, J. A. *J. Chem. Phys.* **1980**, *72*, 650–654.
- (45) Frisch, M. J.; Trucks, G. W.; Schlegel, H. B.; Scuseria, G. E.; Robb, M. A.; Cheeseman, J. R.; Scalmani, G; Barone, V; Mennucci, B; Petersson, G. A.; Nakatsuji, H; Caricato, M; Li, X; Hratchian, H. P; Izmaylov, A. F; Bloino, J; Zheng, G; Sonnenberg, J. L.; Hada, M; Ehara, M; Toyota, K; Fukuda, R; Hasegawa, J; Ishida, M; Nakajima, T; Honda, Y; Kitao, O; Nakai, H; Vreven, T; Montgomery, J. A.; Peralta, J. E.; Ogliaro, F; Bearpark, M; Heyd, J. J.; Brothers, E; Kudin, K. N.; Staroverov, V. N.; Kobayashi, R; Normand, J; Raghavachari, K; Rendell, A; Burant, J. C.; Iyengar, S. S.; Tomasi, J; Cossi,

- M; Rega, N; Millam, J. M.; Klene, M; Knox, J. E.; Cross, J. B.; Bakken, V; Adamo, C; Jaramillo, J; Gomperts, R; Stratmann, R. E.; Yazyev, O; Austin, A. J.; Cammi, R; Pomelli, C; Ochterski, J. W.; Martin, R. L.; Morokuma, K; Zakrzewski, V. G.; Voth, G. A.; Salvador, P; Dannenberg, J. J.; Dapprich, S; Daniels, A. D.; Farkas; Foresman, J. B.; Ortiz, J. V.; Cioslowski, J; Fox, D. J., *Gaussian 09, Revision D.01*, Gaussian Inc., Wallingford CT, 2013.
- (46) Weigend, F.; Häser, M. *Theor. Chem. Acc.* **1997**, 97, 331–340.
- (47) Weigend, F.; Häser, M.; Patzelt, H.; Ahlrichs, R. *Chem. Phys. Lett.* **1998**, 294, 143–152.
- (48) Hättig, C.; Hellweg, A.; Köhn, A. *Phys. Chem. Chem. Phys.* **2006**, 8, 1159–1169.
- (49) Hellweg, A.; Grün, S. A.; Hättig, C. *Phys. Chem. Chem. Phys.* **2008**, 10, 4119–4127.
- (50) Weigend, F.; Ahlrichs, R. *Phys. Chem. Chem. Phys.* **2005**, 7, 3297–3305.
- (51) Grimme, S. *J. Chem. Phys.* **2006**, 124, 0341108.
- (52) Grimme, S.; Ehrlich, S.; Goerigk, L. *J. Comput. Chem.* **2011**, 32, 1456–1465.
- (53) Weigend, F.; Furche, F.; Ahlrichs, R. *J. Chem. Phys.* **2003**, 119, 12753–12762.
- (54) Weigend, F. *Phys. Chem. Chem. Phys.* **2006**, 8, 1057–1065.
- (55) Goerigk, L.; Kruse, H.; Grimme, S. *Chem. Phys. Chem.* **2011**, 12, 3421–3433.
- (56) Goerigk, L.; Hansen, A.; Bauer, C.; Ehrlich, S.; Najibi, A.; Grimme, S. *Phys. Chem. Chem. Phys.* **2017**, 19, 32184–32215.
- (57) TURBOMOLE V7.0 2015, a development of University of Karlsruhe and Forschungszentrum Karlsruhe GmbH, 1989-2007 TURBOMOLE GmbH, since 2007; available from <http://www.turbomole.com>.
- (58) Hättig, C.; Weigend, F. *J. Chem. Phys.* **2000**, 113, 5154–5161.
- (59) Hättig, C.; Hald, K. *Phys. Chem. Chem. Phys.* **2002**, 4, 2111–2118.
- (60) Hättig, C. *J. Chem. Phys.* **2003**, 118, 7751–7761.
- (61) Hättig, C.; Köhn, A. *J. Chem. Phys.* **2002**, 117, 6939–6951.

- (62) Hättig, C.; Köhn, A.; Hald, K. *J. Chem. Phys.* **2002**, *116*, 5401–5410.
- (63) Frieze, D. H.; Törk, L.; Hättig, C. *J. Chem. Phys.* **2014**, *141*, 194106.
- (64) Irikura, K. K.; Johnson III, R. D.; Kacker, R. N. *J. Phys. Chem. A* **2005**, *109*, 8430–8437.
- (65) Andersson, M. P.; Uvdal, P. *J. Phys. Chem. A* **2005**, *109*, 2937–2941.
- (66) Veierov, D.; Bercovici, T.; Fisher, E.; Mazur, Y.; Yogev, A. *J. Am. Chem. Soc.* **1973**, *95*, 8173–8175.
- (67) Kobayashi, A.; Yamaji, M.; Nakajima, S.; Akiyama, K.; Tero-Kubota, S.; Kato, S.; Nakamura, Y. *Chem. Phys. Lett.* **2013**, *555*, 101–105.
- (68) Sobolewski, A. L.; Domcke, W. *J. Phys. Chem. A* **1999**, *103*, 4494–4504.
- (69) Tobita, S.; Ohba, J.; Nakagawa, K.; Shizuka, H. *J. Photoch. Photobio. A* **1995**, *92*, 61–67.
- (70) El-Sayed, M. A. *J. Chem. Phys.* **1963**, *38*, 2834–2838.

6.6 Supporting Information

Table 6.1: Calculated relative energies of the different enol isomers of AA in the electronic ground state at the different levels of theory with respect to the thermodynamically stable CCC isomer.

isomer	B2PLYP-D3(BJ)/ def2-QZVP/ kJ / mol	RI-SCS-MP2/ def2-TZVPP/ kJ / mol	B3LYP-D3/ 6-311++G**/ kJ / mol
CCC	0	0	0
CTC	46	42	44
CTT	49	45	47
TCC	52	46	51
TCT	56	49	54
TTC	58	53	57
CCT	65	58	66
TTT	68	63	68

Table 6.2: Decay times τ_i and relative amplitudes A_i from global analysis of the TVAS data after excitation at $\lambda_{\text{exc}} = 267$ nm in ACN-d₃ and CHX. Error limits refer to 95 % confidence interval.

		τ_1 / ps	A_1 / %	τ_2 / ns	A_1 / %
	CCC (GS)	8 ± 1	63 ± 3.0	0.9 ± 0.6	37 ± 18
ACN-d ₃	CTC (¹ n π^*)	8 ± 1	54 ± 15	0.9 ± 0.6	46 ± 8.0
	CTC (GS)	8 ± 1	8^{+22}_{-8}	0.9 ± 0.6	92 ± 70
CHX	CCC (GS)	9 ± 1	53 ± 2.0	$1.25^{+1.60}_{-1.25}$	47 ± 43
	CTC (GS)	9 ± 1	25 ± 23	$1.25^{+1.60}_{-1.25}$	75 ± 20

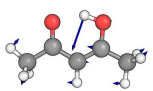
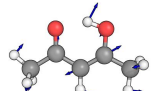
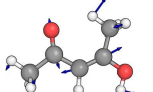
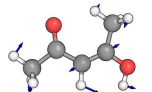
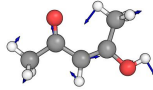
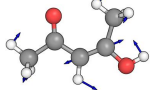
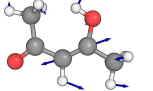
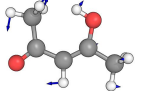

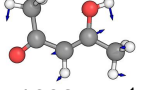
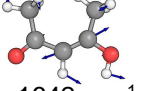





CCC	 1601 (1628) cm^{-1}	 1645 (1528) cm^{-1}
CTC	 1608 (1585) cm^{-1}	 1705 (1690) cm^{-1}
CTT	 1630 cm^{-1}	 1707 cm^{-1}
TCC	 1637 cm^{-1}	 1682 cm^{-1}
TCT	 1675 cm^{-1}	 1682 cm^{-1}
TTC	 1642 cm^{-1}	 1672 cm^{-1}
CCT	 1640 cm^{-1}	 1721 cm^{-1}
TTT	 1666 cm^{-1}	 1673 cm^{-1}

Figure 6.6: Calculated and experimental (in ACN- d_3) vibrational marker modes of all enol isomers of AA in the GS in the spectral range of 1600–1750 cm^{-1} . The calculated values are given first and are scaled by a factor of 0.98. Experimental values obtained from the steady-state FTIR spectrum are given in parenthesis.

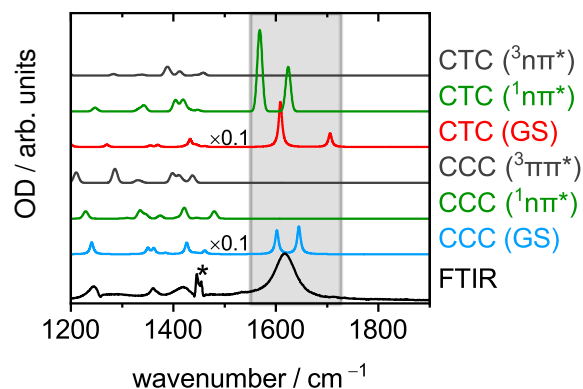


Figure 6.7: Calculated vibrational spectra in the GS (B3LYP D3/6 311++G**), $S_1(n\pi^*)$ and $T_1(\pi\pi^*)/T_1(n\pi^*)$ excited states (RI-SCS-CC2/def2-TZVPP) in the spectral range of 1200–1900 cm^{-1} for the CCC and CTC isomers, respectively. For better comparison, the intensities of the bands in the GS are scaled by a factor of 0.1. The experimental FTIR spectrum of CCC in CHX is shown in black.

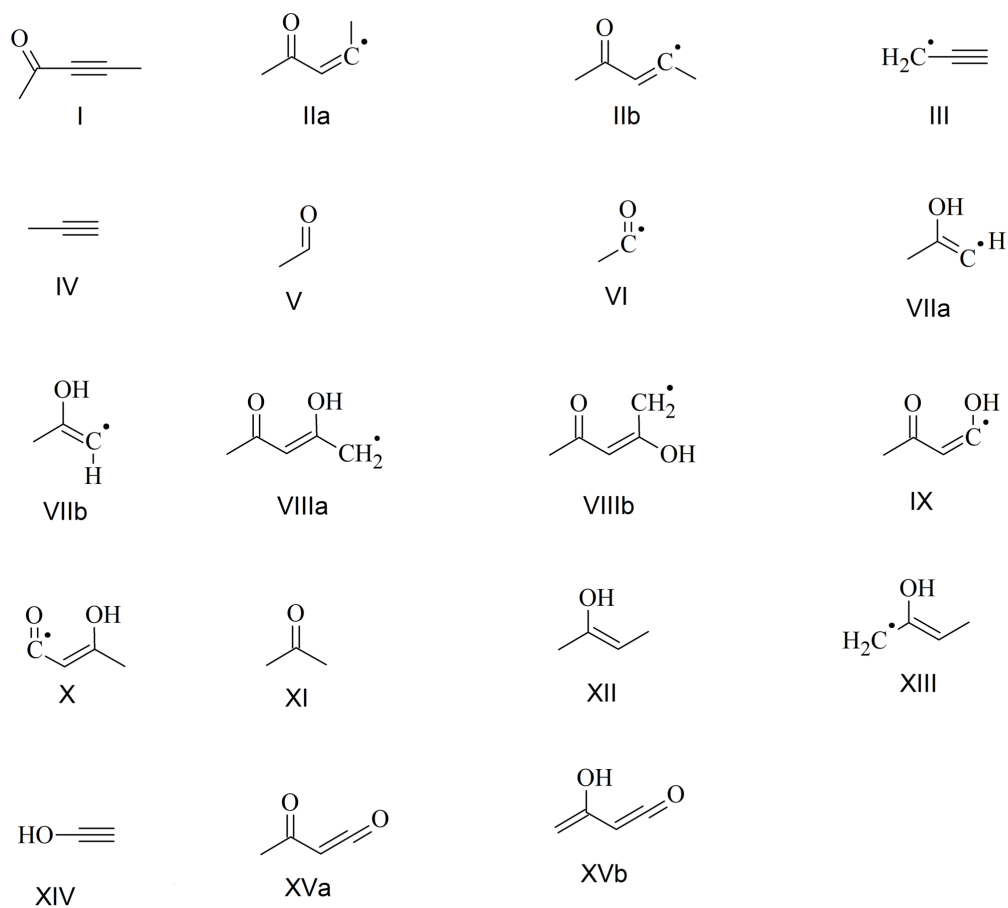


Figure 6.8: Structural representation of possible photofragments upon UV photoexcitation of enol-type CCC.

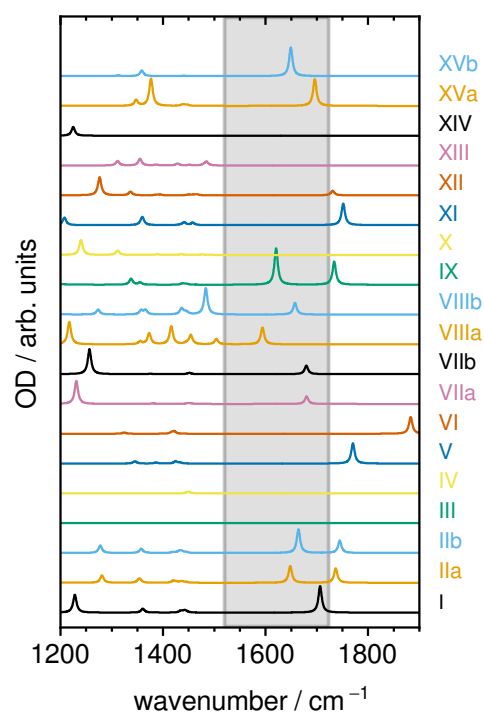


Figure 6.9: Vibrational calculations for all possible CCC photofragments displayed in Fig.6.8 at the B3LYP-D3/6-311++G** level of theory.

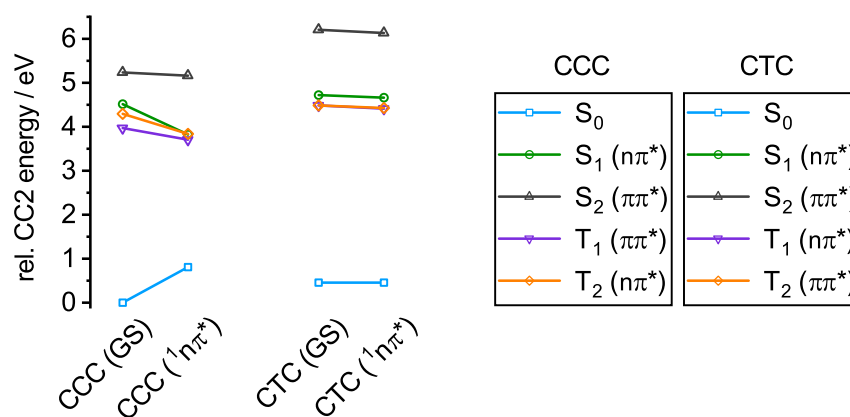


Figure 6.10: Single point calculations of the GS, $S_1(n\pi^*)$, $S_2(\pi\pi^*)$, $T_1(\pi\pi^*/n\pi^*)$ and $T_2(n\pi^*/\pi\pi^*)$ states for the CCC and CTC isomers at the converged minimum structures in the GS and $S_1(n\pi^*)$ states, respectively.

Spectroscopic and theoretical study on the ultrafast deactivation dynamics and dual fluorescence of methyl salicylate

REBECCA HOLTSMANN, JORUNN FUCHS, SEBASTIAN SCHATZ AND FRIEDRICH TEMPS

Institute of Physical Chemistry, Christian-Albrechts-University Kiel, Olshausenstr. 40, D-24098 Kiel, Germany.

Manuscript in preparation.

OWN CONTRIBUTIONS TO THIS MANUSCRIPT:

- Steady-state UV/vis, fluorescence and FTIR spectroscopy,
- quantum chemical calculations,
- time-correlated single photon counting measurements,
- femtosecond time-resolved fluorescence up-conversion,
- femtosecond time-resolved vibrational absorption spectroscopy,
- analyses of all experimental data,
- writing of the manuscript.

Abstract

Methyl salicylate (MS) exhibits dual fluorescence, but the underlying mechanism and the electronic deactivation pathways in the liquid phase are still poorly understood. For MS two rotamers, namely MS I and MS II, can in principle coexist in the electronic ground state (GS). Although both are stabilised by an intramolecular hydrogen bond, MS I represents the thermodynamically stable rotamer. Whether rotamer MS II contributes to the observed fluorescence remains unclear. To elucidate the photo-induced dynamics, we used various time-resolved spectroscopic techniques: time-correlated single photon counting, fluorescence spectroscopy by the up-conversion technique and electronic absorption spectroscopy. Furthermore, we combined transient vibrational absorption spectroscopy as a structure-sensitive method and quantum chemical calculations to unambiguously identify the involved molecular species. After S_1 photoexcitation of MS I, an ultrafast excited-state intramolecular proton transfer (ESIPT) takes place within $\tau_1 \leq 100$ fs. Subsequently, vibrational cooling of the proton-transferred species towards the S_1 minimum occurs with $\tau_2 = 5\text{--}8$ ps which is followed by radiative and non-radiative relaxation back to the GS. Concurrently, formation of a photoproduct is observed. The latter is identified as rotamer MS II in its electronic GS that arises by an internal rotational motion of 180° of the ester moiety. Our results further reveal that the lifetime of the S_1 state is solvent-dependent with $\tau_{3,\text{ACN}} \approx 115$ ps and $\tau_{3,\text{CHX}} \approx 300$ ps. Additionally, our data suggest that a minor fraction of the excited-state population reaches the triplet state. In solution, rotamer MS II coexists in very small amounts in the electronic GS and gives rise to fluorescence in the near-UV. While the dynamics of MS I are governed by ultrashort processes, MS II features a significantly longer excited-state lifetime of $\tau_{\text{MS II}} \approx 1.15$ ns. This study underlines that experimental limitations can be overcome by purposefully combining theoretical and experimental methods. In this way, new insights and a deep understanding of the photo-induced dynamics of MS are provided step by step.

7.1 Introduction

Methyl salicylate (MS) shows two distinctly separated emission bands located in the near-UV at 340 nm and in the visible region at 450 nm. Although its

remarkable fluorescence was already discovered in 1910,¹ it lasted almost 50 years until Weller was the first to propose a proton transfer in the excited state.² This excited-state intramolecular proton transfer (ESIPT) was assumed to be responsible for the experimentally observed pronounced Stokes shift of the fluorescence at 450 nm.^{2,3} Since the pioneering work of Weller, many experimental and theoretical studies on the emission properties as well as on the electronic deactivation pathways of MS and its derivatives have been published.^{4–24} In principle, two rotamers of MS, shown in Fig. 7.1, may coexist in the electronic ground state (GS). Both rotamers are stabilised by an intramolecular hydrogen bond.

Meanwhile, different notations have been used in the literature for these rotamers.^{12–14,18,19,25} Among others, Zhou et al.¹⁸ as well as Law and Shoham¹³ denoted the form, when the methoxy oxygen (–OMe) of the carboxyl function (–COOMe) points to the phenolic OH-group, as rotamer A. The form, when the carbonyl group (C=O) of the carboxyl function (–COOMe) is oriented to the phenol-OH, is labelled as rotamer B. Clearly, the latter is supposed to be the thermodynamically stable one in the gas phase. In contrast, the notation for those rotamers is used vice versa by other authors e.g., Herek et al.¹² and Douhal et al.¹⁴ Thus, to obtain a clear and logical labelling in this paper, we name the thermo stable species “rotamer MS I” and the next one “rotamer MS II” as shown in Fig. 7.1.

In our labelling, rotamer MS I, where the phenolic hydrogen binds intramolecularly via H-bonding to the carbonyl group of the ester moiety, corresponds to the thermodynamically more stable form of MS in the GS. Rotamer MS II arises by an internal rotation of 180° of the ester group and is located about 2.51 kcal/mol (10.5 kJ/mol) higher in energy compared to MS I in the gas phase.^{10,18} While an ESIPT process is not possible for MS II, the phenolic hydrogen can be transferred to the carbonyl oxygen upon photoexcitation of MS I leading to the keto-type species in the excited state (cf. Fig. 7.1). Here, the labels “enol” and “keto” refer to the phenolic OH-groups of the molecules as shown in Fig. 7.1.

However, the involved species and the mechanism of the dual fluorescence of MS remain an open issue. Meanwhile, it is widely accepted that the red-shifted fluorescence at 450 nm arises from the proton-transferred keto-type form in the excited state.^{2,3,12,13,18,21} In contrast, the origin of the near-UV fluorescence is still controversially discussed. Either it arises from the enol form of MS I in the excited state prior to the ESIPT reaction,^{17–19,21,22} or it is explained by the

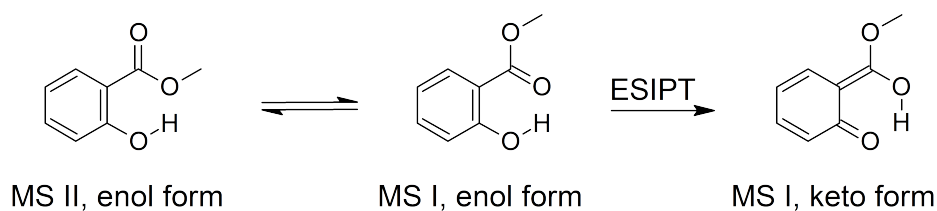


Figure 7.1: Chemical structures of the thermodynamically stable rotamer MS I and the energetically higher rotamer MS II of methyl salicylate in the electronic GS. While no photo-induced proton transfer occurs for MS II, the phenolic hydrogen can be transferred to the carbonyl oxygen leading to the keto-type form of MS I in the excited state. The labelling as “enol” and “keto” refers to the phenolic OH-group, which is of enol-type in the GS and transfers to keto-type in the excited state.

co-existence of MS II next to MS I in the GS.^{7–13,20,25} Due to a high potential energy barrier of 12–15.5 kcal/mol^{17,18,24} for the conversion from MS I to MS II, recent theoretical studies^{17–19,24} excluded an equilibrium between MS I and MS II in the electronic GS. This was also supported experimentally,^{26,27} e.g., by the absence of rotamer MS II in free-jet rotational spectra.²⁷ A new interpretation on the origin of the near-UV fluorescence was provided in 2015 by He and co-workers.¹⁸ As the fluorescence intensity in the near-UV drastically increases in protic solvents such as alcohols, the authors suggested that a solvent-controlled energy barrier between the enol and keto form of MS I exists in the excited state. Moreover, intermolecular hydrogen bonds from the solvent to the carbonyl of the ester group prevent the proton transfer, which implies that the enol species is favoured in protic solvents.^{18,19} This stabilisation of the enol-type form gives rise to the pronounced emission in the near-UV.¹⁸

Consistent with experiments and theory, the ESIPT occurs not only barrierless,^{5,12,17,19–21,24} but also on ultrafast time scales within $\tau \leq 100$ fs.^{12,15,21–23} Additionally, the lifetime of the near-UV fluorescence was found to be in the range of 1–2 ns in protic and aprotic, polar solvents.^{12,13,18} However, this is difficult to reconcile with a double minimum for the enol and keto species of MS I in the excited state. For that reason, other researchers identified rotamer MS II as origin of the near-UV fluorescence.^{4,7–14,20} In line with their assignment, the excitation spectra of both emission bands are different, where the one with $\lambda_{fl} = 340$ nm is slightly blue-shifted.^{6,13,28} Temperature-dependent measurements on MS in cyclohexane (CHX) revealed that the intensity of the near-UV fluorescence

increases at higher temperatures. The amount of MS II in the GS may change with increasing temperatures because the energy barrier can be overcome which shifts the ground-state equilibrium towards MS II.⁷ Besides, rotamer MS II was detected by IR and free-jet spectroscopy.^{9,10} All in all, the findings on MS reported in the literature are complex and contradictory. That is why the question which molecular species leads to the fluorescence at short wavelengths is still not answered. As a majority of the studies focused on the mechanism of the dual fluorescence of methyl salicylate, a detailed understanding on the underlying deactivation pathways after photoexcitation has not yet been provided.

To the best of our knowledge, apart from time-resolved fluorescence measurements, the photo-induced dynamics of MS were solely investigated in the gas phase.^{12,21} Thus, the effect of the solvent on the electronic relaxation pathways has received barely any attention. In the gas phase, the ultrafast ESIPT^{12,21} is followed by intramolecular vibrational redistribution within $\tau = 800\text{--}900$ fs.²¹ Another picosecond time component which strongly depends on the excitation wavelength is attributed to an internal conversion (IC) from the S_1 state to the GS.²¹ However, homosalate (HMS), a derivate of MS, was recently studied by means of transient electronic absorption spectroscopy (TEAS) in various solvents.²² As for MS in the gas phase, the ESIPT process takes place within $\tau \leq 100$ fs.²² Apart from radiative deactivation via fluorescence, a time component of $\tau \approx 10$ ps was detected for HMS in solution and assigned to vibrational cooling and non-radiative decay back to the GS.²² Already in 1994, Herek et al. postulated that an internal rotational motion of the ester moiety will likely occur upon photoexcitation, allowing for new non-radiative deactivation channels.¹² Later, a conical intersection (CI) connecting the S_1 state with the electronic GS at a twisted geometry of the keto-type form was predicted theoretically.¹⁵ For HMS the authors further suggested that solvation enables the excited-state population to deactivate via intersystem crossing (ISC) to a triplet state with $\tau > 2$ ns.²²

In this paper, we report on a comprehensive study on the photo-induced dynamics of methyl salicylate in acetonitrile (ACN) and cyclohexane (CHX) solution. We used a variety of static and time-resolved spectroscopic techniques to gain detailed insight into the underlying deactivation pathways as well as to shed light on the mechanism of the dual fluorescence of MS. To ultimately identify the involved molecular species, we combined femtosecond time-resolved

vibrational spectroscopy (TVAS) as a structure-sensitive method with quantum chemical calculations.

7.2 Methods

Methyl salicylate was purchased from Sigma Aldrich (purity $\geq 99\%$) and used as received. The time-resolved measurements were performed in ACN and CHX (Uvasol grade), or in deuterated acetonitrile (ACN- d_3).

Time-resolved fluorescence spectroscopy

A detailed description of the experimental setup for the time-resolved fluorescence measurements (TFLS) by the up-conversion technique can be found in the preceding literature.^{29,30} In short, a home-built non-collinear optical parametric amplifier (NOPA) provided laser pulses at 620 nm which were temporally compressed to 35 fs (FWHM) with a prism compressor. In a second step, pump pulses at $\lambda_{\text{exc}} = 305$ nm with an energy of 350 nJ per pulse were obtained via second harmonic generation (BBO, $\theta = 38.9^\circ$, $\phi = 90^\circ$). The pump pulses were focused into the sample flow cell which had an optical path length of 1 mm. The emitted fluorescence was collimated by a pair of parabolic mirrors (Melles-Griot, $f = 119$ mm) and focused into a 0.1 mm BBO crystal ($\theta = 51^\circ$, $\phi = 30^\circ$). Another fraction of the Ti:Sa fundamental at $\lambda = 775$ nm with an energy of 75 μJ per pulse was used for the gate pulses and also focused into the BBO crystal. By overlapping the gate pulses and the emitted fluorescence spatially and temporally in the BBO crystal, the sum frequency signal was generated (SFG) which was then detected. In the UV wavelength range from 330–360 nm, a type I non-collinear SFG process was applied, while type II phase-matching conditions were used in the visible region from 410–560 nm. To measure the SFG signals over a certain wavelength range, the BBO crystal was tilted by a few degrees for the different emission wavelengths. The up-converted light was then focused into the detection unit. The latter consisted of a monochromator (Jobin-Yvon HR 10), a photomultiplier (Hamamatsu R1527P), a preamplifier (Stanford Research SR 445) and a gated single-photon counter (Stanford Research SR 400). To record transient fluorescence time profiles, the gate pulses were delayed up to $\Delta t \sim 2$ ns with respect to the pump pulses by a linear translation stage

(Physik Instrumente). The measurements were carried out under magic angle (54.7°) conditions. The measured time profiles in the UV and in the visible range were fitted globally using a sum of exponentials convoluted with a Gaussian accounting for the instrument response function (IRF).

Time-resolved electronic absorption spectroscopy

The femtosecond time-resolved electronic absorption spectrometer has been built around a Clark MXR CPA 2001 Ti:Sa laser system delivering light pulses of 150 fs duration full width at half maximum (FWHM) at $\lambda = 775$ nm and a 1.01 kHz repetition rate. A detailed description of the setup is given elsewhere.^{31–33} In short, a home-built non-collinear optical parametric amplifier (NOPA) provided laser pulses at 630 nm which were temporally compressed to 30 fs (FWHM) with a prism compressor. Afterwards, pump pulses at $\lambda_{\text{exc}} = 313$ nm with an energy of 300 nJ per pulse were obtained via second harmonic generation (BBO, $\theta = 38.1^\circ$, $\phi = 90^\circ$). The pump pulses were focused into the sample flow cell which had an optical path length of 1 mm. Another fraction of the laser fundamental was focused into a moving CaF₂ plate preparing broadband probe pulses in the visible region from $325 \text{ nm} \leq \lambda_{\text{probe}} \leq 700 \text{ nm}$. After splitting them into probe and reference beams, the probe pulses were spatially and temporally overlapped with the pump pulses in the sample flow cell. Finally, the probe and reference pulses were spectrally dispersed in a prism spectrograph and then detected separately with two full frame transfer CCD cameras. Prior to white-light generation, the probe pulses passed a motorised, computer-controlled delay stage to record transient difference spectra as function of time. Here, a maximal pump–probe time delay of $\Delta t = 1.6$ ns was accessible. To improve data quality, optical choppers were inserted into the beam path of the pump and probe pulses, respectively. Every second probe pulse was blocked as the chopper was working at 505 Hz, whereas the chopper for the pump pulse was operating at 252.5 Hz. All measurements were carried out under magic angle conditions. After time-zero and solvent correction, the experimental data were analysed globally by singular value decomposition (SVD).³⁴

Time-resolved vibrational absorption spectroscopy

The femtosecond time-resolved vibrational absorption spectrometer^{35–37} has been built around a Coherent Libra HE Ti:Sa laser system delivering light pulses of 90 fs duration full width at half maximum (FWHM) at $\lambda = 800$ nm and 1 kHz repetition rate. Pump pulses at $\lambda_{\text{exc}} = 313$ nm with an energy of 300 nJ per pulse were used to excite the molecules. For this purpose, laser pulses at 508 nm were provided from a home-built non-collinear parametric amplifier (NOPA) and compressed to 37 fs (FWHM) with a prism compressor. In a second step, a sum frequency generation process (BBO, $\theta = 37.4^\circ$, $\phi = 90^\circ$) of the NOPA output at 508 nm and the laser fundamental at 800 nm (60 μJ per pulse) yielded pump pulses at $\lambda_{\text{exc}} = 313$ nm. The pump pulses were loosely focused into a home-built sample flow cell with CaF_2 windows and an optical path length of 0.1 mm. Every second pump pulse was blocked by a synchronised optical chopper operating at 500 Hz. Another fraction of the laser fundamental was used to pump a two-stage optical parametric amplifier (OPA), which provided tunable signal and idler pulses. Subsequently, broadband mid-infrared probe pulses were generated by difference frequency generation (DFG) in AgGaS_2 of the signal and idler pulses.^{36,37} The pump and probe beams were spatially and temporally overlapped in the sample flow cell. The transmitted probe light was then guided to the grating spectrograph and spectrally dispersed before impinging on the liquid-nitrogen cooled 32-pixel MCT detector array. Transient vibrational difference spectra were then recorded as function of pump–probe delay. After baseline correction of the raw data employing the programme KOALA,³⁸ the recorded transient spectra at each time delay were globally modelled by a sum of Gaussian functions. To extract time profiles, the respective amplitudes determined by the spectral band fits were plotted as function of pump–probe delay time and fitted in a global manner using a sum of exponentials.

Quantum chemical calculations

The minimum energy structures of the molecules and the associated normal mode vibrational wavenumbers of both rotamers of MS in the electronic ground state were calculated at the RI-MP2 level of theory^{39–41} in combination with the def2-TZVPPD basis set^{42–44} as implemented in the TURBOMOLE 7.0 programme package.⁴⁵ Geometry optimisations, vibrational spectra as well as vertical excita-

tion energies (VEEs) in the excited states were performed using the second-order coupled-cluster method under the resolution of the identity approximation (RI-CC2).^{46–50} Here, the def2-TZVPPD basis set^{42–44} was used in the TURBOMOLE 7.0 programme package.⁴⁵ The calculated vibrational wavenumbers in the ground state as well as in the excited states were scaled by factors of 0.973 and 0.985 as recommended in the literature, respectively.^{51,52}

7.3 Results

Quantum chemical calculations

The investigations were initiated by quantum chemical ab initio calculations to elucidate the electronic and chemical structures of both rotameric forms of methyl salicylate, namely MS I and MS II, respectively. Starting from the minimum energy structure in the electronic GS (cf. Fig. 7.2), the vertical excitation energies VEEs, the oscillator strengths f and the involved molecular orbitals (MOs) for each electronic transition are presented in Table 7.1 for both rotamers. The characters of the excited states are determined by inspection of the involved molecular orbitals and the oscillator strengths. For MS I the first excited state is located at a VEE of 4.34 eV above the electronic GS and exhibits $\pi\pi^*$ character, whereas the S_2 state is identified as $n\pi^*$ state. For the $S_3(\pi\pi^*)$ state, the highest oscillator strength with $f = 0.1109$ is computed. Here, four molecular orbitals are involved. The transition from the HOMO–1 to the LUMO dominates with a share of 58 %. Furthermore, the first triplet state T_1 is observed at a VEE of 3.89 eV and has $\pi\pi^*$ character as well.

For MS II the order and characters of the excited states are preserved. However, the energetic position of the calculated transitions is slightly shifted to higher energies. While the oscillator strength of the S_1 state with $f = 0.0816$ is lower compared to MS I, the value of $f = 0.1327$ for the S_3 state is increased.

The obtained optimised minimum energy structures in the ground and in the excited $S_1(\pi\pi^*)$ and $T_1(\pi\pi^*)$ states are displayed in Fig. 7.2. MS I represents the thermodynamically stable rotamer of methyl salicylate in the GS and shows a strong intramolecular hydrogen bond between the phenolic hydrogen and the carbonyl of the ester group. MS II arises by internal rotation about 180° of the ester group and is located 0.14 eV (13.5 kJ/mol) above MS I. MS II corresponds

Table 7.1: Calculated vertical excitation energies VEEs for MS I and MS II in the electronic GS alongside with the characters, the oscillator strengths f and the involved molecular orbitals (MOs) for each transition.

rotamer	state	character	VEE / eV	f	MOs
MS I	S_1	$\pi\pi^*$	4.34	0.0942	HOMO \rightarrow LUMO (86 %)
	S_2	$n\pi^*$	5.36	0	HOMO-2 \rightarrow LUMO (80 %)
	S_3	$\pi\pi^*$	5.63	0.1109	HOMO-1 \rightarrow LUMO (58 %)
					HOMO \rightarrow LUMO+1 (23 %)
	T_1	$\pi\pi^*$	3.89	–	HOMO \rightarrow LUMO (88 %)
MS II	S_1	$\pi\pi^*$	4.44	0.0816	HOMO \rightarrow LUMO (84 %)
	S_2	$n\pi^*$	5.40	0.0001	HOMO-2 \rightarrow LUMO (77 %)
	S_3	$\pi\pi^*$	5.69	0.1327	HOMO-1 \rightarrow LUMO (64 %)
					HOMO \rightarrow LUMO+1 (21 %)
	T_1	$\pi\pi^*$	3.99	–	HOMO \rightarrow LUMO (74 %)

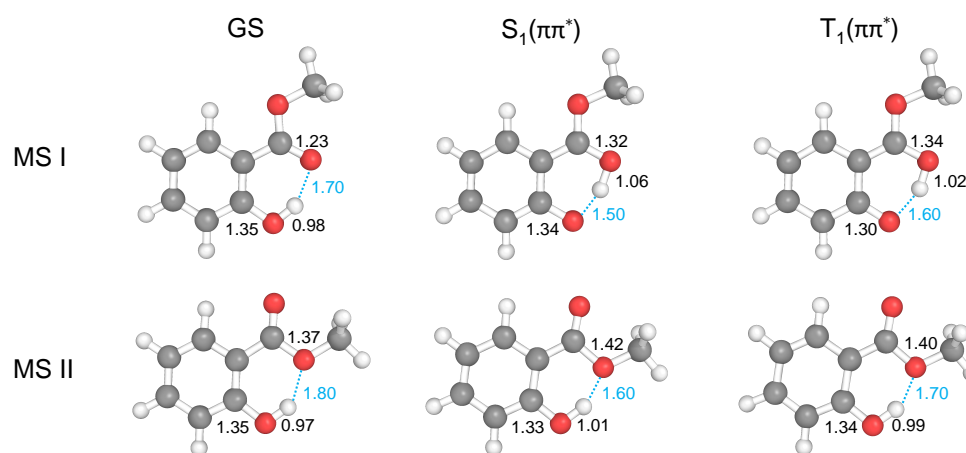


Figure 7.2: Minimum energy structures of MS I and MS II in the electronic GS and in the excited $S_1(\pi\pi^*)$ and $T_1(\pi\pi^*)$ states, respectively. The numbers refer to the lengths of the most relevant bonds in Å. The intramolecular hydrogen bonds are coloured in light blue.

to a local minimum in the GS, where the stabilising intramolecular hydrogen bond is formed between the phenol hydrogen and the methoxy oxygen of the ester moiety.

The proton transfer from the phenolic OH-group to the carbonyl oxygen of the ester group occurs in the $S_1(\pi\pi^*)$ state of MS I, and results in the keto-type structure. It leads to a shortened intramolecular hydrogen bond of 1.5 Å compared to the GS with a length of 1.7 Å. The keto-type structure of MS I is maintained in the triplet state. In contrast, proton transfer is not possible for rotamer MS II. Nonetheless, analogously to MS I, the intramolecular hydrogen bond is shorter in the $S_1(\pi\pi^*)$ state.

Static spectroscopy

The UV absorption spectra of MS in ACN and CHX are depicted in Fig. 7.3. As can be seen, they feature an almost identical spectral shape in both solvents. Two absorption bands showing a minor solvent-dependent shift are observed. While the band maxima are located at 305 and 238 nm in ACN, they are slightly red-shifted to 308 and 239 nm in CHX. In accordance with our calculations, the first absorption band at longer wavelengths is assigned to the $S_1(\pi\pi^*)$ state. The second more intense band corresponds to the transition to the $S_3(\pi\pi^*)$ state. The $S_2(n\pi^*)$ state is optically dark and therefore not observed in the UV absorption spectra. Consequently, excitation at $\lambda_{\text{exc}} \geq 290$ nm will exclusively populate the $S_1(\pi\pi^*)$ state, as the other excited states are shifted to higher energies.^{15,21}

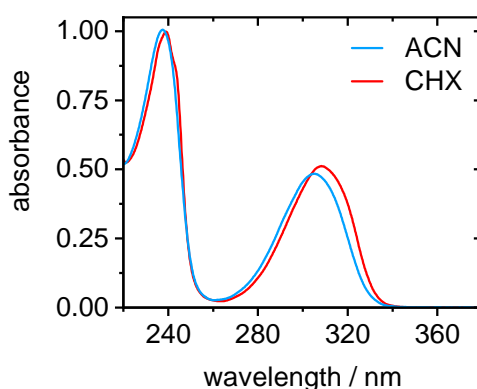


Figure 7.3: UV absorption spectra of methyl salicylate in ACN (light blue) and CHX (red).

Unlike the absorption spectra, the static fluorescence spectra of MS strongly depend on the solvent as presented in Fig. 7.4. MS exhibits dual fluorescence in ACN and CHX. One band is centered in the near-UV around 340 nm, and the second shows a pronounced Stokes shift with a maximum in the visible spectral range peaking at 450 nm. While the fluorescence is almost equally intense in ACN, the red-shifted band clearly dominates in CHX. Excitation at higher energies (cf. Fig. 7.4, grey curves) preserves the spectral shape, but leads to a reduced intensity at long emission wavelengths in both solvents. At the same time, the UV fluorescence increases by 5 % in ACN, but remains almost constant in CHX.

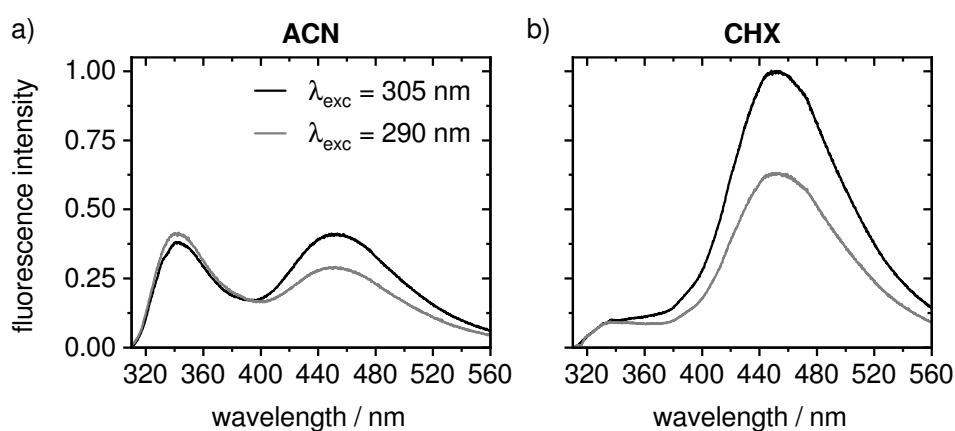


Figure 7.4: Static fluorescence spectra of methyl salicylate after excitation at $\lambda_{\text{exc}} = 305$ nm (black) and $\lambda_{\text{exc}} = 290$ nm (grey) a) in ACN and b) in CHX. The relative fluorescence intensity in CHX after excitation at $\lambda_{\text{exc}} = 305$ nm is normalised to unity at $\lambda_{\text{fl}} = 454$ nm.

Time-correlated single photon counting

TCSPC measurements after excitation at $\lambda_{\text{exc}} = 290$ nm were performed to determine the lifetime of the excited $S_1(\pi\pi^*)$ state. Time profiles were recorded in 10 nm steps from $\lambda_{\text{fl}} = 325$ –525 nm and analysed in a global manner using a sum of two exponentials taking into account the IRF. Two exemplary time profiles at 355 nm and 445 nm in ACN (left column) and CHX (right column) are shown in Fig. 7.5.

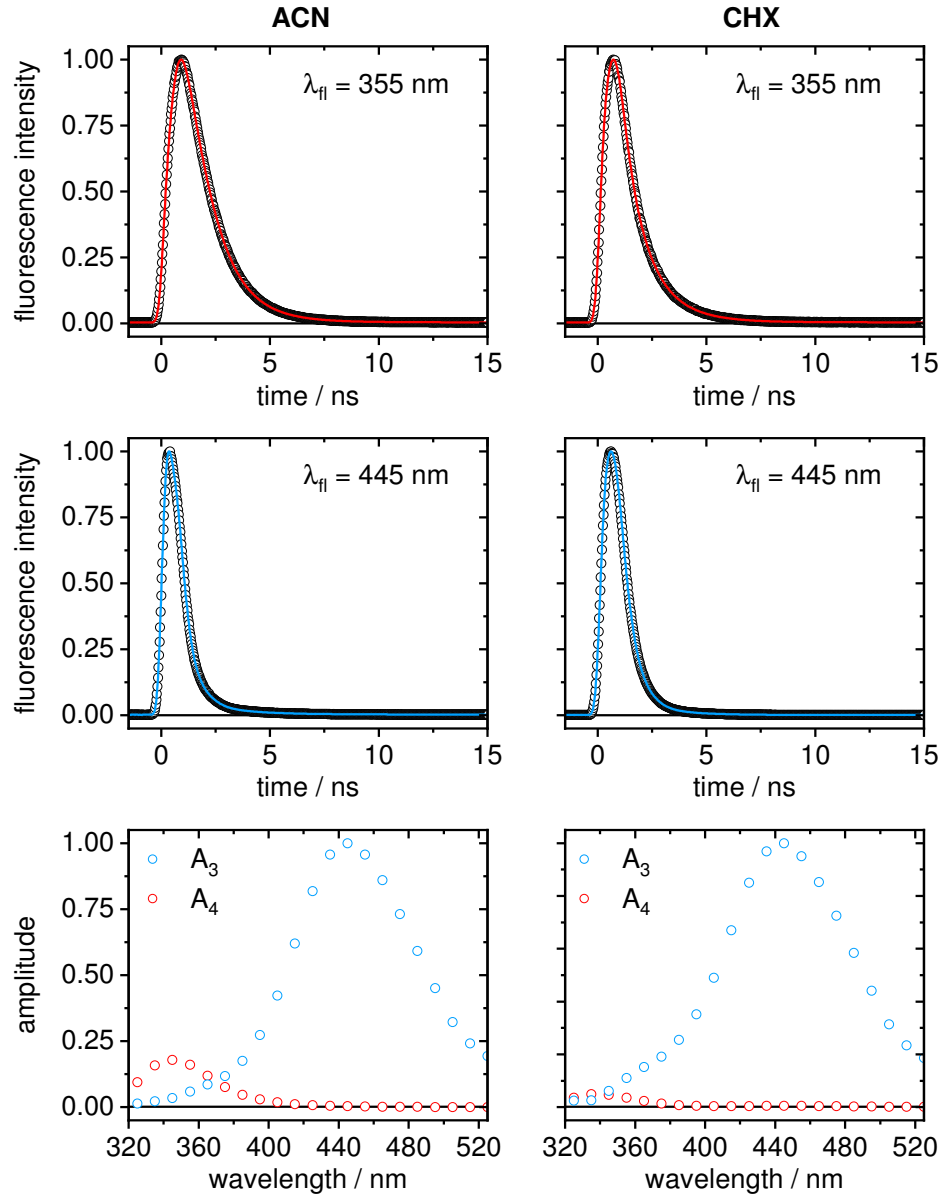


Figure 7.5: Exemplary time profiles at $\lambda_{fl} = 355$ nm and $\lambda_{fl} = 445$ nm obtained from TCSPC measurements ($325 \text{ nm} \leq \lambda_{fl} \leq 525 \text{ nm}$) of MS in ACN (left column) and in CHX (right column) after excitation at $\lambda_{exc} = 290$ nm. Shown are the experimental data (black circles) and the global fits (straight lines). The wavelength-dependent amplitudes A_3 (blue circles) and A_4 (red circles) obtained from the global fits are presented at the bottom.

Two decay components given with included systematic error limits are obtained from the global data analysis:

$$\begin{array}{ll} \tau_{3,\text{ACN}} = 110. \pm 3.00 \text{ ps} & \tau_{3,\text{CHX}} = 300. \pm 3.00 \text{ ps} \\ \tau_{4,\text{ACN}} = 1.12 \pm 0.02 \text{ ns} & \tau_{4,\text{CHX}} = 1.16 \pm 0.03 \text{ ns} \end{array}$$

The values are numbered as τ_3 and τ_4 here because significantly faster values (τ_1 , τ_2) are detected by the other methods below. The fluorescence in the visible region decays monoexponentially with τ_3 in both solvents. The time component τ_4 is associated with the fluorescence at shorter emission wavelengths. Fig. 7.5 also shows the wavelength-dependent amplitudes A_3 and A_4 in the investigated spectral region highlighting that τ_4 plays a minor role in CHX, but clearly dominates in ACN at $\lambda_{\text{fl}} \leq 365$ nm. The nanosecond time constant τ_4 features similar values in both solvents, thus the species being responsible for the near-UV fluorescence seems to be favoured or stabilised in ACN compared to CHX.

Time-resolved fluorescence spectroscopy

To access the early-time dynamics, the results of the femtosecond time-resolved fluorescence (TFLS) measurements by the up-conversion technique in the spectral region from $\lambda_{\text{fl}} = 340\text{--}540$ nm in ACN (left column) and CHX (right column) are displayed in Fig. 7.6. Below $\lambda_{\text{fl}} \leq 340$ nm, the signal is dominated by the impulsive Raman response of the used solvent ($\tau_{\text{Raman}} \leq \sigma_{\text{IRF}} \approx 180$ fs). From the global data analysis, three time components given with the statistical 2σ uncertainty limits are found in both solvents:

$$\begin{array}{ll} \tau_{1,\text{ACN}} = 0.22 \pm 0.02 \text{ ps} & \tau_{1,\text{CHX}} = 0.23 \pm 0.02 \text{ ps} \\ \tau_{2,\text{ACN}} = 5.20 \pm 0.30 \text{ ps} & \tau_{2,\text{CHX}} = 5.50 \pm 0.30 \text{ ps} \\ \tau_{3,\text{ACN}} = 115. \pm 2.00 \text{ ps} & \tau_{3,\text{CHX}} = 285. \pm 6.00 \text{ ps} \end{array}$$

The relative amplitudes A_i from the global analysis of the TFLS data in both solvents are given in Table 7.3 in the Supporting Information (SI). In ACN, a minor offset is observed at 340 nm which is more pronounced at 360 nm. This long-lived fluorescence in the near-UV range is described by $\tau_{4,\text{ACN}} = 1.2 \pm 0.2$ ns (cf. Fig. 7.6, purple line).

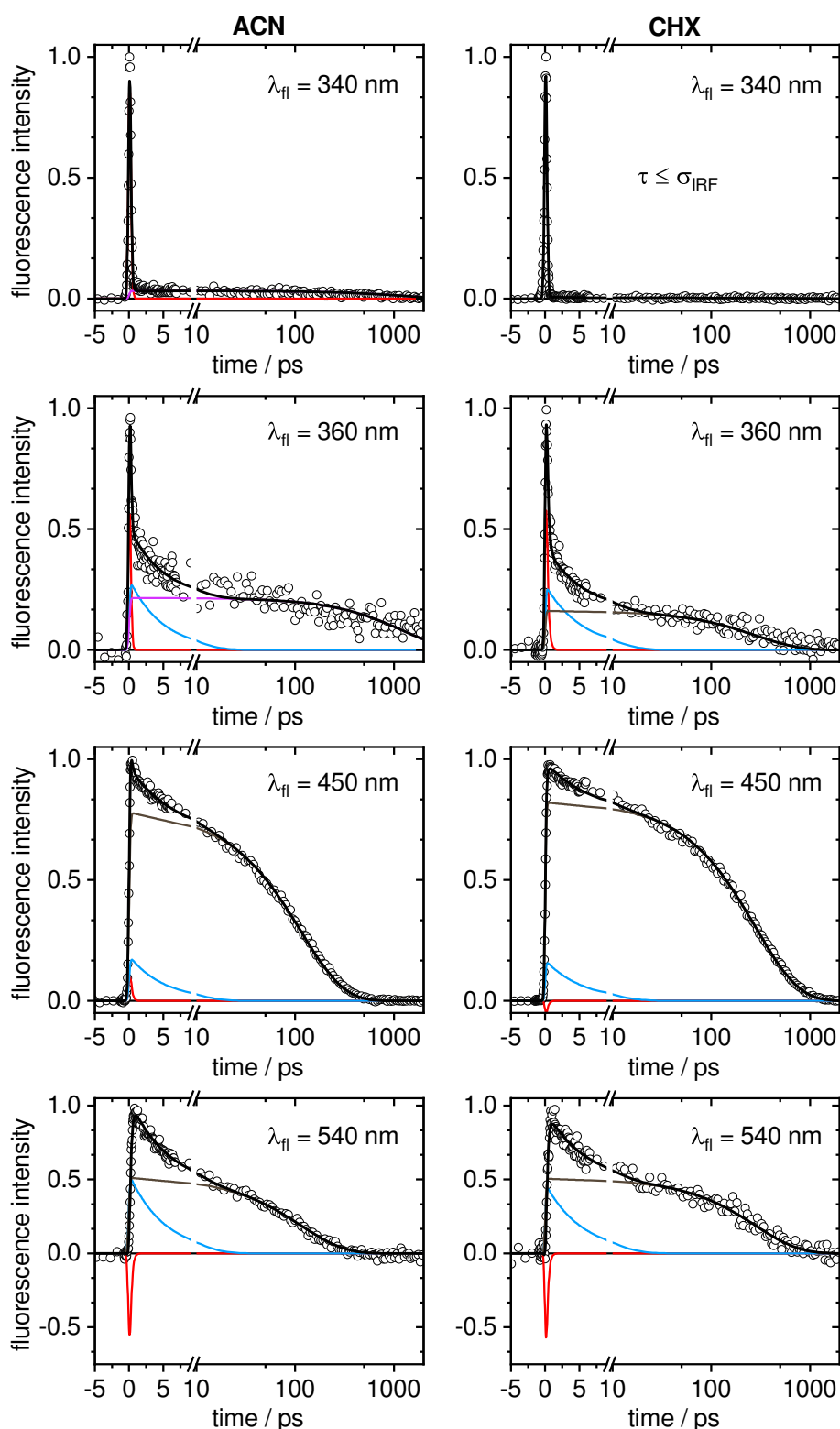


Figure 7.6: Selected TFLS time profiles of MS in ACN (left column) and CHX (right column) after excitation at $\lambda_{\text{exc}} = 305$ nm. Shown are the experimental data (circles) and the global fits (black lines) obtained by a sum of exponentials (red, blue, grey or purple) convoluted with the IRF. At early times up to 10 ps a linear scale is used, a logarithmic scale is chosen thereafter.

In contrast, the fluorescence at longer wavelengths ($\lambda_{\text{fl}} > 360$ nm) decays with $\tau_{3,\text{ACN}}$ (cf. Fig. 7.6, grey line). In CHX, no long-lived fluorescence is detected in the UV region, probably because its amplitude is too small. Although the excitation wavelength was red-shifted to $\lambda_{\text{exc}} = 305$ nm for the TFLS measurements, the obtained time constants τ_3 and τ_4 nicely agree with the TCSPC results after excitation at $\lambda_{\text{exc}} = 290$ nm. Additionally, the TFLS measurements yield two time components on the femto- and picosecond time scale, namely τ_1 and τ_2 , respectively. The amplitude A_1 becomes negative at 540 nm in ACN and at 450 nm in CHX, which implies a delayed rise of the fluorescence at longer wavelengths. While no significant influence of the solvent is observed for τ_1 and τ_2 , τ_3 seems to be solvent-dependent, since its value in CHX is considerably higher compared to ACN.

Time-resolved electronic absorption spectroscopy

The obtained TEAS results in ACN (left column) and CHX (right column) after excitation at $\lambda_{\text{exc}} = 313$ nm are summarised in Fig. 7.7. Presented are the colour-coded two-dimensional spectro-temporal absorption maps (A) together with the transient spectra at early time delays (B) and towards later times (C). The inserted arrows indicate the temporal evolutions of the observed signals. At early times the transient spectrum is dominated by two ESA bands located at 335 nm and 530 nm in both solvents. While the intense ESA band in the UV rises in intensity until it reaches its maximum after $\Delta t \sim 1$ ps, the weaker signal at 530 nm remains almost constant, but features a slight blue-shift. Subsequently, the ESA bands decay back to the baseline within $\Delta t \sim 1.5$ ns. Furthermore, a negative signal at 450 nm is detected in both solvents which shows the same temporal evolution as the ESA signals. In line with the static fluorescence spectra, the negative signal at 450 nm is assigned to stimulated emission. Additionally, a very weak and spectrally broad contribution at ~ 400 nm remains towards late times.

After time-zero and solvent correction, the experimental data were analysed by singular value decomposition (SVD). The singular value weighted time traces were fitted globally by a sum of exponentials convoluted with a Gaussian accounting for the IRE.

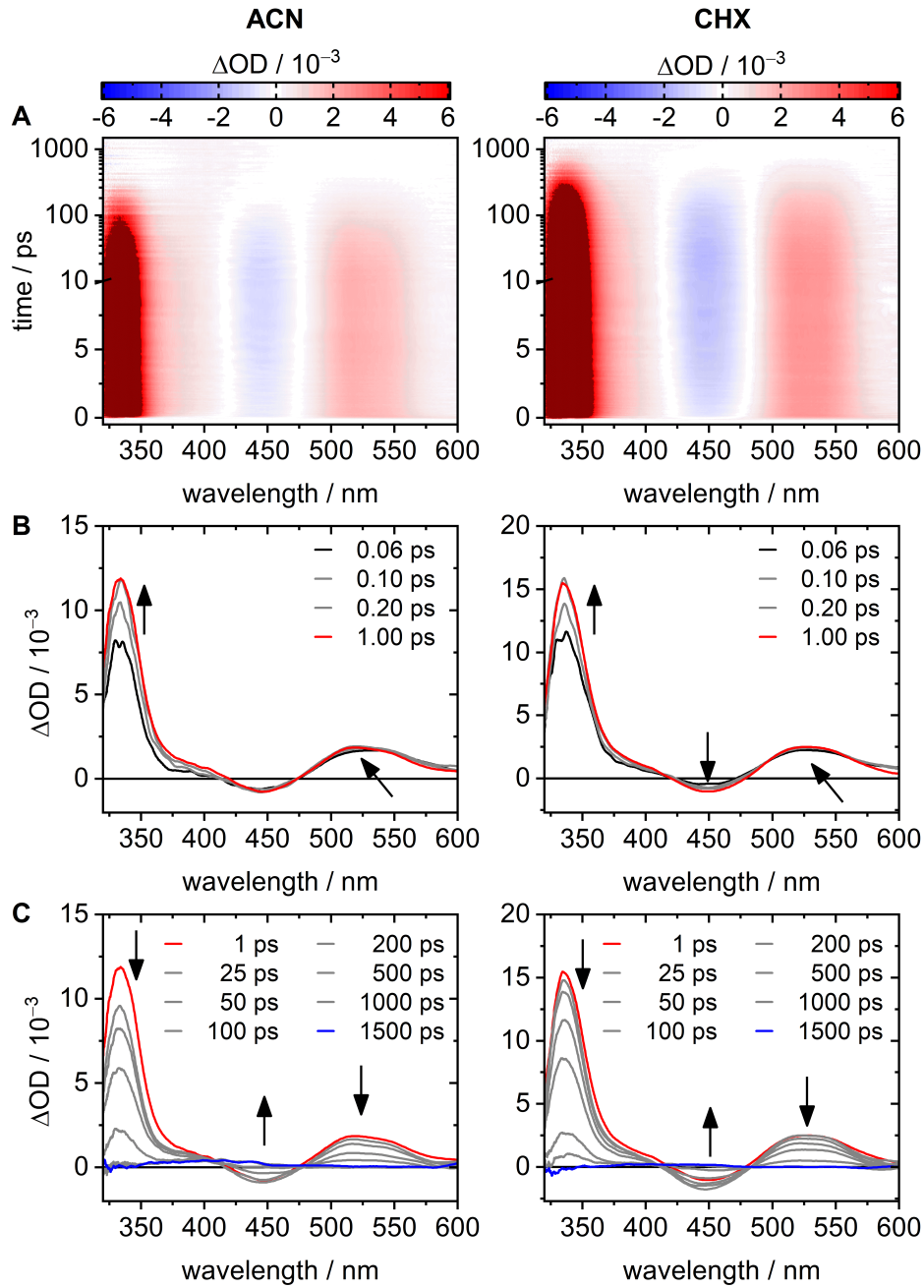


Figure 7.7: TEAS results of MS in ACN (left column) and in CHX (right column) after excitation at $\lambda_{\text{exc}} = 313$ nm. A: Colour-coded two-dimensional spectro-temporal absorption map with a linear scale up to 10 ps, thereafter a logarithmic scale is chosen. B: Recorded transient spectra at early time delays and C: at late time delays. The arrows indicate the temporal evolutions of the observed signals.

From that three time constants given with the statistical 2σ uncertainty limits were obtained:

$$\begin{array}{ll} \tau_{1,\text{ACN}} = 0.07 \pm 0.01 \text{ ps} & \tau_{1,\text{CHX}} = 0.10 \pm 0.02 \text{ ps} \\ \tau_{2,\text{ACN}} = 4.44 \pm 1.60 \text{ ps} & \tau_{2,\text{CHX}} = 6.40 \pm 1.70 \text{ ps} \\ \tau_{3,\text{ACN}} = 114. \pm 3.00 \text{ ps} & \tau_{3,\text{CHX}} = 298. \pm 5.00 \text{ ps} \end{array}$$

The time components are in very good agreement with the results from the TCSPC and TFLS measurements. Due to its higher time resolution, TEAS provides a shorter value of $\tau_1 \leq 0.10$ ps compared to the TFLS data, where $\tau_1 \approx 0.20$ ps was found. From the global SVD-based analysis, decay-associated difference spectra (DADS) as well as evolution-associated difference spectra (EADS) are obtained and displayed in the SI (cf. SI, Fig. 7.11). Based on these results and by inspection of the DADS and EADS, τ_2 is tentatively attributed to vibrational cooling in the excited state, whereas τ_3 is assigned to the lifetime of the excited state.

In a next step, we used transient vibrational absorption spectroscopy (TVAS) as structure-sensitive method, to verify whether the ultrafast time component τ_1 indeed corresponds to the ESIPT reaction which leads to the proton-transferred keto-type form of MS I in the first excited state.

Static and time-resolved vibrational absorption spectroscopy

The experimental FTIR spectra of MS in ACN- d_3 and CHX nicely agree with the calculated ground-state vibrational spectrum of rotamer MS I (cf. SI, Fig. 7.12). In the spectral region from 1200 to 1700 cm^{-1} , the FTIR spectra in both solvents show only minor differences. However, exclusively in ACN- d_3 , a weak signal is observable at 1727 cm^{-1} . Aided by the calculations, this signal corresponds to the carbonyl stretch vibration of rotamer MS II (cf. Fig. 7.12 and Fig. 7.14). This is an indication of the co-existence of rotamer MS II in the GS. Judging from the signal intensity, the fraction of MS II seems to be minor.

A summary of the TVAS measurements for MS after excitation at $\lambda_{\text{exc}} = 313$ nm in ACN- d_3 (left column) and in CHX (right column) is given in Fig. 7.8. This overview consists of three (ACN- d_3) and two (CHX) individual measurements

spliced together. The first row shows the inverted experimental FTIR spectra as well as the calculated vibrational spectra of MS II in the GS and the $S_1(\pi\pi^*)$ state for the keto-type form of MS I which is formed via ESIPT. In the middle, the experimental transient spectra and the global Gaussian band fits to the latter at selected time delays are displayed. To visualise their temporal evolutions, a colour gradient from blue to yellow to dark orange is used. In the corresponding two-dimensional spectro-temporal absorption maps which are presented in the bottom panels, negative signals are coded in blue and positive ones in red. Two more TVAS data sets of MS in ACN- d_3 were recorded in the spectral region from 1350–1200 cm^{-1} and are given in the SI in Fig. 7.16.

After photoexcitation, several negative signals are observed which arise from ground-state bleaching (GSB). These GSB bands in ACN- d_3 (1682, 1487 cm^{-1}) and in CHX (1690, 1300 cm^{-1}) feature an asymptotic permanent offset towards late times, indicating that a small fraction of the initially excited molecules has not returned back to the GS in the investigated time window. However, some GSB signals (ACN- d_3 : 1613, 1594, 1442 cm^{-1} and CHX: 1614, 1337, 1324 cm^{-1}) apparently show complete recovery, because they are superimposed by positive contributions. The positive signals marked with light blue arrows are directly present at early delay times and detected in both solvents (ACN- d_3 : 1642, 1512, 1430 cm^{-1} and CHX: 1639, 1390, 1300 cm^{-1}). As these vibrational signatures decay, positive bands marked with dark blue arrows are rising in at later times (ACN- d_3 : 1732, 1621, 1586, 1477 cm^{-1} and CHX: 1750, 1619, 1331 cm^{-1}). These late-time species can either correspond to a successor excited state, or to the formation of a photoproduct. To assign those experimentally observed positive signals, we turn to the calculated vibrational spectra in Fig. 7.8. Vibrational marker bands of the keto-type form of MS I in the $S_1(\pi\pi^*)$ state are expected at 1633, 1554, 1515, 1489, 1465, 1436, 1391, 1351 and at 1298 cm^{-1} . Therefore, we assign the positive contributions in ACN- d_3 (1642, 1512, 1430 cm^{-1}) and in CHX (1639, 1390, 1300 cm^{-1}) to the keto-type form of MS I in the $S_1(\pi\pi^*)$ state, which is formed after the ESIPT reaction. The marker bands expected at 1489, 1465 and 1351 cm^{-1} are solely observed indirectly as they overlap with the GSB bands at 1487, 1442 and 1337 cm^{-1} . The late-time bands show good agreement with the computed MS II marker bands at 1730, 1624, 1586, 1473 and at 1340 cm^{-1} . The experimental bands at 1621 and 1586 cm^{-1} in ACN- d_3 and at 1331 cm^{-1} in CHX are weak in intensity and hardly observable

because they are superimposed by the GSB signals at 1613 and 1594 cm^{-1} in ACN- d_3 and at 1337 and 1324 cm^{-1} in CHX, respectively. Owing to the structure sensitivity of TVAS, we confirmed experimentally that rotamer MS I undergoes an ultrafast intramolecular proton transfer in the first excited state leading to the keto-type form of the latter. Additionally, a novel deactivation channel via photoproduct formation is detected. This photoproduct is unambiguously identified as MS II in the electronic GS which arises by internal rotation of 180° of the ester group.

To gain detailed insight into the temporal evolutions of the involved species, the respective amplitudes from the global band fitting are plotted as function of time in Fig. 7.9. The time profiles for the GS, the photoproduct MS II in the GS and the keto-type form of MS I in the $S_1(\pi\pi^*)$ state in ACN- d_3 and CHX are described in a global manner by a sum of two exponentials. From that the following decay components given with the statistical 2σ uncertainty limits are obtained:

$$\begin{array}{ll} \tau_{2,\text{ACN}} = 6.40 \pm 1.30 \text{ ps} & \tau_{2,\text{CHX}} = 7.50 \pm 4.60 \text{ ps} \\ \tau_{3,\text{ACN}} = 136. \pm 5.00 \text{ ps} & \tau_{3,\text{CHX}} = 313. \pm 25.0 \text{ ps} \end{array}$$

All in all, the obtained time constants from the global data analysis agree nicely with the data shown previously. The ultrafast processes are not accessible by TVAS due to coherent artifacts at early times $\Delta t \leq 2$ ps. Summaries of the results from the global data analyses for MS after photoexcitation in ACN- d_3 and CHX are given in the SI (cf. Table 7.4 and Table 7.5). The time profiles obtained for the spectral region from 1350–1200 cm^{-1} can also be found in the SI (Fig. 7.17).

As the vibrational marker bands of the keto-type species of MS I decay with τ_3 , this time constant is attributed to the lifetime of the $S_1(\pi\pi^*)$ state of the proton-transferred form of rotamer MS I. Concurrently, photoproduct formation as well as ground-state recovery (GSR) proceed with τ_3 . From the asymptotic offsets of the GSB bands, a GSR of ~ 83 % in ACN- d_3 and ~ 76 % in CHX are determined. The assignment of τ_2 is more challenging. In ACN- d_3 its amplitude A_2 is very low and ranges from 3 % to 7 % (cf. SI, Table 7.4). However, A_2 becomes significantly higher in the spectral region of 1430–1495 cm^{-1} (20–48 %, cf. SI), where signals of different electronic states tend to overlap. According to our calculations, two signals at 1489 and 1464 cm^{-1} arising from the $S_1(\pi\pi^*)$ state

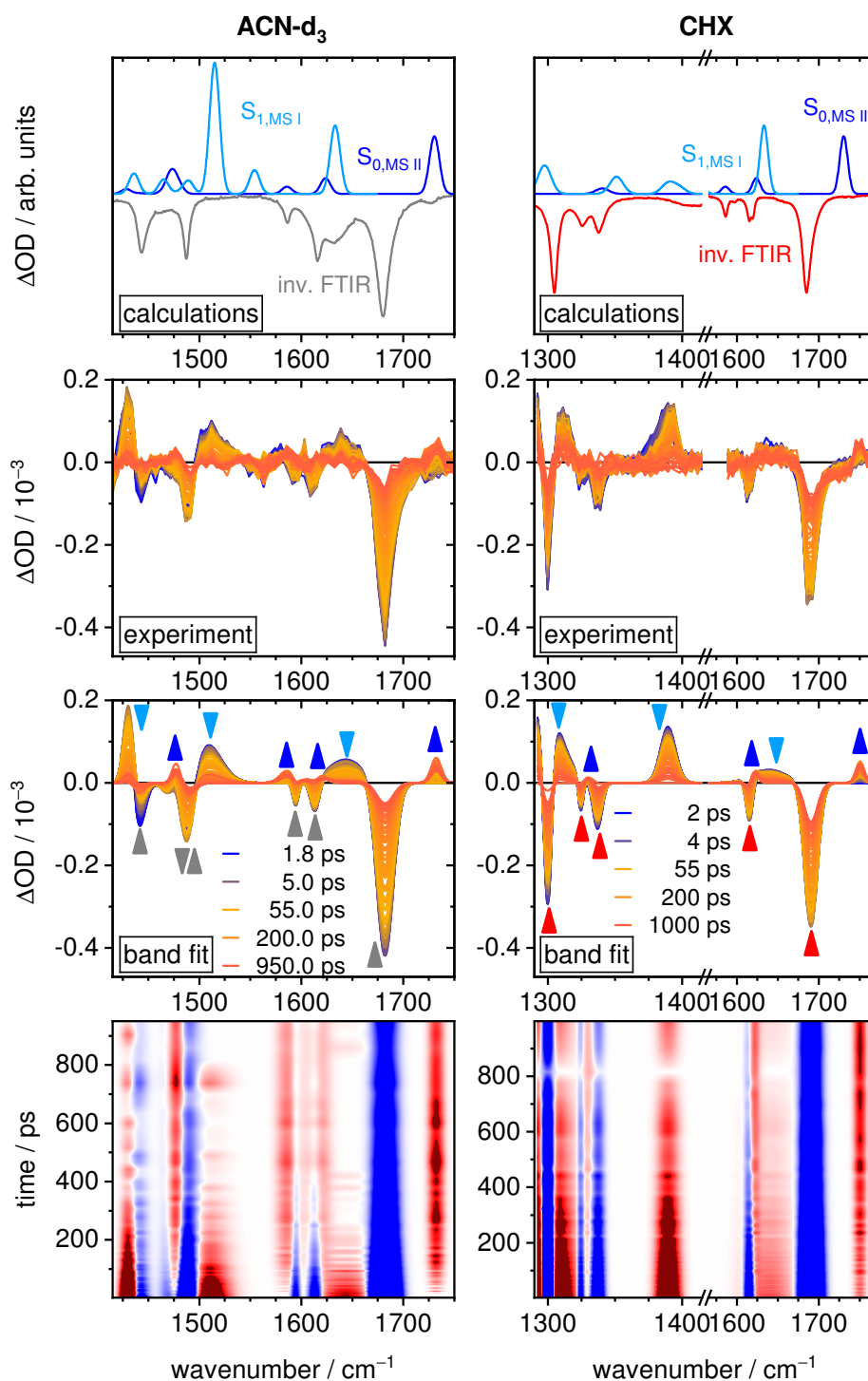


Figure 7.8: TVAS measurements of methyl salicylate after excitation at $\lambda_{\text{exc}} = 313$ nm in ACN-d₃ (left) and CHX (right). Calculations: Computed vibrational spectra of MS II in the GS and the keto-type form of MS I in the $S_1(\pi\pi^*)$ state alongside with the inverted experimental FTIR spectrum. Experiment: Recorded TVA spectra at different delay times. Band fit: Corresponding global band fits to the experimental TVA spectra. At the bottom the colour-coded two-dimensional spectro-temporal absorption maps are presented.

of the keto-type form of MS I are expected. Thus, τ_2 is associated with the deactivation of the latter. In contrast, $A_2 = 6\text{--}10\%$ is slightly higher in CHX (cf. SI, Table 7.5). Additionally, the ESA bands at 1430 cm^{-1} in ACN- d_3 and at 1390 cm^{-1} in CHX feature slight blue-shifts, which is an indication for vibrational cooling in the excited state. Unfortunately, the blue-shift at 1390 cm^{-1} in CHX is poorly described by the global band fit. Furthermore, neither excited-state contributions of the enol-type form of MS I in the S_1 state, nor the nanosecond time component $\tau_4 \approx 1.1\text{ ns}$ are detected in the TVAS data.

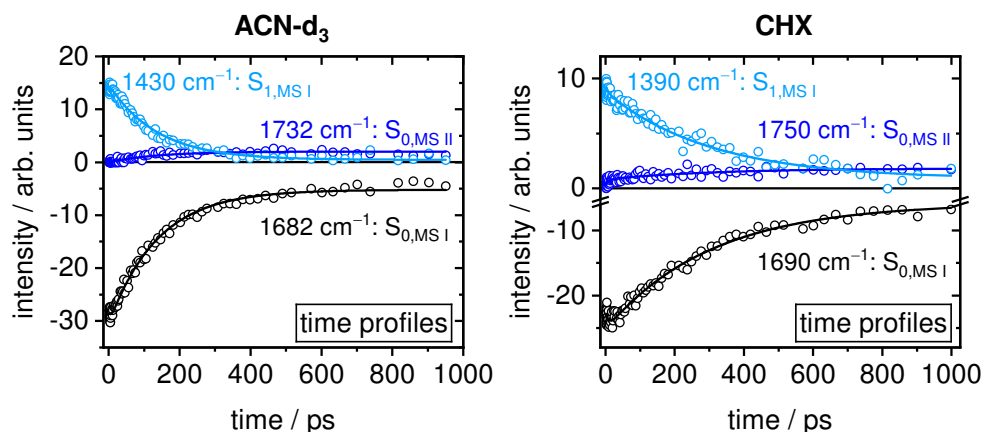


Figure 7.9: Selected time profiles of the GS (black), the photoproduct MS II in the GS (dark blue) and the keto-type form of MS I in the $S_1(\pi\pi^*)$ state (light blue) in ACN- d_3 (left) and CHX (right) after excitation at $\lambda_{\text{exc}} = 313\text{ nm}$. Shown are the amplitudes obtained from the global band fitting (circles) and the global fits (straight lines) obtained by sums of two exponentials.

7.4 Discussion

Origin of the near-UV fluorescence of MS

The question which molecular species give rise to the observed dual fluorescence of MS and its related compounds has not been answered yet and is still subject of ongoing research.^{7–13,17–22,24} Based on the structure sensitivity of TVAS, the fluorescence at 450 nm was identified to arise from the proton-transferred species of MS I in the $S_1(\pi\pi^*)$ state as previously proposed in the literature.^{2,12,13,18,21} The long-lived fluorescence in the near-UV has either been ascribed to the excited-state enol-type species of MS I,^{17–19,21} or has been explained by an equilibrium

between the two rotamers MS II and MS I in the GS.^{7–13,20} Based on our results, we are convinced that the near-UV fluorescence originates from rotamer MS II. Further, we suggest that its amount in the electronic GS strongly depends on the used solvent. While it is stabilised in ACN, it is almost absent in CHX. Consistent with this, the potential energy barrier for the conversion from MS I to MS II in the GS was predicted to become lower in polar solvents.¹⁸ However, even in ACN the fraction of MS II is very low. Therefore, distinct experimental signatures of the excited $S_1(\pi\pi^*)$ state of MS II were solely detectable by static and time-resolved fluorescence spectroscopy due to their high sensitivity. The static fluorescence spectra in ACN and CHX showed that the intensity of the observed bands strongly depends on the excitation wavelength λ_{exc} .^{11,12,14,20} Concurrently, the TCSPC and TFLS data revealed that the time constants determined for the optically bright states do not depend on λ_{exc} . The latter would clearly argue against an excited-state energy barrier between the enol- and keto-type species of MS I. Instead, we propose that excitation at shorter wavelengths leads to a higher fraction of MS II in the $S_1(\pi\pi^*)$ state because the calculations predicted the transition to the $S_1(\pi\pi^*)$ state for MS II to be blue-shifted compared to MS I (cf. Table 7.1). This would explain why the intensity drops in the visible region and increases in the UV. As this trend is more pronounced in ACN, the TCSPC and TFLS measurements further confirm that MS II seems to be stabilised in polar, aprotic solvents. However, the most convincing argument for the presence of MS II in the GS is provided by the experimental FTIR spectrum of MS in ACN- d_3 . As described previously, the weak band centered at 1727 cm^{-1} , unambiguously corresponds to the carbonyl stretching motion of rotamer MS II (cf. SI, Fig. 7.12, Fig. 7.14). Analogously to the time-resolved fluorescence data, this band is not observed in the FTIR spectrum of MS in CHX. Concurrently, we did not detect any vibrational signals of the electronically excited enol-type form of MS I by means of TVAS in both solvents which makes its presence unlikely. In contrast, we do not expect any excited-state signatures of MS II due to its very low concentration. Our assignment is further supported by other experimental data, especially different excitation spectra for both emission bands, as well as temperature- and solvent-dependent studies reported in the literature.^{7,12,13,20} Nevertheless, our findings may be invalid for protic solvents such as water or alcohols, since intermolecular hydrogen bonds with the solvent play a crucial role there.¹⁸

The time constants $\tau_{3,\text{ACN}} \approx 115$ ps, $\tau_{3,\text{CHX}} \approx 300$ ps and $\tau_4 \approx 1.15$ ns obtained from time-resolved measurements are in good agreement with the literature^{7,12,13,28} and underline that not only the ratio of MS I and MS II is solvent-dependent, but also is τ_3 . The influence of the solvent on τ_3 is also reflected by the static fluorescence spectra as the intensity of the band at 450 nm is almost three times higher in CHX compared to ACN.

Deactivation mechanism for MS after photoexcitation

The obtained time components from all performed time-resolved measurements nicely agree well with each other within the error limits and are summarised in Table 7.2 for ACN(-d₃) and CHX.

Table 7.2: Time components τ_i given with the statistical 2σ uncertainty limits from the global data analyses of the experimental TCSPC, TFLS, TEAS and TVAS data of MS in ACN(-d₃) and CHX.

solvent	τ_i	TCSPC	TFLS	TEAS	TVAS
ACN(-d ₃)	τ_1 / ps	–	0.22 ± 0.02	0.07 ± 0.01	–
	τ_2 / ps	–	5.20 ± 0.30	4.44 ± 1.60	6.40 ± 1.30
	τ_3 / ps	110 ± 3.00	115 ± 2.00	114 ± 3.00	136 ± 5.00
	τ_4 / ns	1.12 ± 0.02	1.20 ± 0.20	–	–
CHX	τ_1 / ps	–	0.23 ± 0.02	0.10 ± 0.02	–
	τ_2 / ps	–	5.50 ± 0.30	6.40 ± 1.70	7.50 ± 4.60
	τ_3 / ps	300 ± 3.00	285 ± 6.00	298 ± 5.00	313 ± 25.0
	τ_4 / ns	1.16 ± 0.03	–	–	–

From this, a deactivation mechanism for methyl salicylate after photoexcitation is proposed. The ultrashort time component τ_1 is assigned to the excited-state intramolecular proton transfer after excitation of enol-type MS I. Similar time constants for the proton transfer reaction are reported in the literature for MS,^{12,21} or related compounds like homosalate²² and *o*-hydroxybenzaldehyde.⁵³ We do not observe any contributions from the excited enol-type form of MS I in

our time-resolved experiments. This clearly indicates that the proton transfer is highly efficient and barrierless as suggested in the literature.^{12,20–22,24}

After the ESIPT process, several marker bands of the keto-type species in the first excited state were identified owing to the structure sensitivity of TVAS. The time-resolved measurements yielded an excited-state lifetime of $\tau_{3,\text{ACN}} \approx 115$ ps and $\tau_{3,\text{CHX}} \approx 300$ ps for the keto-type form of MS I. Contrary to the other decay components, τ_3 depends on the used solvent, consistent with other experimental studies.^{7,13,22,28} In the gas phase, a strong dependence of τ_3 on the excitation wavelength λ_{exc} was observed for MS.^{12,21} The authors argued that the molecules in the excited state are vibrationally excited after the photo-induced proton transfer, which leads to a weakening of the intramolecular hydrogen bond. Consequently, the entire ester moiety can rotate, making a large density of states as well as new non-radiative deactivation channels accessible.¹² To access these new channels, a certain energy, provided at higher excitation energies, is required.^{12,21} At low excitation energies, on the other hand, the excited-state population becomes trapped in the $S_1(\pi\pi^*)$ state, reflected by longer lifetimes of the latter.¹² From our TVAS data, we detected and unambiguously identified rotamer MS II as a photoproduct that arises by an internal rotation about 180° of the ester group. This confirms that indeed a rotational motion in the excited state does take place and leads to a conical intersection (CI_{S_1/S_0}). In good agreement, a CI at a twisted geometry of the keto-type form of MS I connecting the $S_1(\pi\pi^*)$ state with the electronic GS has been calculated.¹⁵ Thus, the $S_1(\pi\pi^*)$ state does not only deactivate via fluorescence, but also non-radiatively by funneling through the CI_{S_1/S_0} , from where the photoproduct MS II in the GS is formed and the GS of MS I is repopulated. Those processes are all described by τ_3 . For MS in the liquid phase, a solvent-controlled potential energy barrier can be assumed for the exit relaxation pathway subsequent to the ESIPT process, resulting in a significantly longer excited-state lifetime observed for CHX compared to ACN.

The time constant $\tau_2 \approx 5$ ps is tentatively ascribed to vibrational relaxation of the keto-type form of MS I towards the CI_{S_1/S_0} and to the $S_{1,\text{MS I}}$ minimum. This is in line with the TVAS data, where a slight blue-shift of the $S_{1,\text{MS I}}$ vibrational marker bands at early times is observed. After the ESIPT, the vibrationally excited molecules stay in the $S_{1,\text{MS I}}$ state for a certain time. Apart from fluorescence, the radiationless exit channel back to the GS is reached (with τ_2), when the ester moiety starts to rotate, leading to the CI_{S_1/S_0} .

From the global SVD analysis of the TEAS data, the evolution-associated difference spectra (EADS) are obtained (cf. SI, Fig. 7.11). Here, EADS3 represents the S_1 state. In both solvents, EADS2 evolves to EADS3 with τ_2 and features an almost similar spectral shape as EADS3. Thus, it can be supposed that they arise from the same excited state. In the literature,²² comparable values of $\tau_2 \approx 9\text{--}14\text{ ps}$ are reported for homosalate (HMS) in ACN and CHX solutions, and are assigned to vibrational cooling and internal conversion to the GS.

Moreover, deactivation via intersystem crossing (ISC) to the triplet state is discussed for MS and HMS.^{22,24,54} The absorption of the triplet manifold is centered at $\sim 420\text{ nm}$.^{22,54} In good agreement, we assign the very weak and spectrally broad contribution at 400 nm that was observed in the TEAS spectra at late delay times ($\Delta t \sim 1.5\text{ ns}$) to the triplet state. The decay of the triplet state cannot be followed in time by our time-resolved spectroscopic techniques as this process takes much longer time.^{22,54} The processes after photoexcitation of MS I in solution are summarised in Fig. 7.10.

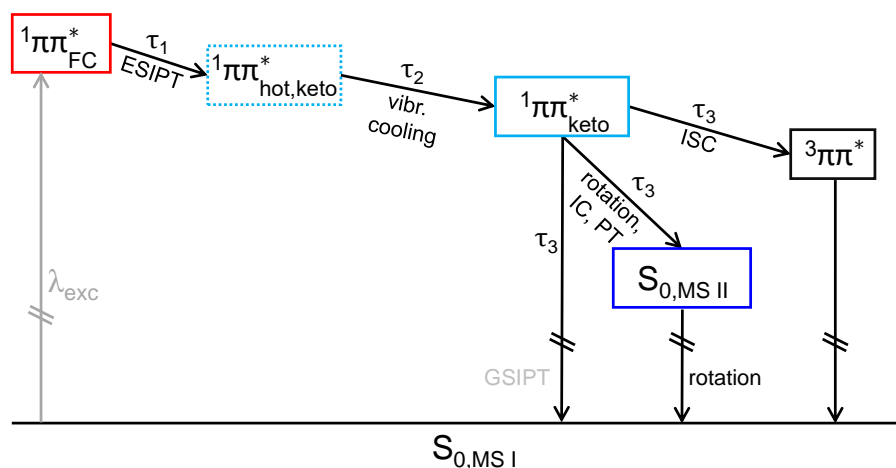


Figure 7.10: Proposed deactivation mechanism for rotamer MS I in the liquid phase after photoexcitation.

As discussed previously, $\tau_4 \approx 1.15\text{ ns}$ corresponds to the lifetime of the S_1 ($\pi\pi^*$) state of MS II, which coexists in very small concentrations in solution.

7.5 Conclusions

We presented a comprehensive study on the photo-induced dynamics of methyl salicylate in ACN and CHX solutions. Based on our results, we conclude that

rotamer MS II, which cannot undergo the ESIPT reaction, is the origin of the near-UV fluorescence. MS II is stabilised in polar, aprotic solvents and exhibits an excited-state lifetime of $\tau_{\text{MS II}} \approx 1.15$ ns. For MS I, the thermal stable rotameric form, photoexcitation leads to a rapid excited-state intramolecular proton transfer within $\tau_1 \leq 100$ fs. From the vibrationally excited $S_1(\pi\pi^*)$ state of the proton-transferred species several radiative and non-radiative relaxation channels are detected: (i) Ground-state recovery of the initially excited enol-type species of MS I, (ii) photoproduct formation, and (iii) intersystem crossing to the triplet state. Owing to the structure sensitivity of TVAS, the photoproduct is identified as rotamer MS II in the electronic GS that arises by an internal rotation of 180° of the ester moiety. The $S_1(\pi\pi^*)$ excited-state lifetime with $\tau_{3,\text{ACN}} \approx 115$ ps and $\tau_{3,\text{CHX}} \approx 300$ ps strongly depends on the used solvent. Our results thus provide a valuable insight into the electronic deactivation pathways of MS in solution. By using a variety of time-resolved spectroscopic techniques and quantum chemical calculations, not only a detailed understanding of the underlying processes, but also identification of the involved species has been established step by step.

References

- (1) Ley, H.; Engelhardt *Zeitschrift für Phys. Chemie* **1910**, *74*, 1–64.
- (2) Weller, A. *Naturwissenschaften* **1955**, *42*, 175–176.
- (3) Weller, A. *Z. Elektrochem.* **1956**, *60*, 1144–1147.
- (4) Sandros, K. *Acta Chem. Scand. A* **1976**, *30*, 761–763.
- (5) Goodman, J; Brus, L. E. *J. Am. Chem. Soc.* **1978**, *100*, 7472–7474.
- (6) Klöpffer, W.; Kaufmann, G. *J. Lumin.* **1979**, *20*, 283–289.
- (7) Ford, D; Thistlethwaite, P. J.; Woolfe, G. J. *Chem. Phys. Lett.* **1980**, *69*, 246–250.
- (8) Acuña, A. U.; Catalán, J; Toribio, F. *J. Phys. Chem.* **1981**, *85*, 241–245.
- (9) Toribio, F.; Catalán, J.; Amat, F.; Acuña, A. U. *J. Phys. Chem.* **1983**, *87*, 817–822.
- (10) Helmbrook, L. A.; Kenny, J. E.; Kohler, B. E.; Scott, G. W. *J. Phys. Chem.* **1983**, *87*, 280–289.
- (11) Orton, E.; Morgan, M. A.; Pimentel, G. C. *J. Phys. Chem.* **1990**, *94*, 7936–7943.
- (12) Herek, J.; Pedersen, S.; Bañares, L.; Zewail, A. H. *J. Chem. Phys.* **1992**, *97*, 9046–9061.
- (13) Law, K. Y.; Shoham, J. *J. Phys. Chem.* **1994**, *98*, 3114–3120.
- (14) Douhal, A.; Lahmani, F.; Zewail, A. H. *Chem. Phys.* **1996**, *207*, 477–498.
- (15) Coe, J. D.; Levine, B. G.; Martínez, T. J. *J. Phys. Chem. A* **2007**, *111*, 11302–11310.
- (16) Massaro, R. D.; Dai, Y.; Blaisten-Barojas, E. *J. Phys. Chem. A* **2009**, *113*, 10385–10390.
- (17) Massaro, R. D.; Blaisten-Barojas, E. *J. Chem. Phys.* **2011**, *135*, 164306.
- (18) Zhou, P.; Hoffmann, M. R.; Han, K.; He, G. *J. Phys. Chem. B* **2015**, *119*, 2125–2131.
- (19) Ghosh, S.; Thomas, J.; Huang, W.; Xu, Y.; Jäger, W. *J. Phys. Chem. Lett.* **2015**, *6*, 3126–3131.

- (20) Catalán, J. *Phys. Chem. Chem. Phys.* **2012**, *14*, 8903–8909.
- (21) Ling, F.; Liu, D.; Li, S.; Li, W.; Zhang, B.; Wang, P. *J. Chem. Phys.* **2019**, *151*, 094302.
- (22) Holt, E. L.; Krokidi, K. M.; Turner, M. A.; Mishra, P.; Zwier, T. S.; Rodrigues, N. D.; Stavros, V. G. *Phys. Chem. Chem. Phys.* **2020**, *22*, 15509–15519.
- (23) Watwiangkham, A.; Roongcharoen, T.; Kungwan, N. *J. Photochem. Photobiol. A Chem.* **2020**, *389*, 112267.
- (24) Chang, X. P.; Zhang, T. S.; Fang, Y. G.; Cui, G. *J. Phys. Chem. A* **2021**, *125*, 1880–1891.
- (25) Acuña, A. U.; Amat-Guerri, F.; Catalán, J.; González-Tablas, F. *J. Phys. Chem.* **1980**, *84*, 629–631.
- (26) Mori, N.; Asano, Y.; Tsuzuki, Y. *Bull. Chem. Soc. Jpn.* **1968**, *42*, 488–491.
- (27) Melandri, S.; Giuliano, B. M.; Maris, A.; Favero, L. B.; Ottaviani, P.; Velino, B.; Caminata, W. *J. Phys. Chem. A* **2007**, *111*, 9076–9079.
- (28) Smith, K. K.; Kaufmann, K. J. *J. Phys. Chem.* **1981**, *85*, 2895–2897.
- (29) Schwalb, N. K.; Temps, F. *J. Phys. Chem. A* **2009**, *113*, 13113–13123.
- (30) Pancur, T.; Schwalb, N. K.; Renth, F.; Temps, F. *Chem. Phys.* **2005**, *313*, 199–212.
- (31) Renth, F.; Siewertsen, R.; Strübe, F.; Mattay, J.; Temps, F. *Phys. Chem. Chem. Phys.* **2014**, *16*, 19556–19563.
- (32) Megow, S.; Fitschen, H. L.; Tuczek, F.; Temps, F. *J. Phys. Chem. Lett.* **2019**, *10*, 6048–6054.
- (33) Megow, S. Ultrafast Dynamics of Spin-Crossover Complexes with Photochromic Ligands Investigated by Time-Resolved Electronic Absorption Spectroscopy, Dissertation, Christian-Albrechts-Universität zu Kiel, 2022.
- (34) Van Stokkum, I. H. M.; Larsen, D. S.; Van Grondelle, R. *Biochim. Biophys. Acta* **2004**, *1657*, 82–104.
- (35) Böhnke, H.; Bahrenburg, J.; Ma, X.; Röttger, K.; Näther, C.; Rode, M. F.; Sobolewski, A. L.; Temps, F. *Phys. Chem. Chem. Phys.* **2018**, *20*, 2646–2655.
- (36) Hamm, P.; Kaundl, R. A.; Stenger, J. *Opt. Lett.* **2000**, *25*, 1798–1800.

- (37) Kaindl, R. A.; Wurm, M.; Reimann, K.; Hamm, P.; Weiner, A. M.; Woerner, M. *J. Opt. Soc. Am. B* **2000**, *17*, 2086–2094.
- (38) Grubbs, M.; Orr-Ewing, A. J.; Ashfold, M. N. R. *Rev. Sci. Instrum.* **2014**, *85*, 064104.
- (39) Weigend, F.; Häser, M. *Theor. Chem. Acc.* **1997**, *97*, 331–340.
- (40) Hättig, C.; Hellweg, A.; Köhn, A. *Phys. Chem. Chem. Phys.* **2006**, *8*, 1159–1169.
- (41) Weigend, F. *Phys. Chem. Chem. Phys.* **2006**, *8*, 1057–1065.
- (42) Weigend, F.; Ahlrichs, R. *Phys. Chem. Chem. Phys.* **2005**, *7*, 3297–3305.
- (43) Weigend, F.; Häser, M.; Patzelt, H.; Ahlrichs, R. *Chem. Phys. Lett.* **1998**, *294*, 143–152.
- (44) Rappoport, D.; Furche, F. *J. Chem. Phys.* **2010**, *133*, 134105.
- (45) TURBOMOLE V7.0 2015, a development of University of Karlsruhe and Forschungszentrum Karlsruhe GmbH, 1989-2007 TURBOMOLE GmbH, since 2007; available from <http://www.turbomole.com>.
- (46) Hättig, C.; Weigend, F. *J. Chem. Phys.* **2000**, *113*, 5154–5161.
- (47) Hättig, C.; Hald, K. *Phys. Chem. Chem. Phys.* **2002**, *4*, 2111–2118.
- (48) Hättig, C. *J. Chem. Phys.* **2003**, *118*, 7751–7761.
- (49) Hättig, C.; Köhn, A. *J. Chem. Phys.* **2002**, *117*, 6939–6951.
- (50) Hättig, C.; Köhn, A.; Hald, K. *J. Chem. Phys.* **2002**, *116*, 5401–5410.
- (51) Frieese, D. H.; Törk, L.; Hättig, C. *J. Chem. Phys.* **2014**, *141*, 194106.
- (52) Kesharwani, M. K.; Brauer, B.; Martin, J. M. *J. Phys. Chem. A* **2015**, *119*, 1701–1714.
- (53) Lochbrunner, S.; Schultz, T.; Schmitt, M.; Shaffer, J. P.; Zgierski, M. Z.; Stolow, A. *J. Chem. Phys.* **2001**, *114*, 2519–2522.
- (54) Lüdemann, H. C.; Hillenkamp, F.; Redmond, R. W. *J. Phys. Chem. A* **2000**, *104*, 3884–3893.

7.6 Supporting Information

The amplitudes from the global analyses of the TFLS data by the up-conversion technique in both solvents are summarised in Table 7.3.

Table 7.3: Relative amplitudes A_i from the global analyses of the TFLS data after excitation at $\lambda_{\text{exc}} = 305$ nm in ACN and CHX.

solvent	$\lambda_{\text{fl}} / \text{nm}$	$A_1 / [\%]$	$A_2 / [\%]$	$A_3 / [\%]$	$A_4 / [\%]$
ACN	330	100	0	0	0
	340	99	0	0	1
	360	85	9	0	6
	410	47	11	42	0
	430	25	13	62	0
	450	22	15	63	0
	540	60	21	19	0
	560	61	21	18	0
CHX	330	100	0	0	–
	340	100	0	0	–
	360	77	14	9	–
	410	33	10	57	–
	430	6	13	81	–
	450	11	15	74	–
	540	59	20	21	–
	550	40	32	28	–

Below $\lambda_{\text{fl}} \leq 340$ nm, the signal is dominated by the impulsive Raman response of the used solvent ($\tau_1 = \tau_{\text{Raman}} \leq \sigma_{\text{IRF}} \approx 180$ fs). Exclusively in ACN, a fourth

time constant (τ_4) is needed to describe the data. The long-lived fluorescence observed at 340 nm and 360 nm is described by $\tau_4 = 1.20 \pm 0.20$ ns.

The DADS and EADS from the global SVD analyses of the TEAS data in ACN (left column) and CHX (right column) are presented in Fig. 7.11. EADS1 is related to the Franck–Condon region of the photo-excited $S_1(\pi\pi^*)$ state.

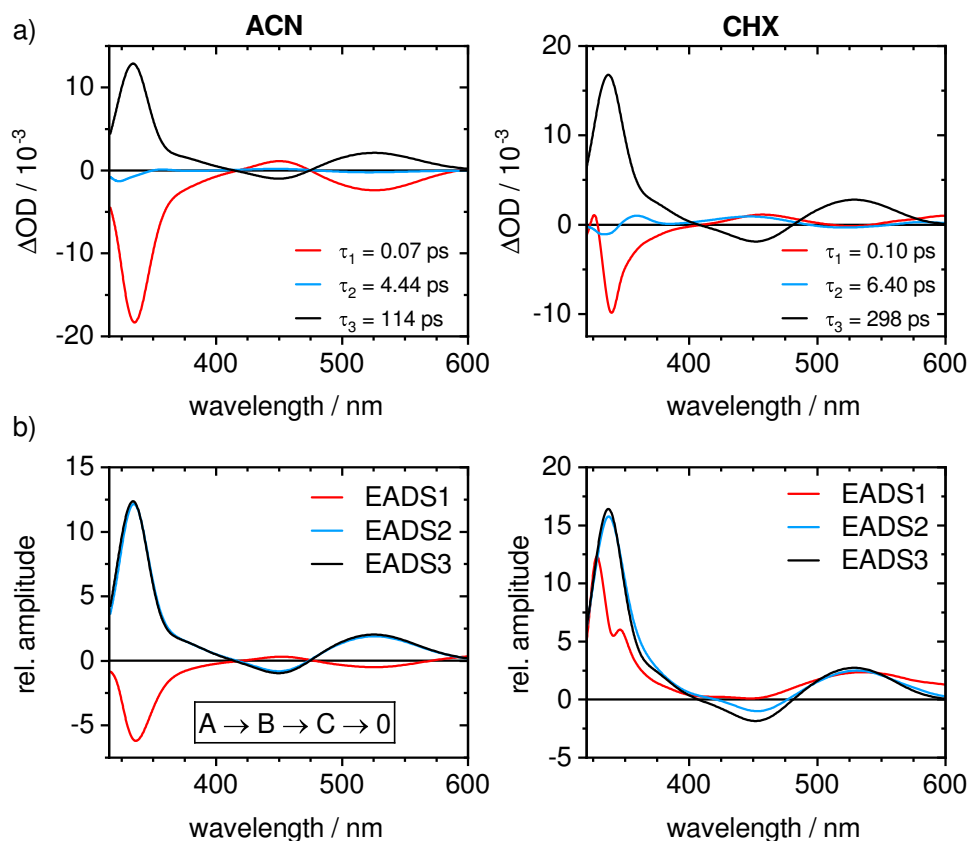


Figure 7.11: a) Decay-associated difference spectra (DADS) and b) evolution-associated difference spectra (EADS) from the global SVD data analysis of the TEAS data for MS in ACN (left column) and in CHX (right column) after excitation at $\lambda_{\text{exc}} = 313$ nm along with the kinetic scheme used for both solvents.

In ACN, the negative signals at 335 nm and 530 nm arise from stimulated emission, whereas in CHX the positive contributions at 330 nm and 545 nm arise from excitation to higher-lying electronic states. EADS1 looks different in both solvents, because in this spectral range positive and negative signals overlap. This can be seen from the wavelength-dependent amplitudes which are visualised by the DADS. Evolution to EADS2 takes place with τ_1 , leading to the

formation of the vibrationally hot proton-transferred keto-type species of MS I (EADS2) as described previously. In both solvents, EADS2 evolves to EADS3 with τ_2 and both feature an almost similar spectral shape. Hence, EADS3 is attributed to the relaxed S_1 state of the keto-type species of MS I. Subsequently, three deactivation channels from the S_1 minimum are accessible: photoproduct formation, ground-state recovery and ISC to the triplet manifold.

The FTIR spectra and calculated vibrational spectra in the GS for both MS rotamers are depicted in Fig. 7.12. Visualisations of the calculated vibrational marker modes of MS I and MS II in the spectral region from 1200 to 1800 cm^{-1} are given in Fig. 7.13 and Fig. 7.14. The positions of the experimental bands in ACN- d_3 and CHX nicely agree with the calculated ground-state vibrational spectrum of rotamer MS I. However, the position of the calculated vibrational band at 1375 cm^{-1} does not fit with the experiment. This band is observed experimentally at 1330 cm^{-1} and splits into two vibrational bands in both solvents. As this band is associated with a bending motion of the hydrogen that forms the intramolecular hydrogen bond (cf. Fig. 7.13), we conclude that the influence of the solvent on the intramolecular hydrogen bond is poorly described by the calculations, which were done in vacuo. The calculated vibrational marker modes of the keto-type form of MS I in the $S_1(\pi\pi^*)$ state are visualised in Fig. 7.15.

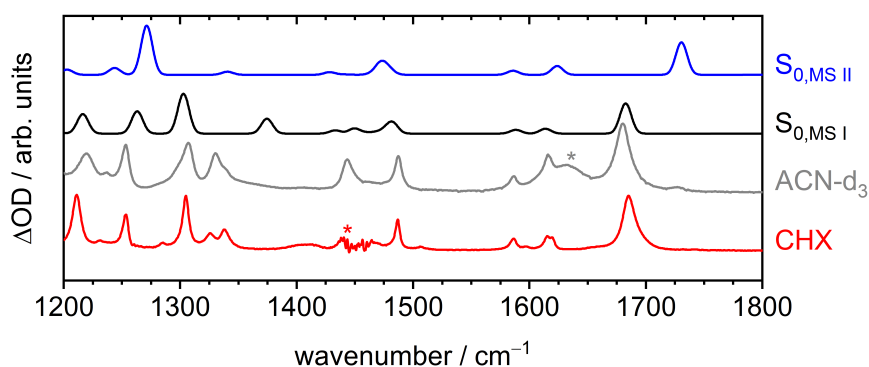


Figure 7.12: Experimental FTIR spectra of MS in CHX (red) and ACN- d_3 (grey) and calculated vibrational spectra of rotamer MS I (black) and MS II (blue) in the GS in the spectral range from 1200–1800 cm^{-1} . The signature at 1450 cm^{-1} in CHX and at 1635 cm^{-1} in ACN- d_3 labelled with an asterisk resemble artefacts from the solvent.

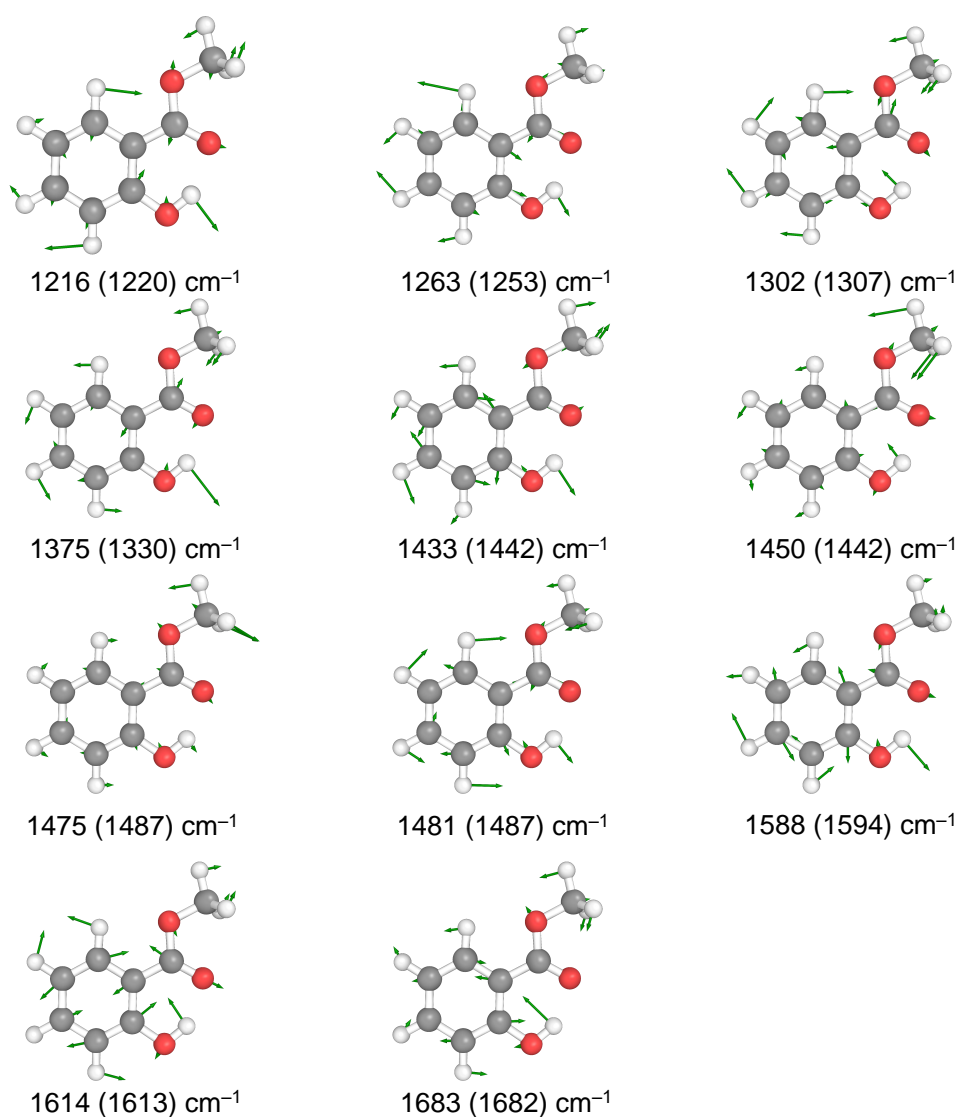


Figure 7.13: Visualisations of the experimental (in ACN- d_3) and calculated vibrational marker modes of rotamer MS I in the electronic GS. The calculated values are given first and are scaled by a factor of 0.973. Experimental values are given in parenthesis.

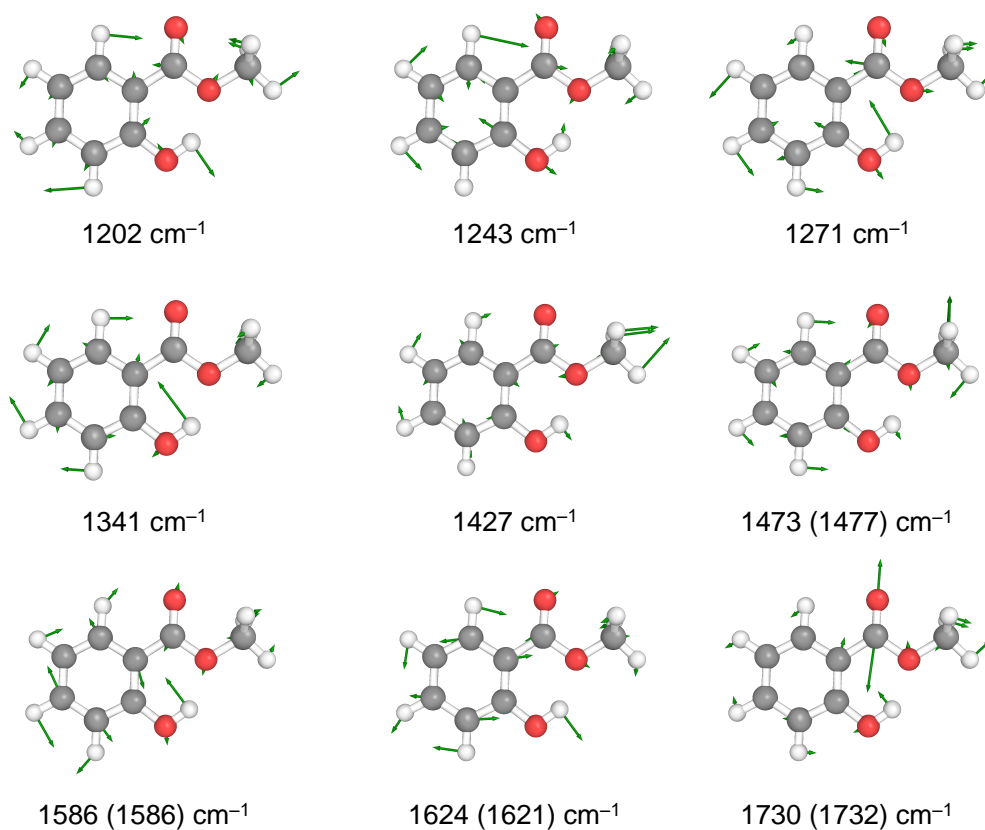


Figure 7.14: Visualisations of the experimental (in ACN- d_3) and calculated vibrational marker modes of rotamer MS II in the electronic GS. The calculated values are given first and are scaled by a factor of 0.973. Experimental values are given in parenthesis.

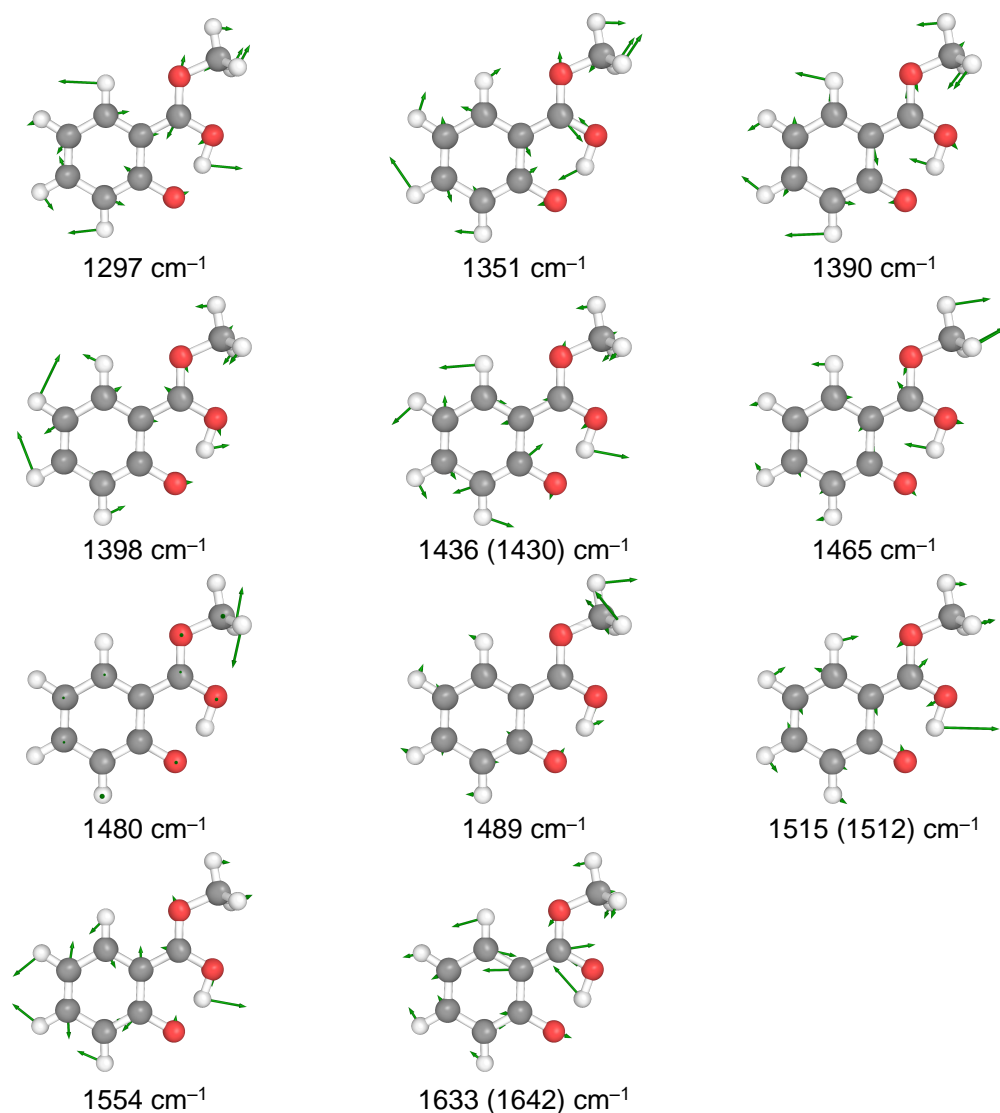


Figure 7.15: Visualisations of the experimental (in ACN- d_3) and calculated vibrational marker modes of the keto-type form of MS I in the $S_1(\pi\pi^*)$ state. The calculated values are given first and are scaled by a factor of 0.985. Experimental values are given in parenthesis.

Summaries of the TVAS results from the global data analyses for MS after photoexcitation in ACN-d₃ and CHX are given in Table 7.4 and Table 7.5, respectively. Additionally, two more TVAS data sets in the spectral region from 1200–1350 cm⁻¹ for MS in ACN-d₃ after excitation at $\lambda_{\text{exc}} = 313$ nm along with selected time profiles of that spectral regions are shown in Fig. 7.16 and Fig. 7.17, respectively.

Table 7.4: Summary of the TVAS data for MS in ACN-d₃ alongside with the relative amplitudes A_i of the time constants from the global data analysis.

$\nu_{\text{exp}} / \text{cm}^{-1}$	$\nu_{\text{calc}} / \text{cm}^{-1}$	assignment	$A_2 / [\%]$	$A_3 / [\%]$
1732	1730	S ₀ , MS II	3	97
1682	1683	S ₀ , MS I	6	94
1642	1633	S ₁ , MS I (keto)	7	93
1613	1614	S ₀ , MS I	6	94
1621	1624	S ₀ , MS II	3	97
1594	1588	S ₀ , MS I	6	94
1586	1586	S ₀ , MS II	3	97
1512	1554	S ₁ , MS I (keto)	4	96
1487	1481	S ₀ , MS I	21	79
1477	1473	S ₀ , MS II	28	72
1442	1450	S ₀ , MS I	47	53
1430	1436	S ₁ , MS I (keto)	3	97

Table 7.5: Summary of the TVAS data for MS in CHX alongside with the relative amplitudes A_i of the time constants from the global data analysis.

$\nu_{\text{exp}} / \text{cm}^{-1}$	$\nu_{\text{calc}} / \text{cm}^{-1}$	assignment	$A_2 / [\%]$	$A_3 / [\%]$
1750	1730	S_0 , MS II	30	70
1690	1683	S_0 , MS I	10	90
1639	1633	S_1 , MS I (keto)	6	94
1619	1624	S_0 , MS II	30	70
1614	1614	S_0 , MS I	10	90
1390	1391	S_1 , MS I (keto)	6	94
1337	1375	S_0 , MS I	8	92
1331	1340	S_0 , MS II	30	70
1324	1375	S_0 , MS I	8	92
1300	1298	S_1 , MS I (keto)	6	94
1300	1303	S_0 , MS I	8	92

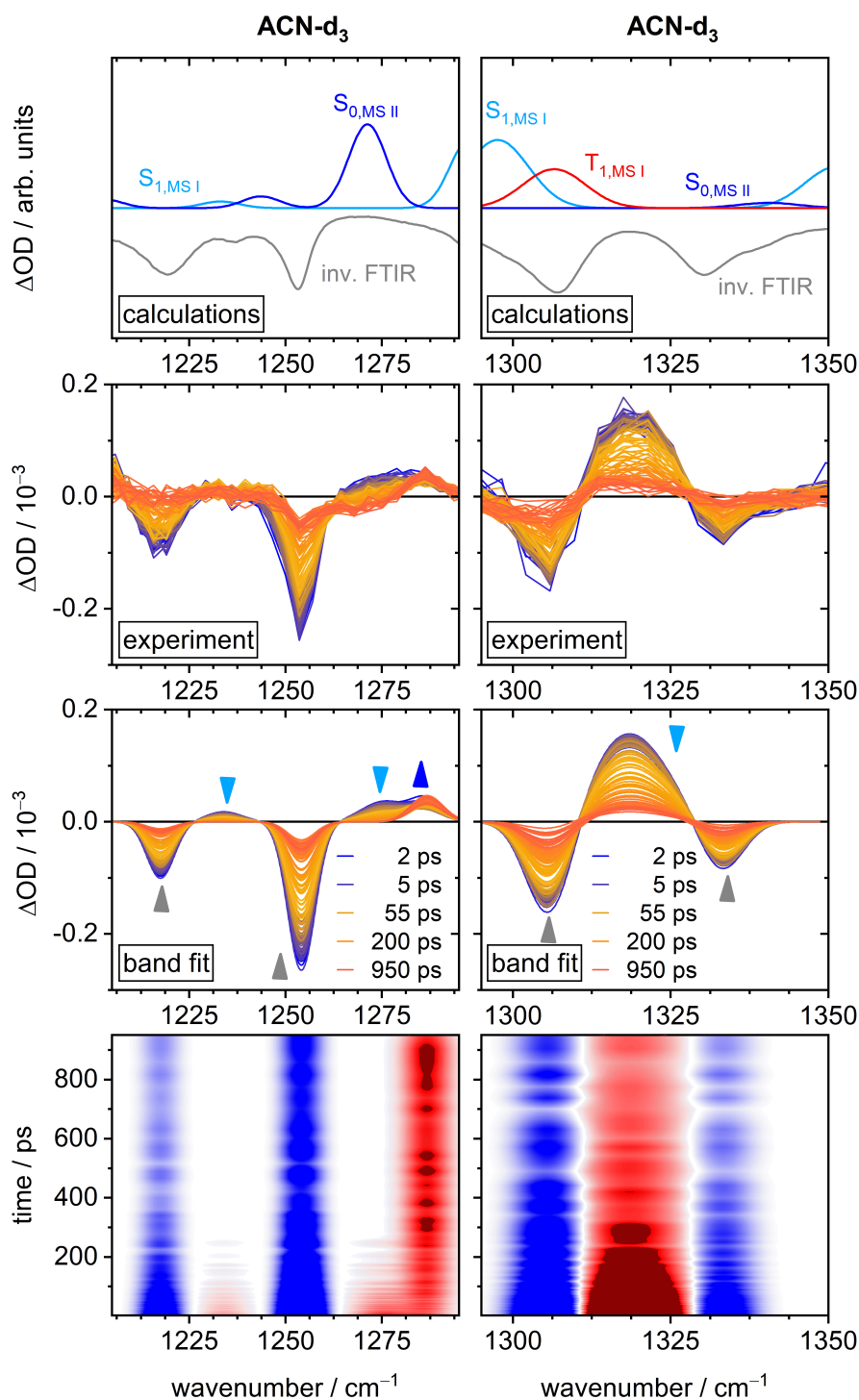


Figure 7.16: TVAS measurements of MS after excitation at $\lambda_{\text{exc}} = 313$ nm in ACN- d_3 . Calculations: Computed vibrational spectra of MS II in the GS and the keto-type form of MS I in the $S_1(\pi\pi^*)$ and $T_1(\pi\pi^*)$ states, respectively, alongside with the inverted experimental FTIR spectrum. Experiment: Recorded TVA spectra at different delay times. Band fit: Corresponding global band fits to the experimental TVA spectra. At the bottom the colour-coded two-dimensional spectro-temporal absorption maps are presented.

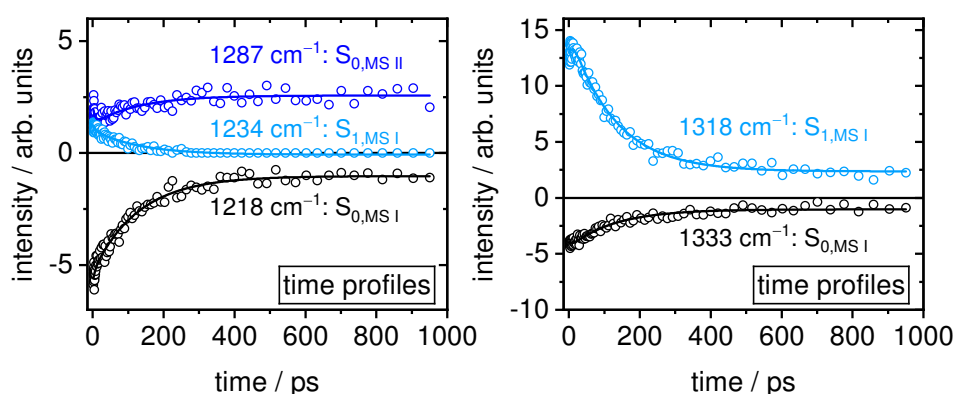


Figure 7.17: Selected time profiles of the GS (black), the photoproduct MS II in the GS (dark blue) and of the keto-type form of MS I in the $S_1(\pi\pi^*)$ state (light blue) in ACN- d_3 after excitation at $\lambda_{\text{exc}} = 313$ nm. Shown are the amplitudes from the global band fitting (circles) and the global fits (straight lines) obtained by a sum of two exponentials. In the spectral region from 1205–1295 cm^{-1} (left) $\tau_2 = (6.10 \pm 4.40)$ ps and $\tau_3 = (129 \pm 12.0)$ ps and from 1295–1350 cm^{-1} (right) $\tau_2 = (9.40 \pm 5.60)$ ps and $\tau_3 = (127 \pm 10.0)$ ps were determined, respectively.

Part III

Concluding Discussion

Discussion

This Thesis represents an exploratory study of the new femtosecond time-resolved vibrational absorption spectrometer in our work group. With this experimental setup, a variety of deactivation and reaction processes in electronically excited molecules were investigated. Highly relevant molecular systems, whose photo-induced dynamics have not previously been well understood, were selected. In the following a critical evaluation of the experiment will be given.

8.1 Experimental requirements

In order to record reliable time-resolved vibrational spectra, high and long-term stability of the applied UV/vis pump and mid-infrared probe pulses must be ensured. For the generation of the pump pulses in the present Thesis, an overall energy of 0.3 mJ / pulse was available. This worked perfectly for UV pump pulses at $\lambda_{\text{exc}} = 267$ nm, which were generated via frequency tripling of the Ti:Sa fundamental. The employed “Femtokit” was easy to adjust and provided highly stable pump pulses with sufficient pump energies of $E_{\text{pump}} = 1.5 \mu\text{J}$ / pulse. In contrast, for the pump pulses at $\lambda_{\text{exc}} = 313$ nm a maximum energy of $E_{\text{pump}} = 300$ nJ / pulse reached the sample cell. A noticeable loss of energy was not only observed at the prism compressor, but also at the retroreflector, which was not equipped with highly reflective mirrors for this particular wavelength. Accordingly, a retroreflector with highly reflective mirrors suited for λ_{exc} will help to significantly reduce the energy loss in future experiments. Since the generation of $\lambda_{\text{exc}} = 313$ nm required more frequency conversions, including the NOPA setup and the SFG process, the pump pulses at $\lambda_{\text{exc}} = 313$ nm were more prone to instabilities and had to be adjusted before each measurement. These problems could be avoided in the future, provided that more energy (> 0.3 mJ / pulse) for the pump pulse generation is available.

The generation of long-term stable mIR probe pulses was more complex. The two-staged OPA as well as the DFG process had to be adjusted on a daily basis. In terms of stability, it turned out that the temporal arrival of the 800 nm laser

beam of the second amplification stage at the OPA crystal as well as the temporal arrival of the signal laser beam at the DFG crystal (cf. Fig. 2.4) were decisive. After the corresponding frequency conversion (OPA, DFG), a balance between the obtained energy and the pulse stability had to be found. This was done by careful adjustment of the delay stages inserted into the probe beam path. Due to the low absorbances of the detected vibrational bands, ranging typically from 0.1 to 1.0 mOD, up to 30 individual measurements were averaged prior to data analysis. The measurement of an averaged data set took between 10 and 15 hours. During this period of time, a sufficient stability of the laser pulses had to be assured to record high-quality data.

Since the mid-infrared probe pulses exhibit a spectral bandwidth of $\sim 150\text{ cm}^{-1}$, up to 5 individual data sets were recorded for each molecule in order to cover a spectral range from 1750 cm^{-1} up to 1200 cm^{-1} . Subsequently, these individual baseline-corrected data sets had to be spliced together for each molecule, yielding the overviews of the transient vibrational spectra presented in this Thesis. In the future, this would be easier and faster to achieve with an MCT detector array equipped with a higher number of individual elements, e.g., by replacing the 32-pixel MCT detector array with a 64- or 128-pixel detector array.

The sample solutions were irradiated with high-energy UV/vis pump pulses ($E_{\text{pump}} \leq 1\text{ }\mu\text{J}$ / pulse) for hours. Therefore, the investigated molecules had to possess a high photostability. The condition for each sample was easily controllable with static UV/vis absorption spectroscopy. Whenever necessary, the pump energy was reduced until the sample integrity was guaranteed. Furthermore, the sample molecules had to be soluble in high concentrations in the used solvents because the thickness of the sample cell was solely 0.1 mm. The latter was required to reduce absorption of the mid-infrared probe intensity by the solvent. In this Thesis, deuterated acetonitrile (ACN- d_3) and cyclohexane (CHX) were used as solvents, because they provide high transmission of the mIR probe intensity in the spectral region of $1100\text{--}1750\text{ cm}^{-1}$. Apart from measurements from 1460 to 1510 cm^{-1} , D_2O was also found to be suitable for TVAS experiments.

8.2 Data analysis and interpretation

The results reported in Chapters 3–7 highlight that valuable new insights into the deactivation and reaction dynamics occurring after photoexcitation were

unravelling by TVAS. Owing to its structure sensitivity, the identities of previously unknown photoproducts and intermediates were unambiguously elucidated. At this point, some examples from this work should be listed: (i) For acetylacetone a photoproduct was identified as the CTC enolic isomer, arising by *cis-trans* isomerisation around the C=C double bond. (ii) The first direct experimental evidence for the population of a twisted wagged intramolecular charge transfer state was provided for N^6,N^6 -dimethyladenine. (iii) For methyl salicylate, a novel non-radiative deactivation pathway via photoproduct formation was detected. (iv) The experimental data for 9- and 7-methylpurine confirmed efficient populations of the optically dark $S_1(n\pi^*)$ and $T_1(\pi\pi^*)$ states, respectively. (v) Moreover, even non-dominant deactivation channels as detected for 9-MePur, or diffuse signatures arising from vibrationally hot intermediates as observed for DMAde were unveiled and identified.

However, the early-time dynamics in the TVAS experiments after photoexcitation were dominated by transient artifacts induced by the pump pulse. The intensity and the duration of the apparent transient lensing processes depend on the pump power E_{pump} , the used solvent, the sample concentration, the focusing conditions, as well as on the investigated spectral region. In general, it was found that transient lensing lasted longer with increasing probe wavelength. Therefore, observation of ultrafast events taking place at $\Delta t \leq 2\text{--}4$ ps were hardly feasible. In this Thesis, additional measurements using other femtosecond time-resolved spectroscopic techniques, like fluorescence spectroscopy and/or time-resolved electronic absorption spectroscopy, were required to gain insights into the early-time dynamics. This approach was successfully adopted in the present Thesis to complement the experimental data. However, a systematic study of, for example, the focusing conditions could also help to shorten and mitigate transient lensing in future experiments.

Complex TVAS data as recorded for N^6,N^6 -dimethyladenine are difficult to analyse. This is the case, when the detected excited-state and ground-state signals strongly differ in intensity, vibrational bands arising from different electronic states and structures tend to overlap, and/or pronounced spectral shifts of the vibrational bands are present. Accordingly, it becomes difficult to unravel all experimental vibrational signatures. As for DMAde, the transient vibrational spectra were poorly described by a sum of Gaussians. To extract the temporal information from the data, the amplitudes at single probe wavelength were

plotted as function of time. Although a global data analysis for DMAd failed, reliable results were obtained, confirmed by comparison of the TVAS data with the literature and other employed spectroscopic techniques. While extracting kinetic insights from the TVAS data might be difficult, the detection of distinct state-specific spectroscopic signatures to identify the species involved nevertheless has been successful and is (in some cases) of greater interest.

Although some experimental requirements and limitations as mentioned previously had to be overcome, the work performed in the present Thesis highlights that time-resolved vibrational absorption spectroscopy provides highly reliable results. Accordingly, virtually perfect agreement with other ultrafast experiments as reported in the literature^{1–4} was observed. The powerful combination of TVAS and quantum chemical calculations unravelled the underlying deactivation dynamics after photoexcitation of the investigated molecules and led to a deeper understanding of the relationship between chemical and electronic structure. More importantly, those valuable new insights are not accessible by TFLS or TEAS because both those methods lack structure sensitivity.

References

- (1) Crespo-Hernández, C. E.; Martínez-Fernández, L.; Rauer, C.; Reichardt, C.; Mai, S.; Pollum, M.; Marquetand, P.; González, L.; Corral, I. *J. Am. Chem. Soc.* **2015**, *137*, 4368–4381.
- (2) Verma, P. K.; Koch, F.; Steinbacher, A.; Nuernberger, P.; Brixner, T. *J. Am. Chem. Soc.* **2014**, *136*, 14981–14989.
- (3) Demeter, A.; Druzhinin, S. I.; Kovalenko, S. A.; Senyushkina, T. A.; Zachariasse, K. A. *J. Phys. Chem. A* **2011**, *115*, 1521–1537.
- (4) Holt, E. L.; Krokidi, K. M.; Turner, M. A.; Mishra, P.; Zwier, T. S.; Rodrigues, N. D.; Stavros, V. G. *Phys. Chem. Chem. Phys.* **2020**, *22*, 15509–15519.

Summary

The goal of the present Thesis was to evaluate the new TVAS setup in the laboratory of our group by unravelling key steps of the deactivation and reaction dynamics for selected molecules in their electronically excited states. The obtained results for the studied molecular systems are summarised in this Chapter.

For the methylated purine analogues 7- and 9-methylpurine, the previously proposed relaxation mechanism¹ was confirmed and updated by TVAS. Valuable new details on the dynamic processes were provided as this method allows for structure-sensitive detection. After photoexcitation, efficient population of the optically dark $S_1(n\pi^*)$ state occurred, followed by intersystem crossing towards the $T_1(\pi\pi^*)$ state for both isomers. While the early-time dynamics proceeded on similar time scales, significantly different excited-state lifetimes of the $S_1(n\pi^*)$ state were determined:

$$\tau_{3,\text{TVAS}}(7\text{-MePur}) = 250 \pm 30.0 \text{ ps}$$

$$\tau_{3,\text{TVAS}}(9\text{-MePur}) = 480 \pm 60.0 \text{ ps}$$

For the 9-methyl isomer, a minor deactivation channel via the relaxed $S_2(\pi\pi^*)$ state taking place on the nanosecond time scale was detected. Nonetheless, a higher ground-state recovery was observed for the latter.

$$\text{GSR}(7\text{-MePur}) = 25 \%$$

$$\text{GSR}(9\text{-MePur}) = 50 \%$$

On the one hand, the obtained results perfectly agree with literature.¹ On the other hand, major differences of the deactivation mechanisms for both isomers after photoexcitation have been elucidated by TVAS. This underlines that even small structural modifications like the position of a methyl group regulate the accessibility and efficiency of electronic relaxation pathways. This interplay between chemical and electronic structure, might help to understand, why purine

and its methylated analogues are not incorporated into the DNA and why the canonical nucleobases are functionalised at the N9 rather than at the N7 position.

N^6,N^6 -dimethyladenine in acetonitrile solution was studied by different ultrafast spectroscopic techniques. The complex photo-induced dynamics were unveiled step by step. TVAS indeed provided the first experimental evidence for the ICT mechanism for DMAd. The combination of quantum chemical calculations and TVAS as structure-sensitive method revealed that pronounced structural modifications took place in electronically excited DMAd. More precisely, the dimethylamino group is strongly tilted and twisted by $\vartheta \sim 60^\circ$ with respect to the purine ring. This detected structure was therefore referred to as twisted-wagged intramolecular charge transfer state (TWICT). Further, diffuse intermediate contributions were observed experimentally and could be assigned to a distribution of vibrationally hot structures with partial twisting and wagging angles. From all employed time-resolved measurements, four time components were found:

$$\tau_1 \approx 0.3 \text{ ps}$$

$$\tau_2 \approx 1.6 \text{ ps}$$

$$\tau_3 \approx 20. \text{ ps}$$

$$\tau_4 \approx 1.0 \text{ ns}$$

After $S_1(\pi\pi^*)$ photoexcitation, depopulation of the initially excited Franck–Condon region proceeded with τ_1 . Once the molecules reached the $\pi\pi_{LE}^*$ minimum, ultrafast ground-state recovery and population of the $\pi\pi_{TWICT}^*$ state were observed. For both processes, a time constant of $\tau_2 \approx 1.6 \text{ ps}$ was determined, which corresponds to the excited-state lifetime of the $\pi\pi_{LE}^*$ state. While time component τ_3 was associated with the decay of the hot pTWICT structures, the relaxed $\pi\pi_{TWICT}^*$ state deactivated on the nanosecond time scale with τ_4 . Furthermore, intersystem crossing to a triplet state was proposed, which was indicated by a permanent offset in the TEAS data. Compared to adenine, methylation of the diamino group in DMAd opened up new deactivation pathways that took place on significant longer time scales. An adenine-like ultrafast relaxation via C^2 -puckering of the short-lived $\pi\pi_{LE}^*$ state competed with the structural rearrangement in the excited state leading to population of the pTWICT and

TWICT state, respectively.

Photoexcitation of acetylacetone in its enolic form led to formation of non-chelated isomers. However, the identity of the latter as well as the details on the mechanism towards photoproduct formation were poorly understood to date. In principle, seven different non-chelated isomers exist for AA (cf. Fig. 6.1). Here, the photoproduct of AA was identified as the previously proposed,² but to date elusive CTC enolic isomer that is formed via a *cis-trans* isomerisation around the C=C double bond. The TVAS measurements impressively showed that even electronically similar isomers could be distinguished by their vibrational spectra. The photoproduct formation proceeded via two distinct pathways on the picosecond and nanosecond time scale, respectively:

$$\begin{array}{ll} \tau_{1,\text{ACN-d}_3} = 8.00 \pm 1.00 \text{ ps} & \tau_{1,\text{CHX}} = 9.00 \pm 1.00 \text{ ps} \\ \tau_{2,\text{ACN-d}_3} = 900. \pm 600. \text{ ps} & \tau_{2,\text{CHX}} = 1.25^{+1.60}_{-1.25} \text{ ns} \end{array}$$

After reaching a conical intersection $\text{CI}_{1\pi\pi^*/\text{GS}}$ that connects the initially excited $\text{S}_2(\pi\pi^*)$ state with the electronic GS, the long-lived photoproduct was formed with τ_1 . Another fraction of the initially excited molecules populated the $\text{S}_1(\text{n}\pi^*)$ state and got trapped in a local minimum. After overcoming the energy barrier with τ_2 , formation of CTC and GSR were observed. The detection of an excited-state intermediate in ACN-d₃, which was identified as the CTC isomer in its $^1\text{n}\pi^*$ state, confirmed that rotamerisation already proceeded in the excited state, which was again described by τ_1 . Additionally, intersystem crossing from the $^1\text{n}\pi^*$ state to the triplet manifold was suggested as a permanent offset remained at late delay times ($\text{GSR}_{\text{ACN-d}_3} \sim 58 \%$, $\text{GSR}_{\text{CHX}} \sim 75 \%$). The obtained results elucidated the influence of the solvent and provided a more detailed understanding on the dynamic processes after photoexcitation of AA in the liquid phase.

The last project focused on the dual fluorescence as well as on the underlying dynamic processes of electronically excited methyl salicylate in the liquid phase.

Methyl salicylate was investigated in ACN and CHX solutions by a variety of spectroscopic techniques which provided the following time constants:

$\tau_{1,\text{ACN}} \approx 0.10 \text{ ps}$	$\tau_{1,\text{CHX}} \approx 0.10 \text{ ps}$
$\tau_{2,\text{ACN}} \approx 5.00 \text{ ps}$	$\tau_{2,\text{CHX}} \approx 6.00 \text{ ps}$
$\tau_{3,\text{ACN}} \approx 115. \text{ ps}$	$\tau_{3,\text{CHX}} \approx 300. \text{ ps}$
$\tau_{4,\text{ACN}} \approx 1.15 \text{ ns}$	$\tau_{4,\text{CHX}} \approx 1.20 \text{ ns}$

The formation of the proton-transferred species of MS I in the $S_1(\pi\pi^*)$ state was unambiguously shown by TVAS. This confirmed that an ESIPT process occurred directly after photoexcitation, as proposed by Weller in 1955.³ Concurrently, no vibrational contributions of the electronically excited MS I enol form were detected in the TVAS data, making its presence unlikely. This indicated that the near-UV fluorescence originated from rotamer MS II, which coexists in small amounts in the electronic GS. To verify this assignment and to access the early-time dynamics, the emission properties of MS were systematically investigated by static and time-resolved fluorescence from the femtosecond up to the nanosecond time regime. These measurements further confirmed that rotamer MS II gave rise to the observed near-UV emission. While τ_4 corresponds to the fluorescence lifetime of MS II, the time components $\tau_1 - \tau_3$ are associated with the electronic deactivation and reaction dynamics of MS I. After S_1 excitation, a rapid ESIPT process occurred within τ_1 , followed by vibrational cooling towards the S_1 minimum with τ_2 . Concurrently, the GS of MS I was recovered and subsequent formation of a photoproduct was observed. Owing to the structure sensitivity of TVAS, the photoproduct was identified as rotamer MS II in its electronic GS which arised by a rotation of 180° of the ester moiety. Furthermore, the results revealed that a solvent-dependent potential energy barrier exists in the $S_1(\pi\pi^*)$ state reflected by different excited-state lifetimes of $\tau_{3,\text{ACN}} \approx 115 \text{ ps}$ and $\tau_{3,\text{CHX}} \approx 300 \text{ ps}$.

To conclude, the present Thesis underlines that TVAS, which allows for time-resolved and structure-sensitive detection, is perfectly suited to unravel complex deactivation and reaction processes in electronically excited molecules. It provides state-specific spectroscopic signatures of the involved species and thus elucidates the molecular identity of intermediate structures and photoproducts formed after photoexcitation. Unfortunately, to gain deep insights into the

early-time dynamics, other ultrafast spectroscopic methods were required, but a detailed understanding is seldom obtained by a single method. Nevertheless, the present Thesis clearly shows that time-resolved vibrational absorption spectroscopy is a highly valuable and powerful tool in the zoo of ultrafast spectroscopy.

References

- (1) Crespo-Hernández, C. E.; Martínez-Fernández, L.; Rauer, C.; Reichardt, C.; Mai, S.; Pollum, M.; Marquetand, P.; González, L.; Corral, I. *J. Am. Chem. Soc.* **2015**, *137*, 4368–4381.
- (2) Veierov, D; Bercovici, T; Fischer, E; Mazur, Y; Yogev, A *J. Am. Chem. Soc.* **1977**, *99*, 2723–2729.
- (3) Weller, A. *Naturwissenschaften* **1955**, *42*, 175–176.

Part IV

Appendix

Danksagung

An dieser Stelle möchte ich mich bei allen bedanken, die maßgeblich zum Gelingen dieser Arbeit beigetragen haben.

Herrn Prof. Temps danke ich für die Möglichkeit und das Vertrauen an einem so spannenden und vielseitigen Thema eigenständig forschen zu dürfen. Ich danke Ihnen für die Unterstützung, den Ansporn und die vielen wegweisenden Momente, die diese Arbeit und mich als Wissenschaftlerin maßgeblich geprägt und vorangetrieben haben. Darüber hinaus bin ich für den Rückhalt und Ihren unermüdlichen Einsatz während der Corona-Pandemie sehr dankbar.

Ein großer Dank geht an Hendrik Böhnke ohne dessen Einsatz und Arbeit, insbesondere am IR-Experiment, meine Doktorarbeit so nicht möglich gewesen wäre. Mit einer wahnsinnigen Geduld hast du mich außerdem in die komplexe Thematik der quantenchemischen Rechnungen eingearbeitet. Ich danke dir von Herzen für deine unerschöpfliche Hilfsbereitschaft und für die zahlreichen Stunden, die wir gemeinsam über meine Daten gegrübelt haben. Ich habe diese enge Zusammenarbeit als sehr bereichernd empfunden und unheimlich viel von dir lernen dürfen. Danke!

Meinen langjährigen Büro-Kumpanen Dennis und Schatzi danke ich für eine unvergessliche und stets lustige Bürozeit. Mit euch war es einfach klasse! Unsere "Unsachlichkeits"-Strichliste, eure Hilfe bei kleinen und großen PC-Problemen und die gemeinsamen Kaffeepausen werden mir sehr sehr fehlen.

Dem gesamten Arbeitskreis Temps: Hendrik, Dennis, Jonas, Megow, Schatzi, Simon, Pascal, Birthe, Simone, Vivian, Malte, Falk, Ole und Joachim danke ich für die tolle Arbeitsatmosphäre, die so manch frustrierende Labormomente doch gut abmildern konnte. Ich danke euch allen für den Zusammenhalt, die gegenseitige Unterstützung und die Hilfsbereitschaft. Danke für die schönen gemeinsamen Aktionen und Unternehmungen wie die Chemiker-Partys, kulinar-

ische Besuche des Weihnachtsmarktes und der Kieler Woche, unsere Kanu-Tour, Lasertag, Bouldern,und so vieles mehr. Ich habe euch alle sehr in mein Herz geschlossen!

Amke, Vivian und Jorunn danke ich für die engagierte und datenreiche Zusammenarbeit während ihrer Bachelor- und Masterarbeiten. Die gemeinsame Zeit im Laserkeller hat mir viel Freunde und Spaß gemacht.

Tanja und Sonja, ohne eure Hilfe wäre ich so manches Mal aufgeschmissen gewesen. Danke, dass ihr auch wiederholte Fragen zu Dienstreisen, Krankmeldungen, Formularen, Bestellungen, uvm. stets geduldig beantwortet habt. Sonja, danke dir für deinen Einsatz während der turbulenten Corona-Zeit und dafür, dass du stets ein offenes Ohr für unsere Sorgen hattest!

Joachim Gripp danke ich dafür, dass wir viele Dinge als selbstverständlich ansehen konnten, wie beispielsweise das Funktionieren der statischen Spektrometer, das Vorhandensein von Lösungsmitteln und Chemikalien, die Pflege des FTIR Spektrometers sowie die Sicherung unserer Daten. Herzlichen Dank für deinen stets verlässlichen Einsatz.

Mark und Haxhi danke ich für den elektronischen Support. Auch dank euch hat das Design der Doktorhüte ein nie dagewesenes Level erreicht, einfach großartig!

Meinen Freunden Chrissi, Belli, Kimmy, Bella, Jule, Doro und Caro danke ich von ganzen Herzen für die langjährige und wirklich einzigartige Freundschaft! Die gemeinsamen Kaffeerunden und Unternehmungen oder auch die unzähligen Spaziergänge während der Coronazeit ließen so manchen Laborfrust verblassen. Trotz weiter Distanzen und langen Zeiten des Nichtsehens seid ihr immer für mich da. Danke!

Ein unendlich großes Danke geht an meine Familie, meinen Mann Jan und die Holtmänner. Ihr habt mich immer unterstützt, motiviert und aufgebaut. Danke für euer Verständnis, den Rückhalt und dass ich euch immer an meiner Seite wissen darf!

Calculated Cartesian Coordinates

Table 9.1: Calculated cartesian coordinates (Å) of 7-MePur in the ground state optimised at the RI-SCS-MP2/def2-TZVPP level of theory.

Atom	X	Y	Z
C	-1.9789165	1.3322143	-0.0000575
N	-2.0531882	-0.0197840	0.0000657
C	-0.9094813	-0.7021684	0.0001208
C	0.2915435	0.0022381	0.0001051
C	0.2547772	1.4124076	0.0000307
N	-0.8925320	2.1019920	-0.0000550
N	1.5351385	1.9278889	0.0001067
C	2.2992963	0.8586995	0.0000542
N	1.6211303	-0.3354727	0.0000400
H	-2.9304964	1.8464076	-0.0002400
H	-0.9680883	-1.7844301	0.0001427
C	2.1886839	-1.6707603	-0.0000598
H	3.2720199	-1.5849888	-0.0001065
H	1.8752526	-2.2157568	-0.8888471
H	1.8753366	-2.2158533	0.8886978
H	3.3783938	0.8731564	0.0000022

Table 9.2: Calculated cartesian coordinates (Å) of 7-MePur in the $S_1(n\pi^*)$ state optimised at the RI-SCS-CC2/def2-TZVPP level of theory.

Atom	X	Y	Z
C	-2.0727556	1.3695889	-0.0000507
N	-2.0134001	0.0586249	-0.0000072
C	-0.8911872	-0.7461199	0.0000530
C	0.3186582	-0.0081478	0.0000695
C	0.2826855	1.3992503	0.0000429
N	-0.9238657	2.0791824	-0.0000235
N	1.5311984	1.9233990	0.0000376
C	2.3386484	0.8564878	0.0000335
N	1.6482738	-0.3370362	0.0000282
H	-3.0238503	1.8785979	-0.0001177
H	-1.0134705	-1.8169567	0.0000866
C	2.2048881	-1.6777973	-0.0000344
H	3.2894099	-1.6014007	-0.0000645
H	1.8840589	-2.2189928	-0.8894075
H	1.8841126	-2.2190518	0.8893222
H	3.4154655	0.8861622	0.0000320

Table 9.3: Calculated cartesian coordinates (Å) of 7-MePur in the $T_1(\pi\pi^*)$ state optimised at the RI-SCS-CC2/def2-TZVPP level of theory.

Atom	X	Y	Z
C	-2.5023456	0.0499444	-0.0651671
N	-2.0220732	-1.1738657	-0.0330044
C	-0.6800899	-1.5209090	-0.0265979
C	0.2058500	-0.4229381	0.0077647
C	-0.2961589	0.8969537	0.0078642
N	-1.6601595	1.1029549	0.0502171
N	0.6967946	1.8105859	-0.0105990
C	1.8187178	1.0770164	-0.0240296
N	1.5643898	-0.2804809	-0.0084328
H	-3.5674069	0.2228167	-0.0825272
H	-0.4228333	-2.5345775	-0.2942442
C	2.5325087	-1.3570251	0.0017814
H	3.5273220	-0.9274255	0.0833391
H	2.4666265	-1.9367564	-0.9176628
H	2.3514359	-2.0096375	0.8541434
H	2.8236927	1.4642173	-0.0309270

Table 9.4: Calculated cartesian coordinates (Å) of 9-MePur in the ground state optimised at the RI-SCS-MP2/def2-TZVPP level of theory.

Atom	X	Y	Z
C	-1.9019613	1.1941756	-0.0569629
N	-2.4910816	-0.0188011	-0.0298264
C	-1.7068008	-1.0997859	0.0064167
C	-0.3213136	-0.9502987	0.0151590
C	0.1503717	0.3744498	-0.0160750
N	-0.5951014	1.4775978	-0.0525462
N	1.5185917	0.2810839	-0.0009664
C	1.7936661	-1.0641892	0.0376975
N	0.7331934	-1.8450728	0.0488902
H	-2.5727553	2.0421431	-0.0858973
H	-2.1857018	-2.0708457	0.0280791
H	2.8136515	-1.4157150	0.0565326
C	2.4573248	1.3889910	-0.0220269
H	2.3014092	2.0255809	0.8457213
H	2.3174097	1.9783319	-0.9251552
H	3.4663934	0.9861985	-0.0021625

Table 9.5: Calculated cartesian coordinates (Å) of 9-MePur in the $S_2(\pi\pi^*)$ state optimised at the RI-SCS-CC2/def2-TZVPP level of theory.

Atom	X	Y	Z
C	-1.8759610	1.2468764	0.0617139
N	-2.5133205	0.0151440	0.0188032
C	-1.7621826	-1.1379320	-0.0067409
C	-0.3365431	-0.9661333	-0.0107798
C	0.1697076	0.3847736	0.0270544
N	-0.5426835	1.5510010	0.0718408
N	1.5206229	0.2589579	0.0047446
C	1.7939166	-1.1147072	-0.0478044
N	0.7014044	-1.8672277	-0.0569340
H	-2.5509537	2.0913292	0.0936627
H	-2.2656909	-2.0912759	-0.0316907
H	2.8087273	-1.4786108	-0.0674783
C	2.4823264	1.3511953	-0.0146785
H	3.3235216	1.1016570	0.6281457
H	1.9806626	2.2414795	0.3548709
H	2.8336258	1.5282495	-1.0301576

Table 9.6: Calculated cartesian coordinates (Å) of 9-MePur in the $S_1(n\pi^*)$ state optimised at the RI-SCS-CC2/def2-TZVPP level of theory.

Atom	X	Y	Z
C	-1.9406939	1.2664816	-0.0592881
N	-2.3625769	0.0280893	-0.0298959
C	-1.7263401	-1.1649600	0.0080167
C	-0.2876390	-0.9854956	0.0164409
C	0.1600836	0.3444907	-0.0151594
N	-0.5805347	1.4947650	-0.0528781
N	1.5208733	0.2651743	-0.0005162
C	1.8346643	-1.0828867	0.0385401
N	0.7552635	-1.8598770	0.0495342
H	-2.6343328	2.0906263	-0.0878589
H	-2.2792286	-2.0894830	0.0277710
H	2.8575863	-1.4203487	0.0569108
C	2.4403292	1.3910777	-0.0222118
H	2.2739764	2.0250154	0.8463850
H	2.2900164	1.9777332	-0.9262303
H	3.4558487	1.0034414	-0.0026826

Table 9.7: Calculated cartesian coordinates (Å) of 9-MePur in the $T_1(\pi\pi^*)$ state optimised at the RI-SCS-CC2/def2-TZVPP level of theory.

Atom	X	Y	Z
C	-1.9216865	1.2057995	0.0436778
N	-2.5224565	0.0398541	0.0481012
C	-1.7806368	-1.1045893	0.0483655
C	-0.3262889	-0.9619919	-0.0026655
C	0.1739541	0.3827497	0.0241309
N	-0.5055794	1.5074631	0.0649032
N	1.5489977	0.2435114	-0.0243887
C	1.8232296	-1.0898277	-0.0578413
N	0.6509718	-1.8507738	-0.0547685
H	-2.5451924	2.0884506	0.0067216
H	-2.2793868	-2.0575404	0.1339755
H	2.8196128	-1.4916853	-0.0994039
C	2.4838501	1.3515214	0.0151610
H	2.6560381	1.6651806	1.0427445
H	2.0521161	2.1797973	-0.5406644
H	3.4201896	1.0405318	-0.4393864

Table 9.8: Calculated cartesian coordinates (Å) of DMAde in the ground state optimised at the RI-SCS-MP2/aug-cc-pVDZ level of theory.

Atom	X	Y	Z
N	-3.4363066	1.9165284	0.0796396
C	-3.5922803	0.5738287	0.1826192
N	-2.6549434	-0.3873317	0.1613454
C	-1.4271235	0.1566758	0.0081863
C	-1.0892414	1.5208095	-0.1184284
C	-2.1918465	2.4365631	-0.0829252
N	-0.2247954	-0.5232094	-0.0785218
C	0.7603106	0.4250694	-0.2537533
N	0.2935587	1.6692998	-0.2857031
N	-2.0962534	3.7920586	-0.2417533
C	-0.8395518	4.5013042	0.0227508
H	0.0153403	3.8558648	-0.2033053
H	-0.7862763	4.8221207	1.0815233
H	-0.7991976	5.3962301	-0.6178645
C	-3.3135789	4.5927109	-0.0729220
H	-4.1344382	4.1596171	-0.6572715
H	-3.0956532	5.6094758	-0.4332935
H	-3.6256993	4.6411061	0.9873451
H	-4.6251840	0.2349987	0.3056422
H	-0.1107357	-1.5288518	-0.0269638
H	1.8101359	0.1536711	-0.3523264

Table 9.9: Calculated cartesian coordinates (Å) of DMAde in the $S_1(\pi\pi_{LE}^*)$ state optimised at the RI-SCS-CC2/aug-cc-pVDZ level of theory.

Atom	X	Y	Z
N	-3.4614749	1.9097344	0.0534132
C	-3.6308329	0.5716880	0.4783155
N	-2.6696083	-0.3508922	-0.0805858
C	-1.4326943	0.1428835	-0.0482012
C	-1.0610412	1.5139534	0.1405979
C	-2.1938217	2.4107363	0.0447683
N	-0.2318477	-0.5076690	-0.3131931
C	0.7786485	0.4495300	-0.2505734
N	0.3205487	1.6763468	-0.0142037
N	-2.0937686	3.7685443	-0.0891874
C	-0.8295597	4.4969394	0.0855768
H	0.0068808	3.7912848	0.1327161
H	-0.8839702	5.0923466	1.0142979
H	-0.7017261	5.1822010	-0.7693985
C	-3.3101152	4.5914342	-0.1498878
H	-4.1018049	4.0215575	-0.6533824
H	-3.0636231	5.5099604	-0.7046245
H	-3.6470218	4.8547674	0.8678677
H	-4.6648145	0.2133205	0.4872813
H	-0.1201008	-1.5061343	-0.4530018
H	1.8279879	0.1860069	-0.3745750

Table 9.10: Calculated cartesian coordinates (Å) of DMAde in the $S_1(\pi\pi^*_{\text{TWICT}})$ state optimised at the RI-SCS-CC2/aug-cc-pVDZ level of theory.

Atom	X	Y	Z
N	-3.4153371	2.0334986	1.0880671
C	-3.6496967	0.7306637	0.8818070
N	-2.8275362	-0.2510361	0.3689121
C	-1.6312713	0.2925318	0.0170777
C	-1.1874524	1.6260615	0.1925991
C	-2.1106384	2.5181292	0.9013670
N	-0.5434667	-0.3594089	-0.5455060
C	0.4626561	0.5786348	-0.7147383
N	0.1109382	1.7954012	-0.2744856
N	-2.0460822	3.8418194	0.2840234
C	-0.8731866	4.6564830	0.5764137
H	0.0071064	4.1588386	0.1226590
H	-0.7416801	4.6770895	1.6690811
H	-1.0079770	5.6647019	0.1570144
C	-2.8498081	4.1244380	-0.9113391
H	-2.2850432	3.8021610	-1.8068442
H	-3.0423178	5.2068680	-0.9633196
H	-3.7825065	3.5484351	-0.8231609
H	-4.6562837	0.3891941	1.1489525
H	-0.5147795	-1.3420707	-0.7981883
H	1.4206030	0.3261065	-1.1663718

Table 9.11: Calculated cartesian coordinates (Å) of DMAde in the $S_1(\pi\pi_{TS}^*)$ state optimised at the RI-SCS-CC2/aug-cc-pVDZ level of theory.

Atom	X	Y	Z
N	0.7635473	-1.6398046	-0.4077823
C	2.0545647	-1.6790673	0.1510667
N	2.7852887	-0.4240293	0.1227659
C	2.0153499	0.5849983	0.5118117
C	0.5808938	0.5836336	0.5955671
C	-0.0124860	-0.5702604	-0.0596937
N	2.3774709	1.9030649	0.7861958
C	1.2071708	2.6047952	1.0485370
N	0.1093240	1.8624734	0.9069730
N	-1.3337704	-0.6679240	-0.3858276
C	-2.3138840	0.4003378	-0.1462434
H	-1.8419496	1.2341648	0.3839502
H	-3.1486572	-0.0123271	0.4441208
H	-2.7028698	0.7437175	-1.1219469
C	-1.8371250	-1.8540420	-1.1019262
H	-1.7166747	-1.7044117	-2.1891321
H	-2.9057092	-1.9604629	-0.8611160
H	-1.2785572	-2.7437935	-0.7936064
H	2.6519151	-2.5615782	-0.0979860
H	3.3278075	2.2496105	0.8629239
H	1.2183420	3.6509154	1.3513340

Table 9.12: Calculated cartesian coordinates (Å) of DMAde in the $T_1(\pi\pi^*)$ state optimised at the RI-SCS-CC2/aug-cc-pVDZ level of theory.

Atom	X	Y	Z
N	-3.4596013	1.9178810	0.1771771
C	-3.6278892	0.6099234	0.2549639
N	-2.6104615	-0.4202237	0.2213296
C	-1.4176019	0.1195217	0.0085833
C	-1.0613288	1.5232167	-0.0989928
C	-2.1932751	2.4494409	0.0623253
N	-0.2107660	-0.5446331	-0.1445931
C	0.7854323	0.3978555	-0.3371093
N	0.2581382	1.6862137	-0.3067251
N	-2.0859987	3.8027007	-0.2277627
C	-0.8531003	4.5106634	0.1236255
H	0.0084710	3.8484454	-0.0258066
H	-0.8956525	4.8316107	1.1840067
H	-0.7624575	5.3997532	-0.5180014
C	-3.3035681	4.6107177	-0.1888280
H	-4.1115128	4.0875215	-0.7129041
H	-3.0837013	5.5735161	-0.6729672
H	-3.6190522	4.7890601	0.8575445
H	-4.6444877	0.2298654	0.3741208
H	-0.1063386	-1.5550611	-0.1335819
H	1.8309919	0.1505507	-0.4923844

Table 9.13: Calculated cartesian coordinates (Å) of the enolic CCC isomer of AA in the ground state optimised at the B3LYP-D3/6-311++G** level of theory.

Atom	X	Y	Z
C	-2.54920	-0.75870	0.00190
C	-1.24930	0.01220	-0.00350
H	-2.57670	-1.46950	-0.82920
H	-3.38830	-0.06840	-0.07320
H	-2.63460	-1.33690	0.92750
C	-0.01020	-0.73160	-0.00320
C	1.19770	-0.08580	0.00010
C	2.52140	-0.77810	0.00060
H	3.09470	-0.47170	-0.87910
H	2.40880	-1.86180	-0.00080
H	3.09310	-0.47370	0.88190
H	-0.03280	-1.81270	-0.00570
O	-1.26470	1.25700	-0.00210
O	1.29210	1.23780	0.00240
H	0.35470	1.58860	0.00150

Table 9.14: Calculated cartesian coordinates (Å) of the enolic CCC isomer of AA in the $S_1(n\pi^*)$ state optimised at the RI-SCS-CC2/def2-TZVPP level of theory.

Atom	X	Y	Z
C	-5.5647244	7.6039959	-0.8579652
C	-4.4760148	6.6865649	-1.3085963
H	-3.6252625	7.2531251	-1.6957401
H	-4.1183385	6.0706282	-0.4795348
H	-4.8603183	6.0385401	-2.0944747
C	-6.8669078	7.6784781	-1.3134452
H	-7.1386928	6.9852196	-2.0976505
C	-7.8514292	8.5493165	-0.8658371
C	-9.2448245	8.5867313	-1.3944706
H	-9.9620233	8.3954080	-0.5929535
H	-9.4703537	9.5733512	-1.8057342
H	-9.3810666	7.8404879	-2.1745310
O	-7.6493683	9.4788690	0.1198463
H	-6.7335276	9.4217416	0.4354594
O	-5.1234592	8.4743091	0.1670519

Table 9.15: Calculated cartesian coordinates (Å) of the enolic CCC isomer of AA in the $T_1(\pi\pi^*)$ state optimised at the RI-SCS-CC2/def2-TZVPP level of theory.

Atom	X	Y	Z
C	-5.4386359	7.8020509	-0.9536616
C	-4.4994277	6.6634743	-1.2818939
H	-3.5001404	7.0610241	-1.4413920
H	-4.4651862	5.9704230	-0.4390781
H	-4.8286722	6.1120399	-2.1617835
C	-6.8529139	7.6407608	-1.1991192
H	-7.2317408	6.6417384	-1.3991687
C	-7.8104933	8.7697009	-1.0092941
C	-9.2138368	8.6226630	-1.4864372
H	-9.7619141	7.8646022	-0.9104325
H	-9.7444207	9.5681098	-1.3826100
H	-9.2297740	8.3262685	-2.5353367
O	-7.7140590	9.3122250	0.2633686
H	-6.7577426	9.4269077	0.4076717
O	-5.0173825	8.8548115	-0.4294127

Table 9.16: Calculated cartesian coordinates (Å) of the enolic CTC isomer of AA in the ground state optimised at the B3LYP-D3/6-311++G** level of theory.

Atom	X	Y	Z
C	-2.56440	-0.70920	0.00000
C	-1.28960	0.12150	-0.00000
H	-2.59640	-1.35780	0.88160
H	-2.59640	-1.35790	-0.88150
H	-3.43000	-0.04860	-0.00000
C	-0.04450	-0.66280	-0.00000
C	1.21970	-0.17670	-0.00000
O	2.29740	-1.00400	-0.00000
H	-0.16740	-1.74410	-0.00000
C	1.65110	1.25030	0.00000
H	2.27480	1.43410	-0.88010
H	2.27340	1.43440	0.88100
H	0.79540	1.91810	-0.00080
O	-1.34730	1.34270	-0.00000
H	2.01200	-1.92620	0.00010

Table 9.17: Calculated cartesian coordinates (Å) of the enolic CTC isomer of AA in the $S_1(n\pi^*)$ state optimised at the RI-SCS-CC2/def2-TZVPP level of theory.

Atom	X	Y	Z
C	-5.9701546	6.9175293	-1.6590565
C	-4.4863153	6.5963798	-1.6214668
H	-4.2972255	5.6834920	-2.1792819
H	-3.9146622	7.4199044	-2.0533292
H	-4.1563888	6.4745308	-0.5881292
C	-6.3430729	8.1433267	-0.9296664
H	-5.5272265	8.6763053	-0.4510483
C	-7.5903153	8.6616049	-0.8012061
C	-8.8641305	8.1227603	-1.3592725
H	-9.5570318	7.9325621	-0.5387240
H	-9.3153785	8.8783535	-2.0035055
H	-8.6818614	7.2122667	-1.9170543
O	-7.8170719	9.8075777	-0.0991829
H	-6.9748658	10.1285810	0.2470833
O	-6.7552708	6.1844328	-2.2615846

Table 9.18: Calculated cartesian coordinates (Å) of the enolic CTC isomer of AA in the $T_1(n\pi^*)$ state optimised at the RI-SCS-CC2/def2-TZVPP level of theory.

Atom	X	Y	Z
C	-5.8962042	7.0267227	-1.5103944
C	-4.4817869	6.5430880	-1.6152506
H	-4.2035707	6.3688861	-2.6575293
H	-3.8181239	7.2957624	-1.1926854
H	-4.3471847	5.6049641	-1.0712822
C	-6.3140888	8.2391142	-0.9642828
H	-5.5047993	8.8594814	-0.5922105
C	-7.6007132	8.7243567	-0.8470550
C	-8.8630183	8.0641240	-1.2793587
H	-9.5287721	7.9273166	-0.4242446
H	-9.3854613	8.6895058	-2.0067623
H	-8.6673118	7.0929250	-1.7293968
O	-7.8497409	9.9561381	-0.2763177
H	-7.0088805	10.3466054	-0.0120730
O	-6.7813152	6.1006166	-2.0365816

Table 9.19: Calculated cartesian coordinates (Å) of MS I in the ground state optimised at the RI-MP2/def2-TZVPPD level of theory.

Atom	X	Y	Z
C	-2.8798691	0.7070205	-0.0157308
C	-1.9663768	1.7644434	-0.0690557
C	-0.6078815	1.4946385	-0.0577027
C	-0.1443526	0.1723304	0.0066872
C	-1.0683206	-0.8904644	0.0603067
C	-2.4368977	-0.6050722	0.0481921
C	1.2925683	-0.1374925	0.0198573
O	2.0780675	0.9447145	-0.0345623
O	-0.6974266	-2.1843075	0.1234349
H	0.1142383	2.2971090	-0.0981989
H	-3.9428435	0.9083115	-0.0241068
H	-2.3160710	2.7858276	-0.1187943
H	-3.1309078	-1.4331887	0.0899276
H	0.2837653	-2.1907042	0.1223547
C	3.4870900	0.6573549	-0.0225189
H	3.7563485	0.1343048	0.8906061
H	3.9734498	1.6240670	-0.0709116
H	3.7536801	0.0469730	-0.8805626
O	1.7506107	-1.2756039	0.0752223

Table 9.20: Calculated cartesian coordinates (Å) of MS I in the $S_1(\pi\pi^*)$ state optimised at the RI-CC2/def2-TZVPPD level of theory.

Atom	X	Y	Z
C	-2.9721663	0.7311597	-0.0163527
C	-2.0706655	1.7587263	-0.0695179
C	-0.6454194	1.5052815	-0.0592610
C	-0.1615306	0.2162698	0.0046127
C	-1.1170218	-0.8787811	0.0612412
C	-2.4760812	-0.6196405	0.0505920
C	1.2456816	-0.0877668	0.0174491
O	2.1141967	0.9333247	-0.0352621
O	-0.6383741	-2.1263461	0.1230376
H	0.0443182	2.3387979	-0.1023031
H	-4.0370309	0.9180770	-0.0238714
H	-2.4067610	2.7864396	-0.1205075
H	-3.1529835	-1.4637358	0.0941460
H	0.8196308	-1.8812133	0.1081895
C	3.5060614	0.5586175	-0.0189254
H	3.7415059	0.0232621	0.8978263
H	4.0476497	1.4965902	-0.0670373
H	3.7383331	-0.0660113	-0.8782031
O	1.7195280	-1.3227894	0.0785915

Table 9.21: Calculated cartesian coordinates (Å) of MS I in the $T_1(\pi\pi^*)$ state optimised at the RI-CC2/def2-TZVPPD level of theory.

Atom	X	Y	Z
C	-2.9800649	0.7247890	-0.0163012
C	-2.0681910	1.7513934	-0.0678122
C	-0.6508262	1.5225811	-0.0586194
C	-0.1422771	0.2195058	0.0043502
C	-1.0982788	-0.8873739	0.0598990
C	-2.4850969	-0.6097589	0.0482794
C	1.2321601	-0.0774944	0.0168816
O	2.1170612	0.9336485	-0.0338301
O	-0.6846835	-2.1151687	0.1193971
H	0.0269788	2.3639805	-0.1007625
H	-4.0436503	0.9151657	-0.0241230
H	-2.4155847	2.7761502	-0.1174436
H	-3.1501089	-1.4630657	0.0909967
H	0.8839396	-1.8912553	0.1061125
C	3.5040824	0.5501917	-0.0172156
H	3.7397573	0.0135448	0.8986646
H	4.0517285	1.4848548	-0.0638095
H	3.7370067	-0.0733682	-0.8770335
O	1.7249188	-1.3180588	0.0768139

Table 9.22: Calculated cartesian coordinates (Å) of MS II in the ground state optimised at the RI-MP2/def2-TZVPPD level of theory.

Atom	X	Y	Z
C	-6.4269175	-0.4799191	0.0035528
C	-6.3106358	0.9122605	-0.0213043
C	-5.0513263	1.4869580	-0.0256788
C	-3.8920264	0.6966745	-0.0056146
C	-4.0157924	-0.7058500	0.0193958
C	-5.2922899	-1.2758871	0.0236018
C	-2.6069913	1.4316283	-0.0127879
O	-2.4865077	2.6351142	-0.0341900
O	-1.5220572	0.6012999	0.0076608
C	-0.2537327	1.2822899	0.0014112
H	-0.1606938	1.8860601	-0.8961697
H	0.4934156	0.4976717	0.0193785
H	-0.1693388	1.9184379	0.8772189
O	-2.9742669	-1.5719709	0.0402820
H	-4.9250589	2.5606356	-0.0446814
H	-7.4031968	-0.9459498	0.0073113
H	-7.1928481	1.5362270	-0.0369989
H	-5.3630612	-2.3547377	0.0429641
H	-2.1582139	-1.0462429	0.0346582

Table 9.23: Calculated cartesian coordinates (Å) of MS II in the $S_1(\pi\pi^*)$ state optimised at the RI-CC2/def2-TZVPPD level of theory.

Atom	X	Y	Z
C	-3.0753119	-0.0104885	-0.0157871
C	-2.4886920	1.2616141	-0.0086084
C	-1.0700891	1.4578739	-0.0022865
C	-0.1736139	0.3716048	-0.0031496
C	-0.8036534	-0.9467167	-0.0105980
C	-2.1982653	-1.1300298	-0.0167833
C	1.2380092	0.6161486	0.0032156
O	1.8069021	1.7134300	0.0097148
O	1.9937337	-0.5916833	0.0012688
C	3.4182290	-0.3870372	0.0078084
H	3.7181190	0.1709221	-0.8753209
H	3.8539999	-1.3811088	0.0046207
H	3.7112742	0.1621875	0.8986885
O	-0.0467615	-2.0458162	-0.0118331
H	-0.6586931	2.4585873	0.0032348
H	-4.1466554	-0.1403082	-0.0205070
H	-3.1197188	2.1415943	-0.0076609
H	-2.5642619	-2.1485318	-0.0221129
H	0.9100697	-1.7224353	-0.0069184

Table 9.24: Calculated cartesian coordinates (Å) of MS II in the $T_1(\pi\pi^*)$ state optimised at the RI-CC2/def2-TZVPPD level of theory.

Atom	X	Y	Z
C	-3.0375929	0.0103592	-0.1169334
C	-2.4063063	1.3240127	-0.0260357
C	-1.0469306	1.4917662	0.0596687
C	-0.1729213	0.3676435	0.0263561
C	-0.8434153	-0.9857130	0.0379196
C	-2.2219661	-1.1125052	-0.0552173
C	1.2414744	0.5979839	-0.0048947
O	1.7998892	1.6999616	0.0275861
O	1.9862931	-0.5881822	-0.0715802
C	3.4126821	-0.3822031	-0.0538939
H	3.7104455	0.2232064	-0.9055847
H	3.8463802	-1.3747242	-0.1131051
H	3.7068578	0.1171518	0.8656905
O	-0.0867807	-2.0850601	0.2004267
H	-0.6039293	2.4765986	0.1180960
H	-4.1104319	-0.0726753	-0.1947152
H	-3.0391992	2.2029339	-0.0225851
H	-2.6335252	-2.1138089	-0.0534023
H	0.8562427	-1.7914683	0.1622316

List of Figures

1.1	Schematic illustration of the pump–probe principle.	3
1.2	Schematic visualisation of the deactivation pathways, the transient spectra and the time profiles after photoexcitation of isomer A. . .	5
1.3	Overview of the four selected molecular systems which have been investigated.	8
2.1	Schematic representation of the singular value decomposition of data matrix A and the corresponding reduced data matrix \tilde{A}	23
2.2	Schematic representation of the time-resolved vibrational absorption spectroscopy setup.	25
2.3	Schematic representation of the pump pulse generation for $\lambda_{\text{exc}} = 267 \text{ nm}$	26
2.4	Detailed representation of the time-resolved vibrational absorption spectroscopy setup.	27
2.5	Schematic representation of the Hartree–Fock self-consistent field procedure.	36
3.1	Summary of the TVAS results for 7-MePur and 9-MePur.	52
4.1	Chemical structures of purine and its methylated analogues.	57
4.2	Static absorption and fluorescence spectra of 7- and 9-methylpurine in ACN.	63
4.3	TFLS and TCSPC measurements on 7- and 9-MePur in ACN after photoexcitation.	64
4.4	TVAS results for 7-MePur in ACN- d_3 after photoexcitation.	67
4.5	TVAS results for 9-MePur in ACN- d_3 after photoexcitation.	70
4.6	Single point calculations of the GS, $S_2(\pi\pi^*)$, $S_1(n\pi^*)$ and the T_1 and T_2 states for 7- and 9-MePur.	72

4.7	Proposed electronic deactivation pathways for 7- and 9-MePur in ACN after photoexcitation.	76
4.8	Minimum energy structures of 7- and 9-MePur in different electronic states.	81
4.9	Calculated and experimental vibrational spectra for 7-MePur and 9-MePur.	82
4.10	Experimental and calculated vibrational marker modes of 7-MePur in the electronic GS.	83
4.11	Experimental and calculated vibrational marker modes of 7-MePur in the $S_1(n\pi^*)$ state.	84
4.12	Experimental and calculated vibrational marker modes of 7-MePur in the $T_1(\pi\pi^*)$ state.	85
4.13	Experimental and calculated vibrational marker modes of 9-MePur in the electronic GS.	86
4.14	Experimental and calculated vibrational marker modes of 9-MePur in the $S_1(n\pi^*)$ state.	87
4.15	Experimental and calculated vibrational marker modes of 9-MePur in the $S_2(\pi\pi^*)$ state.	88
4.16	Experimental and calculated vibrational marker modes of 9-MePur in the $T_1(\pi\pi^*)$ state.	89
4.17	Static and time-resolved fluorescence spectroscopy of purine in ACN.	90
4.18	TVAS results for purine in CD_3OD after photoexcitation.	92
4.19	TVAS results for purine in $ACN-d_3$ after photoexcitation.	93
4.20	Selected time profiles for Pur in CD_3OD and $ACN-d_3$ after photoexcitation.	94
5.1	Chemical structure and static absorption and fluorescence spectra of DMAde.	97
5.2	Minimum energy structures of DMAde in the GS and in the $S_1(\pi\pi_{LE}^*)$ and $S_1(\pi\pi_{TWICT}^*)$ excited states.	106
5.3	Fluorescence time profiles for DMAde in ACN after excitation at $\lambda_{exc} = 266$ nm.	108
5.4	Reconstructed and normalised transient fluorescence spectra of DMAde in ACN after excitation at $\lambda_{exc} = 266$ nm.	109
5.5	Experimental results of the TEAS measurements of DMAde in ACN after excitation at $\lambda_{exc} = 266$ nm.	110

5.6	DADS and EADS from the SVD data analysis of the TEAS data for DMAde in ACN after excitation at $\lambda_{\text{exc}} = 266$ nm.	111
5.7	TVAS measurements of DMAde in ACN-d ₃ after excitation at $\lambda_{\text{exc}} = 267$ nm.	114
5.8	Single point calculations for the GS, $S_1(\pi\pi^*)$, $S_2(\pi\pi^*)$, $S_4(n\pi^*)$ and $^3\pi\pi^*$ states for DMAde.	118
5.9	Deactivation mechanism for DMAde in ACN after photoexcitation at $\lambda_{\text{exc}} = 267$ nm.	122
5.10	Fluorescence time profiles in the UV for DMAde in ACN after excitation at $\lambda_{\text{exc}} = 266$ nm.	129
5.11	Fluorescence time profiles in the visible region for DMAde in ACN after excitation at $\lambda_{\text{exc}} = 266$ nm.	130
5.12	TCSPC time profiles at $\lambda_{\text{fl}} = 340$ nm and $\lambda_{\text{fl}} = 480$ nm for DMAde in ACN after excitation at $\lambda_{\text{exc}} = 265$ nm.	131
5.13	Natural transition orbitals involved in the electronic transitions for DMAde.	132
5.14	Calculated vibrational spectra in the GS, $S_1(\pi\pi_{\text{LE}}^*)$, $S_1(\pi\pi_{\text{TWICT}}^*)$ and $T_1(\pi\pi^*)$ states for DMAde.	132
5.15	Calculated and experimental vibrational marker modes of DMAde in the electronic GS.	133
5.16	Calculated and experimental vibrational marker modes of DMAde in the $S_1(\pi\pi_{\text{TWICT}}^*)$ excited state.	134
5.17	Calculated and experimental vibrational marker modes of DMAde in the $T_1(\pi\pi^*)$ excited state.	135
6.1	Tautomeric equilibrium of AA along with an overview of the different isomers of enol-type AA.	140
6.2	Static experimental spectra of AA alongside with the calculated vibrational spectra for all enolic isomers of AA.	143
6.3	TVAS measurements of enol-type AA after excitation at $\lambda_{\text{exc}} = 267$ nm in ACN-d ₃ and CHX.	146
6.4	Calculated and experimental vibrational marker modes of CCC and CTC in the different electronic states.	149
6.5	Proposed electronic deactivation and isomerisation pathways for enol-type AA after UV excitation.	153

6.6	Calculated and experimental vibrational marker modes of all enol isomers of AA in the GS.	161
6.7	Calculated vibrational spectra in the different electronic states for the CCC and CTC isomers.	162
6.8	Structural representation of possible photofragments upon UV photoexcitation of enol-type CCC.	163
6.9	Vibrational calculations for all possible CCC photofragments.	164
6.10	Single point calculations of the different electronic states for the CCC and CTC isomers.	164
7.1	Chemical structures of MS I and MS II in the GS along with the keto-type form of MS I in the excited state.	168
7.2	Minimum energy structures of MS I and MS II in the different electronic states.	174
7.3	UV absorption spectra of MS in ACN and CHX.	175
7.4	Static fluorescence spectra of MS in ACN and CHX.	176
7.5	TCSPC measurements of MS in ACN and CHX after excitation at $\lambda_{\text{exc}} = 290$ nm.	177
7.6	TFLS time profiles of MS in ACN and CHX after excitation at $\lambda_{\text{exc}} = 305$ nm.	179
7.7	TEAS results of MS in ACN and CHX after excitation at $\lambda_{\text{exc}} = 313$ nm.	181
7.8	TVAS measurements of MS in ACN-d ₃ and CHX after excitation at $\lambda_{\text{exc}} = 313$ nm.	185
7.9	TVAS time profiles of the involved species for MS in ACN-d ₃ and CHX after excitation at $\lambda_{\text{exc}} = 313$ nm.	186
7.10	Proposed deactivation mechanism for rotamer MS I in the liquid phase after photoexcitation.	190
7.11	DADS and EADS from the SVD data analysis of the TEAS data for MS in ACN and CHX after excitation at $\lambda_{\text{exc}} = 313$ nm.	196
7.12	Experimental FTIR spectra of MS in CHX and ACN-d ₃ and calculated vibrational spectra of MS I and MS II in the GS.	197
7.13	Visualisations of the experimental and calculated vibrational marker modes of rotamer MS I in the electronic GS.	198
7.14	Visualisations of the experimental and calculated vibrational marker modes of rotamer MS II in the electronic GS.	199

7.15	Visualisations of the experimental and calculated vibrational marker modes of the keto-type form of MS I in the $S_1(\pi\pi^*)$ state.	200
7.16	TVAS measurements of MS in ACN-d ₃ after excitation at $\lambda_{\text{exc}} = 313$ nm.	203
7.17	TVAS time profiles of the involved species for MS in ACN-d ₃ after excitation at $\lambda_{\text{exc}} = 313$ nm.	204

List of Tables

4.1	Calculated vertical excitation energies for 7- and 9-MePur.	62
4.2	Time components τ_i for 7-MePur, 9-MePur and Pur in acetonitrile.	73
5.1	Calculated vertical excitation energies for DMAd.	104
5.2	Molecular and structural properties of the minimum structures in different electronic states for DMAd.	107
5.3	Time components τ_i for DMAd from the experimental TFLS, TEAS and TVAS data.	120
6.1	Calculated energies of all enol isomers of AA in the GS with respect to the thermodynamically stable CCC isomer.	160
6.2	Global fit results from the TVAS data for AA after excitation at $\lambda_{\text{exc}} = 267$ nm in ACN- d_3 and CHX.	160
7.1	Calculated vertical excitation energies for MS I and MS II.	174
7.2	Time components τ_i obtained from the TCSPC, TFLS, TEAS and TVAS data of MS in ACN(- d_3) and CHX.	188
7.3	Relative amplitudes A_i from the global analyses of the TFLS data of MS after excitation at $\lambda_{\text{exc}} = 305$ nm in ACN and CHX.	195
7.4	Summary of the TVAS data for MS after excitation at $\lambda_{\text{exc}} = 313$ nm in ACN- d_3	201
7.5	Summary of the TVAS data for MS after excitation at $\lambda_{\text{exc}} = 313$ nm in CHX.	202
9.1	Calculated cartesian coordinates of 7-MePur in the ground state.	223
9.2	Calculated cartesian coordinates of 7-MePur in the $S_1(n\pi^*)$ state.	224
9.3	Calculated cartesian coordinates of 7-MePur in the $T_1(\pi\pi^*)$ state.	225
9.4	Calculated cartesian coordinates of 9-MePur in the ground state.	226
9.5	Calculated cartesian coordinates of 9-MePur in the $S_2(\pi\pi^*)$ state.	227
9.6	Calculated cartesian coordinates of 9-MePur in the $S_1(n\pi^*)$ state.	228

9.7	Calculated cartesian coordinates of 9-MePur in the $T_1(\pi\pi^*)$ state. .	229
9.8	Calculated cartesian coordinates of DMAde in the ground state. .	230
9.9	Calculated cartesian coordinates of DMAde in the $S_1(\pi\pi_{LE}^*)$ state. .	231
9.10	Calculated cartesian coordinates of DMAde in the $S_1(\pi\pi_{TWICT}^*)$ state.	232
9.11	Calculated cartesian coordinates of DMAde in the $S_1(\pi\pi_{TS}^*)$ state. .	233
9.12	Calculated cartesian coordinates of DMAde in the $T_1(\pi\pi^*)$ state. .	234
9.13	Calculated cartesian coordinates of CCC in the ground state. . .	235
9.14	Calculated cartesian coordinates of CCC in the $S_1(n\pi^*)$ state. . .	236
9.15	Calculated cartesian coordinates of CCC in the $T_1(\pi\pi^*)$ state. . .	237
9.16	Calculated cartesian coordinates of CTC in the ground state. . .	238
9.17	Calculated cartesian coordinates of CTC in the $S_1(n\pi^*)$ state. . .	239
9.18	Calculated cartesian coordinates of CTC in the $T_1(n\pi^*)$ state. . .	240
9.19	Calculated cartesian coordinates of MS I in the ground state. . .	241
9.20	Calculated cartesian coordinates of MS I in the $S_1(\pi\pi^*)$ state. . .	242
9.21	Calculated cartesian coordinates of MS I in the $T_1(\pi\pi^*)$ state. . .	243
9.22	Calculated cartesian coordinates of MS II in the ground state. . .	244
9.23	Calculated cartesian coordinates of MS II in the $S_1(\pi\pi^*)$ state. . .	245
9.24	Calculated cartesian coordinates of MS II in the $T_1(\pi\pi^*)$ state. . .	246